Modeling the Residual Stress Distribution and Experimental Characterization of Shot Peening on AZ31B Rolled Sheet

by

Amir Yazdanmehr

A thesis
presented to the University of Waterloo
in fulfillment of the
thesis requirement for the degree of
Doctor of Philosophy
in
Mechanical and Mechatronics Engineering

Waterloo, Ontario, Canada, 2019

Examining Committee Membership

The following served on the Examining Committee for this thesis. The decision of the Examining Committee is by majority vote.

External Examiner	Mario Guagliano Professor
Supervisor	Hamid Jahed Professor
Internal Member	Duane Cronin Professor
Internal Member	Giovanni Montesano Assistant Professor
Internal-external Member	Scott Walbridge Associate Professor

AUTHOR'S DECLARATION

This thesis consists of material all of which I authored or co-authored: see Statement of Contributions included in the thesis. This is a true copy of the thesis, including any required final revisions, as accepted by my examiners.

I understand that my thesis may be made electronically available to the public.

Statement of Contributions

Chapter 3 of this thesis consists of a paper, ready for submission to a peer-reviewed journal, co-authored by myself and my supervisor (Dr. Jahed). The hole-drilling experiments have been done by a FATSLab colleague, Mrs. Bahareh Marzbanrad. All other parts are my contributions.

Chapter 4 has been incorporated within a paper to be submitted in a peer-reviewed journal for publication. I am the first author of this paper. The article is co-authored by Dr. Roostaei and my supervisor (Dr. Jahed). Regarding the contents published in this thesis, Dr. Roostaei has assisted me with the writing of this chapter and preparing the experiments' set-ups. All other parts are my contributions.

Chapter 5 of this thesis consists of a paper, ready for submission to a peer-reviewed journal, co-authored by myself and my supervisor (Dr. Jahed). Again, the hole-drilling experiments have been done by Mrs. Bahareh Marzbanrad. All other parts are my contributions.

Chapter 6 of this thesis consists of a paper, ready for submission to a peer-reviewed journal, co-authored by myself and my supervisor (Dr. Jahed).

Chapter 7 of this thesis consists of a paper, ready for submission to a peer-reviewed journal, co-authored by myself and my supervisor (Dr. Jahed).

The balance of the research is my own work.

Abstract

The drive to reduce fossil fuel consumption due to its environmental impacts has generated renewed interest in employing magnesium (Mg), the lightest industrial metal, and its alloys in vehicle manufacturing. One of the qualifying metrics for structural application of Mg in transportation vehicles is its high durability. The low fatigue strength of these alloys has been an obstacle to using them in load-bearing components. Thus, methods for improving the fatigue properties of Mg alloys are of interest. Shot peening is a cold-working process employed to improve the fatigue properties of materials. The shot peening process induces compressive residual stress at the material's surface and at a layer in the order of a few hundred micrometers deep, which improves the fatigue life by retarding the crack initiation as well as growth; however, the increased surface roughness has a detrimental effect on fatigue life. These competing effects of peening have created interest in finding the optimum peening intensity that will maximize fatigue life. Modeling reduces the cost of experimentally evaluating optimum peening conditions. However, modeling the shot peening of Mg alloys remains complicated due to the anisotropic and asymmetric properties of wrought Mg alloys, and the complex unloading behavior and rate-sensitivity behavior of these materials. To address these challenges, a comprehensive experimental and numerical-analytical study of shot peening on AZ31B-H24 rolled sheet was conducted and is reported in this thesis.

First residual stress distributions through the depth of the material were measured. Among the methods for residual stress measurement, X-ray diffraction (XRD) has attracted researchers' attention because: 1) it is a non-destructive method; 2) it can measure residual stress at the surface, and 3) the spatial resolution can be less than 0.3 mm. However, due to the low x-ray mass attenuation coefficient of Mg alloys, x-ray penetration in the material is significant which needs to be accounted for. The residual stresses in as-received and shot peened AZ31B-H24 rolled sheet samples were measured using the 2D-XRD method. The electro-polishing layer removal method was used to find the residual stress pattern through depth. Due to the high depth of penetration, a correction had to be made to account for the penetration depth. The results showed that the corrected residual stresses in a few tens of micrometers layer from the surface were different from the raw stresses. To better estimate the residual stress distribution in a few micrometers from the surface, the grazing-incidence x-ray diffraction (GIXD) method was applied to evaluate the stresses in the surface layer. This study also showed how small uncertainty in measuring the observed residual stress and in evaluating the depth of the polished area in layer removal leads to high uncertainty in the corrected residual stresses. The XRD results showed the creation of compressive residual stress through the depth as well as a good agreement between the XRD and hole-drilling and GIXD results.

Modeling the shot peening process first requires an understanding of how Mg alloys behave at large strain values during loading-unloading. The tension-compression (TC) and compression-tension (CT) in the in-plane directions were obtained using an anti-buckling fixture. By comparing the compression part of the CT curves along the rolling direction (RD) with the ones using a cuboid sample, the negligible effect of using the anti-buckling fixture was shown. A novel fixture was designed to obtain the CT and TC curves in the through-thickness (normal direction: ND) of the rolled sheet, which is only 6.3 mm thick. FEM was employed to evaluate the consistent area for strain measurement using DIC in the designed setup. The CT and TC curves along ND were obtained using the new fixture. The results of the new fixture were verified by comparing the curves obtained by the new fixture in RD with those obtained by using the anti-buckling fixture.

Different effects of shot peening on the AZ31B-H24 rolled sheet were characterized in this study by measuring the residual stress and micro-hardness distribution through the depth, followed by measuring surface roughness and texture evolution at the surface of samples shot peened under Almen intensities ranging from 0.05 mmN to 0.6 mmN. To obtain the optimum peening intensity, rotating bending fatigue tests were performed on peened samples at different intensities. It was found that increasing the peening intensity, increases the surface roughness and hardness at the surface layer. In addition, the depth of the maximum compressive stress and the depth of the induced compressive residual stress layer have a direct relation with the peening intensity. The material showed a high sensitivity to shot peening under different intensities, due to the over-peening effects in the peening on Mg alloys. Peening at the optimum intensity increases the fatigue strength moderately, from 130 MPa to 150 MPa.

During investigations to find an accurate and a computationally efficient method for capturing the complex behavior of Mg alloys, it was found that stringent assumptions are needed to allow for a closed-form analytical solution when calculating residual stresses induced by shot peening. This limits the application of these models to idealized conditions. On the other hand, and because of the complex behaviors of Mg alloys, such as complex unloading behavior and rate-sensitivity, it is difficult to provide numerical solutions such as finite element that are capable of mimicking actual material's behavior once it is released from an over-strain loading state. Moreover, modeling full coverage shot peening condition is time-consuming and computationally expensive. A single-shot finite element model was combined with an analytical model using actual loading-unloading material behavior to propose a hybrid FEM-analytical model for prediction of the residual stress distribution in shot peening. First, the shot peening process was divided into a loading phase, modeling the impact of a shot and substrate, and an unloading phase, modeling the rebounding of the shot. Finite element was employed to model a single shot impingement on a substrate using the actual loading properties of the substrate. Using the results of the loading phase, an analytical

model was proposed to predict stresses due to the unloading phase, using the actual unloading behavior of the material. The proposed hybrid model accounts for the actual behavior of a material, actual elastic-plastic contact analysis, strain rate effect, and friction. The model was then verified by predicting residual stresses induced in a SAE1070 and an Al2024-T351 sheet. Results were compared with the available experimental results and showed close agreements.

The application of the proposed hybrid numerical-analytical model was extended to use with an asymmetric and anisotropic material that also has complex unloading behavior, i.e., Mg alloys. First, the loading state of material under peening and the effects of the material's asymmetry and anisotropy were discussed, then the numerical modeling of the loading step was provided. Finally, the actual unloading curves, measured using the designed fixture, of the material were used to estimate the residual stress profiles. The strain rate effect was also considered in the modeling. The results were matched closely with the XRD and hole-drilling experimental measurements.

Acknowledgments

First of all, I wish to praise and thank God for all His blessings. I would not have made any progress without His providence.

I would like to express my sincere gratitude to my supervisor, Professor Hamid Jahed, for his valuable supports and insightful guidance.

My heartfelt gratitude goes to my family, my parents, parents-in-law, brother and sister, and (brothers/sisters)-in-law for their boundless love and encouragement all through my Ph.D. career. I owe my deepest gratitude to my dear wife, Mahya, for her understanding, encouragement, and patience, which made this research possible.

I greatly appreciate my FATSLab research colleagues, Dr. Seyed Behzad Behravesh, Bahareh Marzbanrad, Dr. Ali Asghar Roostaei, Sasan Faghih, Dr. Andrew Gryguc, Dwayne Toscano, Dr. Sugrib Shaha, and Ali Karparvardfard for their precious thoughts and discussions, and helping me with the experiments.

I am also grateful to Javaid Khan and Sheamus Doherty from Metal Improvement Co., at Brampton, Ontario, for their in-kind contributions by performing controlled shot peening on my samples.

Furthermore, I would like to acknowledge the support of Natural Sciences and Engineering Research Council of Canada (NSERC) through the Automotive Partnership Canada (APC) under APCPJ 459269–13 grant throughout this work.

Table of Contents

List of Figures

List of Tables

Nomenclature

a	Radius of indentation
A	Cross-section area of the target material
D	Shot diameter
d	Lattice spacing
E	Young’s modulus
E_H	Contact equivalent Young’s modulus
h	Target thickness
I	Moment of inertia of the target material
I	X-ray Intensity
k	Efficiency coefficient
p_0	Maximum contact pressure
V	Shot velocity
w	Target width
z	Depth
α	Ratio of plastic to elastic radius of indentation
γ	The angle along each diffraction ring, orthogonal to the 2θ direction
ε	Strain
2θ	Diffraction angle
λ	Wavelength
μ	Linear absorption coefficient
ν	Poisson’s ratio
ρ	Density
σ	Stress
φ	Rotation angle about the surface normal
ψ	Tilt angle between the specimen’s normal surface and the diffraction vector
ω	X-ray incident angle

Subscripts

0	Stress-free
eq	Equivalent
s	Shot

t	Target
y	Yield
z	Depth

Superscripts

0	Initial
e	Elastic solution
ep	Elastic-plastic solution
un	Unloading

Chapter 1

Introduction

1.1 Research motivations

Steel and aluminum have been the dominant materials in vehicle manufacturing since the 1920s [1]. The material selected for a vehicle's construction is a key factor in the vehicle's overall weight and therefore is directly linked to its fuel efficiency. As legislative requirements for cleaner and safer vehicles are forcing automakers to reduce the amount of exhaust emissions, and as carbon dioxide emission is in direct proportion to fuel consumption [2], car weight has become one of the most critical criteria in efficient designing of vehicles. Reducing the automotive weight by a certain amount will result in a similar percentage of improvement in the fuel economy [1]; as a result, interest in magnesium (Mg), the lightest engineering metal commercially available, has increased in the auto industry [2], [3].

Volkswagen was the first automotive company to apply Mg, in its Beetle model, which used 22 kg of Mg in each car [4]. Porsche first worked with a Mg engine in 1928 [2]. Since then, the average usage of Mg in the automotive industry has grown by 10-15 percent annually over the past 15 years to an average of 10-12 lbs. (range 1-35 lbs.) [5]. To decrease the weight of a car, the use of light metals should be extended to load-bearing structural components. Many such components are under cyclic loading that can fail due to the fatigue mechanism. Thus, significant research is still needed to enhance Mg's mechanical properties in order to extend its applications in this industry.

Shot peening has been widely used to improve the fatigue life of different materials since the 1920s. The shot peening process induces compressive residual stress at the material's surface and at a layer in the order of a few hundred micrometers deep; this is beneficial, but it also increases surface roughness, which has a negative effect on fatigue strength. The trade-off of these effects forces researchers to find the optimum peening process parameters. To this end, a verified method for finding the optimum peening conditions for Mg alloys is needed. However, while the investigation of optimal peening parameters has been an active research topic for the past 15 years [6], the modeling of shot peening and the gathering of experimental measurements on Mg alloys remain challenging due to the material anisotropy, asymmetry and high depth of x-ray penetration through the depth of Mg alloys. A key factor in evaluating the optimum peening condition is to model the residual stress distribution through the depth of peened samples. Available modeling methods of the shot peening process are not capable of modeling the anisotropic and asymmetric materials. Therefore, developing a method that can capture the actual complex properties of Mg alloys is of significance. In addition, there is no study regarding the characterization and finding the optimum peening condition for the AZ3B-H24 rolled sheet. These needs have motivated the research as described in this thesis.

1.2 Research objectives

The major objectives of this study are as follows:

1.2.1 Modeling the residual stress distribution after shot peening of Mg alloys

The main objective of this study is to provide a method to capture the complex material properties of Mg alloys in modeling the residual stress profile induced in the peening process. The new method should automatically be capable of evaluating the residual stresses in materials with isotropic and symmetric properties such as steel and aluminum alloys. Therefore, first, the proposed model is verified by modeling the residual stress distribution on steel and aluminum alloys, then extended to capture the properties of Mg alloys.

1.2.2 Characterization and experimental evaluation of the optimum shot peening condition to enhance the fatigue life of AZ31B-H24 rolled sheet

This study characterizes the effects of shot peening under different conditions on the AZ31B, most widely used Mg alloy, rolled sheet, including residual stress, micro-hardness, surface roughness, and texture evolution. This characterization is necessary to investigate reasons for improved fatigue life. In addition, such characterization could be employed in future studies to verify the modeling of different effects of peening on the material. The optimum peening situation is experimentally obtained by evaluating the fatigue lives of the peened samples under different peening conditions. Then, the samples are peened at the optimum intensity, and the S-N curves of the as-received samples and peened ones are compared to investigate the effect of peening on the improvement of the fatigue life of the material.

1.3 Thesis overview

In addition to the current chapter, there are seven more chapters, including five manuscripts either submitted or ready for submission in peer-reviewed journals.

Chapter 2 is divided into two sections: background and literature review. The background section discusses the significance of using Mg alloys in the automotive industry, then the shot peening process is introduced and different parameters involved in this process are discussed. The background section is followed by an introduction to the fundamentals of measuring residual stress using two-dimensional x-ray diffraction (2D-XRD). In the literature review section, two types of shot peening modeling, analytical and finite element modeling (FEM), are introduced and reviewed. Finally, relevant studies on the effects of shot peening on Mg alloys are discussed.

Chapter 3 discusses the residual stress measurement through the depth of Mg alloys, using XRD. The primary purpose of this study is to model the residual stress distribution through the depth of the AZ31B-H24 peened samples. To verify the modeling, it is necessary to accurately measure the residual stresses experimentally. XRD is among the most used methods for residual stress measurement. As x-rays penetrate Mg alloys too deeply, one of the objectives of the current research is to address the challenges involved in residual stress measurement of Mg alloys using XRD and to show the steps required to evaluate the errors in stress measurement on Mg alloys.

In Chapter 4, large-strain loading and unloading behaviors of the AZ31B rolled sheet are evaluated. Shot peening generates large plastic deformations on the substrate as the shots impact the material. Modeling the residual stress distribution induced in a material requires the loading-unloading properties to be known in advance, so the tension-compression (TC) and compression-tension (CT) stress-strain curves need to be evaluated. As Mg alloys are asymmetric and anisotropic, its TC and CT curves differ from each other and they also differ when tested in different directions. In this research, the properties in the rolling direction (RD) and transverse direction (TD) are evaluated using a new anti-buckling fixture and the effect of using the anti-buckling has been discussed. In normal direction (ND) of the sheet, a novel fixture has been designed in order to obtain the CT and TC curves of a sample with a total length of 6.1 mm.

In Chapter 5, different effects of shot peening on the AZ31B rolled sheet are evaluated. These effects include residual stress and micro-hardness distributions through the depth, surface roughness measurement and texture evolution at the surface, and fatigue life. The samples are peened under different conditions and in different directions. Rotating bending tests are conducted to obtain the optimum peening intensity at which the peening maximizes fatigue life. Finally, the S-N curves of the as-received samples and peened samples at the optimum intensity are obtained and compared to each other.

Chapter 6 discusses the analytical and finite element modeling of the shot peening process in detail and discusses the shortages of existing methods and proposes a new hybrid analytical-numerical method that predicts the residual stress distribution more accurately and easily. It also provides a general solution that accounts for the actual loading-unloading behavior of a material, actual elastic-plastic contact analysis, strain rate effect, and friction. In this method, the loading step of the peening process is modeled using FEM, and the unloading part is modeled analytically. The results are compared with the available experimental measurements for steel and aluminum alloys and show that this hybrid modeling provides accurate residual stress distribution prediction through the depth of the materials.

Chapter 7 employs the hybrid analytical-numerical method proposed in the previous chapter to model an asymmetric and an anisotropic material that also has complex unloading behavior such as the Mg alloys. The results of residual stress distribution through the depth of Mg alloys are compared with experimental measurements done by XRD and hole-drilling methods. This section extends the application of the hybrid method to asymmetric and anisotropic materials with customized hardening behavior and confirms the capability of the proposed hybrid method to model materials with complex behavior.

The main contributions of this work and future research directions are presented in Chapter 8: Conclusions and Future Works.

Chapter 2

Background and literature review

This chapter consists of two major parts: 1) introducing background knowledge on magnesium (Mg) alloy, the shot peening process, and residual stress measurement using X-ray diffraction (XRD); and 2) assessing the current literature on modeling the shot peening process, including on the analytical and the numerical modeling of residual stress distribution. This section concludes with a discussion of the peening of Mg alloys and a review of studies that have attempted to identify the optimum peening parameters.

2.1 Background

2.1.1 Mg alloys

One of the world's lightest known metals, Mg, is abundant in both seawater and the earth's crust and was first extracted and refined by Sir Humphrey Davy in 1808 [7]. About a century later, this metal began to be employed in the automotive industry, especially in the manufacture of the Volkswagen beetle [4]. At that time, Mg was generally used as an alloying element in aluminum alloys rather than as a structural material. However, some technical problems and a demand for higher performance in the automotive industry led to a decline in the use of Mg [8].

Since 1990, the drive to reduce fossil fuel consumption due to its environmental impact has generated renewed interest in employing Mg and its alloys in the automobile and aerospace industries and for other structural applications [9]. Currently, the use of Mg alloys, particularly wrought Mg, which has specific valuable characteristics, is expanding rapidly in North America and Europe [2].

Magnesium has a range of useful properties that enables it to be exploited on a commercial scale. It has a density of 1.75 gr/cm^3, roughly one quarter that of steel and two-thirds that of aluminum, and offers the highest stiffness to weight ratio among the common engineering metals [7]. Other advantages of Mg and its alloys are their good castability, suitability for high pressure die-casting, good machining behavior, weldability under controlled atmosphere, and availability [8]. However, some of Mg's shortcomings (e.g., inadequate strength at high temperatures, poor cold workability, weak corrosion resistance [10]–[13]) have restricted its use for many applications [9]. Moreover, its complicated behavior (e.g., asymmetric mechanical behavior under tension and compression, anisotropic properties related to the direction of a structure in some cases) can make analyzing the behavior of Mg difficult [9], [14]. The asymmetry in Mg alloys, unlike strength differential effect [15] which is pressure dependent, is due to its hexagonal lattice crystal structure. The hexagonal close-packed (HCP) crystal does not have enough basal slip systems at room temperatures to provide uniform deformation [16]–[18], causing the poor deformability at low temperatures. Another deformation mechanism in HCP metals is twinning [17], [18]; however, only the extension twinning on the $(10\bar{1}2)$ plane is active at room temperature [16]–[18]. Figure 2.1 shows the primary slip deformation mechanisms and also the pyramidal twin plane.

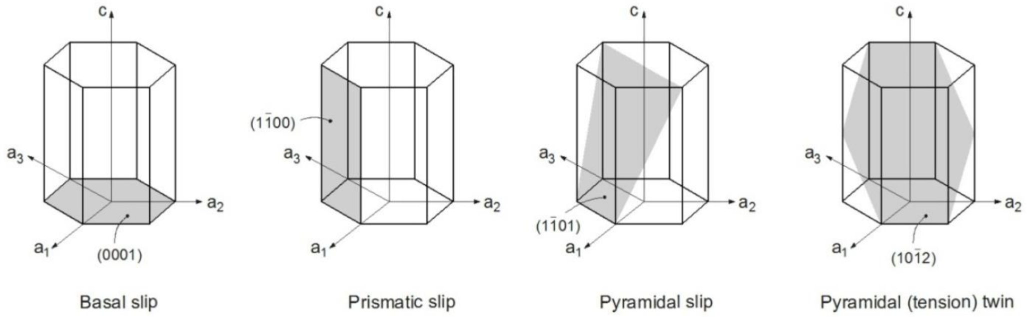

Basal slip	Prismatic slip	Pyramidal slip	Pyramidal (tension) twin

Figure 2.1 Predominant slip and twin planes in HCP metals [19]

Several researchers have investigated the monotonic and fatigue behavior of Mg alloys (AZ31 in [20]–[33], ZEK-100 in [34], AZ80 in [35]–[39], and ZK60 in [40], [41]) including the loading path sensitivity [42], [43] . The other disadvantage of Mg is that it is not possible to use conventional alloying techniques to alleviate some of these undesirable properties. The solubility of alloying elements in Mg is limited, restricting the possibility of improving its mechanical properties and chemical behavior. In addition, some of its properties are related to its microstructure; for example, the hexagonal crystal structure of Mg limits its inherent ductility [8]. Adding various elements to Mg such as aluminum, zinc, manganese, and zirconium can improve some of its properties. For example, aluminum is added to Mg to provide solid solution strengthening and to facilitate age-hardening [44]. This combination also increases tensile strength and hardness. The addition of small amounts of zinc to Mg elevates its corrosion resistance [45]. Aluminum and zinc combined with Mg constitute the AZ group of alloys, which have greater mechanical strength, castability, workability, formability, weldability, and corrosion resistance than pure Mg alone. In AZ alloys, manganese is often added (usually less than 1wt%) to refine the grain size of the alloy [46]. This combination results in better ductility and castability, higher strength, and enhanced energy absorption. When zinc and zirconium are added to Mg to produce the ZK group of alloys, the hot workability of the material is improved [47]–[51]. This enhancement is important to the manufacture of parts that require hot working processes such as hot rolling and forging.

2.1.2 Shot peening process

Shot peening is a cold-working process primarily used to enhance the fatigue life of metallic structural components. Small particles – typically made of hard metal, glass, and ceramics – are used to impact the surface of the structural component at a velocity of 30-100 m/s. The result of these impacts is the local plastic deformation. The induced plastic layer is approximately several hundred micrometers thick, and a compressive residual stress field develops in the near-surface layer of the structural component.

Residual stress is defined as stress that remains in material, at equilibrium, after removal of all external loads [52]. The compressive stress induced by shot peening prevents a crack from forming by negating the tensile loading contribution of the cyclic stress amplitude of fatigue. A crack cannot grow theoretically through the compressive stress field; hence, fatigue life increases.

Many shot-peening parameters that affect the residual stress and fatigue properties of shot-peened samples can be classified into the following three groups [53]:

- Shot parameters: Type, size, shape, density, hardness, yield strength, stiffness, etc.
- Target parameters: Hardness, yield strength, stiffness, work hardness, chemical composition, pre-stress condition, etc.
- Flow parameters: Mass flow rate, pressure, velocity, angle of impingement, standoff distance

In industry, two control parameters – peening intensity and surface coverage– have been suggested as sufficient to characterize the effectiveness and the repeatability of the shot peening process. Shot peening intensity is related to the amount of kinetic energy transferred from the shot stream to the sample during the process. The Almen intensity method, widely used to quantify peening intensity [54], is calculated by measuring the maximum height of the standard Almen strips after shot peening. To determine the Almen intensity of a given process, a certain number of strips must be peened under the same peening parameters but for different exposure times. A saturation curve can then be evaluated by plotting the arc height at different exposure times. Saturation time (T) is the earliest point at which doubling the exposure time (2T) changes the height of the strips by no more than 10%. Under those conditions, the Almen intensity is the specific arc height obtained at saturation time (T). In Figure 2.2, Almen strips are shot peened under the same conditions as the sample under the peening process. When they are removed from the fixture, strips are deformed due to unbalanced residual stresses. Figure 2.3 shows the saturation curve of the shot peening.

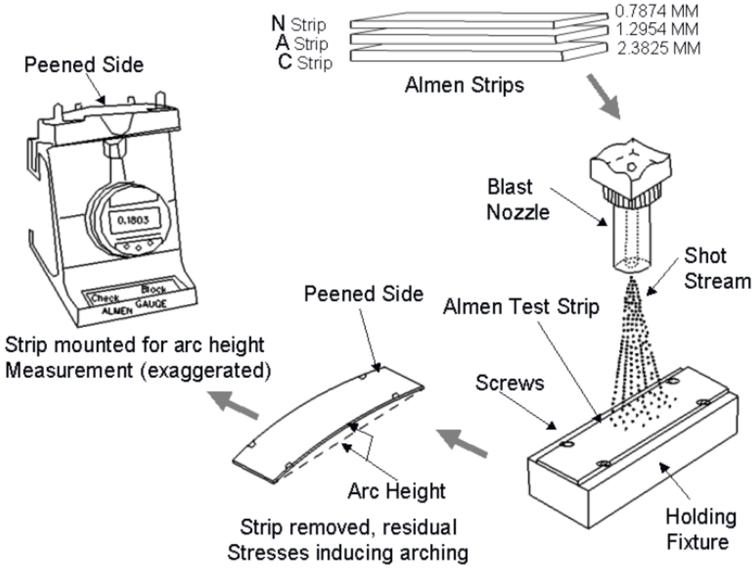

Figure 2.2 Almen intensity measurement [55]

The second key shot-peening parameter is surface coverage, which is defined as the ratio of the area covered by peening impingement to the total treated surface area, expressed as a percentage [56]. In general, it is difficult to confirm a 100% coverage rate; thus, 98% of surface coverage is usually considered as a full coverage condition. A higher coverage percentage can be achieved by extending the duration of full coverage (e.g., 200% coverage by doubling the exposure time of full coverage) [57].

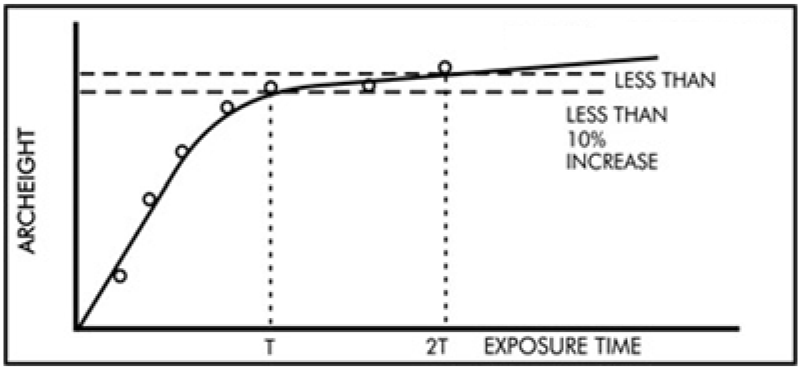

Figure 2.3 Saturation curve of the shot peening [58]

2.1.3 Residual stress measurement using XRD

The measurement of residual stress by XRD relies on the fundamental interactions between the wave-front of the x-ray beam and the crystal lattice. A crystalline material is made up of many crystals, defined as solids composed of atoms arranged in a periodic pattern in three dimensions. These periodic planes of atoms can cause constructive and/or destructive interference patterns by diffraction. The nature of the interference depends on the inter-planar spacing (d), and the wavelength of the incident radiation (λ). The strain-free crystal Bragg's law is given by equation (2.1). As shown in Figure 2.4, in a stress-free sample, the x-rays are diffracted at an angle of θ_0; changing the lattice spacing (d) causes a shift in the diffraction angle.

$$\lambda = 2d_0 \sin(\theta_0) \tag{2.1}$$

The application of stress will change the lattice spacing, and that, according to Bragg's law, leads to a change in the diffraction angle. Bragg's law for the second state is given by equation (2.2).

$$\lambda = 2d \sin(\theta) \tag{2.2}$$

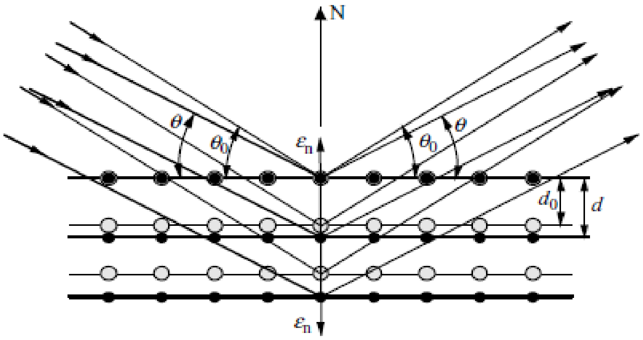

Figure 2.4 Bragg's law for strain measurement [59]

The $\sin^2\psi$ method is one of the most common and simplistic XRD methods for residual stress measurement, and standardized approaches using this method have already been suggested [60]. One problem with the $\sin^2\psi$ method, however, is that it is not easy to make accurate residual stress measurements for large grain or highly textured metals when employing only one-dimensional detectors. In the last twenty years, an XRD method for residual stress measurement, which uses two-dimensional (2D) detectors, has been developed. The method focuses on the direct relationship between the stress tensor and the distortion of the diffraction cones.

The fundamentals and details of 2D-XRD have been described well in a book [59]. However, a standard methodology for 2D-XRD has not been established yet, as this method has only been relatively recently applied to residual stress measurements. 2D-XRD approaches collect data with an area detector (also referred to as a 2D detector), collecting more data points in less time than previous 1D-XRD approaches. The diffraction pattern gathered with an area detector provides a 2D frame. Figure 2.5 shows the sample orientation on the machine stage that will be used in the residual stress measurements using 2D-XRD.

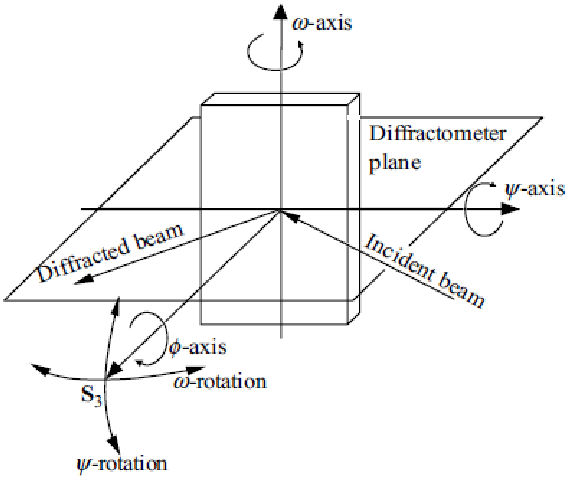

Figure 2.5 Sample orientation angles on stage [59]

When the x-ray incident beam reaches a specimen, the x-rays are reflected through diffraction in two conic sections. 1D detectors capture only one point of the cones, while 2D detectors capture a part of the diffraction cone as a diffraction ring. Figure 2.6 shows the diffraction cones.

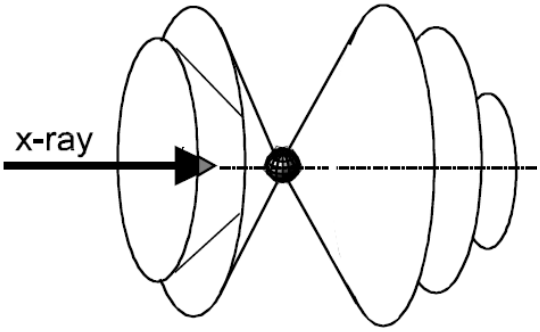

Figure 2.6 Diffraction cones [59]

For residual stress measurement using 2D detectors, there are two cones (a distorted diffraction cone due to the applied stress and a diffracted cone from the unstressed sample) as shown in Figure 2.7. The bright rings (unstressed diffraction cones) are stress-free and, as a result, the 2θ angles are constant at all γ angles. However, the dark rings are the cross-sections of the distorted diffraction cones due to the presence of stresses.

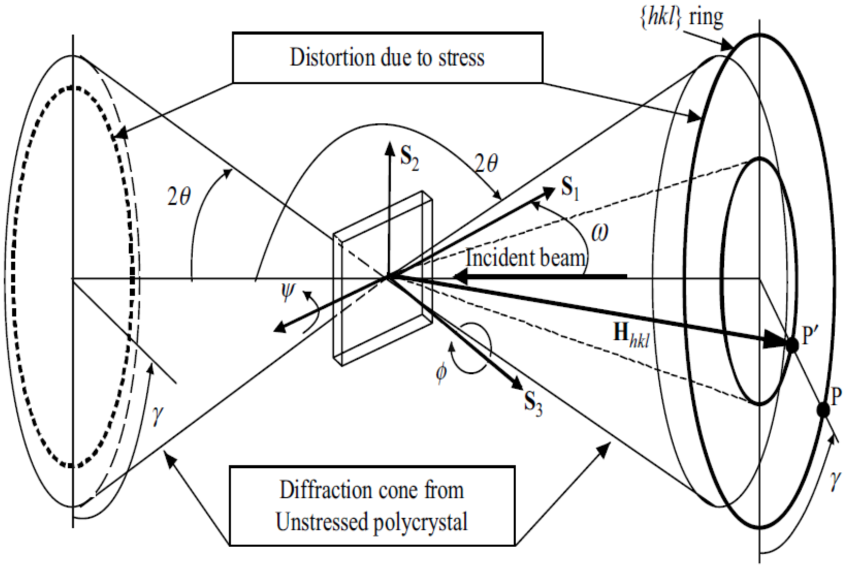

Figure 2.7 Diffraction cones and distorted diffraction cones [59]

2θ is a function of angles γ, ω, ψ, and φ and can be shown as 2θ = 2θ (γ, ω, ψ, φ) [59]. Thus, the strain calculated by the 2θ shift is a function of (γ, ω, ψ, φ), as shown in equation (2.3).

$$\varepsilon(\gamma,\omega,\psi,\phi)=\ln\frac{d}{d_0}=ln\frac{\sin(\theta_0)}{\sin(\theta)}=\ln\frac{\lambda}{2d_0\sin(\theta)} \tag{2.3}$$

where d_0 and θ_0 are the stress-free values, and d and θ are measured values from the points on the distorted diffraction ring corresponding to (γ, ω, ψ, and φ).

To measure the residual stress using the XRD method, it is necessary to obtain the diffraction ring of one specific lattice plane in different orientations, given there are six unknown values to be determined. Equation (2.4) shows the system of equations that should be solved to obtain the residual stress tensor.

$$f_{11}\sigma_{11}+f_{22}\sigma_{22}+f_{33}\sigma_{33}+f_{12}\sigma_{12}+f_{13}\sigma_{13}+f_{23}\sigma_{23}=F(\theta_0,\theta) \tag{2.4}$$

Takakuwa and Soyama [61] optimized the number of orientations to achieve acceptable results. Their experiments were conducted on three stainless steel specimens. Different combinations of the tilt angle between the specimen's normal surface and the diffraction vector (ψ) and the rotation angle about its surface normal (φ) were studied with a view to finding the optimum condition.

2.2 Literature review

This section reviews the literature on analytical and numerical modeling of the shot peening process and the effects of shot peening on Mg alloys.

2.2.1 Analytical modeling of the shot peening process

Shot peening dynamically transfers a small amount of energy to the surface of a target workpiece via small metallic, glass, or ceramic shots. In effect, the energy transferred to the workpiece creates a small indentation. This permanent indentation indicates that plastic deformation has occurred, and residual stress at and under the surface of the target material has formed. Plasticity theory is an integral part of modeling the residual stress. The theory of plasticity has been in development throughout the last 100 years. As a result, shot peening has received considerable theoretical attention only during the last 40 years. Plasticity theory provides the tools necessary to predict when yielding in a material will occur. Several yield criteria have been proposed and employed to model plastic flow in a large variety of materials. For example, the Von Mises criterion is widely used to solve the residual stresses induced by shot peening [56].

In general, the process of shot peening can be divided into two phases: 1) shot impacting and penetrating into the substrate-the loading phase; and 2) shot rebounding from the substrate-the unloading phase. The loading phase includes high strain-rate impact and severe localized plastic deformation. The unloading phase includes elastic unloading, which may or may not include reverse yielding. Therefore, shot peening is a highly nonlinear process due to severe plasticity, shot-substrate contact, and elastoplastic unloading.

The earliest analytical technique used to solve the residual stresses induced by shot peening, developed by Flavenot [62], was based on the concept of a stress source. The source of stress is introduced to the material from the peening process, take for example an Almen strip confined by a holder. During and just after peening, the holder exerts an axial force and bending moment on the strip to prevent it from elongating and deflecting. However, once removed, the strip is free to bend and elongate, and therefore an axial and bending stress is induced within the specimen. The stress source is not equilibrated and is considered to be the residual stress that develops in a semi-infinite surface (e.g., very thick plate) and is governed by the laws of elasticity. Using the principle of superposition, the stress source (σ_x^{ind}) is summed with both the axial (σ_x^{force}) and bending ($\sigma_x^{bending}$) stresses to allow for equilibrium to occur (Figure 2.8). Flavenot used the experimental equation for the normal strain through the depth and developed his proposed function for the residual stress. In this semi-analytical method, the distribution of residual stress through the depth is modeled as a function of the plate deflection and the diameter of plastic indentation on the surface of the sample. Al-Hassani [63] used an analogy with the pressurized spherical cavities to model the shot peening of materials with elastic-perfectly plastic behavior. He assumed that the stress field below the indentation can be interpreted as a spherical cavity undergoing elastic-plastic deformation.

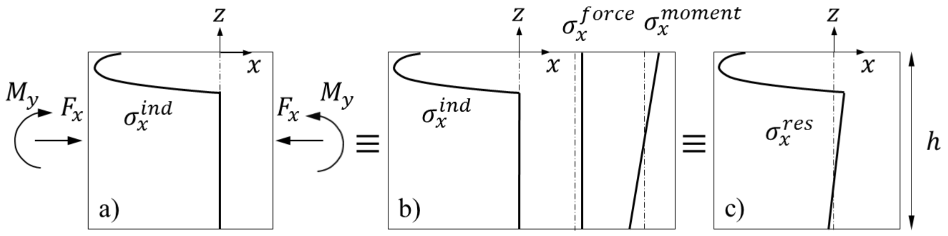

Figure 2.8 Definition of the stress source ($\boldsymbol{\sigma_x^{ind}}$) and equilibrium of peened sample after relaxation from the fixture [64]**: a) Sample is peened inside a fixture, $\boldsymbol{\sigma_x^{ind}}$is the induced residual stress, $\boldsymbol{F_x}$ and $\boldsymbol{M_y}$are the axial force and bending moment applied by the fixture, b) the axial normal and bending stresses due to the force and moment of the fixture, c) residual stress profile (**$\boldsymbol{\sigma_x^{res}}$**) after relaxation of the plate from the fixture**

Li et al. [65] developed a method for considering the strain hardening in modeling. They employed the Hertz contact theory [66] to estimate stress components in the surface layer of a peened material. They considered the modeling as a quasi-static problem where a shot is pressed into a semi-infinite solid. Based on the assumption of the relevancy of the ratio of the plastic to elastic indentation radii to the ratio of the plastic strain to elastic strain, they converted their proposed elastic solution to a plastic one. Iliushins elastic-plastic theory [67] was employed to calculate the elastic-plastic stresses. In the unloading step, Li et al. [65] assumed that after reverse yielding, the plastic strain deviators take on a form similar to that of the elastic strain deviators. A noticeable limitation in their approach was the use of an empirical equation based on a static force.

To remove the empirical equation, Shen and Atluri [68] proposed calculating the plastic indentation by using the average pressure distribution put forward by Al-Hassani [69], which acts to counter the force of the impinging shot and accelerates it away from the surface. Later, Franchim et al. [70] investigated the effect of the plastic behavior of the target material on the compressive residual stress profile using the Ramberg–Osgood and Ludwick constitutive models. Their results showed that the hardening properties of materials play a significant role in residual stress profile prediction.

Miao et al. [64] presented an analytical model based on the Hertz contact theory for the prediction of Almen intensity and residual stress distribution on an Almen strip. Using their model, the influence of shot-peening parameters (e.g., shot type, size, velocity, and peening angle) on the Almen intensity can be studied easily. This study was aimed at estimation of the velocity of shot peening based on a desired Almen intensity for industrial applications. Their results showed a fairly accurate estimation of the residual stress profiles for the shot peening of steel alloys [64].

Sherafatnia et al. [71] produced an analytical model by modifying the work of Shen [68], in which the modifications are related to the friction coefficient effect and the fraction of kinetic energy transmitted to the treated material. Moreover, the effect of the Coulomb friction between the target surface and the shots was evaluated. To accomplish this, the interior stresses caused by tangential tractions of friction force were determined analytically. They developed an analytical model with two modifications as follows: (1) the stresses created due to Coulomb friction are added to the stresses caused by normal pressure, and (2) the percentage of the energy transferred from a shot stream to the media is developed with the function of shot velocity. Experiments were carried out on medium carbon steel to validate the results from the analytical model. The results of the comparison indicate that the analytical relations agree well with the experimental data.

Sherafatnia et al. [72] extended the analytical modeling of shot peening to consider the initial residual stresses in the material. The effect of a primary hardened surface layer was also taken into account by adjusting the yield stress of the material for each point through the depth. They used silicon carbide to grind 0.4 mm off the surface, and then peened the samples. The evaluations of the residual stress distribution were obtained for both conditions, peening of the ground samples, and also for peening on the as-received material without initial surface treatment.

2.2.2 Finite element modeling of the shot peening process

The development of FEM and computational power have made numerical modeling of the shot peening process possible. Numerical modeling provides more details such as different stress and strain components, which are not possible to obtain in the analytical modeling. It also needs fewer assumptions than the ones in analytical modeling. The earliest numerical modeling of the peening process involved modeling a limited number of shots and predicting the residual stress profile based on those shots. These models (shown in Figure 2.9) gradually developed from 2D simulations [73] to 3D modeling [74]–[76]. These studies mostly focused on how changing the peening parameters affects residual stress distribution. The 2D model was introduced by Mori et al. [73] and simulated the plastic deformation of the target. They used an axisymmetric 2D model to predict the plastic deformation in peening by one shot. In FEM of the peening process, symmetry cells were employed to lower the computational costs. The modeling of a finite number of shots is important because it cannot be assumed that the residual stress due to one-shot is similar to the residual stress in full coverage peening. In addition, in the case of modeling only a single shot, evaluation of the surface roughness is impossible. Meguid et al. developed FEM for single-shot [74] and twin-shot impacts [75] to investigate the effects of shot velocity and separation distance on plastic deformation and residual stresses. They also employed a multiple impingement model using a rate-sensitive material to conduct dynamic analysis [76] and determined the material damping parameters in order to dampen numerical oscillations [76]. They found that shot peening involves strain rates in the order of 10^5 1/s (i.e., quite a high rate); therefore, strain rate effects should be incorporated into any modeling. Using a 3D model with two symmetry surfaces, Guagliano found a relation between the residual stresses in a peened samples to Almen intensity. As such he was successfully able to relate the Almen intensity to the shot velocity [77].

The next step in modeling the peening process was to approximate 100% coverage peening by using a finite number of shots and calculating the average of residual stresses through the depth so as to obtain the residual stress distribution. Multiple impact models with predefined assembly patterns have also been widely studied in the literature. Majzoobi et al. [78] presented a numerical model that included multiple shot impacts of 4, 6, 8, 9, 13, and 25 beads at specified locations, in order to reproduce a uniform residual stress profile through the depth. They found that under those peening conditions and symmetry cell geometry (0.8 x 0.8 x 1.6 mm), 25 shots lead to a consistent residual stress distribution between points A, B, C, and D (Figure 2.10 (b)). Comparing the uniform residual stress with the experimental results showed satisfactory results. Meguid et al. [79], Kim et al. [80], and Kubler et al. [81] applied the idea of an area average solution to a symmetry cell to obtain a realistic residual stress distribution through the depth. In this approach, the average residual stress, in all elements at a specific depth from the surface, is introduced as the amount of shot peening induced residual stress at that depth.

Later, random multiple impact models were proposed to simulate the shot peening process more realistically. In this approach, the number of shots to achieve the full coverage condition should be known and is obtained using one of two approaches. First, the number of shots is estimated in advance using the Avrami equation [82]. This statistical-based method evaluates an appropriate number of impingements in the simulation, in an effort to achieve a given coverage for a given target area and is used in studies by Miao [57]. Second, the surface treatment after each shot impact is monitored, and the coverage at each step is evaluated. In this method, a subroutine is linked to the FEM software to compute the coverage in each step and stop the modeling when full coverage occurs. Gangaraj [83], Bagherifard et al. [84], and Xiang et al. [85] employed this method to present an actual coverage evolution.

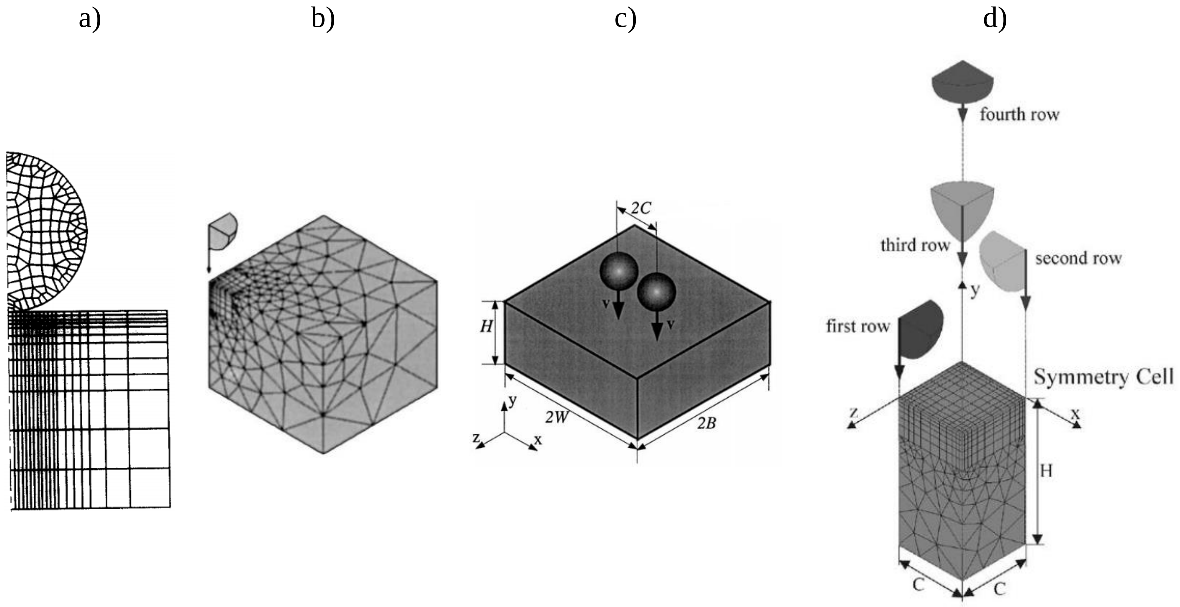

Figure 2.9 Development of FEM modeling of shot peening process from a) 2D [73] **to b) 3D model with two symmetry surfaces** [74]**, c) modeling twin shot impact** [75]**, d) 3D model with four symmetry surfaces** [76]

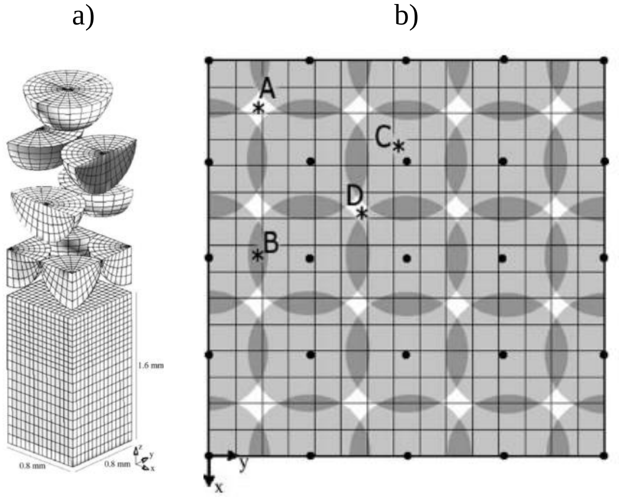

Figure 2.10 FEM of peening [78] **using four symmetry cells a) nine-shot impingement b) the target plate the impact points of 25-shot impingement modeling**

To optimize multiple random peening modeling computationally while keeping it accurate, mesh analysis and assembly studies have been done by Miao et al. [57] and Gariepy et al. [86]. The random FEM proposed by Miao et al. [57] consisted of four square regions in the surface plane and two regions through the depth. In Figure 2.11 (a), the shots impact the surface within region 3, and region 4 is used for the residual stress measurements.

Later, Gariepy et al. [86] modified and optimized the geometry introduced by Miao et al. [57] and proposed the geometry dimensions of the surface regions (Figure 2.12) for I, t_{int}, and t_{ext} to be 0.75, 0.125, and 0.75 mm. The element sizes are also mentioned in Table 2.1.

a) b)

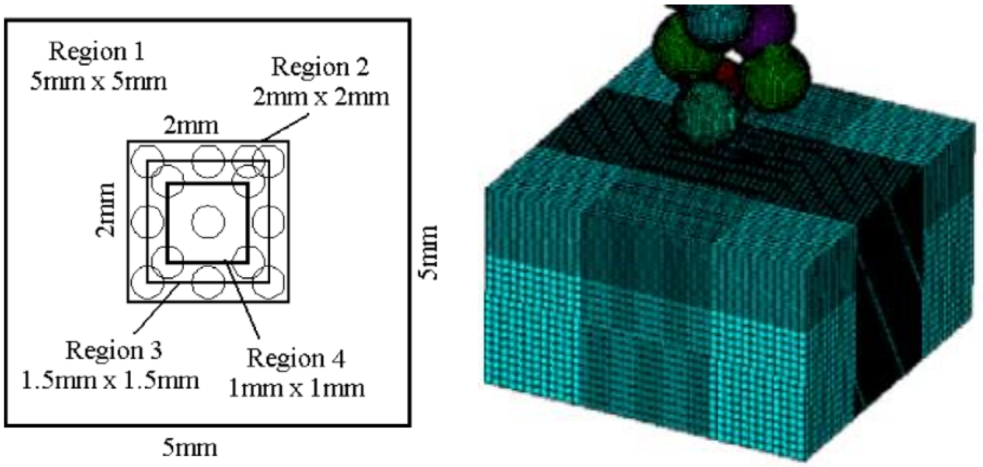

Figure 2.11 Surface geometry and regions for 3D random FEM [57]**, a) surface geometry and regions, and b) the meshed sample and two regions through the depth.**

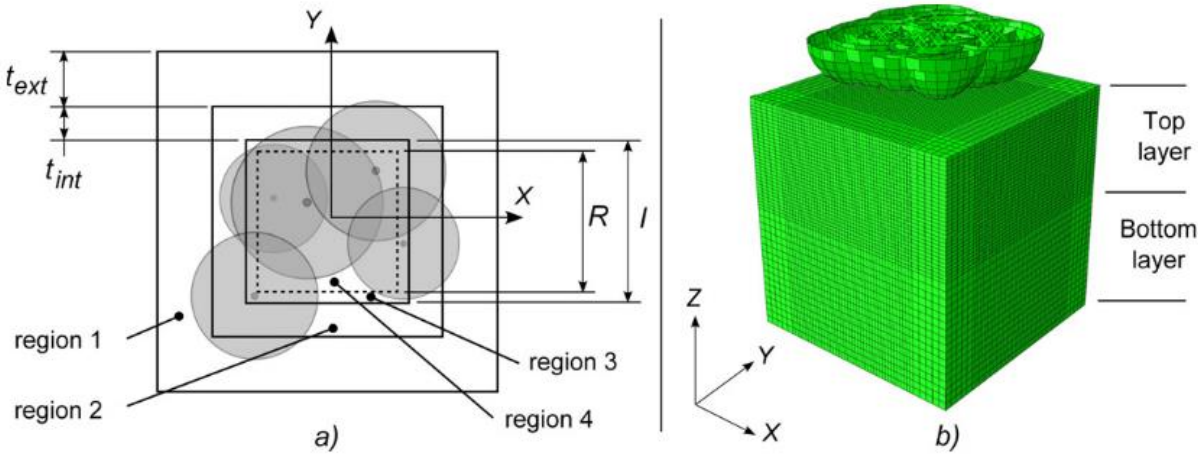

Figure 2.12 a) Schematic view of the regions at the surface and b) 3D meshing and assembly of multiple random peening

In addition, to optimize the modeling time of multiple random shot impingement, Gariepy et al. [86] showed that two shots have independent effects if they are 0.1 mm apart in the z-direction. They also determined that two simultaneous impacts (two shots at the same height) can be considered separately if the minimum distance between them is $2xD_{shot}$. Using a DSLR camera with a macro lens, they also experimentally confirmed the distance between the two shots is greater than the minimum distance obtained for shot assembly in FEM.

Table 2.1 element size [86]

Mesh type	Dimension	Location, X-Y	Location, Z
Coarse	$0.1x\ D_{shot}$	Region 1	Lower layer
Fine	$0.05x\ D_{shot}$	Regions 2-4	Upper layer

Regarding the modeling on Mg alloys, Shayegan et al. [87] modeled the cold spray process on an AZ31B substrate, then evaluated the effect of cold spray parameters on the residual stress profile through the depth using LS-DYNA software. An asymmetric material model was used to capture the asymmetric behavior of AZ31B. The minimum difference between the predicted and measured stress at the surface was 27%.

2.3 Shot peening on Mg alloys

This section discusses the literature related to the shot-peening of Mg alloys. It is notable that only experimental studies exist; there is no modeling in the literature investigating shot peening on Mg alloys. The various substrate materials, shot materials and sizes, and Almen intensities, used in the peening processes of Mg alloys are summarized in Table 2.2.

Dorr et al. [88] reported the results of shot peening on 2024 Al-T4 and Mg alloy AZ80 using various peening media (cast steel, ceramic, and glass beads), peened at various intensities. It was shown that the fatigue performance depends mainly on the Almen intensity, and a change in the shot material at the same intensity does not affect fatigue performance. They captured the sensitivity of the fatigue life of AZ80 to the peening intensity, as shown in Figure 2.13. However, they did not observe high sensitivity in 2024 Al alloy.

Table 2.2 Summary of studies on the effect of shot peening on Mg alloys

Reference	Material	Shot material	Shot diameter (mm)	Almen intensity (mmN)
[88], 1999	AZ80	Glass, Steel, …	0.66	0.03-0.9
[89], 1999	AZ80	Glass, Steel	0.36 and 0.65	0.04-0.62
[90], 2003	wrought AZ80	Steel	0.36	0.18- 0.55
[91], 2005	wrought AZ80	Glass	0.3-0.4	0.04-0.4
[92], 2009	Cast Magnesium A8	Glass	0.245	0.127
[93], 2009	ZK60-T5	Glass	0.35	0.02-0.4
[94], 2010	wrought AZ80	Glass, B30, Ce-ZrO2	0.3-0.8	0.04-0.06
[95], 2011	Mg-10Gd-3Y alloys	Glass	0.35	0.05-0.6
[96], 2011	ZK60	Glass	0.35	0.02-0.4
[97], 2011	ZK60-T5, ZK60	Glass	0.35	0.1-0.4
[98], 2018	AZ31B	Ceramic	0.1-0.15	0.15

Wagner [89] investigated the effect of shot peening on the fatigue performance of titanium, Al, and magnesium alloys. He also discovered the high sensitivity of AZ80 to the peening intensity, as shown in Figure 2.14. He concluded that although compressive residual stress occurs with the peening of Mg alloys, surface roughness or tiny cracks induced during the shot peening process critically affect the materials' fatigue performance.

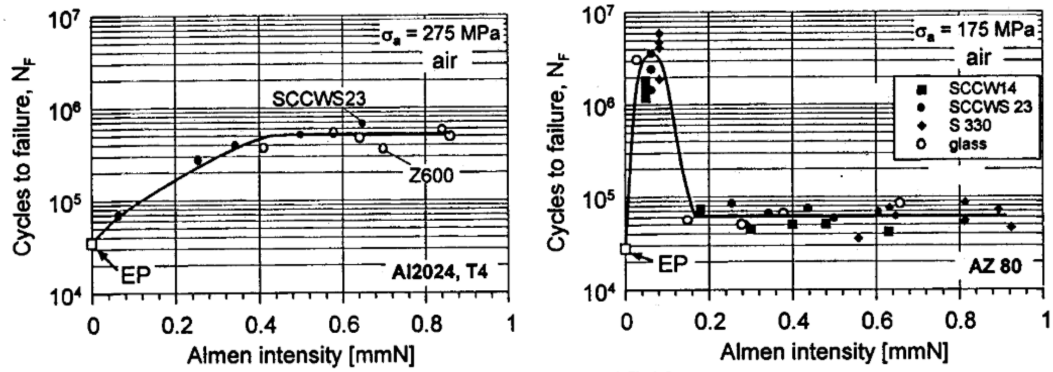

a) 2024 Al

b) AZ 80

Figure 2.13 Fatigue life of a) 2024 Al-T4 and b) AZ80 alloys peened at different intensities [88]

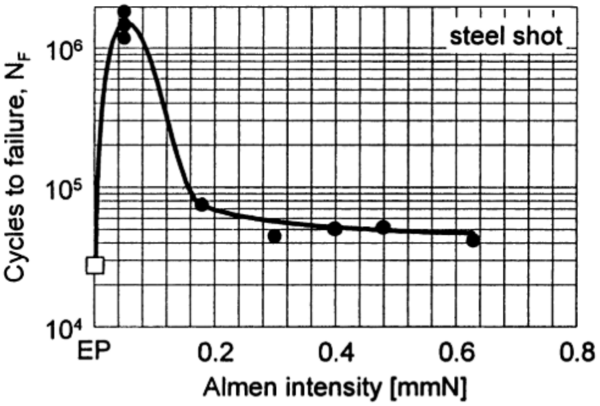

Figure 2.14 Fatigue life of AZ80 peened at different intensities [89]

Wendt et al. [90] evaluated the effects of test temperatures ranging from -25℃ to 50℃ on the fatigue life of peened AZ80. They found that shot peening improves fatigue life at all temperatures, but minimal improvement occurs at 0℃. Zhang et al. [91] studied the influence of shot peening on the fatigue performance of extruded AZ80., and also reported on AZ80's sensitivity to the peening intensity (Figure 2.15). After evaluating the effects of peening intensity on the surface roughness and micro-hardness through the depth, they concluded that higher Almen intensity leads to a higher roughness and micro-hardness at the surface and a deeper plastically deformed layer. Shot peening at the optimum intensity improved the endurance limit of AZ80 by about 60%. They claimed that the reason for the over-peening effect is the increase of the surface roughness and also the creation of micro-cracks at higher intensities.

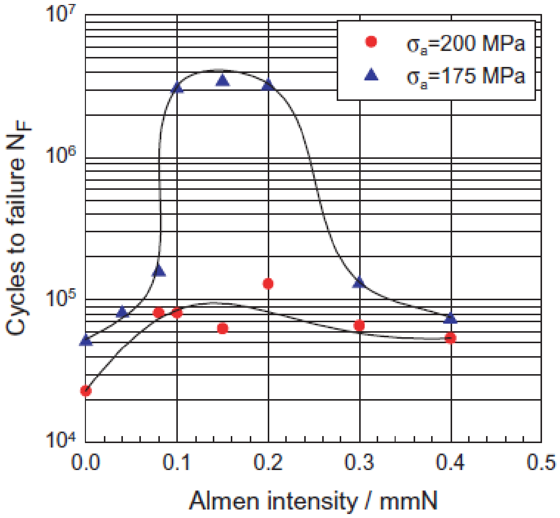

Figure 2.15 Fatigue life of AZ80 versus Almen intensity, tested at stress amplitudes of 175 and 200 MPa [91]

Barry et al. [92] explored how shot peening affects the fatigue life of the sand-cast A8 Mg alloy. After peening at one intensity (0.245 mmN) and a coverage of 200%, they reported an increase of 30% in the endurance limit of this material. In addition, the peened samples had significantly higher surface roughness than the as-machined samples.

Liu et al. [93] studied the effects of shot peening at different intensities on the fatigue performance of ZK60-T5 and also observed the over-peening effect on ZK60 (Figure 2.16). Peening at the optimum intensity of 0.05 mmN was found to increases the fatigue strength (at 10^7 cycles) from 150 to 195 MPa.

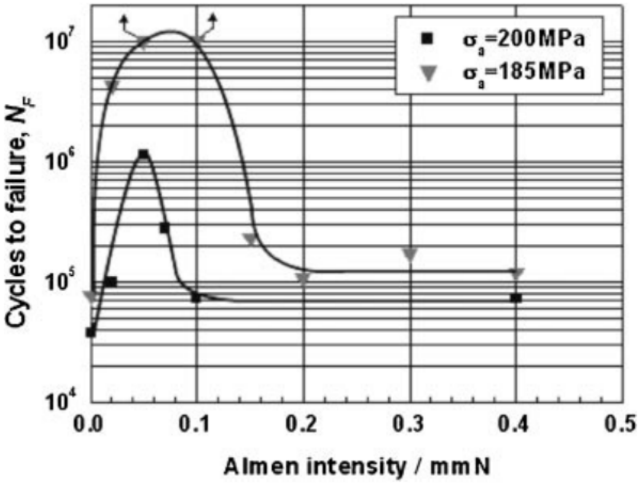

Figure 2.16 Fatigue life of ZK60 at different Almen intensities, tested at stress amplitudes of 185 and 200 MPa [93]

To assess the effect of shot peening on notched AZ80 (Kt=2.3), Zhang et al. [94] used various shot peening media at various Almen intensities. They claimed that no over-peening effect is observed in the peening of notched samples. Moreover, in contrast to the smooth samples, in notched samples, the fatigue cracks initiate from the materials' surface due to their high stress concentration factor.

Liu et al. [95] studied how shot peening affects the fatigue performance of Mg–10Gd–3Y Mg alloys under four different conditions: as-cast, cast-T6, as-extruded, and extruded-T5. They found that the optimum peening intensities for the four conditions were 0.40, 0.50, 0.10 and 0.10 mmN, respectively. Peening at the optimum intensities for each material improved fatigue endurance limits by about 35%, 19%, 43%, and 45%, respectively.

An examination of shot peening's influence on the fatigue life enhancement of extruded ZK60 Mg alloy by Dong et al. [96] concluded that the process can significantly improve the fatigue life of a smooth ZK60 sample (e.g., the fatigue strength at 10^7 cycles changed from 140 to 180 after peening at the optimum intensity). They claimed that the limited deformability of magnesium alloys at room temperature leads to micro-crack initiation and results in Mg alloys' sensitivity to peening intensity.

Liu et al. [97], considering the effect of shot peening on notched ZK60 and ZK60-T5 Mg alloys (K_t=2.3), observed the optimum intensities of 0.3 and 0.4 mmN, followed by fatigue strength changes from 150 and 155 MPa to 220 and 240 MPa for the two material respectively.

Bagherifard et al. [98] studied severe shot peening on AZ31B to get nano-grains to improve the properties of this alloy for a biological environment. They considered an Almen intensity of 0.4 mmN, 1000% coverage as the severe shot peening condition (SSP) and compared the results with a conventionally shot peened (CSP) sample (Almen intensity of 0.15 mmN and 100% coverage). They found a thicker affected surface layer in the SSP and finer grains than in the CSP. In addition, both of the processes involved randomized textures at the surface layer. As expected, the CSP has a smoother and less-defective surface. The residual stress measurements showed higher and deeper compressive residual stresses after the SSP treatment.

Chapter 3

On the Residual Stress Measurement of Mg alloys Using Two-dimensional X-ray Diffraction

Abstract

Due to the low x-ray mass attenuation coefficient, x-ray penetration in magnesium alloys is significant. To measure the surface, and through the depth residual stresses in magnesium alloys, a correction needs to be made to account for the depth of penetration. The residual stresses in as-received and shot peened AZ31B-H24 rolled sheet samples were measured using the 2D-XRD method. The electro-polishing layer removal method was used to find the residual stress pattern through the depth. The results showed that the corrected residual stresses in a few tens of micrometers layer from the surface are different from the raw stresses; the corrected stresses predict negligible tensile residual stresses up to 40 micrometers below the surface, while the raw data shows compressive residual stress between -10 to -20 MPa. To better estimate the residual stress distribution in a few micrometers from the surface, grazing-incidence x-ray diffraction (GIXD) method was applied to evaluate the stresses in the surface layer. Additionally, the lateral cross-section of the peened specimens confirmed the presence of micro-cracks in this region, causing to vanish the residual stresses. The difference between the corrected and raw data becomes negligible after around 100 micrometers below the depth. Also due to the low x-ray absorption coefficient of Mg alloys, this study shows how small uncertainty in measuring the observed residual stress and in evaluating the depth of the polished area in layer removal lead to high uncertainty in the corrected residual stresses. The XRD results show the creation of compressive residual stress through the depth as well as a good agreement between the XRD and hole-drilling and GIXD results.

Keywords- ***Residual stress measurement, X-ray diffraction, Magnesium alloys, Stress correction factors, Shot peening***

3.1 Introduction

Magnesium (Mg), the lightest commercially available industrial metal, is of growing interest to automotive companies who are now motivated to increase the fuel efficiency of vehicles by decreasing their weight through employing lightweight materials such as Mg alloys. Using these alloys in load-bearing components, first requires that their fatigue life be improved. Different processes induce different residual stresses in materials. Shot peening, welding, machining, cold spray, and laser shock peening are examples of processes that induce residual stress in a material. Among the methods for residual stress measurement, x-ray diffraction (XRD) has attracted researchers' attention because: 1) it is a non-destructive method; 2) it can measure residual stress at the surface, and 3) the spatial resolution can be less than 0.3 mm. The $\sin^2\psi$ method is the most common XRD method for residual stress measurement, and standardized approaches using this method have already been suggested [60]. One problem with this method, however, is that accurate residual stress measurement for large grain or highly textured metals is difficult when employing only one-dimensional detectors. Applications for two-dimensional x-ray diffraction (2D-XRD) theory discovered in 1999 have since been developed [59]. The 2D-XRD method focuses on the direct relationship between the stress tensor and the distortion of the diffraction cone. The fundamentals and details of 2D-XRD have been described well in [59]. However, a standard methodology has not yet been established as this method has only recently been applied to residual stress measurements.

One of the most applicable equations governing x-rays, Bragg's law (equation 3.1), shows that diffraction patterns are produced when diffracted beams interfere constructively.

$$n\lambda=2d\sin(\theta) \tag{3.1}$$

In equation 3.1, d is the interatomic lattice spacing between two planes, and θ is half of the diffraction angle. The concept of measuring the residual stress using XRD is based on the relation between the lattice spacing and the diffraction angle, meaning that the applied stress changes the diffraction angle in 1D detectors or distorts the diffraction ring in 2D detectors. To measure the residual stresses using the 2D-XRD method, it is necessary to obtain the diffraction ring of one specific lattice plane in different orientations. Takakuwa and Soyama [61] optimized the number of sample orientations to achieve acceptable results. They measured the residual stresses from three different processes, annealing, cavitating jet in the air, and disc grinding, using combinations of sample orientations, aiming to obtain the minimum number of orientations for reliable measurements.

For measuring the residual stress distribution through the depth of material, there are two methods: layer removal technique and grazing-incidence x-ray diffraction (GIXD) method. The layer removal method is widely used to polish the surface of a material to remove a thin layer from the surface of a material using an elector-polisher. GIXD is a non-destructive method that uses different low incident angles for providing the different depth of penetrations through the depth [59], [60], [99]. Depending on the material's mass attenuation coefficient, the maximum penetration depth achievable with the GIXD method varies significantly. Both methods require the application of corresponding stress correction factors [59], [60], [99].

XRD method has been employed to measure the residual stress in Mg alloys in several studies. All use $\sin^2\psi$ method for stress measurement and layer removal for evaluation of residual stress distribution through the depth. In the shot peening process, Zhang and Lindemann [91], Liu et al. [95], Liu et al. [97], Zinn and Scholtes [100], and Bagherifard et al. [98] evaluated the residual stress distribution due to the shot peening of AZ80, Mg–10Gd–3Y, ZK60, AZ31, and AZ31B, respectively. In welding processes, different studies have been done on measurement of the residual stresses due to welding of Mg alloys at different distances from the weld centerline: friction stir welding/processing of AZ31 [101]–[103], friction stir welding of ZK60 [104], tubular laser welding of AZ31 [105], butt joint welding of AZ31B and 304L steel alloy by hybrid laser-TIG [106], and laser beam welding of AZ31B [107]. The residual stress in longitudinal and transverse directions of AZ91 welded by a CO_2 laser as well as the in-depth distribution of residual stress using layer removal method was studied by Kouadri and Barrallier [108]. Various researchers have measured the residual stresses induced in manufacturing of various materials: due to machining of AZ31B [109], due to dry and cryogenic machining of AZ31B on the surface and sub-surface in circumferential and axial directions [110], cold expansion of AZ31B sheets [111], [112], and due to equal-channel angular pressing of AZ31 [113]. A few other studies have considered processes such as cold spray [87], [114]–[117] and laser shock peening [118]. Shayegan et al. [87] measured the residual stress in cold sprayed AZ31B and mentioned that corrections have been applied, but did not discuss the calculation of error bars. Finally, the in-depth residual stress distributions in laser shocked peened samples of AZ31B were measured using the layer removal method by Zhang et al. [118].

The x-ray mass attenuation coefficient is a material constant that indicates the level of x-ray penetration through the depth of a material. The higher the coefficient, the lower the penetration through the depth. As Mg has a low density and low atomic number, its x-ray mass attenuation coefficient is very low resulting in deeper x-ray penetration as compared to materials with higher atomic numbers such as steel alloys. In this case, measured residual stress by XRD will only be an average over considerable depth and would require correction. Most of the literature on the measurement of residual stress through the depth of Mg alloys have not addressed this shortfall, or have not discussed how it was handled when processing the XRD raw data. In this paper, we have addressed the effect of low x-ray mass attenuation coefficient of Mg on residual stresses induced after shot peening of an AZ31B-H24 Mg sheet. The stress correction factors due to the x-ray depth penetration and layer removal are applied to raw data to evaluate the actual residual stress at each depth. The error bars associated with the corrected stresses are calculated by combining the uncertainties in observed residual stresses and in depth measurements of removed layers in electro-polishing. The corrected stress profiles are compared with the results of GIXD in the vicinity of the surface layer. To verify the results of having no residual stress close to the surface after shot peening, the surface topography of the lateral cross-section of the as-received and peened samples are evaluated using an optical microscope to confirm the existence of micro-cracks. Further comparison is made with residual stress measurement using the hole drilling method.

3.2 Material and Experimental Procedure

3.2.1 Material

The material used in this study is the AZ31B-H24 rolled sheet with a thickness of 4 mm. The chemical composition of this alloy is shown in Table 3.1 [119]. The density and Young’s modulus of elasticity are 1770 Kg/m3 and 45 GPa, respectively [120].

Table 3.1 Chemical composition of AZ31B rolled sheet [119]

Composition	Al	Zn	Mn	Mg
Weight %	2.73	0.915	0.375	Bal.

Texture measurements were carried out on a Bruker D8 Discover X-ray diffractometer equipped with a VÅNTEC-500 2D detector using Cu-K_{α} beam radiation at 40 kV and 40 mA. The process involved measuring the incomplete pole figures of $\{0001\}$, $\{10\bar{1}0\}$, $\{10\bar{1}1\}$ and $\{1\bar{1}02\}$ planes for tilt angle ψ between 0° and 75° and in axis rotation φ between 0° and 360°, as described in [121]. The complete pole figures were obtained using DIFFRAC.TEXTURE software, version 3.0.4 developed by Bruker AXS.

3.2.2 Shot peening

Shot peening is widely used in the industry to enhance the fatigue strength of materials. This process impinges small shots on the target surface at a velocity of 30-100 m/s. The resulting specific plastic deformation of the surface layer creates compressive residual stress in this layer. Inducing the compressive residual stress is beneficial as it retards the crack initiation and growth in load-bearing components. Metal Improvement Co., in Brampton, shot peened the samples with an Almen intensity of 0.4 mmN, a working distance of 10 cm, in full coverage, and vertical peening. Glass and steel shots with respective diameters of 350 and 280 micrometers were used. The Mg samples were cut to the dimensions of 35 x 35 x 4 mm.

3.2.3 X-ray diffraction

The residual stress measurements were performed on the samples, using a Bruker D8-Discover equipped with a VÅNTEC-500 area detector, with a radius of 135 mm. The two main tubes used in XRD machines are Cu and Cr ones. The effects of these two x-ray sources on the diffraction pattern of AZ31B and on residual stress measurement are discussed in the results section. Due to the higher mass attenuation coefficient of the Cr tube compared to the Cu one, x-rays penetrate Mg alloys less when a Cr tube is used. However, as the most commonly used tube for XRD is the copper radiation source [122]–[124], in this study, the Cu tube has been selected for stress measurements. It provides bright and sharp peaks for many materials; however the use of Cu-Kα radiation in alloys containing iron results in fluorescent background intensities that reduce the signal-to-noise ratio [122], [125]. Thus, Cu-Kα radiation was used at 40kV and 40 mA. The collimator size was 1.0 mm. Samples were mounted on a motorized stage. To obtain the optimum x-ray exposure time, the AZ31B samples were impinged at different exposure times, with and without sample oscillation. For testing with sample oscillation, amplitudes of 1.3 and 1.2 mm, and speeds of 3.5 mm s−1 and 5.5 mm s−1 for the X and Y axis were used, respectively. As discussed in the introduction, according to Bragg's law, the d value is related to the diffraction angle, so any change in the lattice spacing shifts the diffraction angle to the left or right. The diffraction angle (2θ) shifts can be used to calculate residual stress. In general, to obtain the stress tensor at a point, there are six unknown stress values. Thus, to evaluate the residual stress components, the sample should be tested in different orientations to find all the stress values. Different angles and orientations are demonstrated schematically in Figure 3.1 [61].

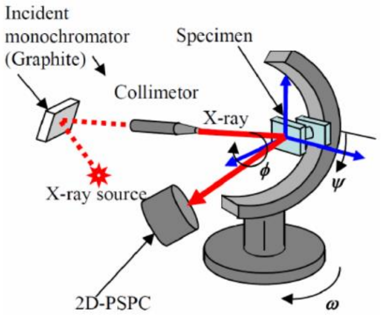

Figure 3.1 Sample orientation guide [61]

The orientations used for each residual stress measurement are listed in Table 3.2 [61].

Table 3.2 Different sample orientations [61]

Ψ (°)	Φ (°)
0	0
25	0, 45, 90, 135, 180, 225, 270, 315
50	0, 45, 90, 135, 180, 225, 270, 315

Equation 3.2 shows the system of equations that should be solved to obtain the residual stress tensor.

$$f_{11}\sigma_{11} + f_{22}\sigma_{22} + f_{33}\sigma_{33} + f_{12}\sigma_{12} + f_{13}\sigma_{13} + f_{23}\sigma_{23} = F(\theta_0, \theta) \quad (3.2)$$

Based on the results of x-ray exposure time, samples were scanned for 60 s at each orientation. The Debye–Scherrer diffraction rings were collected using the area detector in a 2-D diffraction image. The planes of $11\bar{2}4$ ($2\theta_0 = 99.22°$), $20\bar{2}3$ ($2\theta_0 = 90.45°$), and $21\bar{3}1$ ($2\theta_0 = 96.833°$) were used for stress measurements. Leptos software, version 7.8 developed by Bruker AXS, was used for residual stress calculation.

3.2.4 Layer removal for through-depth measurement

Electro-polishing, a chemical etching process, is used to remove a thin layer of surface material. In this process, a sample is made to act as the anode in an electrolytic cell. A thin material layer is removed, without inducing any residual stress that can happen in mechanical layer removal. A probe is placed at the surface of the sample and, by applying a voltage over a specific time, the material is removed via the electro-polishing process. To measure the residual stress through the depth, the layer removal method using an electro-polishing device was employed. For this purpose, the Proto electrolytic Model 8818-V3, working at the voltage of 50V and the probe diameter of 15 mm, was used to remove a layer without inducing residual stresses. The electrolyte was mixed as a combination of ethanol 95%, distilled water, and perchloric acid 60%, based on the ASTM standard [126]. For measuring the residual stress through the depth, first, the stress was measured at the surface using XRD, then a few micrometers of the surface were removed by the electro-polisher, and the depth of polishing was measured using a dial indicator. Again the newly revealed surface was exposed to the x-ray for stress measurement.

3.2.5 Stress correction methods

There are two stress correction factors that must be applied; first, due to the x-rays penetration depth [59] and second, because of the effect of the stress re-distribution after layer removal [60]. The first stress correction factor, related to the x-ray depth penetration, is necessary for measuring the residual stress through the depth of Mg alloys because of its low mass attenuation coefficient (39.79 cm^2/gr for the Cu-$K\alpha_1$ beam) [127]. Respectively, 50% and 90% of the exposed x-rays are diffracted from the surface up to 36.2 μm and 126.8 μm through the depth. These penetration depths for steel alloys in which the mass attenuation coefficient is 299.7 cm^2/gr [127] are 1.1 μm and 3.7 μm for 50% and 90% of x-ray diffraction, respectively. As such, for steel alloys, the observed stress can be considered as a surface (actual) stress, but in Mg alloys, the stress correction factor should be applied to compensate for the volume of element exposed to the ray. Consequently, by measuring the stress before and after polishing, and knowing the depth of polishing, the actual residual stress at the surface can be evaluated. Figure 3.2 shows the concept of the diffraction of x-rays from different locations through the depth.

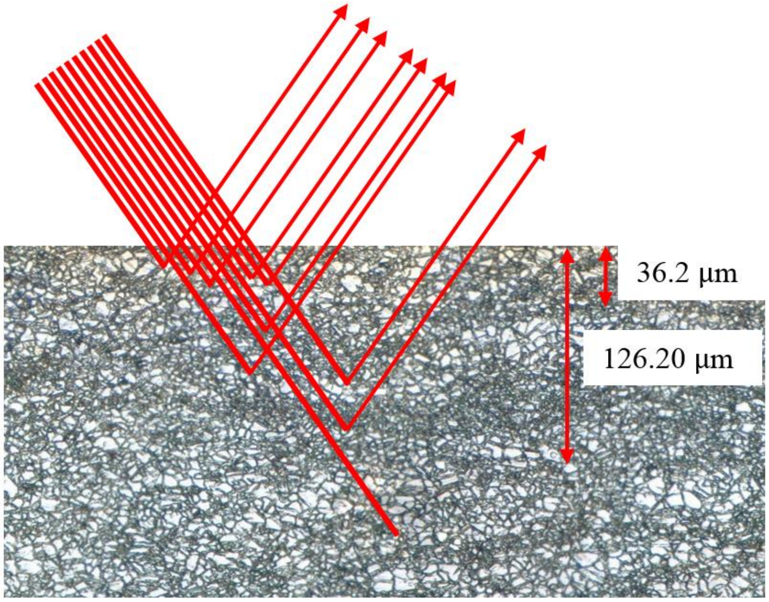

Figure 3.2 Concept of stress correction factor due to x-ray depth penetration through the depth

The method of correcting the observed residual stress after each polishing step is described in [60] and [128]. The ratio, G_z, of the diffracted beam from the surface to the depth z, I_z, to the total impinged intensity, I_T is calculated using equation 3.3,

$$G_z = \frac{I_z}{I_T} = 1 - \exp[-\mu z(\frac{1}{\sin\omega} + \frac{1}{\sin(2\theta-\omega)})] \tag{3.3}$$

where μ, z, ω, and 2θ are the linear absorption coefficient, depth, incident angle, and diffraction angle, respectively. The linear absorption coefficient is calculated by multiplying the density by the mass attenuation coefficient. By defining A as shown in equation 3.4,

$$A = \mu(\frac{1}{\sin\omega} + \frac{1}{\sin(2\theta-\omega)}) \tag{3.4}$$

equation 3.3 can be rewritten to equation 3.5.

$$G_z = 1 - e^{-Az} \tag{3.5}$$

Using the concept of weight averaging, the observed stress at each depth is obtained by equation 3.6 [59].

$$\hat{\sigma}(z) = \frac{\int_z^\infty \sigma(\tau)e^{-A(\tau-z)}d\tau}{\int_z^\infty e^{-A(\tau-z)}d\tau} \tag{3.6}$$

By differentiating equation 3.6 with respect to z and simplifying, the corrected stress (σ) is evaluated from the measured (observed) residual stresses ($\hat{\sigma}$), using equation 3.7.

$$\sigma_i = \hat{\sigma}_i - \frac{1}{A}\left(\frac{\hat{\sigma}_{i+1} - \hat{\sigma}_i}{z_{i+1} - z_i}\right) \tag{3.7}$$

The second stress correction factor is concerned with the re-distribution of residual stresses after removing a layer. When a stressed layer is removed, the residual stress measured in the sub-surface layer must be corrected to consider the effect of stress relaxation created by removing that stressed layer. Figure 3.3 demonstrates the concept of the correction factor due to the re-distribution of residual stresses after layer removal, showing the actual residual stresses σ_i before polishing, plus the measured residual stresses after each layer-removal step $\hat{\sigma}_i$.

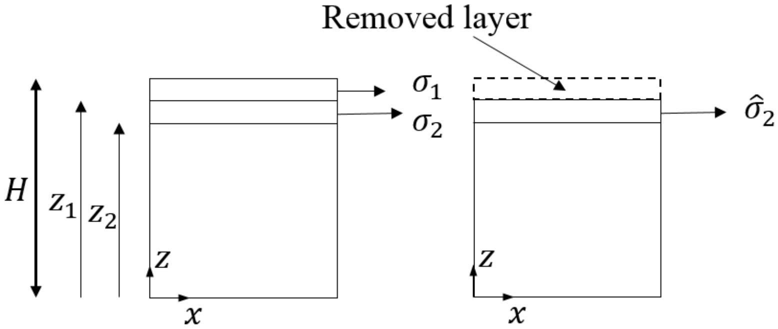

Figure 3.3 Stress correction factor due to re-distribution of residual stress after layer removal for flat plate

Using the theory of elasticity and Taylor's series, equation 3.8 provides the method for stress correction after layer removal for a flat sample [60], where H is the initial thickness of the substrate, and z_i is the updated thickness of the material after layer removal.

$$\begin{aligned} &\sigma_1 = \hat{\sigma}_1 && \text{For surface point} \\ &\sigma_i = \hat{\sigma}_i - 4\hat{\sigma}_{i-1}\left(\frac{z_i - z_{i-1}}{H - z_{i-1}}\right) && \text{For other points} \end{aligned} \tag{3.8}$$

3.2.6 Grazing-incidence X-ray Diffraction method (GIXD)

The grazing-incidence method is introduced to non-destructively measure the residual stresses in samples having a stress gradient in the surface and sub-surface layer. As shown in equation 3.3, the x-ray depth penetration is a function of the linear absorption coefficient, incident angle, and diffraction angle. Thus, to change the penetration depth, one or a combination of these three parameters should be modified. The first approach to change the x-ray penetration depth starts with a change in the linear absorption coefficient and uses incident rays with a different energy. This approach is used in some methods such as neutron diffraction [129]. The second approach uses different diffraction angles and has been used in [130] and [131] for measuring the residual stress in thin films and coatings, respectively. The third approach uses various incident angles, which provides different penetration depths in each measurement [99], [132], [133]. The relation of the incident angle and x-ray depth penetration provides an opportunity to obtain the stress profile within a few to several tens of micrometers without layer removal in Mg alloys. In this method, a corresponding depth for an incident angle is defined as a thickness in which 50% of the impinged rays are diffracted up to the desired depth [59]. So, considering $G_z = 0.5$, the associated effective depth can be calculated by equation 3.9. Figure 3.4 shows the concept of reducing the x-ray penetration depth through the thickness of a material and effective depth ($\bar{z}$), where 50% of the incident beams are diffracted up to that depth.

$$\bar{z} = \frac{0.693 \sin\omega \,.\, \sin(2\theta - \omega)}{\mu(\sin\omega + \sin(2\theta - \omega))} \tag{3.9}$$

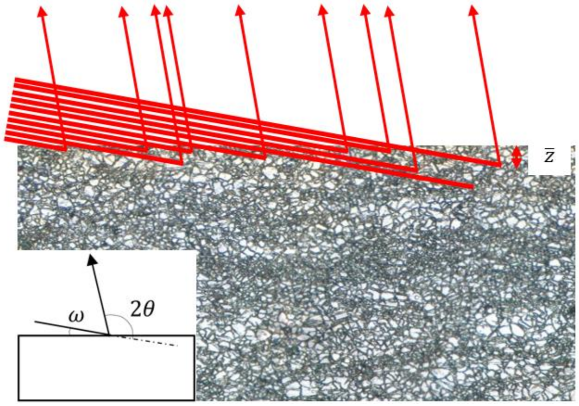

Figure 3.4 X-ray penetration through the depth of material, using lower incident angle and corresponding effective depth

Therefore, the corrected stress values are calculated as shown in equation 3.10 [59].

$$\sigma_1 = \hat{\sigma}_1 \qquad \text{For surface point}$$
$$\sigma_i = (\hat{\sigma}_i - \hat{\sigma}_{i-1})exp\left(\frac{z_{i-1}}{z_i}\right) + \hat{\sigma}_{i-1} \qquad \text{For other points} \tag{3.10}$$

To avoid the defocusing problem in small incident angles, a smaller collimator with a diameter of 0.3 mm was used in this study. Thus, the x-ray exposure time was increased to 12 min in each orientation to capture enough intensity. Table 3.3 shows the effective depth that x-ray penetrates Mg alloys using the Cu-Kα source, associated with each x-ray incident angle for $2\theta_0 = 99.22°$.

Table 3.3 Cu-Kα effective penetration depths for Mg alloys, corresponding to different incident angles

ω (°)	$\bar{z}$ (µm)
5	7.7
10	14.3
15	19.8
25	28.3
35	33.8

3.2.7 Error calculation

This section attempts to provide a method for calculating error in the corrected stresses due to the layer removal and depth penetration corrections. The error of corrected stresses was calculated based on the root mean square approach. In this method, if R is a function of X_1, X_2, …, X_n with respective errors of ω_1, ω_2, …, ω_n (equation 3.11),

$$R = f(X_1 \pm \omega_1, X_2 \pm \omega_2, \dots, X_n \pm \omega_n) \tag{3.11}$$

then the error in R is calculated using equation 3.12.

$$\omega_R = \left(\left(\omega_1 \frac{\partial R}{\partial X_1}\right)^2 + \left(\omega_2 \frac{\partial R}{\partial X_2}\right)^2 + \cdots + (\omega_n \frac{\partial R}{\partial X_n})^2\right)^{1/2} \tag{3.12}$$

The error bar of the observed stress measurement was obtained to include the three measurements at different hkl planes plus the error bar calculated by the Leptos software for each stress measurement. The accuracy of measuring the polishing depth using the dial indicator was ±6 µm.

3.2.8 Hole drilling

The residual stresses were measured by the hole-drilling method as well. In this method, strain gauges are attached to the surface of a material, and a drill tool creates a hole. By measuring the strain relaxation through the drilling, the residual stress distribution through the depth can be calculated [134]. In this study, an MTS3000, Sint Technology hole-drilling machine was used to measure the residual stress profile through the depth. Conventional HBM three-element strain gauge rosettes were installed on the surface of the AZ31B rolled sheet. The 400,000 rpm rotation speed of a drill tool with a 2 mm diameter was performed to create a shallow hole in the center of the strain gauge rosettes as shown in Figure 3.5.

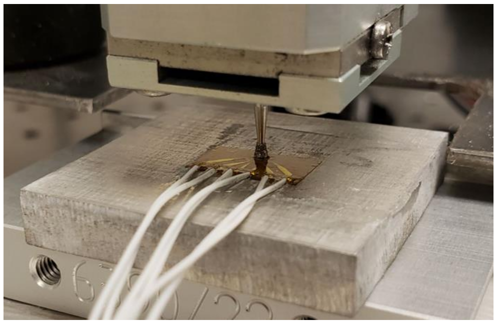

Figure 3.5 Hole drilling experiments set-up, showing the drilling tool in the center of the strain gauge rosettes

3.3 Results and Discussion

Figure 3.6 shows the texture of the as-received material, showing a strong basal texture in the normal direction (ND) of the sheet, which is typical in rolled magnesium alloy.

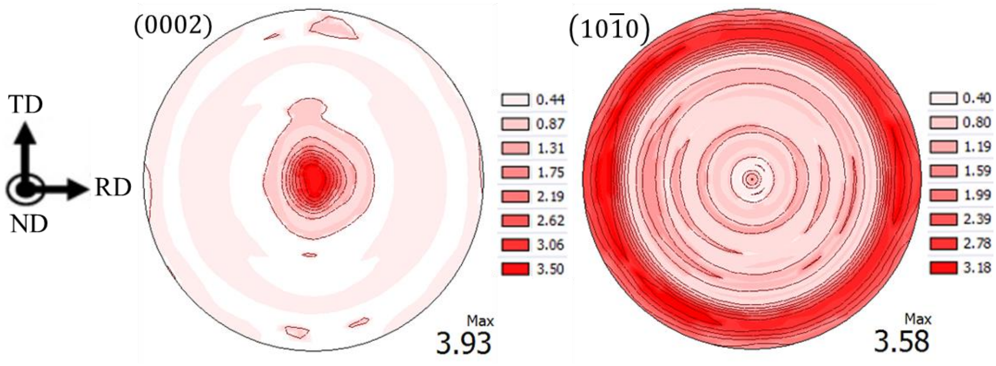

Figure 3.6 Texture of AZ31B-H24 rolled sheet with 4 mm thickness

Figure 3.7 shows the effect of sample oscillation and exposure time on the estimation of the diffraction angle. It indicates that 60s exposure time when using oscillation would be enough. As expected, the sample oscillation yields less variation and dampens the variation of peak angle measurement. Oscillating the sample also has the benefit of measuring the residual stress based on the residual stress distribution at different locations. In this case, the results would be the average residual stress in the x-ray exposed area.

The diffraction patterns of AZ31B-H24 using Cu-Kα_1 and Cr-Kα_1 are shown in Figure 3.8. Using the Cu tube, the peaks are much sharper and more intense. However, when the goal is to find the high diffraction angles in stress measurements (Figure 3.9), both Cu and Cr tubes provide comparable peak to noise ratios.

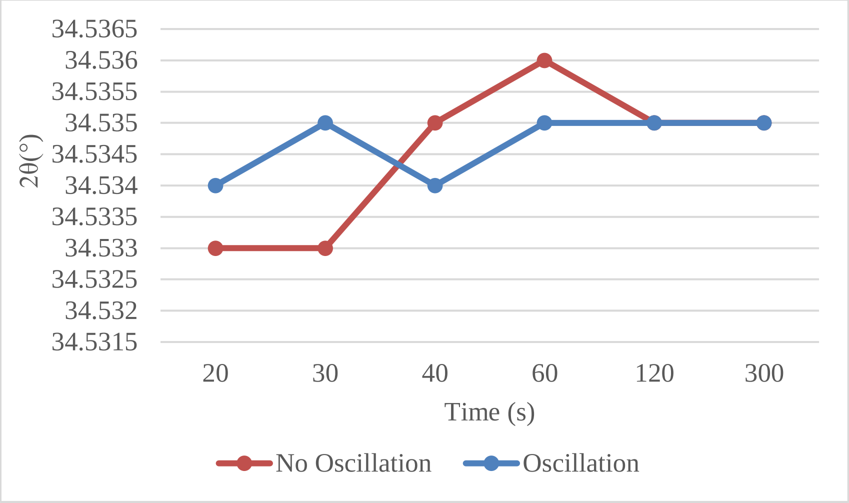

Figure 3.7 Effect of x-ray exposure time on the estimated diffraction angle, with and without sample oscillation

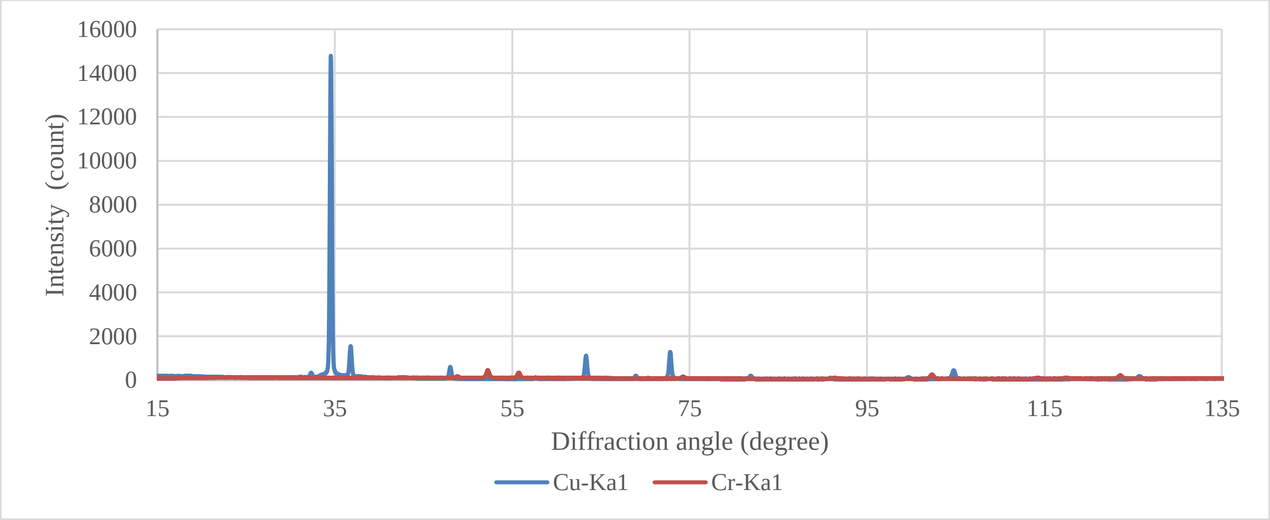

Figure 3.8 Diffraction pattern of AZ31B-H24, using Cu-Kα$_1$ and Cr- Kα$_1$ beams

The main difference between Cu and Cr tubes in stress measurement is in their mass attenuation coefficients, which result in each having different penetration depth through the Mg alloys. Table 3.4 provides the mass attenuation coefficients of these two x-ray beams, used in stress measurement of Mg alloys, and also provides associated depths where 50% and 90% of the x-rays are diffracted. Cr-Kα$_1$ has lower penetration, with 90% of the detected beams diffracted up to 40.05 μm. Although this depth is 68% less than the corresponding depth when using the Cu tube, the stress correction factors must still be applied when there is a high residual stress gradient through the thickness of a material. This penetration depth is calculated assuming the same diffraction angle of 99.22° for both tube materials, and it is assumed that the tube and the source are at the same angle, half of the diffraction angle (Brag's condition). As discussed in section 2, the Cu tube has been selected for the rest of the stress measurements.

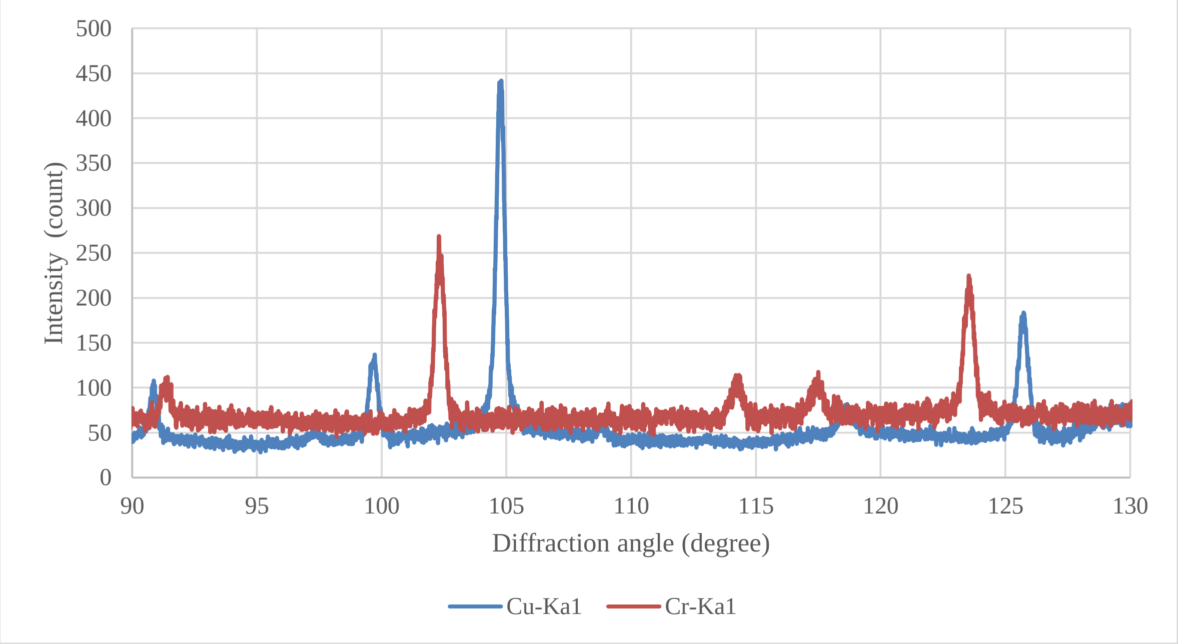

Figure 3.9 Diffraction pattern of AZ31B-H24, using Cu-Kα_1 and Cr- Kα_1 beams

Figure 3.10 demonstrates the results of the observed (before stress correction) residual stress in the shot peened plate using the steel shot in the rolling direction (RD) and transverse direction (TD). It shows that the residual stresses are very close to each other in RD and TD, a fact which is in agreement with the axisymmetric nature of the texture along the ND (Figure 3.6). Thus, as the material is approximately in-plane isotropic [121], the residual stresses are similar in RD and TD. From this point on, the reported residual stress measurement results are the average values of residual stresses in RD and TD.

Table 3.4 Mass attenuation coefficients of different x-ray beams used in stress measurement of Mg alloys and associated depths where 50% and 90% of the x-rays are diffracted

Beam	Mass attenuation coefficient (cm^2/gr) [127]	Depth associated with 50% of diffraction (µm)	Depth associated with 90% of diffraction (µm)
Cu-Kα_1	39.79	38.16	126.78
Cr-Kα_1	125.9	12.06	40.05

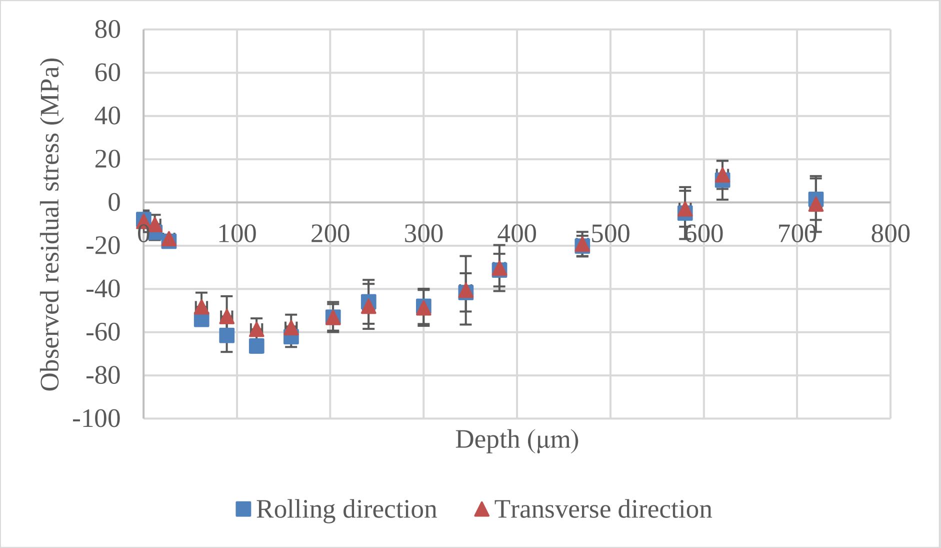

Figure 3.10 Observed residual stresses (before stress correction) induced after peening using steel shots along RD and TD

Figure 3.11 shows the observed residual stress measurement results obtained from the Leptos software. The error bars were calculated based on three measurements at three lattice planes of $11\bar{2}4$ ($2\theta_0 = 99.22°$), $20\bar{2}3$ ($2\theta_0 = 90.45°$), and $21\bar{3}1$ ($2\theta_0 = 96.833°$). This figure indicates a negligible residual stress in the as-received AZ31B-H24 rolled sheet, and also compressive residual stress distributions in the sub-surface layer of the peened samples. The two peened profiles are in a good agreement at the measurements of the surface residual stress, maximum compressive residual stress and its corresponding depth. However, the sample peened with steel shots shows a deeper depth of compressive residual stress. The results of this figure should be corrected using the two stress correction factors as they are shown in Figure 3.12.

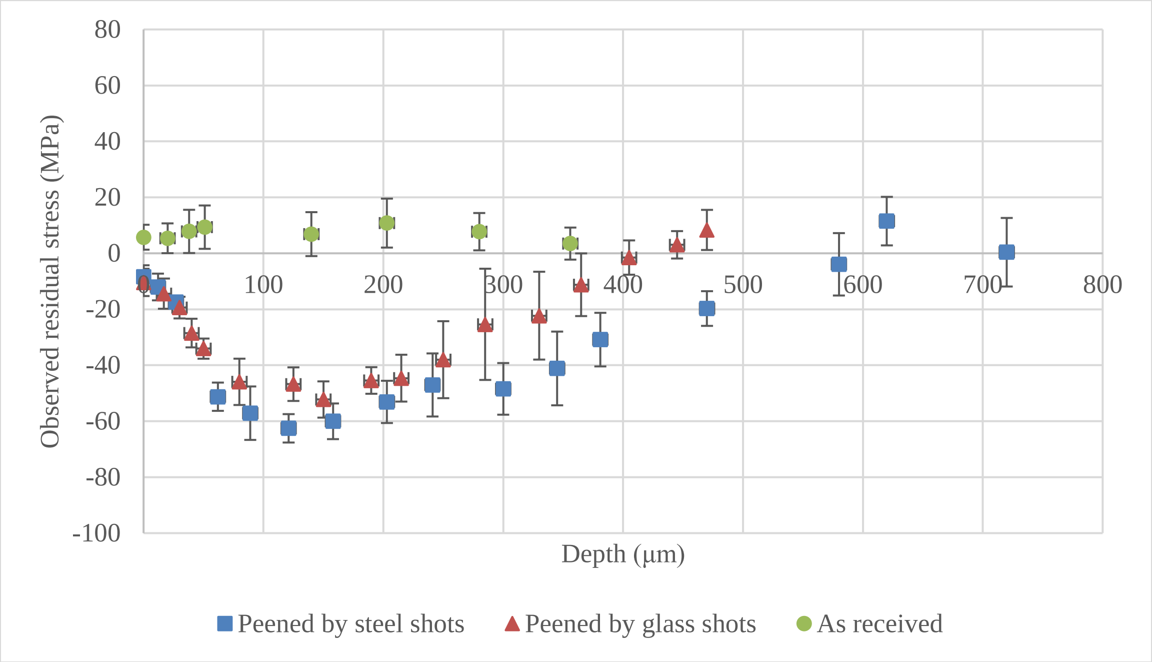

Figure 3.11 Observed (before stress correction) residual stress on as received AZ31B—H24 plate and after shot peening with steel and glass shots

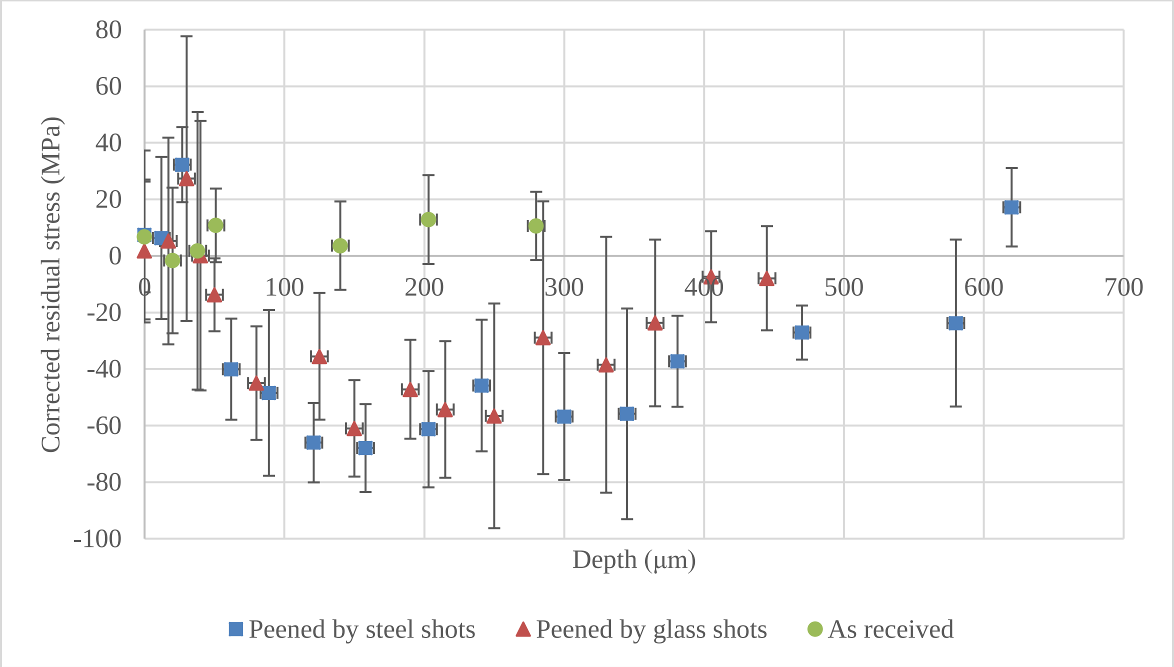

Figure 3.12 Corrected (actual) residual stress on the as-received AZ31B—H24 plate and after shot peening with steel and glass shots

The hole-drilling method was also used to measure the residual stress in the same as-received and shot peened samples. Figure 3.13, Figure 3.14, and Figure 3.15 show the results of the corrected residual stresses in the as-received sample and induced by the peening process with steel and glass shots, respectively, and a comparison with the hole-drilling results. All the XRD and hole-drilling methods evaluate a similar residual stress distribution through the depth. In the as-received sample, both XRD and hole drilling methods predict negligible residual stresses through the depth. In the peened samples, in particular, the hole drilling predicts a shallower depth with compressive residual stress. The hole drilling is not able to measure the residual stress at the surface, and the closest data point in depth is 25 micrometers below the surface. Therefore, a more detailed comparison close to the surface, where XRD corrections showed considerable changes as compared to observed measurements, was not possible.

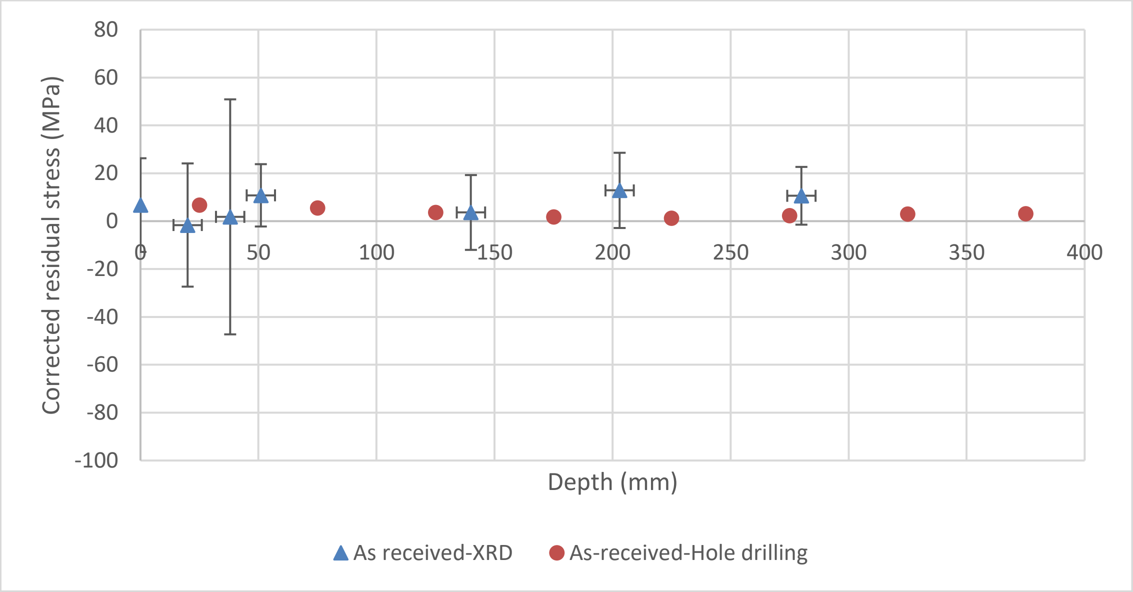

Figure 3.13 Residual stress distribution of the as-received sample and comparison with the hole-drilling method

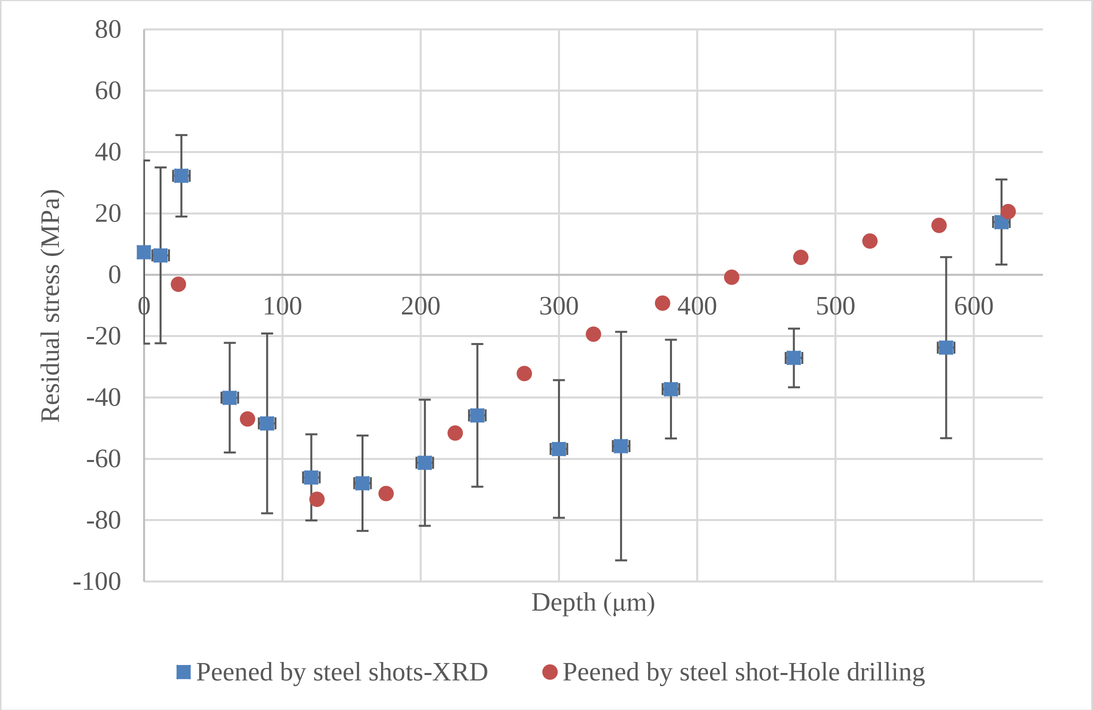

Figure 3.14 Residual stress distribution of shot peened AZ31B using steel beads and comparison with the hole-drilling method

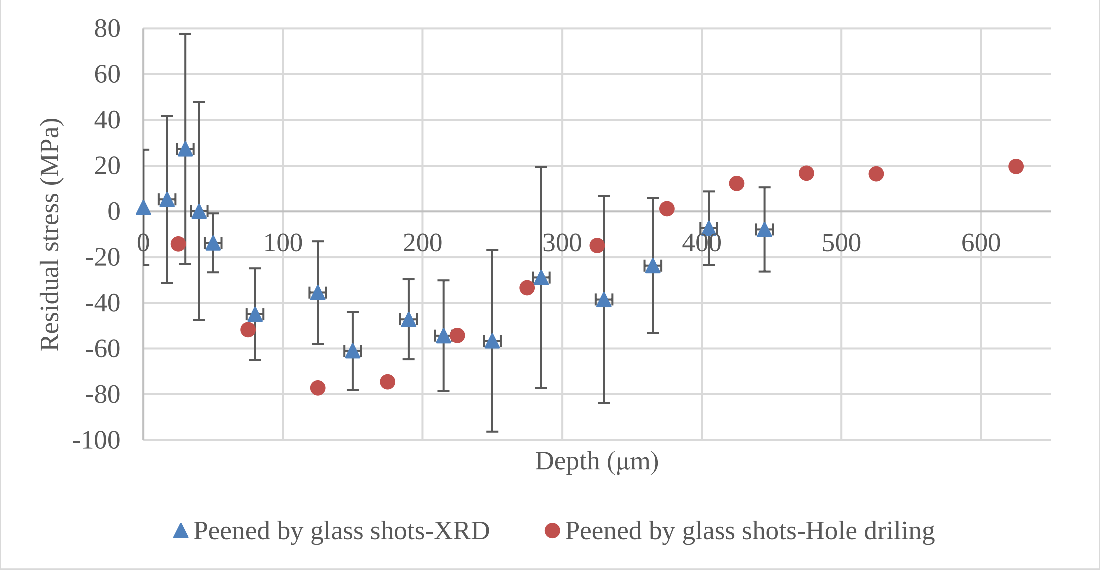

Figure 3.15 Residual stress distribution of shot peened AZ31B using glass beads and comparison with the hole-drilling method

To further examine the considerable impact of corrections near the surface, the GIXD method was considered. The residual stresses in a thin layer from the surface were measured using the GIXD method. Figure 3.16 and Figure 3.17 show the results of the GIXD method on peened samples using steel and glass shots, respectively, and comparison with the corrected stresses evaluated by XRD. It shows that the GIXD method's results follow the corrected residual stresses, confirming that the stress correction factors impact on the residual stress measurements of Mg alloys.

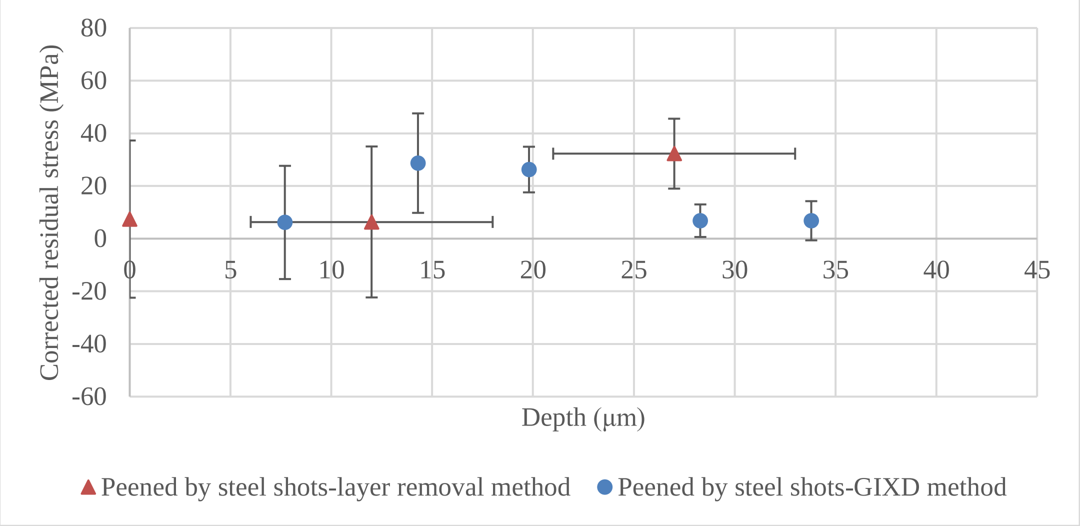

Figure 3.16 Results of the GIXD method on the shot peened sample using steel shots, and comparison with corrected stress evaluated by XRD

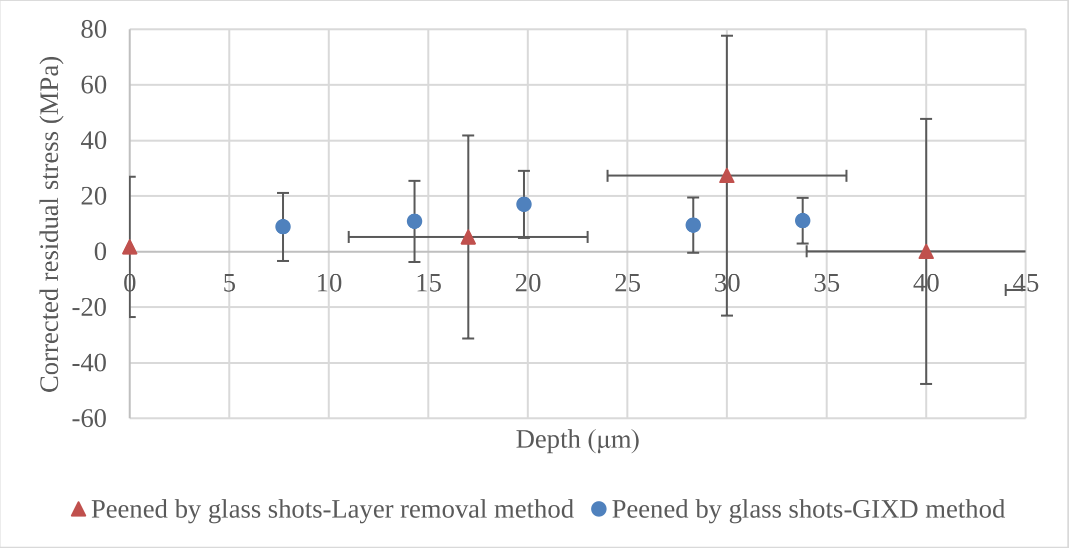

Figure 3.17 Results of the GIXD method on the shot peened sample using glass shots, and comparison with corrected stress evaluated by XRD

In general, shot peening creates compressive residual stress at the surface and sub-surface layer of a material, however here, as concluded by the corrected XRD results and confirmed by the hole-drilling and GIXD methods, there is no compressive residual stress up to 40 micrometers below the surface. To investigate what is the cause of these unexpected results, the microstructure of the as-received and peened samples were examined. Samples from as-received and peened sheets near the surface were cut and polished, and then observed under an optical microscope. Figure 3.18 shows the cross-section of the as-received and peened samples. It indicates that the as-received sample has a uniform and undamaged microstructure and smooth surface, but the peened sample shows clear damage and much rougher surface near the surface where the material was work hardened due to the peening. This figure also shows the presence of micro-cracks up to 34.4 micrometers below the surface, where the corrected residual stresses are showing negligible residual stress even though the observed measurements show increasing compressive residual stress within this layer. In the presence of micro-cracks, the residual stresses are expected to vanish in this section. Thus, the corrected residual stress profiles agree with the surface topography of the peened sample.

a) As-received

b) Peened sample

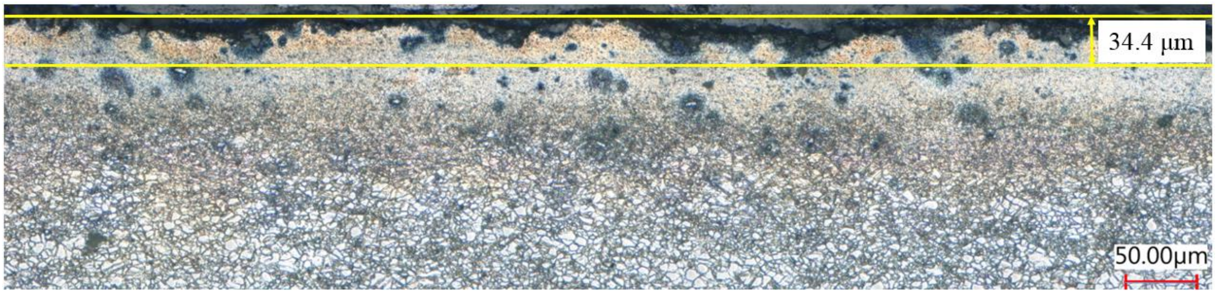

Figure 3.18 Lateral cross-section of a) as the received sample, b) peened using steel shots

Conclusion

Several studies have used the XRD method for residual stress measurement, however, the effect of the depth of x-ray penetration in Mg alloys on the results of measurements has not been fully studied. To study this effect, the residual stress distribution of AZ31B-H24 before and after peening under two different peening conditions were measured using conventional 2D-XRD, GIXD, and hole-drilling methods. For the evaluation of residual stress profiles through the depth, the electro-polishing method for layer removal was employed, and the critical effect of stress correction factors was discussed. It was shown that due to the low mass attenuation coefficient of Mg, that results in a high depth of penetration of Cu-kα_1 rays, the uncertainty of the residual stress measurement is high. To account for the high depth of penetration, a correction to the measured residual stress was proposed. However, due to the low x-ray absorption coefficient of Mg alloys and as suggested by equation 3.7, the error in corrected values will be high. Therefore, this high uncertainty should always be considered when using XRD on magnesium. The difference between the corrected and measured residual stress profiles was proven to be significant in the first 40 micrometers from the surface. To verify the accuracy of the corrected values, two other methods were used; GIXD technique and hole drilling. Both GIXD and hole-drilling measurements were in good agreement with the corrected stresses, showing there is no compressive residual stress within a layer close to the surface. Examination of as-received and peened microstructure near the surface revealed the surface deterioration within the 34.4 micrometers from the surface, where the stresses are believed to be released due to the local damage caused by the peening process. For the residual stress values beyond this layer, the measured and corrected residual stresses were close and in agreement with the hole-drilling method results.

Chapter 4

Large strain loading and unloading behavior of AZ31B rolled sheet in thickness and in-plane directions

Abstract

Understanding the behavior of Mg alloys at large strain values in loading-unloading is important in many processes such as deep drawing, shot peening, laser shock peening, cold spray, and hole cold expansion. The main problem in obtaining the tension-compression (TC) and compression-tension (CT) in the in-plane directions is the buckling which researchers have used two approaches: 1) using anti-buckling fixtures and 2) using bulk materials for testing. In addition, the main problem in the CT and TC behavior in the normal direction (ND) of the rolled sheet is the short sample length. This paper evaluates the CT and TC behavior of the AZ31B-H24 rolled sheet in different directions. The TC and CT curves unloaded at different strain values are obtained using an anti-buckling fixture in the rolling direction (RD) and a novel fixture in ND. The results show the negligible effect of using the anti-buckling fixture on stress-strain curves in RD. The results of ND confirms the efficiency of the new fixture to evaluate TC and CT curves in ND of sheets. Finite element method has been employed to evaluate the consistent area for strain measurement using digital image correlation (DIC) in the new setup. The TC and CT results of the new fixture have been verified by comparing the curves obtained by the new fixture in RD by those obtained by using the anti-buckling fixture.

Keywords: ***Large strain loading-unloading, Normal direction, Compression-tension, Tension-compression, Mg alloys***

4.1 Introduction

The application of Mg, the lightest industrial metal, in the automotive industry is increasing. Since the initial employment of Mg alloys in vehicles in the 1920s [2], recent legislation and competition among automotive companies have created renewed interest in increasing fuel efficiency through weight reduction. In order to expand the application of Mg, its properties should be known to design processes such as machining, deep drawing, shot peening, laser shock peening, cold spray, and hole cold expansion. These processes induce residual stresses, meaning the loading-unloading behavior of the material should be known for modeling purposes. The loading step in these processes creates a significant work-hardening in a material, which requires large strain loading-unloading behavior. Buckling is the main problem in the compression part of the loading-unloading tests. Using bulk material and using anti-buckling guides are two approaches for compression tests; however, the bulk material cannot be used in the tensile part of the CT and TC curves.

Using a bulk material to measure the compression stress-strain curve has been standardized [135]. This experimental set up requires accurate machining, as described in [135]. Depending on the as-received material type (e.g., sheet, bar, etc.), the geometry of the sample could be different. The acceptance criteria require getting an acceptable Young's modulus of elasticity. The compression behavior of 6 mm long and 4 mm wide cuboid AA6060 samples was studied using a customized fixture in which the extensometer was installed on the grip to measure the strain. In studies concerned with the Mg properties, the same fixture was employed to obtain the compression behavior of AZ31B and ZEK100 using rectangular sheet samples [136]. Ghaffari Tari et al. [137] evaluated the compression stress-strain curve of cuboid AZ31B samples, using a different customized fixture.

For evaluation of compression-tension behavior, an anti-buckling fixture can be used. Packing several samples such as a laminate with an external lateral support was the initial attempt to prevent buckling [138]. Using a similar method, recently, Yoshida et al. [139] packed several samples and used a special fixture with coil-springs to obtain the cyclic behavior of steel sheets. To reduce friction between the anti-buckling fixture and the plates, they employed Teflon sheets which are covered with vaseline. The next step was to employ glue to keep the plates together [140], followed by using lateral plates as a support [141]–[145]. In this approach, one specimen is used instead of packed specimens or glued samples in previous approaches. One disadvantage of these fixtures is the buckling in high compression loads at the small unsupported length between the machine grip and the anti-buckling fixture. The next generation of anti-buckling fixtures was developed by Kuwabara et al. [146] to support the whole length of a sample between two grips. Their novel fixture uses comb-type dies to support a specimen. In this case, the anti-buckling fixture moves by the machine's cross-head movement to support the whole length of a material. Cao et al. [147] designed two angular blocks on each side of a material connected by a pre-loaded spring. This design also provides full-length support of a specimen. Dietrich et al. [148] developed a fixture to support the whole length of a sample during cyclic loading by connecting the lateral-supporting plates with the machine's grips. [149], [150] employed the same fixture in their research. Concerned with the bi-axial stress state when using an anti-buckling fixture, made [151]–[154] to use a servo-hydraulic system to apply consistent and small lateral force on a specimen to guarantee that stress remains uniaxial. Researchers assembled setups to measure the friction between an anti-buckling fixture and a sample to compensate for its effect on the evaluation of the stress-strain curve [148], [150]. They reported that the friction values are relatively small, and the friction forces are negligible compared to the loading on a sample.

Modeling of some processes requires understanding the loading-unloading stress-strain curves in the normal direction (ND) of sheets. Park et al. [155] obtained the cyclic behavior of 50 mm thick AZ31B rolled sheet in ND, using a cylindrical specimen. Due to the high thickness of the material, they were able to machine scaled dog-bone samples in ND. Wu [156] used the in-situ XRD and neutron diffraction to evaluate strains in the cyclic loading of ZK60-T5 and AZ31B-H24 plates in the normal direction. He machined cylindrical specimens, with a gauge length of 6.35 mm and a gauge diameter of 2.92 mm. The total length of the specimen was 22.35 mm. A servo-hydraulic MTS machine with a miniature extensometer with a gauge length of 5 mm was used. There are other studies for evaluation of tensile behavior of mini-specimens [157]–[159] however their sample geometries and fixtures are not designed for reverse loads.

In this paper, we provide the CT and TC properties of the 4 mm thick AZ31B-H24 rolled sheet in the rolling direction (RD). The samples are loaded and unloaded from different compressive/tensile strains. It is also shown that the anisotropy between RD and TD is negligible. By comparing the results when using the anti-buckling fixture and results obtained from cuboid samples, the negligible effect of using anti-buckling on the stress-strain curve is confirmed. We also introduce a new experimental set up for obtaining the TC and CT curves along the ND of the rolled sheets. The accuracy of using the new fixture and experimental set-up have been verified, first by evaluating the Young’s modulus of elasticity from experiment, second by modeling the experiment using FE analysis to verify the consistent area of uniform strain and stress field, and third by comparing the TC and CT curves obtained with new set up with small specimens machined in the RD with the results obtained by employing the anti-buckling fixture with standard samples. The results show Young’s modulus of close to 45 MPa in ND. The FEM results confirm that an area in the middle of the sample can be used for TC and CT testing of a material. Finally, the obtained curves of the samples tested in RD are in good agreement with the ones obtained using the anti-buckling fixture.

4.2 Material and experiments

4.2.1 Material

AZ31B-H24 rolled sheets with thicknesses of 4 and 6.35 mm, provided by Magnesium Elektron of North America (MENA) were used in this study. The chemical composition of the experimental material is tabulated in [119].

Table 4.1 Major alloying elements in the composition of the AZ31B-H24 rolled sheet [119]**.**

Element	Al	Zn	Mn
Wt. %	2.73	0.915	0.375

Texture measurements were carried out on a Bruker D8 Discover X-ray diffractometer equipped with a VÅNTEC-500 2D detector using Cu-K_α beam radiation at 40 kV and 40 mA, by measuring the incomplete pole figures of $\{0001\}$, $\{10\bar{1}0\}$, $\{10\bar{1}1\}$ and $\{1\bar{1}02\}$ planes for tilt angle ψ between 0° and 75° and in axis rotation φ between 0° and 360°, as described in [121]. The complete pole figures were obtained using DIFFRAC.TEXTURE software, version 3.0.4, developed by Bruker AXS.

4.3 Monotonic compression test

Monotonic compression tests were performed on cuboid specimens to obtain the compression stress-strain curve at large strain values. The cuboid specimens, 6×6×8 mm, were machined with parallelism and perpendicularity tolerances shown in Figure 4.1. In order to ensure proper positioning of the cuboid specimens between compression anvils, an adjustment tool was designed (Figure 4.1). Compression anvils were gripped between jaws of a 50 KN MTS 810 servo-hydraulic material test frame.

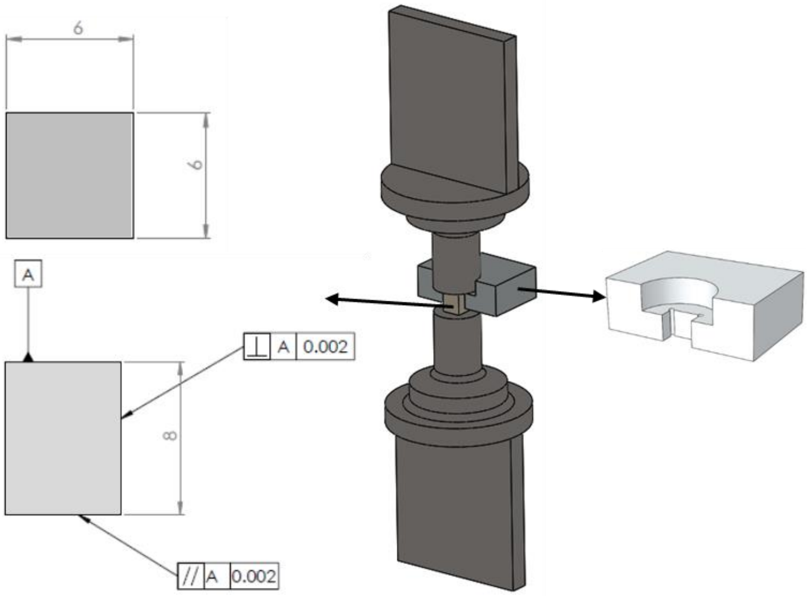

Figure 4.1 Schematics of the compression test setup with the adjustment tool (numbers in mm).

GOM ARAMIS 5M digital image correlation (DIC) system, equipped with Titanar 50 mm lenses, was employed for strain measurement during all conducted experiments. Prior to measurement, speckle pattern was painted on the specimen's face.

4.4 CT and TC tests along RD

For the purpose of preventing specimen buckling during CT and TC loading of the AZ31B-H24 sheet in RD, the proposed anti-buckling fixture in [148] was herein customized. Figure 4.2a depicts the schematic assembly of the fixture. In this design, on one hand, side plates, which move together while the test is running, provide lateral support to avoid buckling. Springs, on the other hand, allow deformation in ND during compressive loading. Teflon sheets were used to minimize friction between contacting surfaces.

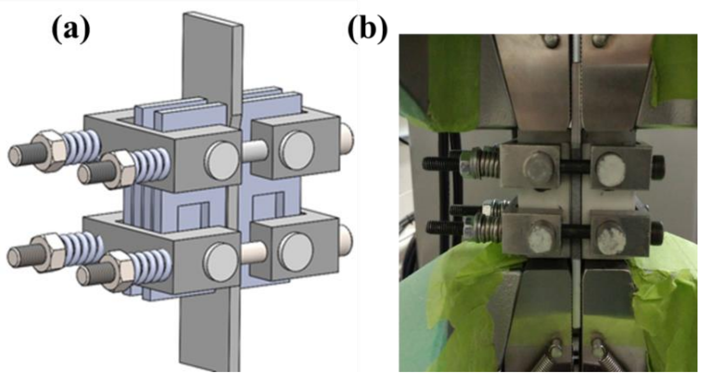

Figure 4.2 a) Conceptual design of anti-buckling fixture and sheet specimen assembly; b) the assembly mounted on the test frame facing DIC cameras.

The geometry of the 4 mm-thick sheet specimen for CT and TC tests is shown in Figure 4.3. The experiments were conducted on the MTS test frame at ambient temperature. The specimen's side (thickness) surface was painted and faced DIC cameras for strain measurement, as depicted in Figure 4.2b.

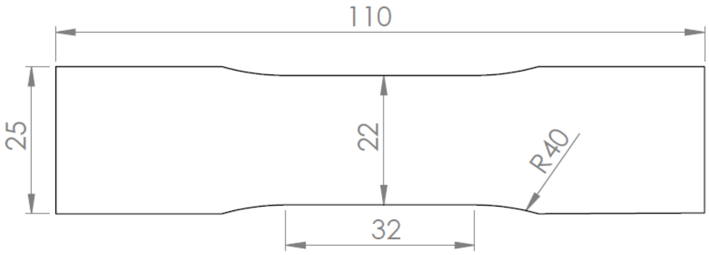

Figure 4.3 Specimen geometry used with the anti-buckling fixture for CT and TC tests in RD (dimensions in mm).

4.5 CT and TC tests along ND

Considering dimensional limitation along ND of rolled sheets, sub-sized I-shaped specimens, with the geometry, shown in Figure 4.4a, were machined from 6.35 mm-thick AZ31B-H24 rolled sheet. The specimen's thickness is 1.20 mm. In order to test such small specimens under CT and TC loading, a new fixture is designed, as partly displayed in Figure 4.4b. The proposed fixture includes three stacked steel plates on each gripper side, with the middle one being 1.55 mm shorter than the side ones. This gap is filled with the specimen's grip section, providing a lateral mounting force on the specimen via the side plates as the fixture is clamped between the universal machine's jaws. This configuration allows compressive force to be applied to the specimen through the middle plate. Tensile force, on the other hand, is applied to flanges of the specimen, through four mounting brackets (see Figure 4.4), which are fixed to the stacked plates by bolts.

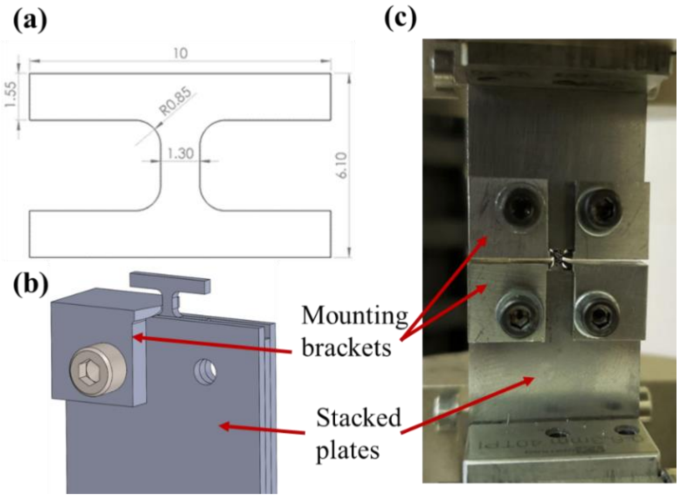

Figure 4.4 Setup for CT and TC tests in ND; a) specimen geometry (dimensions in mm), b) conceptual design, and c) clamped fixture and specimen assembly.

To identify an appropriate area for strain measurement, finite element modeling of the compression-tension test has been carried out using Abaqus. Due to the symmetry, only 1/8 of the assembly is modeled. The stacked sheets and mounting brackets are involved in this model. For the compression stage, the top surfaces of the center and side stacked sheets, and the mounting bracket are moving down together, and during tensile unloading, all are moved up. The side stacked sheet is only allowed to move in the y-direction. The mounting bracket does not play a role in compression, but it is the main contributor in the tensile unloading. The results of the compressive loading are considered as an initial state for the tensile unloading.

The compressive behavior of the Mg sample along ND is the input of the modeling, and the material is assumed to follow isotropic hardening. Figure 4.5 shows the geometry and meshing of the experiment's set-up. The model uses eight-node linear brick elements with reduced integration (C3D8R) and an element size of 10 x 10 x 10 μm for the sample. Symmetry conditions were applied at the xz, xy, and yz planes. The penalty contact algorithm was applied with isotropic coulomb friction coefficient of 0.2.

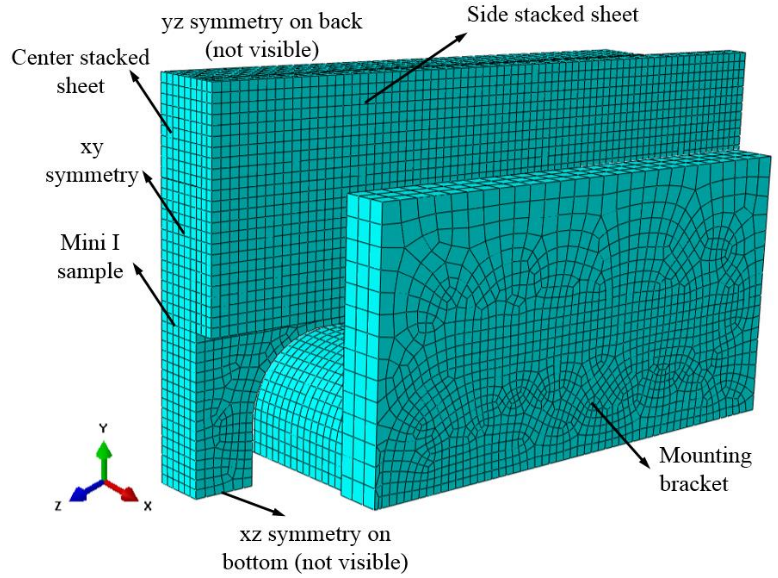

Figure 4.5 FEM modeling of the new fixture: geometry and meshing

4.6 Results and discussion

Figure 4.6 and Figure 4.7 show the basal (0002) and prismatic $(10\bar{1}0)$ pole figures for the AZ31B-H24 rolled sheets with 4 mm and 6.35 mm thicknesses, respectively, showing strong basal texture in the normal direction (ND) of the sheet, which is typical in wrought magnesium alloy. The two sheets have approximately the same initial texture.

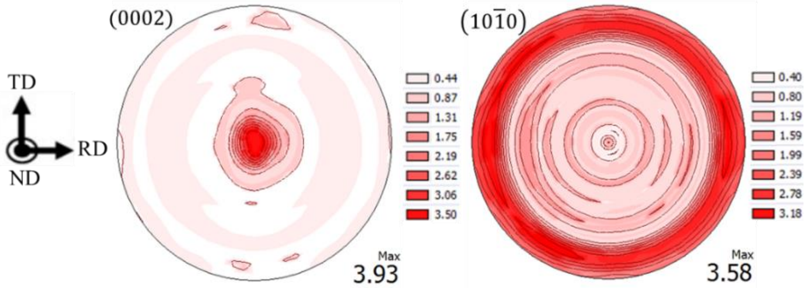

Figure 4.6 Basal (0002) and prismatic $(10\bar{1}0)$ pole figures for the 4 mm thick AZ31B-H24 rolled sheet

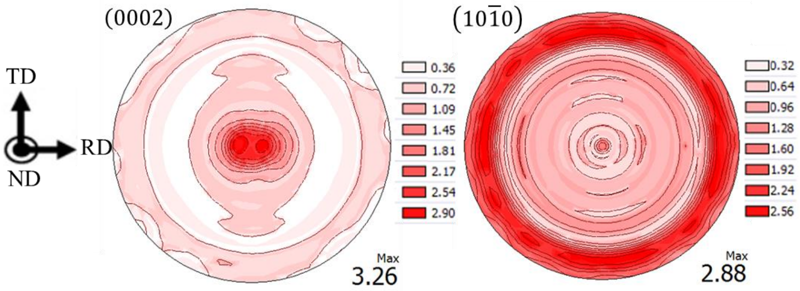

Figure 4.7 Basal (0002) and prismatic $(10\bar{1}0)$ pole figures for the 6.35 mm thick AZ31B-H24 rolled sheet CT and TC curves in RD

The CT test results in RD are shown in Figure 4.8. The twinning of the material in compression, followed by the tension-twinning, is clearly shown in the CT curves of the material in RD. This figure also shows a comparison between the curves obtained using the anti-buckling fixture and the cuboid specimen. The results are in a good agreement, confirming that there is no need to use a hydraulic servo-motor to apply constant pressure to reduce the effect of stress biaxiality. Using the method as mentioned above for the anti-buckling fixture leads to equally acceptable results.

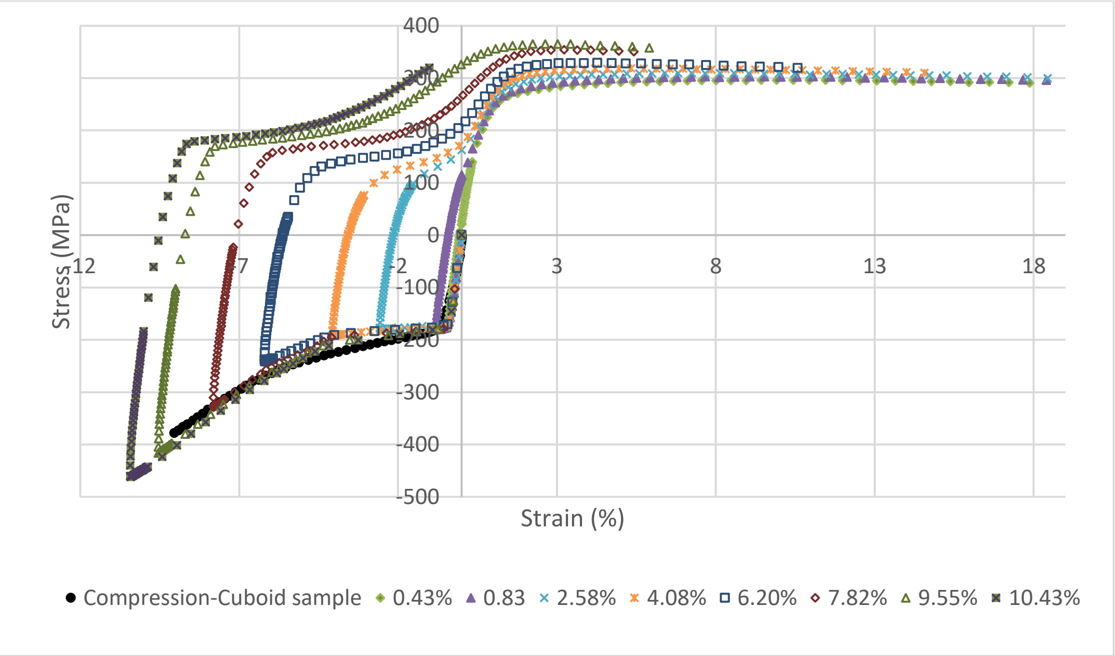

Figure 4.8 Experimental CT results of AZ31B rolled sheet in rolling direction using the anti-buckling fixture and comparison with the cuboid sample

The results of the Young's modulus and yield stresses in the RD obtained from the compression tests are mentioned in Table 4.2. The compression tests' results using the anti-buckling fixture predict the Young's modulus of elasticity and yield stress accurately in compression. It shows that the predicted Young's modulus and yield stress when using the anti-buckling and cuboid geometry are 4.66% and 5.16% different, respectively. This table also shows that there is no significant difference between the properties of 6.35 and 4 mm sheets. To better compare the compression behavior of 6.35 mm and 4 mm sheets, the compression test on 6.35 mm sheet was compared with the experimental results on the 4 mm sheet [120]. Figure 4.9 shows the comparison of the two sheets, confirming that the difference is negligible, specifically in the plastic region.

Table 4.2 Young's modulus and yield stress of AZ31B-H24 in the rolling direction in the compression test

Compression test	Young's modulus in GPa (standard deviation)	Yield stress in MPa (standard deviation)
Using anti-buckling (4 mm sheet)	46.07 (1.12)	170.36 (8.31)
Cuboid specimen test (6.3 mm sheet)	44.02 (6.59)	159.08 (1.53)
Cuboid specimen test (4 mm sheet) [120]	40.8 (3.1)	162 (2.8)

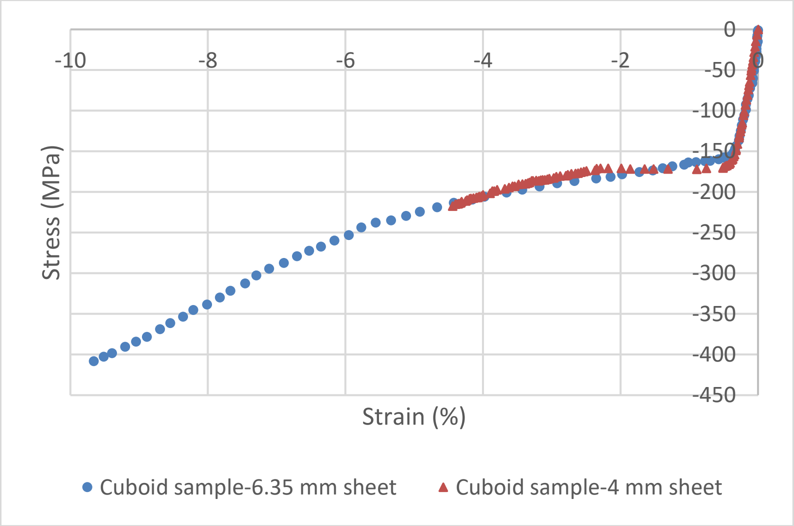

Figure 4.9 Compression test of cuboid samples machines from 6.35 mm sheet, and 4 mm sheet [120]

To confirm the negligible effect of anisotropy in RD and TD, the CT behavior of one sample in RD and one in TD are compared in Figure 4.10. Having the same stress-strain curve in CT, the isotropic behavior of the AZ31B-H24 sheet in RD and TD is confirmed, although due to the axisymmetric texture of the material along the ND (Figure 4.6), this isotropic behavior was predictable. Thus, the TC and TC properties are obtained in the RD only.

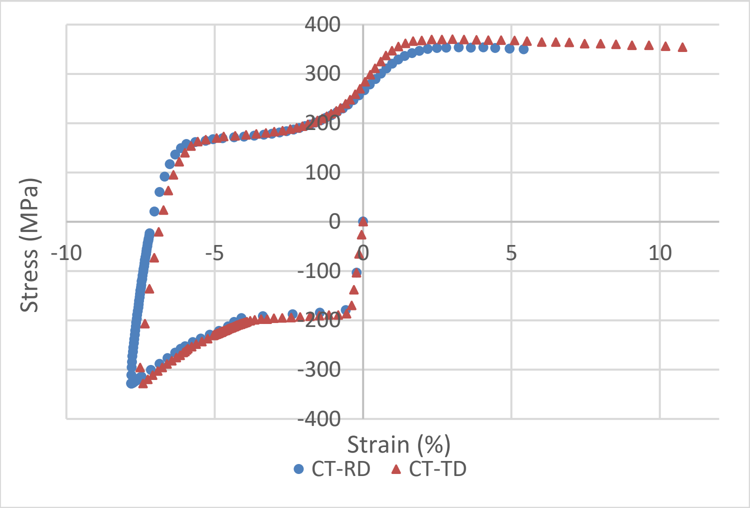

Figure 4.10 CT curves in RD and TD of AZ31B rolled sheet

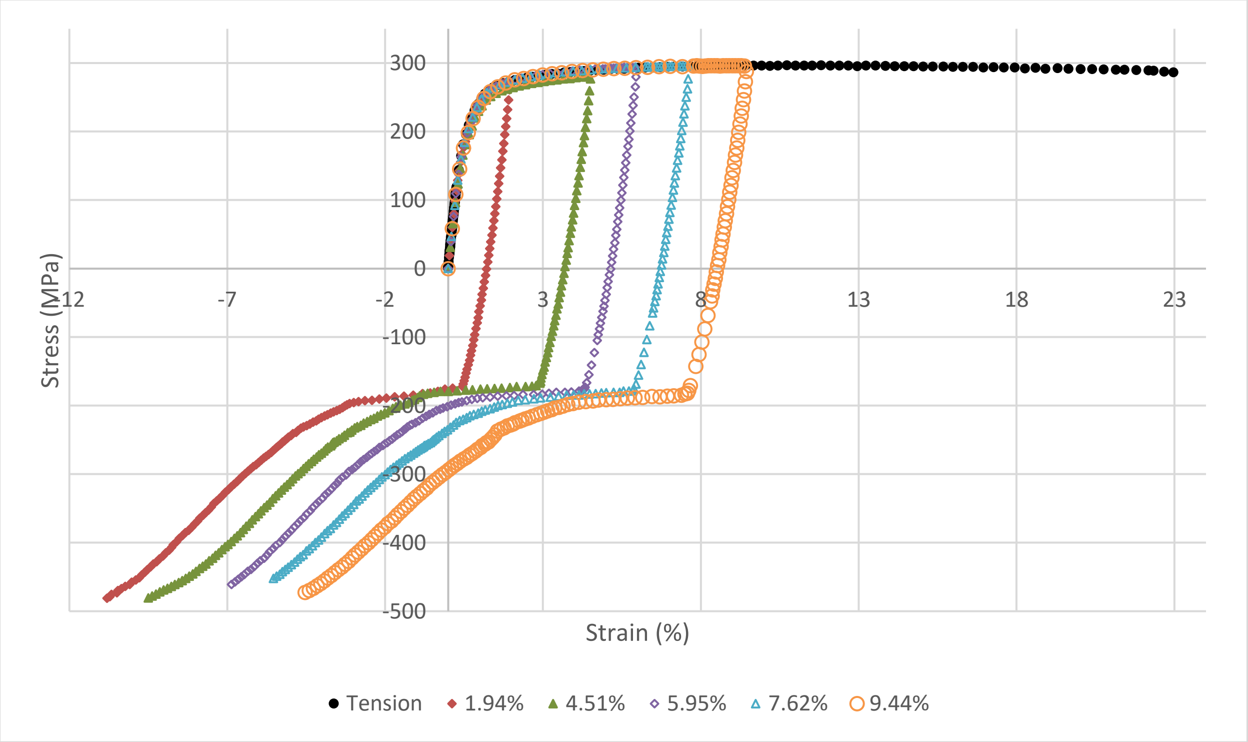

Figure 4.11 Experimental TC results of AZ31B rolled sheet in rolling direction using the anti-buckling fixture [160]

Figure 4.11 shows the TC results of AZ31B-H24 in the RD [160]. Faghih et al. [160] used the same material and anti-buckling fixture to obtain the TC behavior of the material at large strain values. As expected, based on the initial texture of the material (Figure 4.6), the TC curves demonstrate slip deformation during the tensile loading, followed by twinning in the compressive unloading.

4.6.1 CT and TC in the ND

The FEM results of the new fixture indicate that the 1 mm x 1mm area at the center of the sample provides a region in which the stress states are uniaxial with less than 5% error. This conclusion has been made by comparing the stress and plastic strain in the loading direction with the equivalent stress and equivalent plastic strain of elements in this region.

a) Compressive loading

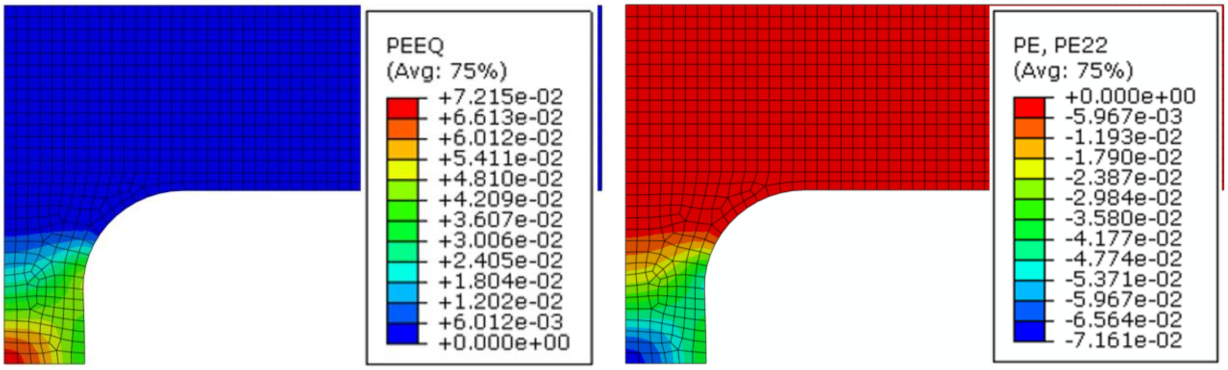

Equivalent plastic strain

Plastic strain in the loading direction

b) Tensile unloading

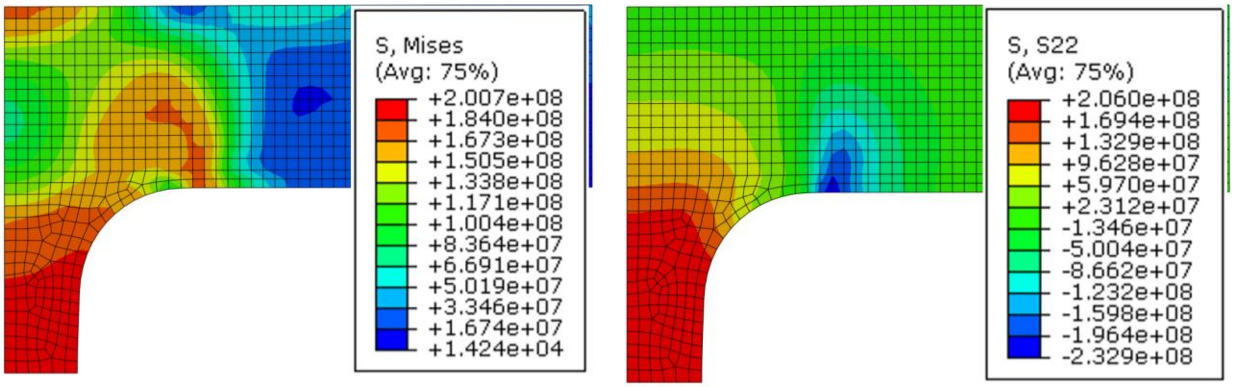

Equivalent stress

Stress in the loading direction

Figure 4.12 FEM results of the new fixture for cyclic testing in the normal direction of plates, a) Compressive loading, b) Tensile unloading

Figure 4.12 demonstrates the strain field under compressive loading and the stress field under the tensile unloading as representatives of the stress-strain field in the loading-unloading modeling. It compares the plastic strain in the loading direction and equivalent plastic strain at the end of the compressive loading. It also compares the stress in the loading direction and equivalent stress at the end of the tensile unloading step. As shown, to obtain the stress-strain curve using DIC, the FEM model predicts that extracting the stress-strain curve from the 1 mm x 1mm area at the center of the sample produces accurate results.

The results of the CT tests in the ND of the sheet are shown in Figure 4.13. Due to the initial texture of the material (Figure 4.7), the basal planes are aligned in the ND; thus, the deformation mechanism in the CT of the material would be similar to those in the TC in the RD: slip in the loading and twinning in the unloading. This figure clearly shows slip deformation during the compressive loading, followed by twinning in the tensile unloading.

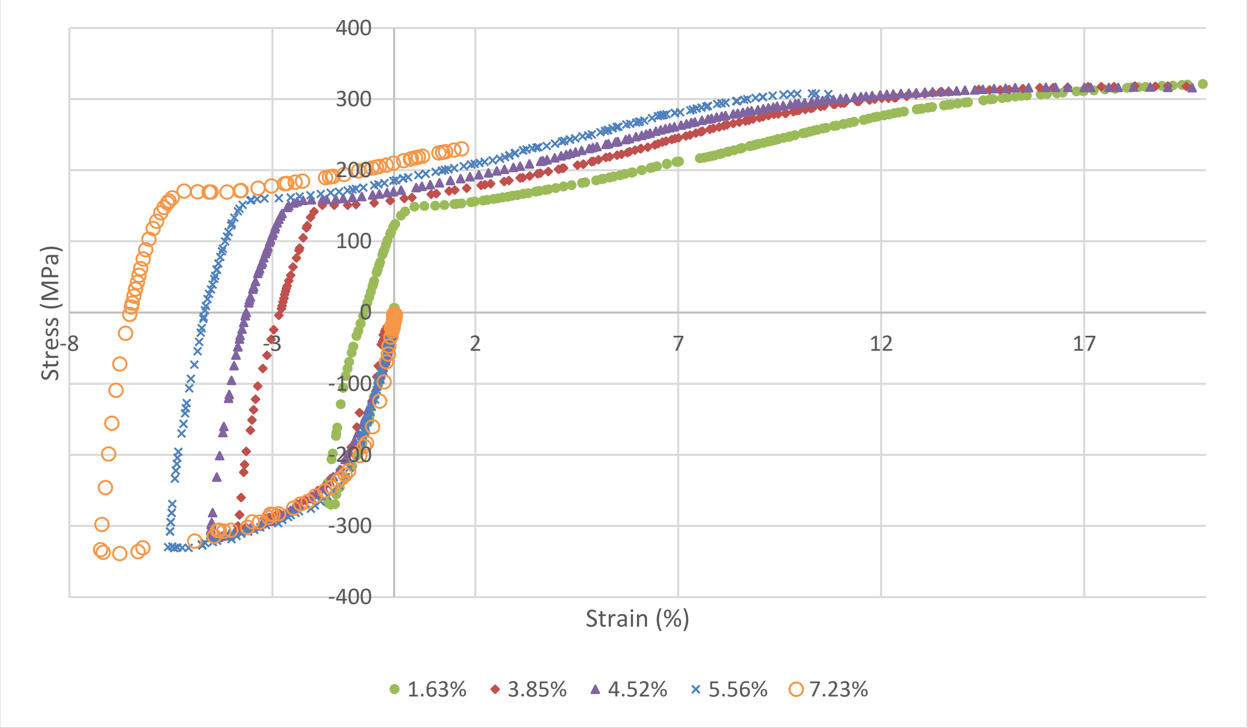

Figure 4.13 Experimental CT results of the AZ31B rolled sheet in the normal direction, using the proposed fixture

Figure 4.14 shows the TC results of the material in the ND. Again, as the deformation mechanism in this case is similar to the CT in the RD, the material twins in the tensile loading, and de-twins in the compressive unloading. The compressive curves unloaded at lower strains show small twining and behave closer to the monotonic compressive stress-strain curve along the ND. As the unloaded strains increases, the level of twinning in the material increases.

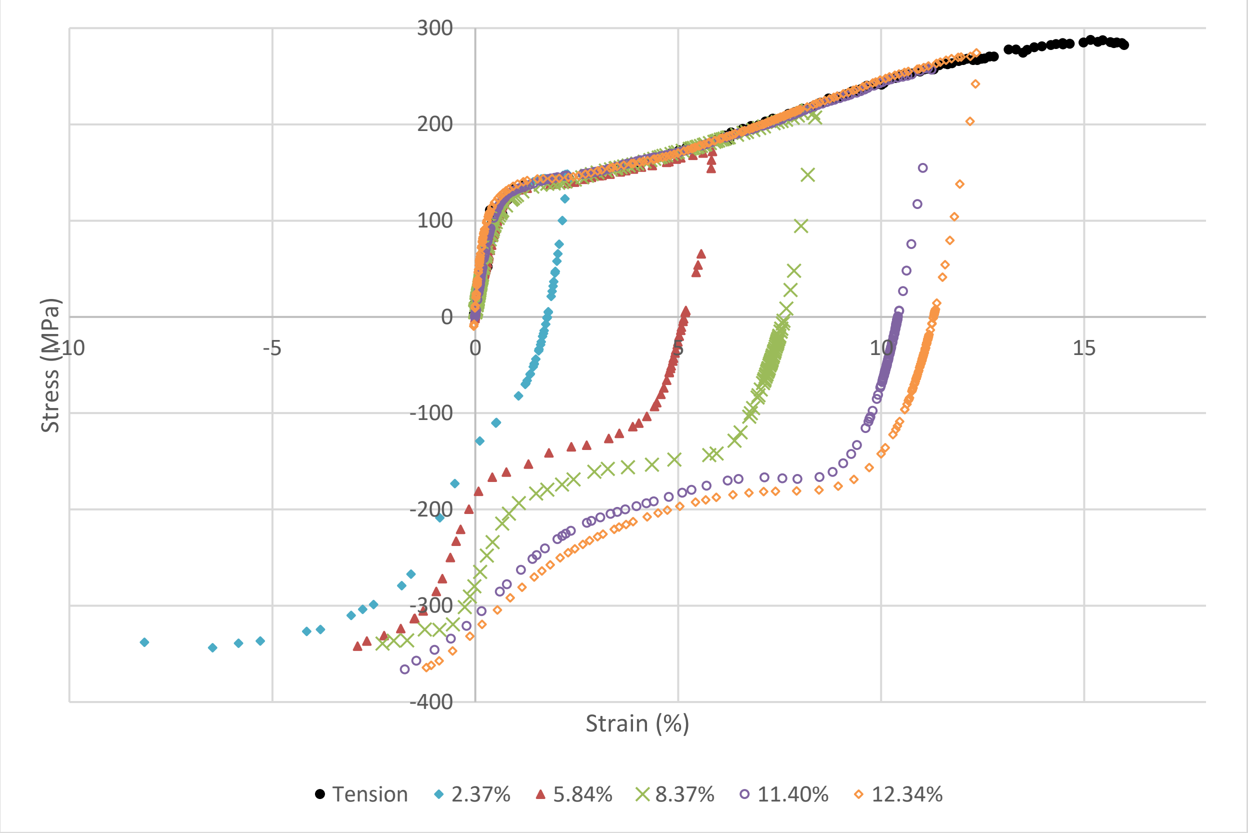

Figure 4.14 Experimental TC results of AZ31B rolled sheet in the normal direction, using the proposed fixture

Table 4.3 provides the elastic modulus of elasticity and yield stress of the samples tested in the RD and ND, demonstrating that the Young's modulus is accurately estimated, at around 45 GPa. The yield stresses in the RD are higher than those in the ND, by 54.93% and 122.27% in compression and tension, respectively.

Table 4.3 Elastic modulus and yield stress in compression and tension tests in RD and ND

Direction	Elastic modulus in GPa (standard deviation)	Yield stress in MPa (standard deviation)
Compression-RD	46.07 (1.12)	170.36 (8.31)
Tension-RD	46.06 (0.89)	204.58 (4.05)
Compression-ND	46.77 (3.35)	111.08 (4.94)
Tension-ND	43.19 (3.27)	92.04 (5.06)

To verify the results of TC and CT using the proposed fixture, the same experiments were done with the mini I samples machined in the RD. Figure 4.15 and Figure 4.16 show the results of TC and CT curves obtained by testing the samples in the RD, and comparison with the results obtained by employing the anti-buckling fixture, respectively. Comparison of the CT curves shows that the new fixture estimates the CT behavior accurately and in a good agreement with the curves obtained using the anti-buckling fixture. The maximum difference between the experimental data is 17.5 %, which is related to the estimation of the yield stress. Other than that, the two methods predict the plastic behavior and unloading behavior very similarly. The TC results of these experimental methods are also in a good agreement in the plastic region; however, the mini I samples predicts the yield stress 23% less than those obtained in the experiments using an anti-buckling fixture.

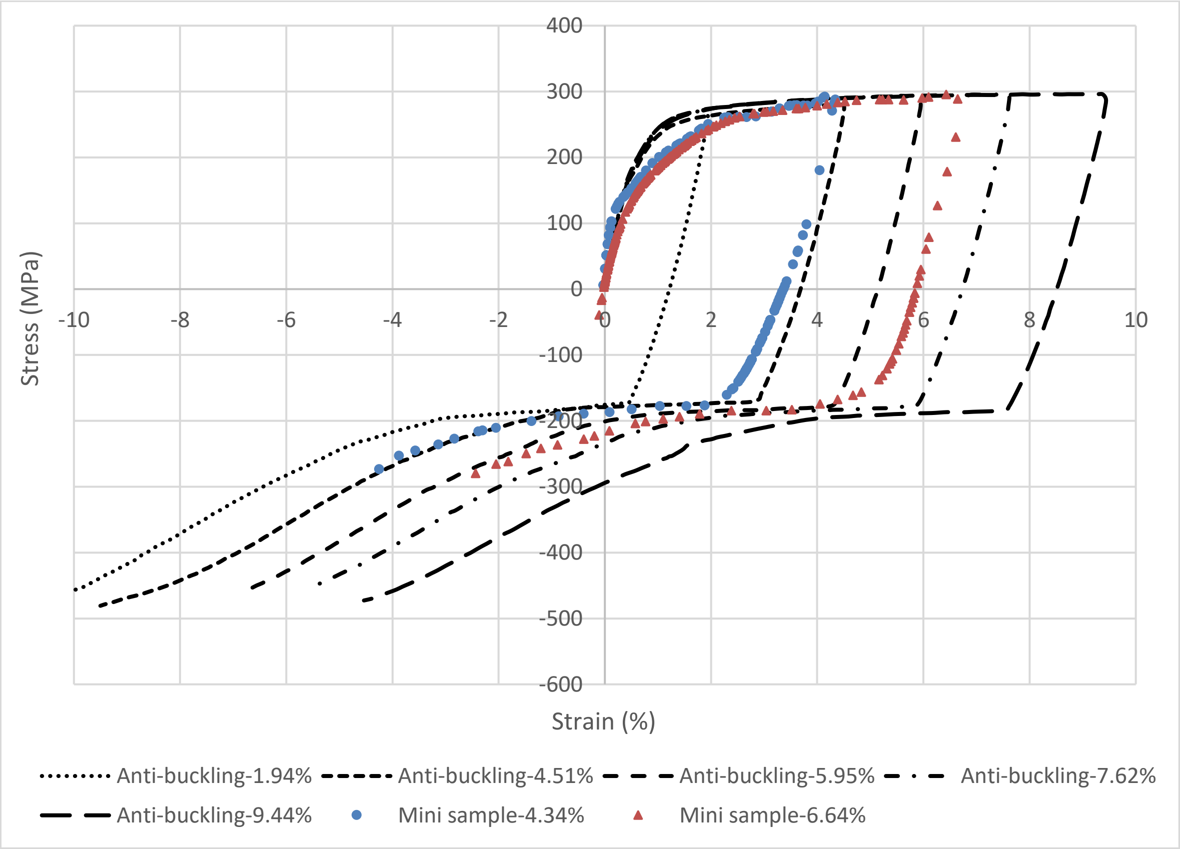

Figure 4.15 TC results of AZ31B rolled sheet in the rolling direction, using the mini I sample and comparison with samples tested using the anti-buckling results

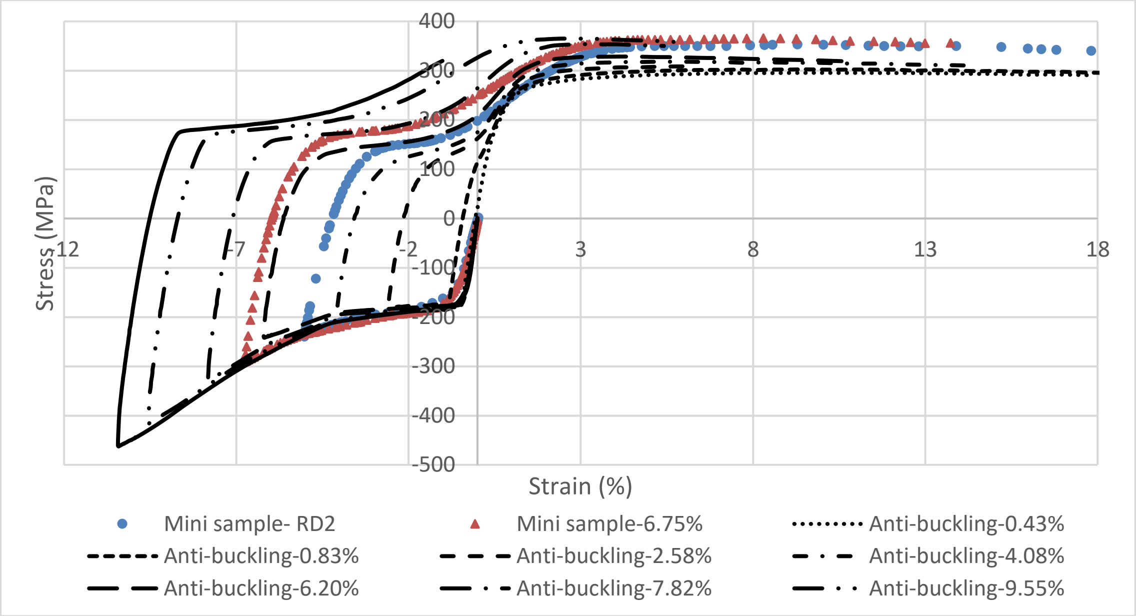

Figure 4.16 CT results of AZ31B rolled sheet in the rolling direction, using the mini I sample and comparison with samples tested using the anti-buckling results

Conclusion

In this study, we proposed a modified version of an anti-buckling fixture used to obtain the CT and TC curves of AZ31B-H24 sheet at different large strain values. The negligible effects of using an anti-buckling fixture were experimentally confirmed by comparing the results with the results of compression tests using cuboid samples and a corresponding fixture. A new fixture and adjustment tool were introduced that can increase the accuracy of compression tests using cuboid samples. A new fixture was designed to obtain the CT and TC curves of the material in the ND of the sheet. FEM evaluated the uniaxial region for strain measurement. Comparison of the results obtained using the mini samples machined in RD and those tested using the anti-buckling verified the accuracy of the new fixture. As predicted by the deformation mechanism and initial texture of the material, the CT in ND and TC in RD behave similarly, deforming by slip mechanism in the loading and twinning in the unloading step. Similarly, the same deformation behavior was obtained in TC tests in ND and CT ones in RD. The results show that the rolled sheet exhibits strong asymmetry in tension and compression, and strong anisotropy between the RD and ND, but negligible anisotropy in the RD and TD.

Chapter 5

Characterization and experimental optimization of shot peening intensity to enhance the fatigue life of AZ31B rolled sheet

Abstract

There is renewed interest in using the magnesium (Mg), the lightest industrial metal, and its alloys in vehicle components. This study characterizes the effects of shot peening on AZ31B-H24 rolled sheet by measuring the residual stress and micro-hardness distribution through the depth, followed by measuring surface roughness and texture evolution at the surface. To obtain the optimum peening intensity, rotating bending fatigue tests are done at different intensities. The material shows a high sensitivity to shot peening under different intensities, due to the over-peening effects in the peening on Mg alloys. Peening at the optimum intensity increases the fatigue strength from 130 MPa to 150 MPa.

Keyword: Shot peening, Magnesium (Mg) alloy, Fatigue life, Residual stress, Surface roughness, Micro-hardness, Texture

5.1 Introduction

Strong competition between automotive companies to increase the fuel efficiency of vehicles has created renewed interest in the lightest industrial metals, magnesium (Mg) and its alloys. Mg, widely available in both seawater and the earth's crust, has been in use since the early 19th century [7], although its application in the automotive industry dates back to early in the 20th [9]. The environmental impacts of fuel consumption have led manufacturers to decrease the weight of vehicles through the use of Mg and its alloys [9]. Expanding the application of Mg alloys to components with failures driven by fatigue loads requires their fatigue properties to be improved.

Shot peening is a process of impinging small spherical particles on the surface of a material to enhance its fatigue properties [161], [162]. The compressive residual stress induced during this process retards crack initiation as well as growth, and improves the fatigue life; however, the increased surface roughness has a detrimental effect. These competing effects of peening on fatigue life create interest in finding the optimum peening intensity that will maximize fatigue life.

To date, the effects of shot peening on certain Mg alloys, ZK60 [93], [96], [97], [163], AZ80 [88]–[91], [94], AZ91 [164], Mg A8 [92], Mg-10Gd-3Y [95] and AZ31B [98], have been studied experimentally. These studies were mostly concerned with determining the residual stress and microstructure after shot peening, and also with finding the optimum peening conditions for maximum fatigue life. The residual stresses after peening on Mg alloys have been measured using two methods, hole drilling [92], [94] and XRD $\sin^2\psi$ [6], [8], [9], [18], [19]. During these measurements, the maximum compressive residual stresses of 20-110 MPa were induced at the depth of about 100-150 μm below the surface, depending on the material and peening conditions. Recently, the authors of this paper discussed the challenges and required considerations for measuring the residual stress of Mg alloys using XRD, as shown in chapter 3. Studies on how shot peening affects surface roughness show that the surface roughness after peening of Mg alloys increases, and that a higher intensity leads to a higher surface roughness [89]–[98], [163]. Micro-hardness distribution through the depth before and after shot peening has been evaluated for ZK60 [93], [96], [97], [163], and AZ80 [91]. In these studies, 40-100 gf were used for micro-hardness measurements. It was found that the hardness values at the surface and the affected depth increase as the peening intensity increases. Texture evolution after peening has also been investigated by [93], [98]. They concluded that the process randomizes the texture compared to the as-received conditions. Experimental evaluation of optimum peening intensity has been done for AZ80 [89], [91] and ZK60 [96], using rotating bending fatigue tests for samples peened at different Almen intensities in one or two stress amplitudes. The fractography of failed ZK60 samples showed that cracks are initiated in the subsurface region when samples are peened at optimum intensity value [163], indicating the shift of the traditional initiation region where the cracks initiate from the surface to subsurface areas. Liu et al. [163] also showed that increasing the peening intensity beyond this optimum point of ZK60 creates more crack nucleation areas, and these critical regions move from the subsurface to the surface of the material. The same behavior was observed by Zhang and Lindemann [91] in the peening of AZ80. Additionally, they showed that at low intensities, the crack initiation region is in agreement with the depth of the plastically deformed layer evaluated by micro-hardness measurement. [91], [96], [97], [163] introduced brittle second phases as crack initiation sources.

The present research explores the characterization of different effects of shot peening on AZ31B rolled sheet at different intensities, including the residual stress, surface roughness, texture evolution, rotating bending fatigue tests, micro-hardness, and fractography after failure. Finally, this study aims to find the optimum intensity for peening AZ31B rolled sheet. The fatigue life curves are obtained before and after peening at optimum intensity.

5.2 Materials and experiments

5.2.1 Material

The material used in this study is AZ31B-H24 rolled sheet with a thickness of 6.35 mm. Its chemical composition and texture are shown in [119] and Figure 5.1, respectively. The density and Young's modulus of elasticity are 1770 Kg/m3 and 45 GPa, respectively [120].

Table 5.1 Chemical composition of AZ31B rolled sheet [119]

Composition	Al	Zn	Mn	Mg
Weight %	2.73	0.915	0.375	Bal.

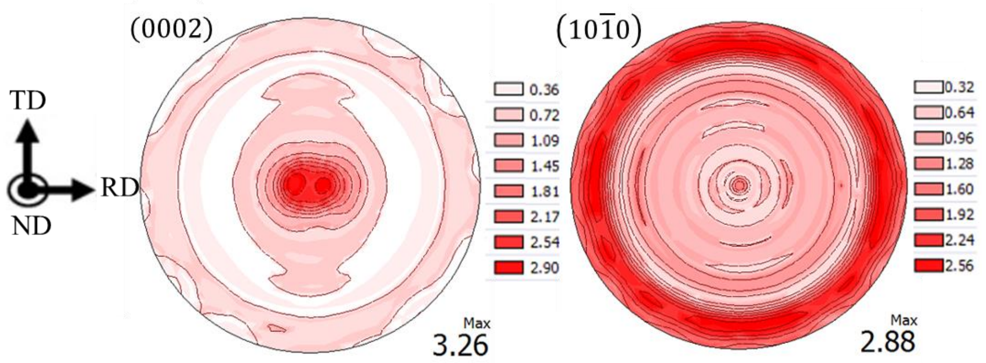

Figure 5.1 Texture of AZ31B-H24 rolled sheet

Figure 5.2 shows the machining direction (a) and the drawing of the samples (b). The samples are aligned lengthwise in the rolling direction (RD). The samples are stress-relieved at 150℃ for 60 minutes, according to the ASTM standard [167].

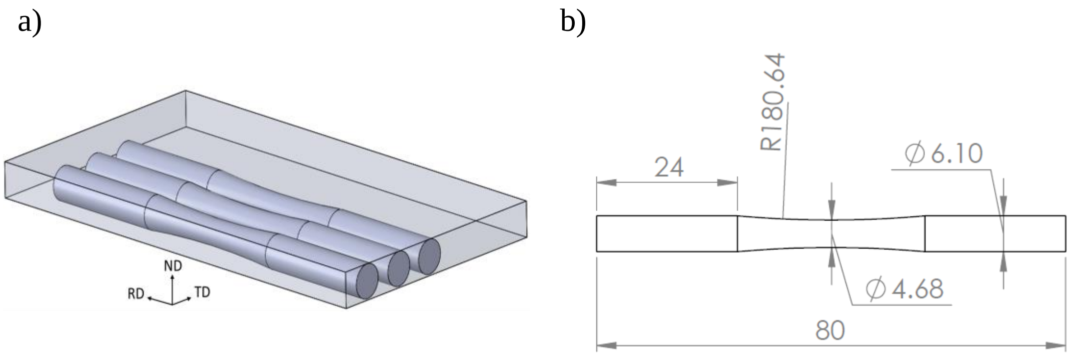

Figure 5.2 Machining of rotating bending samples, a) sample machining from a rolled sheet, b) drawing of the samples

5.2.2 Shot peening

The shot peening treatment was done at Metal Improvement Co., in Brampton under Almen intensities of 0.05, 0.075, 0.1, 0.15, 0.2, 0.3, 0.4, 0.6 mmN, under the full coverage. Flat samples of 35 x 35 x 6.35 mm cut from the sheet were also shot peened under the same conditions. The samples were peened with the probe perpendicular to the surface in all directions, but due to the anisotropy of the sample, two peening directions are discussed here; peening in the normal direction (ND) and in the transverse direction (TD) (peening the thickness of the sheet parallel to the transverse direction). Thus, there are regions that were peened in ND or in TD, as shown in Figure 5.3.

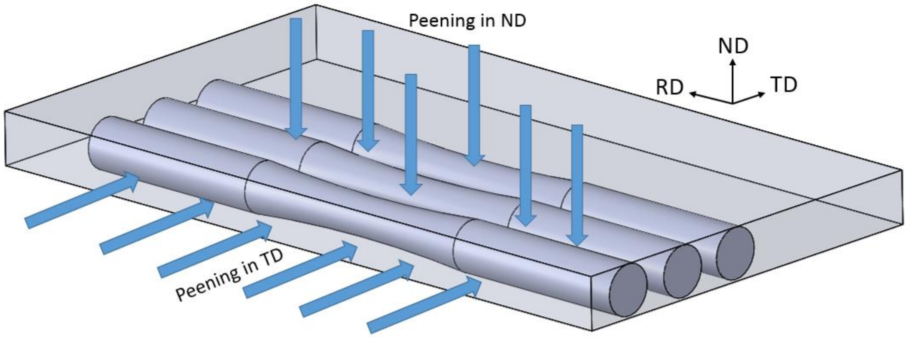

Figure 5.3 Peening directions, peening in ND and peening in TD

5.2.3 Residual stress measurement

The residual stresses are measured using two methods; x-ray diffraction (XRD) to measure the residual stresses at the surface layer of the material to compare the values evaluated at different directions, and hole-drilling method to obtain the residual stress distributions through the depth.

In XRD, residual stresses at the surface layer were measured using two-dimensional x-ray diffraction (2D-XRD). The Bruker D8-Discover equipped with a VÅNTEC-500 area detector, with a radius of 135 mm and using Cu-Kα radiation at 40kV and 40 mA, was used in this measurement. The samples were located on the motorized stage with the oscillation amplitudes of 1.3 and 1.2 mm, and speeds of 3.5 mm/s and 5.5 mm/s for the X and Y axes, respectively. The sample orientations used in the 2D-XRD method are shown in Table 5.2. A 1 mm collimator was used to expose x-rays to the material for 60 s in each orientation. The diffraction ring from the plane of $1\bar{2}14$ ($2\theta_0 = 99.22°$) was employed for stress measurement, using the Leptons software. The XRD measurements were employed to compare the residual stresses at the surface layer of the samples, peened under different directions and different intensities. Due to the low atomic number of Mg, the x-rays penetrate significantly through the depth (e.g., under the experiment condition, respectively, 50% and 90% of the x-rays are diffracted from the surface layer of up to 36.2 μm and 126.8 μm through the depth). Thus, the stresses evaluated by XRD cannot be considered as surface residual stresses in Mg alloys, and are considered to be the average residual stresses of the surface layer.

Table 5.2 Different sample orientations for stress measurement using 2D-XRD

Ψ-tilt (°)	Φ-tilt (°)
0	0
25	0, 45, 90, 135, 180, 225, 270, 315
50	0, 45, 90, 135, 180, 225, 270, 315

The residual stress measurement through the depth was carried out using the hole-drilling method, by means of an MTS3000, Sint Technology hole-drilling machine with conventional HBM three-element strain gauge rosettes, installed on the material’s surface. Drilling with a 2 mm diameter tool and speed of 400,000 rpm was performed to create a shallow hole in the center of the strain gauge rosettes.

5.2.4 Texture evolution

To determine the effect of shot peening under different Almen intensities on the surface texture evolution of the material, the same XRD machine was employed. The experiment included measuring the incomplete pole figures of $\{0001\}$, $\{10\bar{1}0\}$, $\{10\bar{1}1\}$ and $\{1\bar{1}02\}$ planes for tilt angle ψ between 0° and 75° and in axis rotation φ between 0° and 360° using Cu-Kα radiation at 40 kV and 40 mA, as described in [121]. The complete pole figures were obtained using DIFFRAC.TEXTURE software, version 3.0.4, developed by Bruker AXS.

5.2.5 Surface roughness

Surface roughness measurements were performed using a Keyence VK-X250 confocal laser microscope. For each peening condition, three replicates with the area dimensions of 1500 μm by 1000 μm were scanned, and waveform correction was done during the post-processing of results.

5.2.6 Micro-hardness

Micro-structure samples were prepared initially by hand-sanding with 600, 800 and 1200 grit SiC paper, then by finely polishing with 6, 3, 1 μ diamond paste and an oil-based lubricant on imperial cloth. The micro-hardness distribution was measured on the lateral cross-section of the peened samples. Indentations of 50 gf (HV0.05) were performed, using Wilson Instruments 402 MVD on two paths, from the surface of the material towards the depth. To measuring the hardness at the depth of 25 μm, the 10 gf

(HV0.01) was used, in order to meet the minimum distance criteria for both between-the-indentations and from the surface edge.

5.2.7 Rotating bending fatigue tests

An Instron RR Moore four-point rotating-bending fatigue testing machine was employed for fatigue tests. All tests were performed at fully reversed loading (R=-1), and at the frequency of 90 Hz. Based on the initial results, two stress amplitudes of 150 and 185 MPa were selected to compare fatigue lives at high and low cycle fatigue regions. The tests were stopped after the full failure of the material, and the run-out life is considered to be 10^7 cycles. Two samples were tested at each intensity and at each stress amplitude. The optimum intensity was then selected to peen afterward to complete the S-N curve and allow comparison with the as-received condition.

5.3 Results and discussion

The residual stresses measured at the surface layer of the peened samples show that the peening induces small average compressive residual stress at the surface layer, as shown in Figure 5.4. The residual stresses in RD and TD at the surface layer in the samples peened in ND are the same, which is reasonable as the sheet is assumed to be isotropic in RD and TD. The texture evaluation shown in Figure 5.1 confirms the sheet's isotropic properties in RD and TD. Moreover, the residual stresses in RD in both flat and rounded samples are equal, meaning that the residual stress measurement through the depth of the flat samples can be considered as the residual stress measurement through the depth of the rounded samples when peened under the same conditions. This fact is also predictable because the thickness of the peened material in flat samples and the diameter of the rounded samples are similar, and the peening conditions are the same. As such, the same residual stress distribution is expected in both flat and rounded samples when peening conditions and directions, and also the substrates' thicknesses are the same. The geometrical difference between the RD and TD in rounded samples in peening in ND is significant (as shown in Figure 5.3), causing the residual stresses to differ. Figure 5.4 shows that the as-received stress-relieved samples have only negligible residual stresses, and the peened samples acquire average compressive residual stresses in their surface layers. It is also found that the average compressive residual stresses at the surface layer of samples peened under the intensities of 0.05 and 0.075 mmN are higher than samples peened under higher intensities.

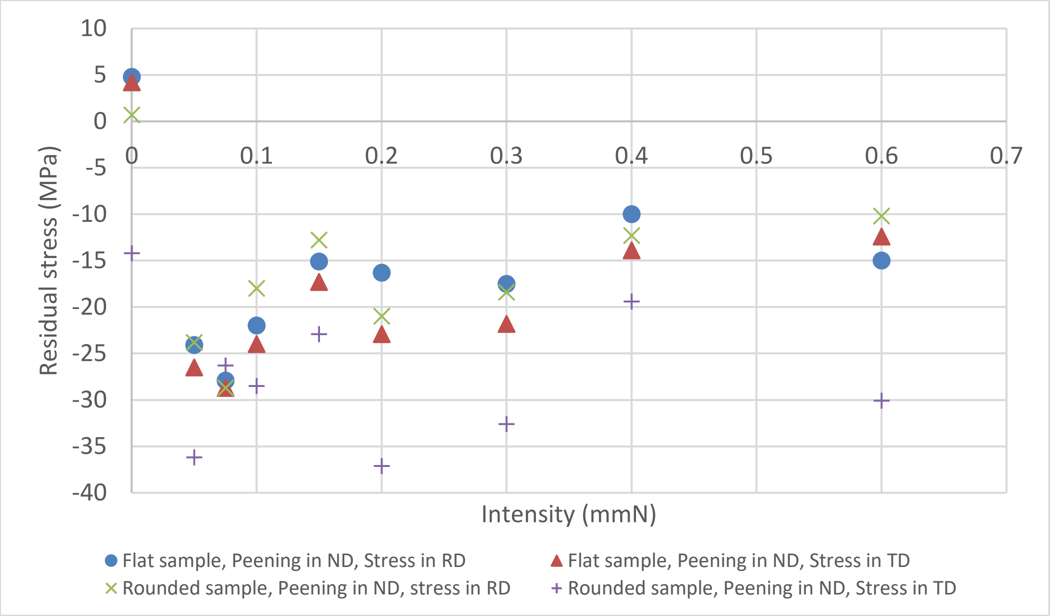

Figure 5.4 Residual stress at the surface of the peened and as-received flat and rounded samples in different directions

Figure 5.5 shows the results of residual stresses at the surface layer of the rounded peened samples. The absolute value of average compressive residual stresses at the surface layers of the areas peened in ND are less than those in TD. This fact increases the chance of failure from the locations peened in ND.

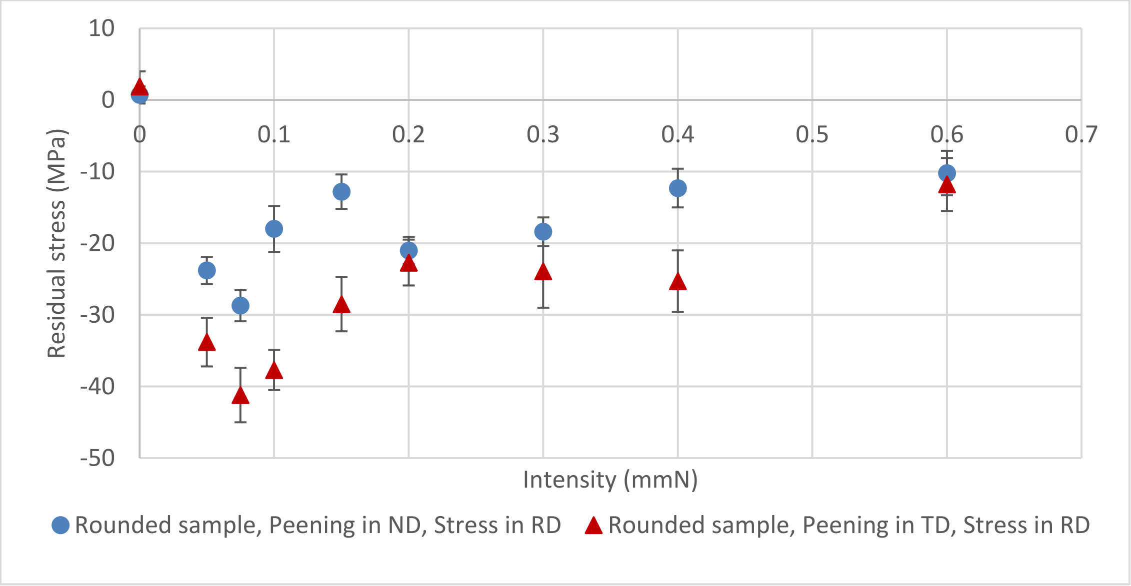

Figure 5.5 Residual stresses at the surface of the rounded samples, peened at two perpendicular directions

Figure 5.6 shows the residual stress distribution through the depth of as-received and peened samples under different intensities. The hole-drilling result of the as-received sample clearly indicates that the stress-relieved sample has no residual stress at the surface and through the depth; however, the peening process induces compressive residual stress in the material. This figure also shows that the peened sample at the intensity of 0.05 mmN has the highest compressive residual stress at the surface. The trend of the residual stress distributions shows that the maximum residual stress and the corresponding depth increase with an increase in the peening intensity, and the higher the intensity, the higher the depth of the layer with the compressive residual stress.

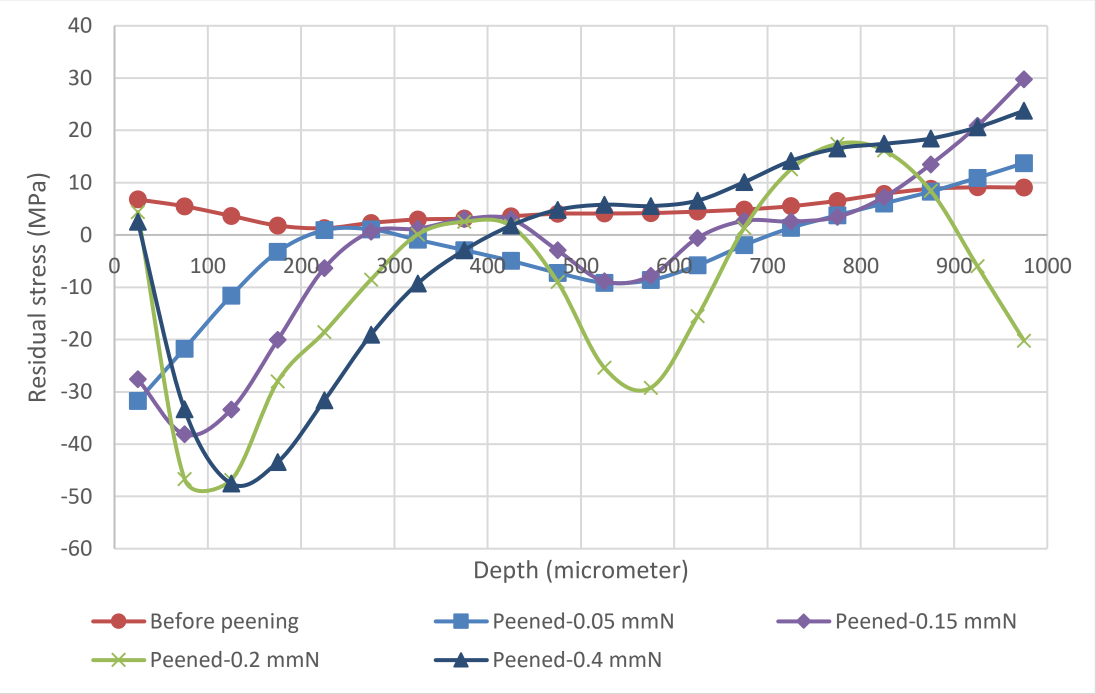

Figure 5.6 Residual stress measurement through the depth of stress-relieved and peened samples under different intensities

Figure 5.7 shows the distribution of micro-hardness through the depth of the as-received and peened samples under different intensities. As the peening creates plastic deformation, the hardness increases in the affected area of the peened samples. Increasing the intensity is shown to increase the hardness of the surface layer and the depth of the affected layer.

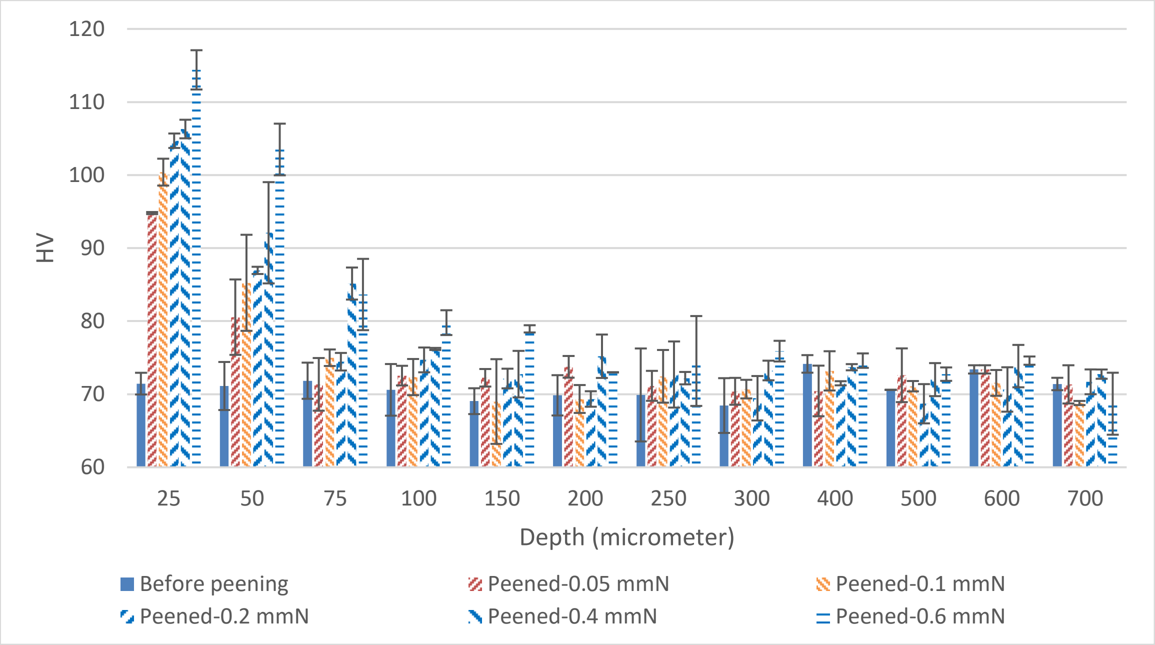

Figure 5.7 Micro-hardness measurement through the depth of as-received and peened samples

Figure 5.8 demonstrates the results of surface roughness (R_a and R_z) at the surface of the as-received (0 mmN) and peened samples. At lower intensities, the peening intensity has a direct relationship with the surface roughness parameters; however, this figure shows saturation after 0.4 mmN.

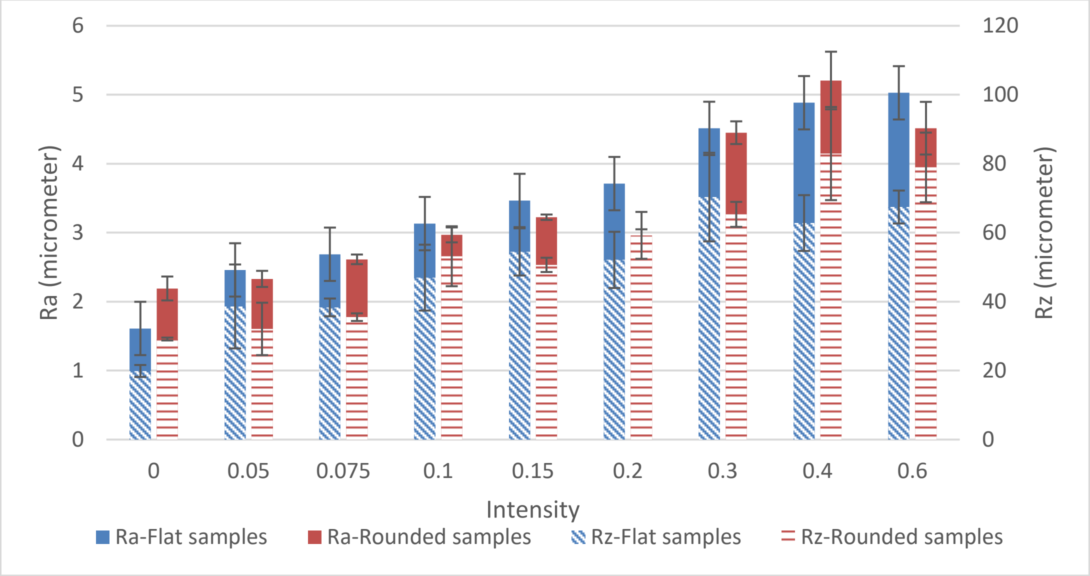

Figure 5.8 Surface roughness measurements of the as-received and peened samples, including the flat and rounded samples

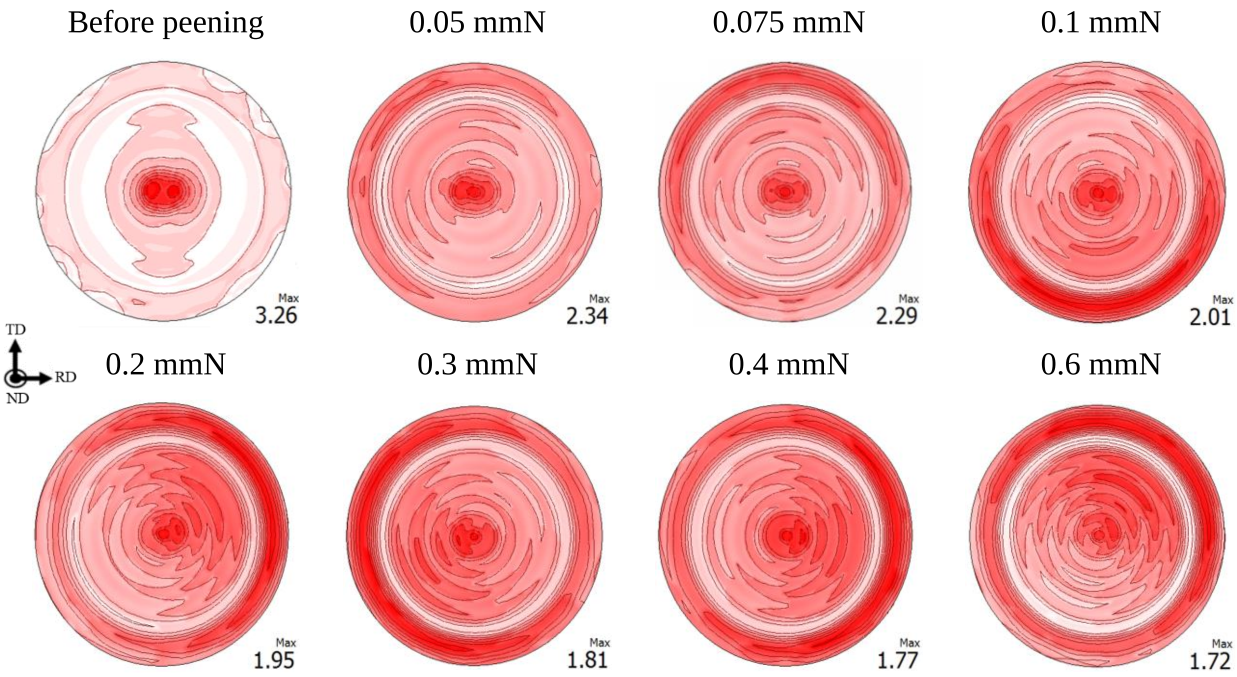

Figure 5.9 Texture evolution of the flat samples, peened in ND

Figure 5.9 shows the texture evolution of the as-received and peened samples in the ND under different intensities. The initial texture shows strong basal orientation aligned in ND; however, the peening rotates the c-axis from ND and randomizes the texture. As the peening intensity increases, the maximum texture intensity decreases, meaning more and more grains have basal texture tilted from the ND due to the twinning.

Figure 5.10 shows the RBM results of the as-received and peened samples under two stress amplitudes: 150 and 180 MPa. The over-peening effect of Mg alloys is clearly seen, and the optimum intensity occurs at 0.05 mmN. It is notable that in the peening industry, 0.05 mmN is considered to be a very low intensity, and practically it is impossible to get lower intensities. At the stress amplitude of 150 MPa, peened samples of both intensities of 0.05 and 0.075 mmN passed the 10^7 cycles, but at a stress amplitude of 180 MPa, the intensity of 0.05 mmN shows better results than 0.075 mmN. Thus, the intensity of 0.05 was selected as the optimum peening intensity.

To determine why the fatigue life drops after the 0.1 mmN (over-peening effect), the surfaces of the peened samples were examined for surface morphology. Figure 5.11 shows the surface topology of the as-received and peened samples under different intensities. The high level of surface degradation at the surface of the peened samples is obvious, especially after 0.1 mmN. These surface topologies create a large stress concentration, consequently reducing the fatigue life. The root cause of such deterioration even in low intensities could be associated with the limited deformability of magnesium alloys at room temperature [168].

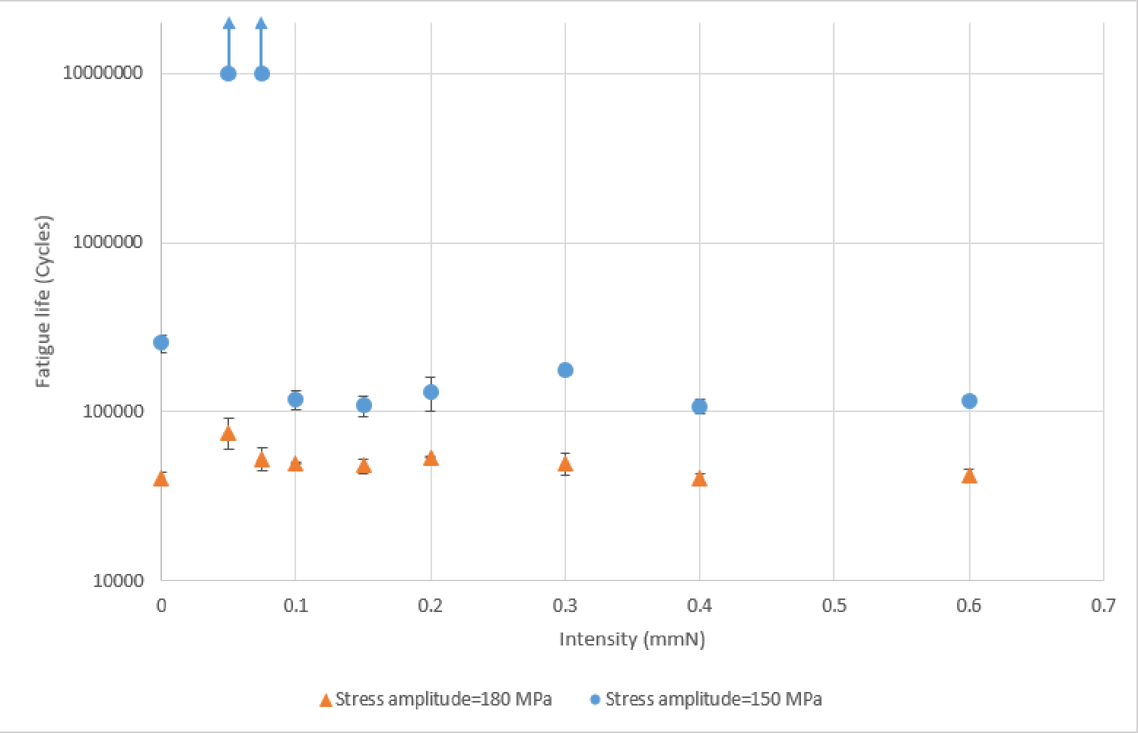

Figure 5.10 Fatigue life vs. peening intensity

Figure 5.12 shows the S-N curves of the as-received and peened samples under the optimum intensity (0.05 mmN). Shot peening is found to improve fatigue life, both in low-cycle and high-cycle regimes. In this study, the fatigue strength is considered to be when two replicates do not fail before 10^7 cycles. In this case, peening improved the fatigue strength from 130 MPa to 150 MPa.

Fracture surfaces of the as-received and peened samples, both tested at 180 MPa, are shown in Figure 5.13 and Figure 5.14, respectively. As the level of induced compressive residual stress is very low, cracks are initiated at the surface or very close to the surface (<100 µm) where the β–phases present. The EDX of some crack initiation zones shows that the aluminum, silicon, and manganese oxides initiate cracks in the surface and subsurface layers of the material.

Before peening

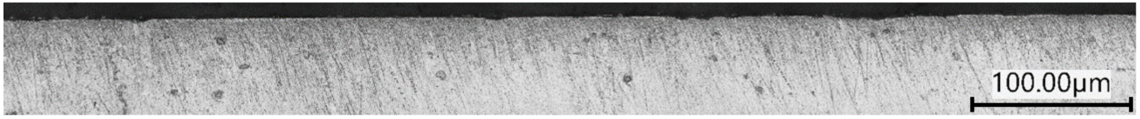

Peened-0.05 mmN

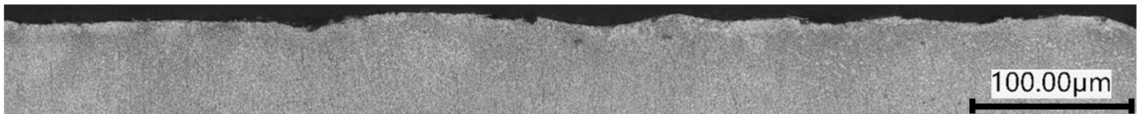

Peened-0.075 mmN

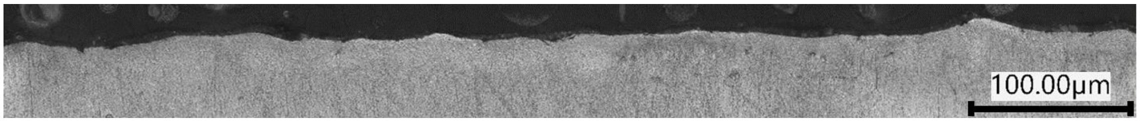

Peened-0.1 mmN

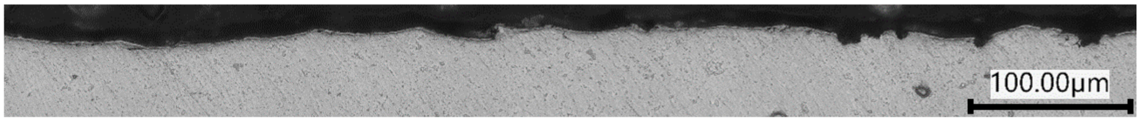

Peened-0.15 mmN

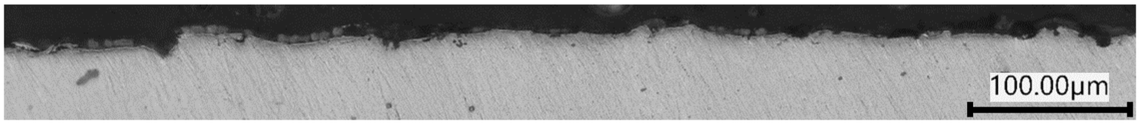

Peened-0.3 mmN

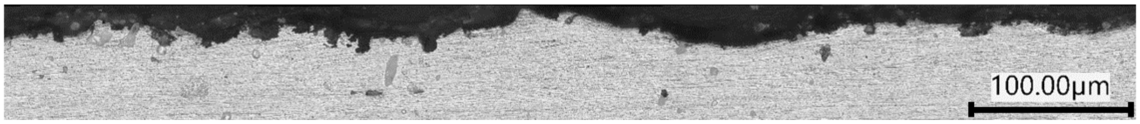

Figure 5.11 The surface profile of the as-received and peened samples under different intensities

It was noted in the discussion of Figure 5.5 that due to the lower average compressive residual stresses in the range of 0 to 126.8 μm from the surface in areas along the ND than those along TD, the chance of failure from the areas along the ND is higher. The fractography of the failed peened samples under different intensities indicates that the crack initiation zones (Region 1) are along the ND, although the exact location depends on the presence of the second phases.

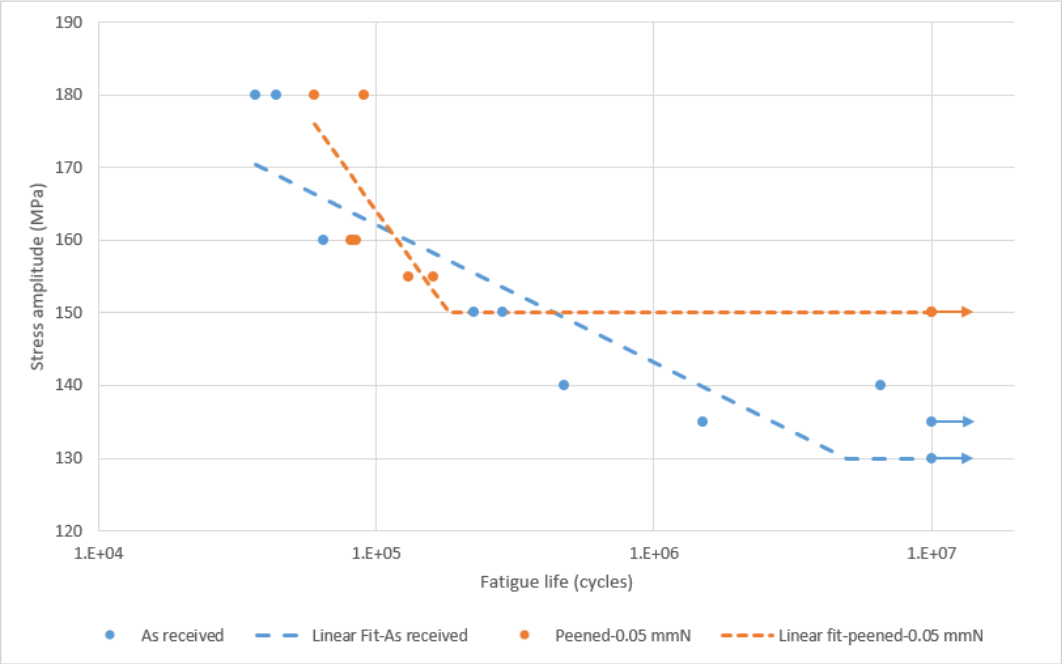

Figure 5.12 S-N curves of as-received samples and peened ones under the optimum intensity (rotating bending tests in the air)

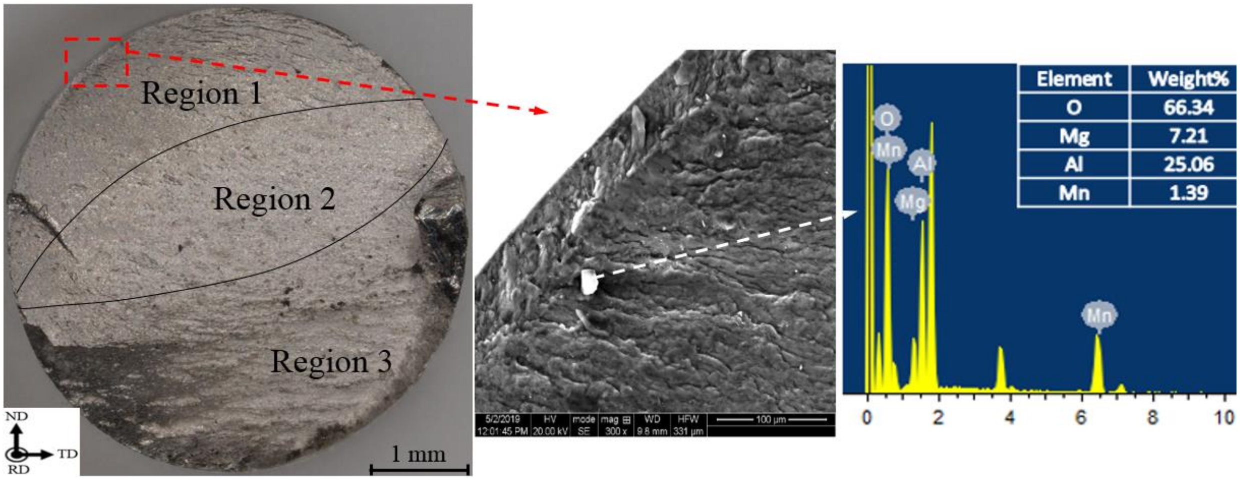

Element	Weight%
O	66.34
Mg	7.21
Al	25.06
Mn	1.39

Figure 5.13 SEM images with EDX spectrums of the crack initiation zone in the fracture surface of the as-received sample

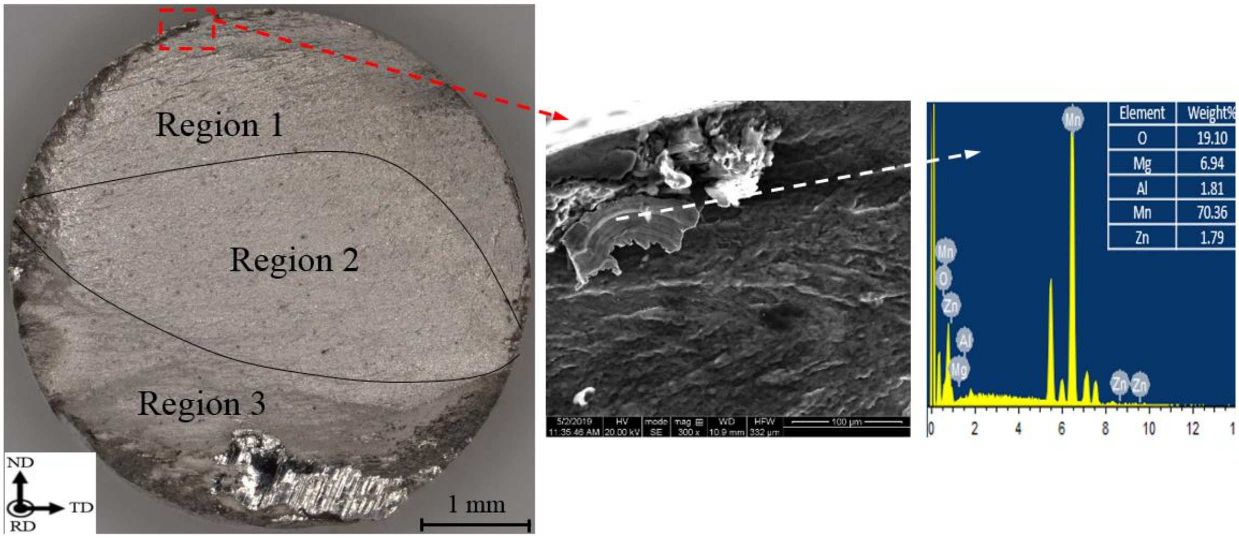

Element	Weight%
O	19.10
Mg	6.94
Al	1.81
Mn	70.36
Zn	1.79

Figure 5.14 SEM images with EDX spectrums of the crack initiation zone in the fracture surface of the peened sample at 0.05 mmN

Conclusion

This study evaluated the different effects of peening on AZ31B-H24. The following conclusions are made from the above results and discussion:

1. Small on-average compressive residual stresses (<30 MPa) at the surface layer of up to around 130 μm are induced by peening under all intensities. Peening at 0.05 and 0.075 mmN intensities induces the maximum on-average compressive residual stress in the surface layer.
2. Residual stress distributions through the depth reveal that, as the peening intensity increases, the depth of the maximum compressive stress and the depth of the induced compressive residual stress layer increase, but the induced compressive residual stress at the surface is at its maximum at 0.05 mmN.
3. The hardness increases in the plastically deformed area of the peened samples. It is found that the higher the intensity, the higher and deeper the hardness of the surface layer.
4. Both R_a and R_z increase when the peening intensity increases.
5. The peening randomizes the surface layer’s texture due to the twinning.
6. Shot peening on AZ3B-H24 clearly shows the over-peening effect where the optimum intensity is 0.05 mmN. The deteriorated surfaces cancel the beneficial effect of compressive residual stress, causing fatigue life to decrease at higher intensities.
7. Peening at optimum intensity increases the endurance limit of the material by 15%.

8. Fractography of the fracture surfaces reveals that cracks are initiated where the second phases are present in the surface layer of the material.

Chapter 6

A hybrid numerical-analytical model for residual stress distribution prediction in shot peening

Abstract

Stringent assumptions need to be made to allow for closed-form analytical solutions for calculations of residual stresses induced by shot peening. This limits the application of these models to idealized conditions. On the other hand, and because of phenomena like Bauschinger Effect in high strength metals and the complexity associated with their modeling, it is difficult to provide numerical solutions such as finite element that are capable of mimicking actual material behavior once they are released from an over-strain loading state. Moreover, modeling of full coverage shot peening condition is time-consuming and computationally expensive. A single-shot finite element model is herein combined with an analytical model using actual loading-unloading material behavior to propose a hybrid FEM-analytical model for prediction of the residual stress distribution in shot peening. First, the shot peening process is divided into a loading phase, modeling the impact of shots and substrate, and an unloading phase, modeling the rebounding of the shots. Finite element is employed to model a single shot impingement on a substrate using the actual loading properties of the substrate. Using the results of the loading phase, an analytical model is proposed to predict stresses due to the unloading phase, using the actual unloading behavior of the material. The proposed hybrid model accounts for the actual behavior of a material, actual elastic-plastic contact analysis, strain rate effect, and friction. The model is then employed to predict residual stresses induced in a SAE1070 and an Al2024-T351 sheet. Results are compared with the available experimental results which show close agreements.

Keyword: ***Shot peening, Residual stress, Hybrid modeling, Finite element, Analytical modeling***

Nomenclatures

a	Radius of indentation	Subscripts	
A	Cross-section area of the target material	eq	Equivalent
D	Shot diameter	s	Shot
E	Young’s modulus	t	Target
E_H	Contact equivalent Young’s modulus	y	Yield
h	Target thickness		
I	Moment of inertia of the target material	Superscripts	
k	Efficiency coefficient	0	Initial
p_0	Maximum contact pressure	e	Elastic solution
V	Shot velocity	ep	Elastic-plastic solution
w	Target width	un	Unloading
α	Ratio of plastic to elastic radius of indentation		
ε	Strain		
ν	Poisson’s ratio		
ρ	Density		
σ	Stress		

6.1 Introduction

Shot peening is a cold-working process primarily used to enhance the fatigue life of metallic components [161], [162]. In this process, small spherical particles are propelled at the surface of the component, impacting it at velocities in the range of 30-100 m/s, and creating a local plastic deformation. The induced plastic layer is approximately a few hundred micrometers in thickness, causing a compressive residual stress field to develop in the near-surface layer of the structural components [169]. The compressive stress induced by the shot peening prevents crack formation by negating the tensile loading contribution of the cyclic stress loading, which results in increased fatigue life. Hence the ability to estimate the residual stress magnitudes and distributions induced by the peening process is of paramount importance in preparing fatigue life calculations for treated parts.

In general, the process of shot peening can be divided into two phases: first, the loading phase of shot impacting and penetrating into the substrate, and second, the unloading phase of shot rebounding from the substrate. The loading phase includes high strain-rate impact and severe localized plastic deformation. The unloading phase includes elastic unloading, which may or may not include reverse yielding. Therefore, shot peening is a highly nonlinear process due to severe plasticity, shot-substrate contact, and elastoplastic unloading. Modeling is, therefore, an essential tool in providing a better understanding of this complex process and also offering a reliable estimation of the residual stresses. There have been numerous studies on the modeling of shot peening. These studies can be categorized into two approaches: analytical modeling, and finite element (FEM) modeling.

The analytical modeling of the shot peening provides a low-cost estimation of the residual stress through the depth of a material. Al-Hassani [63] was amongst the first to propose an analytical solution for materials with elastic-perfectly plastic behavior. He discussed different static and dynamic aspects involved in the peening process and used an analogy with the pressurized spherical cavity to propose a method to evaluate the residual stress distribution after shot peening of a surface. Li et al. [65] developed a method to consider the strain hardening in the modeling. They employed the Hertz contact theory [66] to estimate stress components in the surface layer of a peened material. They considered the modeling as a quasi-static problem where a shot is pressed into a semi-infinite solid. Based on the assumption of the relevancy of the ratio of the plastic to elastic indentation radii to the ratio of the plastic strain to elastic strain, they converted their proposed elastic solution to a plastic one. They employed Iliushin's elastic-plastic theory [67] to calculate the elastic-plastic stresses. In the unloading step, Li et al. [65] assumed that after reverse yielding, the plastic strain deviators take on a form similar to that of the elastic strain deviators. A noticeable limitation in their approach was the use of an empirical equation that was based on a static force. To remove the empirical equation in [65], Shen and Atluri [68] proposed calculating the plastic indentation by using the average pressure distribution put forward by the work of Al-Hassani [69] that acts to counter the force of the impinging shot and accelerates it away from the surface. Later, Franchim et al. [70] suggested the use of Ramberg–Osgood and Ludwick relations to model the effect of the actual plastic behavior of a material on the residual stress distribution. Their results showed that the hardening properties of materials play a major role in the residual stress profile prediction. More recently, Miao et al. [64] employed an analytical model based on the Hertz contact theory to predict the Almen intensity and residual stress distribution of an Almen strip. They were able to study the influence of shot-peening parameters like shot type and size, velocity, and peening angle on the Almen intensity. This study was aimed at estimation of the velocity of shot peening based on a desired Almen intensity for industrial applications. Their results demonstrated a fairly accurate estimation of the residual stress profiles for the shot peening of steel alloys [64].

With the development of the FEM and computational power, numerical modeling of the shot peening process was made possible. Numerical modeling provides more details such as different stress and strain components, which are not possible to obtain in the analytical modeling. Also, the assumptions involved in the FEM are much less than those involved in the analytical modeling. The initial numerical modeling of the peening process involved the prediction of the residual stress profile due to the impingement of one or a limited number of shots. These models gradually developed from 2D simulations [73] to 3D modeling [74]–[76], [170]–[173]. These studies were mostly focusing on the effects of different parameters on residual stress distribution. Using a few numbers of shots, Guagliano related the Almen intensity to the velocity of shot peening [77]. To account for full coverage, Kim et al. [80] and Meguid et al. [174] applied the concept of an area average solution to a symmetry cell to obtain a realistic distribution of shot peening residual stress. In this approach, the average of the residual stress values in all elements at a specific depth was introduced as the amount of the shot peening induced residual stress at that depth. Further treatments included random impact models to capture the stochastic nature of shot peening. This method begins with the required number of shots for a specific coverage being calculated by methods like using Avrami equation [82] as well as the results from the single shot impingement, or by examining the treated surface step by step [175], [176]. The residual stress profile is then calculated by averaging the residual stress distributions through the depth for different points [177]–[180]. Later, combined DEM-FEM methods were employed to simulate the peening process more realistically by modeling the shot impingement from the nozzle, where the shots are impinged to the target. This method considers the shot-shot and shot-target interactions and monitors the surface to reach the full coverage [181]–[183].

A comprehensive review of the literature on the analytical and FEM modeling of the shot peening process reveals that several assumptions have been made that are far from the actual behavior of the material or the characteristics of the processes. The analytical modeling has several shortfalls: 1) the elastic-perfectly plastic behavior is assumed for evaluation of plastic radius of indentation, 2) evaluation of the loading strains assuming the ratio of the plastic to elastic indentation radii is the same as the ratio of the plastic strain to elastic strain, 3) friction is negligible and 4) strain rate variation in time and position through the depth is ignored. In the FEM approach, the actual unloading behavior of material may not be modeled closely by the available hardening models in FEM commercial software. In particular, materials with a strong Bauschinger Effect can show a strong dependency on the loading overstrain in their unloading stress-strain curve that the available kinematic or combined hardening models in commercial FEM packages are unable to capture [184]–[186]. Also, multiple random peening models are computationally expensive.

In this paper, to overcome the shortfalls of analytical and FEM approaches, we propose a hybrid FEM-analytical modeling of the shot peening process. The suggested hybrid modeling is based on modeling the loading step of the shot peening by FEM and the unloading step analytically. In this case, assumptions normally made in the loading step of the analytical solution are removed, making it possible to capture the actual hardening behavior of a material, friction effect, and actual strain rate effect in the loading step. In the unloading phase, an analytical model capable of considering the actual unloading behavior of the material is proposed. The proposed hybrid modeling of the shot peening process is capable of considering the actual loading and unloading behavior of a material, accounts for the elastic-plastic contact between shot and substrate, allows for the inclusion of the actual high strain rate effect of shot impingement in the solution, and incorporates the friction between shot and substrate.

The simplicity of the hybrid method over the FEM methods can be demonstrated by comparing the one-shot impingement modeling in the hybrid method with multiple random peening or symmetry cell modeling in the literature. The multiple random peening or symmetry cell models [175]–[179], due to the presence of multiple shots, has a very high cost of simulation. As an example, for a standard PC, the computational time required for multiple random shots using the FEM model of this study is 72 hours as opposed to 10 minutes for one-shot impingement. Therefore, the proposed hybrid model needs significantly less computational power for residual stress prediction. Another advantage of the hybrid method over the fully FEM modeling is its capability to easily capture the actual hardening behavior of a material. This actual unloading behavior includes the Bauschinger Effect, the changes of the unloading Young's modulus based on the loading strains, and the different unloading curves for different loading strains. Such details allow for better prediction of the plastic and reverse yielding zones upon unloading.

6.2 Theoretical background

As the unloading step of the proposed hybrid method is based on the analytical solution, a theoretical background of the available analytical model [64] is reviewed in this section. The problem is the impingement of a single spherical shot to an infinite target plate. The analytical modeling is divided into four parts. The first section covers how to obtain the loading elastic solution based on the Hertz contact theory. As shown in Figure 6.1a, the elastic loading assumes elastic behavior for both shot and target, and evaluates different parameters at the end of the loading step when the shot velocity becomes zero, and after that, the rebounding happens. The second section describes how to evaluate the elastic-plastic stresses and strains by converting the elastic solution into elastic-plastic solution (Figure 6.1b). The third section describes the elastic-plastic unloading step which the induced residual stresses are evaluated (Figure 6.1c). The fourth section describes a method for the evaluation of the residual stresses after full coverage condition, based on the results of one-shot impingement (Figure 6.1d).

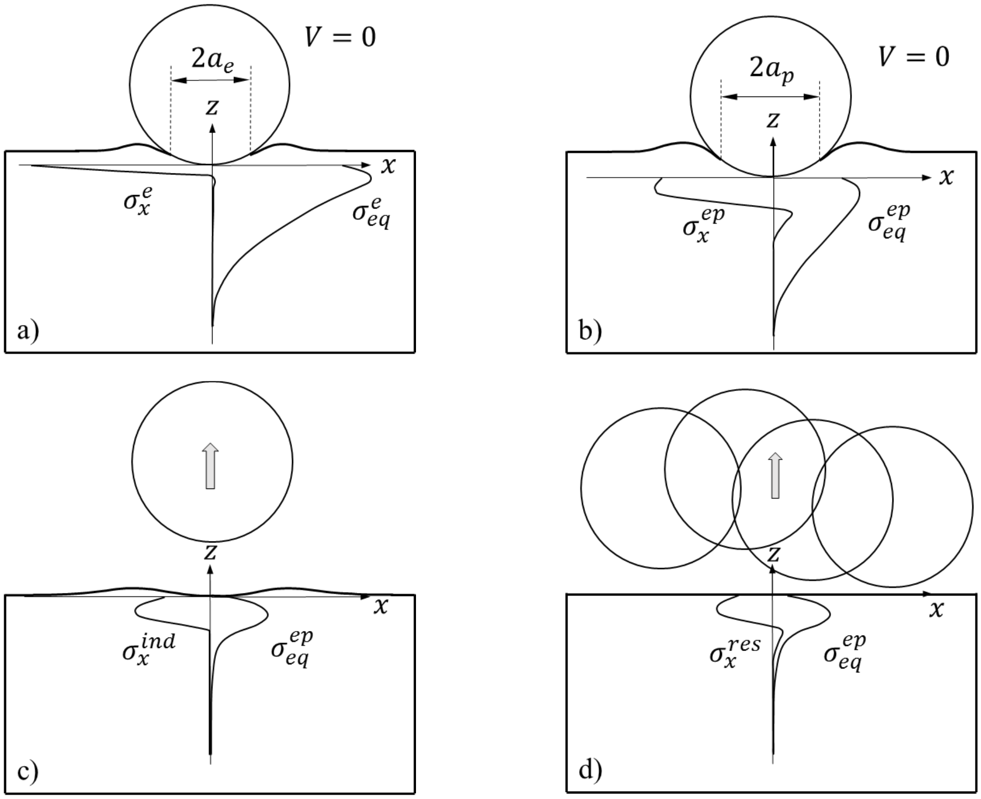

Figure 6.1 Schematic view of the impact zone and stresses a) at the end of the loading step showing radius of elastic indentation of $2a_e$ and elastic loading equivalent stress and its in-plane component through plate depth, b) at the end of the loading with elastic-plastic correction on indentation radius $2a_p$ and stresses, c) after unloading step showing induced residual stress and d) after application of multiple shots for the full coverage conditions and the induce residual stress relaxation due to sample released from the substrate.

Step 1: Elastic contact analysis

In this step, the loading stresses are obtained by assuming that the material is elastic. The Hertzian contact stresses and elasticity rules are employed in this section. First, the radius of elastic indentation is calculated by equation 6.1,

$$a_e = \frac{D}{2}\left[\frac{5}{4}\pi k \rho_s \frac{V^2}{E_H}\right]^{\frac{1}{5}} \tag{6.1}$$

where D, ρ_s, V are the shot diameter, shot density, and shot velocity, respectively. E_H is the equivalent Young's modulus and is calculated by equation 6.2,

$$\frac{1}{E_H} = \frac{1-\nu_t^2}{E_t} + \frac{1-\nu_s^2}{E_s} \tag{6.2}$$

where $\nu_t, \nu_s, E_t, and\ E_s$ are the target (substrate) Poisson's ratio, shot Poisson's ratio, target Young's modulus of elasticity, and shot Young's modulus of elasticity, respectively. k is an efficiency coefficient which is defined as the ratio of transmitted energy during the impact to the supplied total kinetic energy of a shot. As proposed by Johnston [187], k is assumed to be 0.8 [56], [64], [68], [70]. The maximum contact pressure applied at the point of impact can be then estimated by equation 6.3.

$$p_0 = \frac{1}{\pi}[40\pi k \rho_s E_H^4 V^2]^{\frac{1}{5}} \tag{6.3}$$

The Hertz contact stresses are used to evaluate the elastic stresses in the loading step. Considering the z-axis to be along through the depth direction, $\sigma_x^e(z), \sigma_y^e(z)$, and $\sigma_z^e(z)$ are obtained using equation 6.4 [188].

$$\begin{gathered}\sigma_x^e(z) = \sigma_y^e(z) = -p_0\left[-\frac{1}{2}\left[1+\left(\frac{z}{a_e}\right)^2\right]^{-1} + (1+\nu_t)(1-\frac{z}{a_e}\tan^{-1}(\frac{a_e}{z}))\right] \\ \sigma_z^e(z) = -p_0\left[1+\left(\frac{z}{a_e}\right)^2\right]^{-1}\end{gathered} \tag{6.4}$$

The Von Mises equivalent stress defined as:

$$\sigma_{eq}^e = \frac{1}{\sqrt{2}}\left[(\sigma_x^e-\sigma_y^e)^2 + (\sigma_x^e-\sigma_z^e)^2 + (\sigma_z^e-\sigma_y^e)^2\right]^{\frac{1}{2}} \tag{6.5}$$

Then, the equivalent strain is calculated using Hooke's law.

$$\varepsilon_{eq}^e = \frac{\sigma_{eq}^e}{E_t} \tag{6.6}$$

Figure 6.2 shows the schematic stress-strain curve of target materials and the parameters involved in the analytical modeling [64].

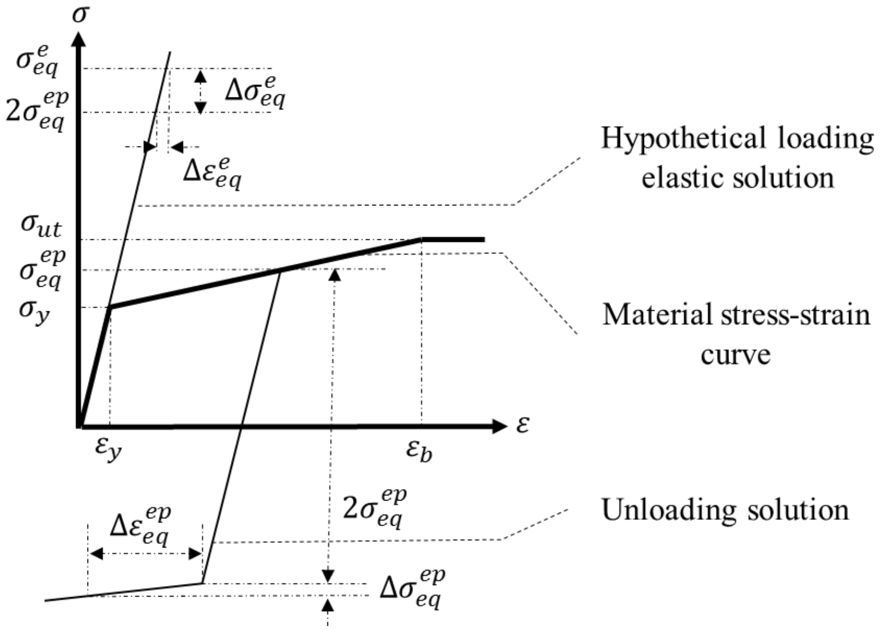

Figure 6.2 Schematic material stress-strain curve and analytical modeling parameters [64]

Step 2: Elastic-plastic analysis

The radius of plastic indentation can be calculated using equation 6.7,

$$a_p = \frac{D}{2}\left[\frac{8\rho_s V^2}{9\sigma_t^y}\right]^{\frac{1}{4}} \tag{6.7}$$

where σ_t^y is the yield strength of the target material. Based on the method proposed in the [65], the ratio of the radius of plastic indentation to the radius of the elastic indentation ($\alpha = \frac{a_p}{a_e}$) is assumed to be equal to the ratio of the equivalent plastic strain to the elastic strain, so the elastic-plastic strain can be calculated by equation 6.8.

$$\varepsilon_{eq}^{ep} = \begin{cases} \varepsilon_{eq}^{e} & for \;\; \varepsilon_{eq}^{ep} \le \varepsilon_y \\ \varepsilon_y + \alpha\left(\varepsilon_{eq}^{e} - \varepsilon_y\right) & for \;\; \varepsilon_{eq}^{ep} > \varepsilon_y \end{cases} \tag{6.8}$$

ε_y is calculated using $\frac{\sigma_t^y}{E_t}$ and shows the strain value where the yield occurs. σ_{eq}^{ep} can then be calculated using the material’s stress-strain curve.

Step 3: Residual stresses after unloading

Assuming that material follows isotropic hardening behavior and that the hydrostatic stresses do not introduce plastic deformation, the equation 6.9 can be used to obtain the induced residual stress,

$$\sigma_{ij}^{r}=\begin{cases}0 & for\quad \sigma_{eq}^{e}\leq\sigma_{t}^{y}\\ s_{ij}^{ep}-s_{ij}^{e} & for\quad \sigma_{t}^{y}<\sigma_{eq}^{e}\leq 2\sigma_{eq}^{ep}\end{cases}\tag{6.9}$$

where s_{ij}^{e} and s_{ij}^{ep} are the deviatoric components of stress in the elastic and elastic–plastic domain, respectively. If the x, y, and z are the principal axes, then the components of induced residual stresses are calculated by equation 6.10.

$$\begin{cases}\sigma_{x}^{r}=\sigma_{y}^{r}=\dfrac{1}{3}(\sigma_{eq}^{ep}-\sigma_{eq}^{e})\\ \sigma_{z}^{r}=-2\sigma_{x}^{r}\end{cases}\qquad for\quad \sigma_{t}^{y}<\sigma_{eq}^{e}\leq 2\sigma_{eq}^{ep}\tag{6.10}$$

In the case of isotropic hardening assumption $\sigma_{eq}^{e}>2\sigma_{eq}^{ep}$, reverse yielding occurs; in this condition, the same assumption is made for the relation between the elastic-plastic and elastic strain. In this case, first, the elastic unloading stress is subtracted from elastic equivalent stress shown by equation 6.11.

$$\Delta\sigma_{eq}^{e}=\sigma_{eq}^{e}-2\sigma_{eq}^{ep}\tag{6.11}$$

Next, the elastic strain released in unloading can be calculated by equation 6.12.

$$\Delta\varepsilon_{eq}^{e}=\frac{\Delta\sigma_{eq}^{e}}{E_{t}}\tag{6.12}$$

Then, the plastic strain after reverse yielding is obtained by equation 6.13.

$$\Delta\varepsilon_{eq}^{ep}=\alpha\Delta\varepsilon_{eq}^{e}\tag{6.13}$$

Knowing the unloading strain, the increase in unloading plastic stress ($\Delta\sigma_{eq}^{ep}$) can be evaluated. Finally, if $\sigma_{eq}^{e}>2\sigma_{eq}^{ep}$, the induced residual stress can be estimated by equation 6.14.

$$\begin{cases}\sigma_{x}^{r}=\sigma_{y}^{r}=\dfrac{1}{3}(\sigma_{eq}^{ep}-2\sigma_{eq}^{ep}-\Delta\sigma_{eq}^{ep})\\ \sigma_{z}^{r}=-2\sigma_{x}^{r}\end{cases}\qquad for\quad \sigma_{eq}^{e}>2\sigma_{eq}^{ep}\tag{6.14}$$

Step 4: Extending one-shot results to full coverage

The induced residual stresses obtained by equations 6.10 and 6.14 represent one-shot impingement condition. The stresses obtained by these equations do not satisfy the equilibrium equations. In order to resolve that, a portion of these stresses should be relaxed, which can be considered using Hooke’s law. The induced residual stresses after the full coverage peening can be calculated using equation 6.15.

$$\begin{cases}\sigma_{x}^{ind}=\sigma_{y}^{ind}=\dfrac{1+\upsilon_{t}}{1-\upsilon_{t}}\sigma_{x}^{r}\\ \sigma_{z}^{ind}=0\end{cases}\tag{6.15}$$

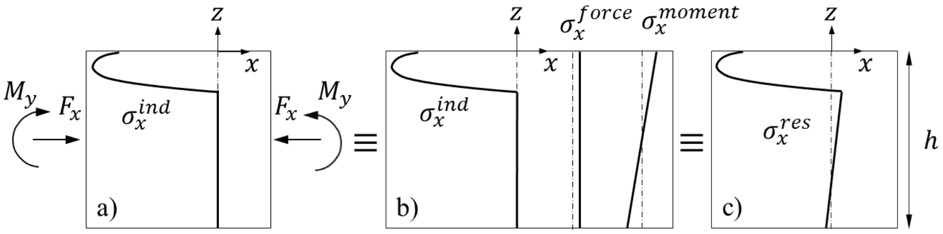

Figure 6.3 Equilibrium of peened sample after separation from the fixture [64]**: a) Sample is peened inside a fixture, $\sigma_x^{ind}$is the induced residual stress, F_x and $M_y$are the axial force and bending moment reactions of the fixture, b) the axial normal and bending stresses due to the force and moment of fixture, c) residual stress profile (σ_x^{res}) after relaxation when it is separated from the fixture**

This stress distribution is not self-equilibrated and there will be a force and a bending moment that will be released by removing a sample from the shot peening fixture. Figure 6.3a shows that the induced residual stress is not self-balanced and the final residual stress, Figure 6.3c, is the summation of the induced stress, the released force, and moment stresses after relaxation from the peening fixture (Figure 6.3b). The force and the bending at the cross-section is obtained using equation 6.16,

$$\begin{cases} \int \sigma_x^{ind} w dz + F_x = 0 \\ \int \sigma_x^{ind} (\frac{h}{2} - z) w dz + M_y = 0 \end{cases} \tag{6.16}$$

where h and w are the height and width of the plate. Then the residual stress distribution can be evaluated using equation 6.17,

$$\sigma_x^{res} = \sigma_x^{ind} + \frac{F_x}{A} + \frac{M_y(\frac{h}{2} - z)}{I} \tag{6.17}$$

where A and I are the cross-section area and area moment of inertia of the target material, respectively.

This background review discloses several assumptions that are made in the analytical modeling, most importantly the assumption in the loading step of the peening process modeling, the impact of a shot. As discussed in the introduction, these assumptions include the effects of friction and actual strain rate, in addition to the assumptions in the conversion of the elastic to elastic-plastic solution in the loading step. The unloading step of the present analytical modeling [64] also employs the conversion of the elastic to elastic-plastic solution similar to the loading step.

6.3 Proposed hybrid numerical-analytical modeling

As discussed in the introduction, the shortfalls of the analytical modeling are mostly in the loading step of the peening process. The introduction also reviewed how in the unloading step, modeling the actual unloading behavior of materials may not be possible in FEM commercial software. In addition, modeling the full coverage in FEM simulation requires modeling multiple random shots which is computationally expensive. To leverage the advantages of both analytical and FEM, and remove the main shortfalls of current literature, we are proposing a new hybrid numerical-analytical modeling of the shot peening process. The proposed method models the loading step using FEM, which enables the model to capture the effects of strain rates, friction and provides more realistic simulations for evaluating stresses and strains. In the unloading step, an analytical approach is developed to calculate the residual stresses by capturing the actual unloading behavior of materials and allows for expanding the solution to multiple shots.

6.3.1 Modeling the loading step

In the hybrid method and in the loading step, the FEM modeling of the single-shot peening is done in two steps. First, the elastic material behavior is assigned for a target plate to obtain the equivalent stress of each element (Figure 6.4a). Next, the elastic-plastic modeling is performed to evaluate the equivalent plastic strain and equivalent stress for each element (Figure 6.4b). The end of the loading step is defined when the shot velocity becomes zero, and after that, the rebounding happens.

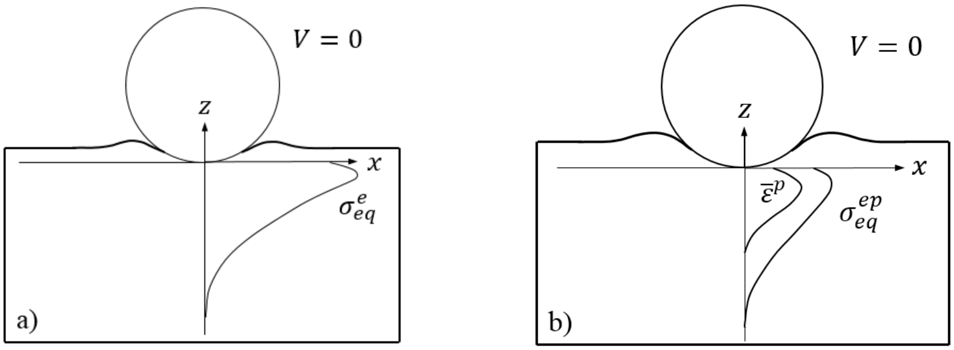

Figure 6.4 Schematic view of the impact zone and stresses and strains a) at the end of the loading step showing elastic loading equivalent stress through the plate depth, assuming the elastic behavior for the substrate, b) at the end of the loading, showing equivalent stress and equivalent plastic strain distribution through the plate depth

The single-shot peening process was modeled in Abaqus/Explicit to generate the FEM solution for the loading process. Shots are assumed to be elastic, and targets are considered to follow the elastic-plastic behavior. Figure 6.5 shows the geometry and meshing of the single shot simulation. The model uses eight-node linear brick elements with reduced integration (C3D8R) and element size of 5 x 5 x 5 μm at the impact point. The sample width and height are greater than 5R where R is the radius of the shot. Mesh sensitivity was performed to finalize the element size of the model. The accuracy of the selected element type and size have been confirmed by getting similar results when using a more computationally expensive element type and finer meshes. All degrees of freedom at the bottom of the target were fixed and symmetry conditions were applied at the xz and yz planes as depicted by Figure 6.5. Although employing a damping model has a negligible effect in the single-shot modeling, however, the damping model proposed in [76] was used to damp unnecessary oscillations. It is notable that applying a damping model and infinite boundary conditions are necessary for the multiple shot peening to damp the results of previous shots before impinging the next one. The penalty contact algorithm was applied with isotropic coulomb friction coefficient of 0.2 [57], [189].

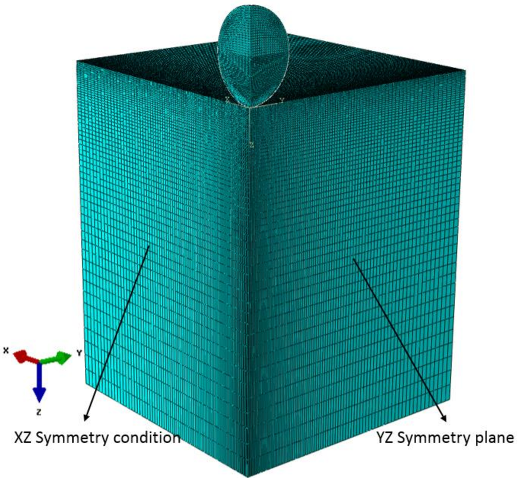

Figure 6.5 Single-shot FEM modeling: geometry and meshing

6.3.2 Modeling the unloading step

In the proposed unloading step the assumption made by equation 6.13 is replaced by a method based on the strain compatibility equations to obtain the unloading strains. In addition, the proposed hybrid method includes the actual unloading behavior of a material. The unloading solution starts with equation 6.18 to calculate the resulting residual stress components. Therefore, the material does not have to follow the isotropic hardening rule, as enforced by earlier models (e.g., [64]). Figure 6.6 demonstrates the schematic stress-strain curve of the substrate and the parameters involved in the proposed modeling.

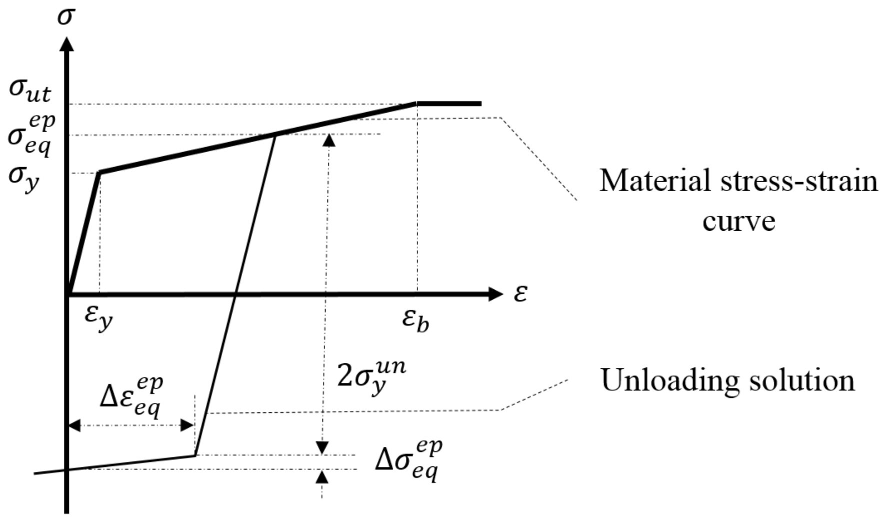

Figure 6.6 Schematic material stress-strain curve and proposed hybrid modeling parameters

$$\sigma_{ij}^r = \begin{cases} 0 & for \quad \sigma_{eq}^e \le \sigma_t^y \\ s_{ij}^{ep} - s_{ij}^e & for \quad \sigma_t^y < \sigma_{eq}^e \le 2\sigma_y^{un} \end{cases} \tag{6.18}$$

where σ_y^{un} is yield stress in the unloading process. (e.g. in isotropic hardening, $\sigma_y^{un} = \sigma_{eq}^{ep}$). Equation 6.19 determines the components of induced residual stress.

$$\begin{cases} \sigma_x^r = \sigma_y^r = \frac{1}{3}(\sigma_{eq}^{ep} - \sigma_{eq}^e) \\ \sigma_z^r = -2\sigma_x^r \end{cases} \quad for \quad \sigma_t^y < \sigma_{eq}^e \le 2\sigma_y^{un} \tag{6.19}$$

Using the strain compatibility equations, Davis and Ramulu [190], showed that in-plane strains after the full coverage is zero. This means that ε_{xx} and ε_{yy} at the end of the loading step vanish during the unloading step to satisfy the full coverage condition. Since the elastic part of strain components is negligible compared to the plastic ones, to satisfy compatibility conditions ε_{xx}^{ep} and ε_{yy}^{ep} become zero at the end of the unloading step. Consequently, ε_{zz}^{ep} becomes zero due to the incompressibility condition [64]. Therefore, it is assumed that $\bar{\varepsilon}^p$ of the elements in the path from the impact point through the depth of a target at the end of the loading step is equal to $\bar{\varepsilon}^p$ in the unloading step. As such, in the cases when $\sigma_{eq}^e > 2\sigma_y^{un}$, the plastic strain is obtained by equation 6.20.

$$\Delta\varepsilon_{eq}^{ep} = \bar{\varepsilon}^p \tag{6.20}$$

Knowing the unloading behavior of a material and a strain value at the end of the unloading step, an increase in the unloading stress ($\Delta\sigma_{eq}^{ep}$) can be calculated. Finally, if $\sigma_{eq}^e > 2\sigma_y^{un}$, the induced residual stress is estimated by equation 6.21.

$$\begin{cases}\sigma_x^r = \sigma_y^r = \frac{1}{3}(\sigma_{eq}^{ep} - 2\sigma_y^{un} - \Delta\sigma_{eq}^{ep}) \\ \sigma_z^r = -2\sigma_x^r\end{cases} \qquad for \quad \sigma_{eq}^{e} > 2\sigma_y^{un} \tag{6.21}$$

The next steps in the hybrid method are to follow equations 6.15-6.17 to obtain the residual stress distribution through the depth of a target.

6.4 Model verification

To verify the proposed model, two examples are considered here. The first example is shot peening of a steel alloy SAE 1070; and the second example is shot peening of an aluminum alloy AL2024-T351, with properties and experimental results given in [64], [191] and [192], respectively. These two examples have been selected based on the availability of experimental and peening process data. First, the material properties and peening parameters are described, then the FEM loading solutions are obtained. Next, the residual stresses calculated by the proposed hybrid numerical-analytical model are compared with the experimental data.

6.4.1 Material properties and peening parameters

The steel alloy is an Almen strip type A, SAE1070 spring steel, with dimensions 76 mm×19 mm×1.29 mm [64]. The aluminum alloy sheet is Al2024-T351 with a thickness of 12.5mm [192]. The strain-rate effect can be modeled using the well-known Johnson-Cook model [193]:

$$\sigma_{eq}^{ep} = \left(A + B{\varepsilon_{eq}^{ep}}^{n}\right)(1 + C\ \ln\dot{\varepsilon}^{*}) \tag{6.22}$$

where A, B, C, and n are material constants. σ_{eq}^{ep} is the equivalent stress, ε_{eq}^{ep} is the equivalent plastic strain, and $\dot{\varepsilon}^{*}$is the strain rate parameter defined as

$$\dot{\varepsilon}^{*} = \frac{\dot{\varepsilon}}{\dot{\varepsilon}_{ref}} \tag{6.23}$$

with $\dot{\varepsilon}_{ref}$ being a reference strain rate. For the SAE1070 stress-strain curve can be closely approximated by a bilinear curve with the average elastic properties given in Table 6.1. The Johnson-Cook parameter for strain rate effect is C=0.0134 and the reference strain rate is taken to be 7500 1/s [194], [195]. The material unloading curve follows the isotropic hardening [64].

Table 6.1 Mechanical properties of SAE1070: E and ν are modulus of elasticity and Poisson's ratio; σ_y and σ_{ut} are yield and ultimate strength, and ε_b is the strains at which perfectly plastic behavior starts

Material	E (GPa)	ν	Density (Kg.m^{-3})	$\sigma_y (MPa)$	ε_b	$\sigma_{ut}\ (MPa)$
SAE1070 spring steel (Almen strip A)	200	0.31	7800	1120	0.082	1270

For the Al2024-T351, the average elastic properties, as shown in Table 6.2, are E=74.2 GPa and ν=0.33 [192]. The plastic behavior is approximated by the Johnson-Cook model [193] with the coefficients of A=299 MPa, B=471MPa, and n=0.406 [196]. Seidt [196] showed that the strain-rate has no considerable effect on the Al2024-T351 sheet and hence C=0.

Table 6.2 Mechanical properties of Al2024-T351: E and ν are modulus of elasticity and Poisson's ratio; A, B, n, and C are the Johnson-Cook model parameters

Material	E (GPa)	ν	Density (Kg.m^{-3})	$A (MPa)$	$B\ (MPa)$	n	C
Al2024-T351	74.2	0.33	2800	299	471	0.406	0

For the unloading, the Bauschinger Effect has been considered using equation 6.24 to obtain the reverse yield stress in unloading from each equivalent plastic strain,

$$\sigma_y^{un} = \sigma_y^0 + Q_\infty(1 - e^{-b\varepsilon_{eq}^{ep}}) \tag{6.24}$$

where $\sigma_y^0 = 299$ MPa is the initial yield stress. $Q_\infty = 220\ MPa$ and $b = 14$ are the material constants [197].

The SAE1070 spring steel alloy [64] and the Al2024-T351 sheet [192] were shot peened using steel shots and Zirshots ceramic beads, respectively. The shot peening parameters and shot properties are given in Table 6.3.

Table 6.3 Shot peening conditions and shot properties: D, V are the shots diameter and velocity [64] [192]

Shot material	E (GPa)	ν	Density (Kg.m^{-3})	D (mm)	V (m/s)	Coverage
Steel shot	210	0.31	7800	0.4	45	100 %
Zirshot Ceramic Z425	300	0.27	3850	0.512	66.2	100%

6.4.2 Results of the loading analysis

The three parameters that are needed from the loading step analysis for the estimation of the residual stress distribution are $\bar{\varepsilon}^p, \sigma_{eq}^{ep}$, and σ_{eq}^{e}. Figure 6.7 and Figure 6.8 present the FEM results of one-shot impingement on the SAE1070 spring steel and Al2024-T351 sheet, respectively, showing the three parameters $(\bar{\varepsilon}^p, \sigma_{eq}^{ep}, \sigma_{eq}^{e})$ needed for the estimation of the residual stress distribution.

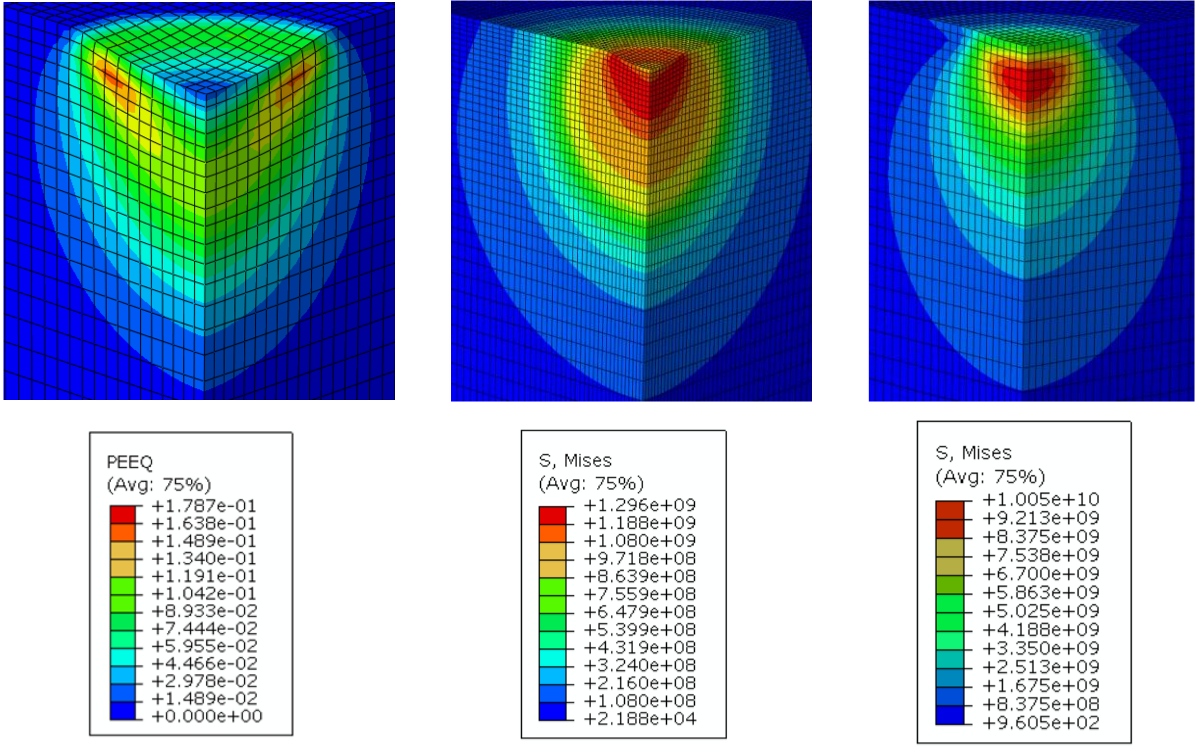
a) Equivalent plastic strain

b) Equivalent stress in elastic-plastic modeling

c) Equivalent stress in elastic modeling

Figure 6.7 FEM results of single-shot impingement on steel alloy SAE1070 at the end of loading; a) Equivalent plastic strain, b) Equivalent stress (in Pa) in elastic-plastic modeling, c) Equivalent stress (in Pa) in elastic modeling

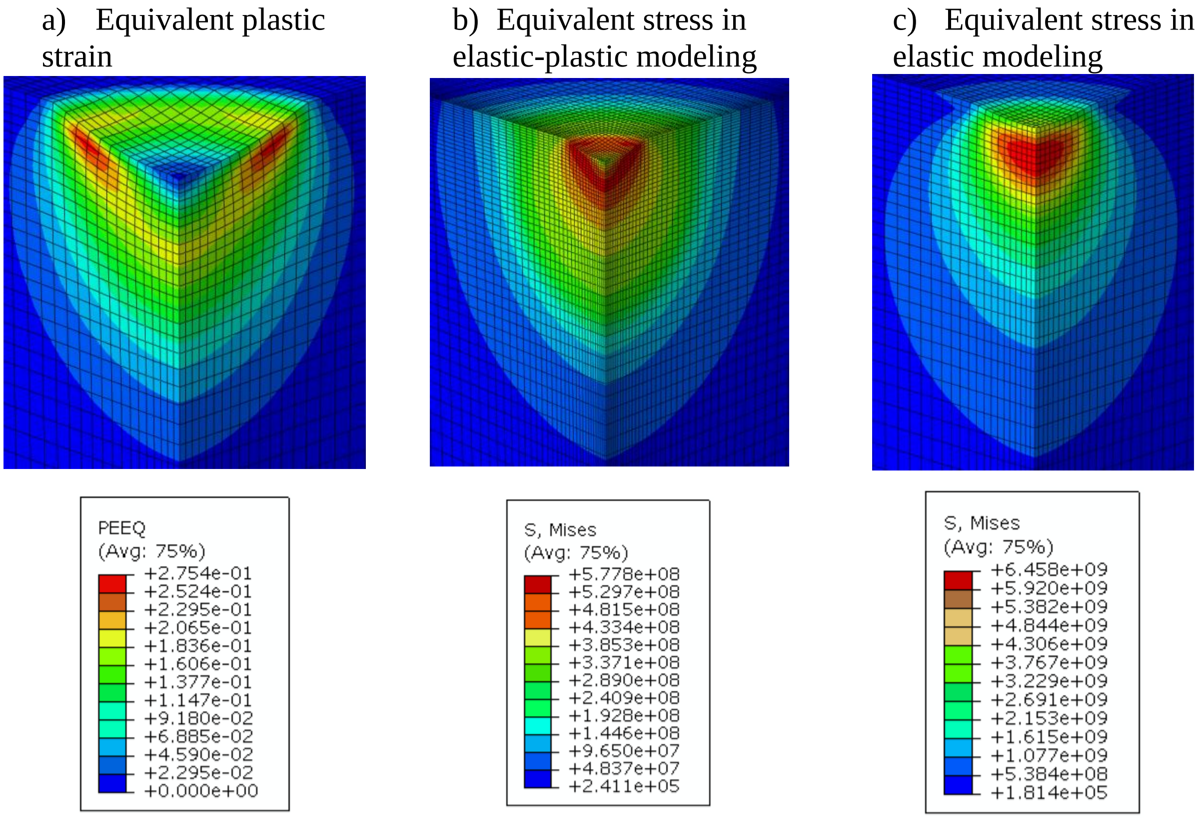
a) Equivalent plastic strain

b) Equivalent stress in elastic-plastic modeling

c) Equivalent stress in elastic modeling

Figure 6.8 FEM results of single-shot impingement on aluminum alloy Al2024-T351 at the end of loading: a) Equivalent plastic strain, b) Equivalent stress (in Pa) in elastic-plastic modeling, c) Equivalent stress (in Pa) in elastic modeling

Figure 6.9 and Figure 6.10 shows the results of the loading step in modeling the SAE1070 and Al2024-T351 that are required for the residual stress evaluation in the unloading step, respectively.

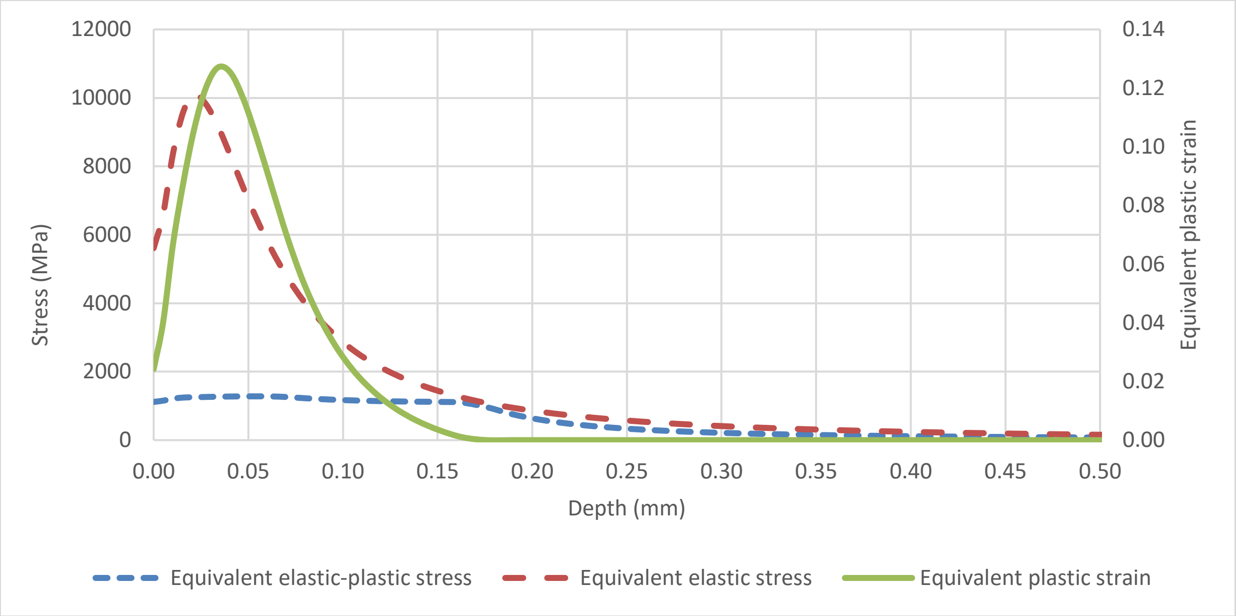

Figure 6.9 Distribution of the required parameters through the depth from the loading at the end of the loading step, equivalent plastic strain, equivalent elastic stress, and equivalent elastic-plastic stress in modeling the peening on SAE 1070

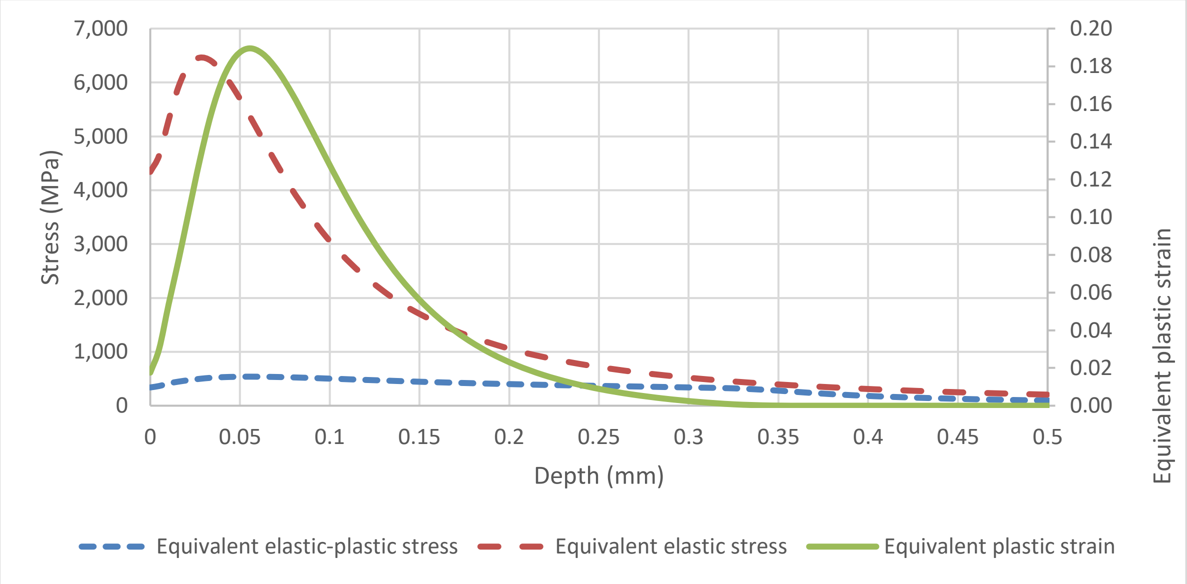

Figure 6.10 Distribution of the required parameters through the depth from the loading at the end of the loading step, equivalent plastic strain, equivalent elastic stress, and equivalent elastic-plastic stress in modeling the peening on Al2024-T351

6.4.3 Prediction of the residual stress

The unloading phase of the shot peening in the proposed hybrid method is modeled analytically; however, it incorporates experimentally obtained actual unloading curves. The unloading stresses, as discussed, are calculated analytically after the full coverage conditions. In the unloading step, equations 6.18-6.21 are utilized to calculate the induced residual stresses followed by equations 6.15-6.17 to obtain the residual stress distribution through the depth of a target.

Figure 6.11 shows the residual stress distribution results of the proposed method for the evaluation of the residual stress distribution through the depth of the SAE1070 spring steel in the full coverage condition. The figure also provides a comparison with the experimental residual stress measurement data [64]. The proposed hybrid method's predicted profile follows the experimental results, including the prediction of reverse yielding, the extent of the compressive region and the maximum value of residual stress, closely.

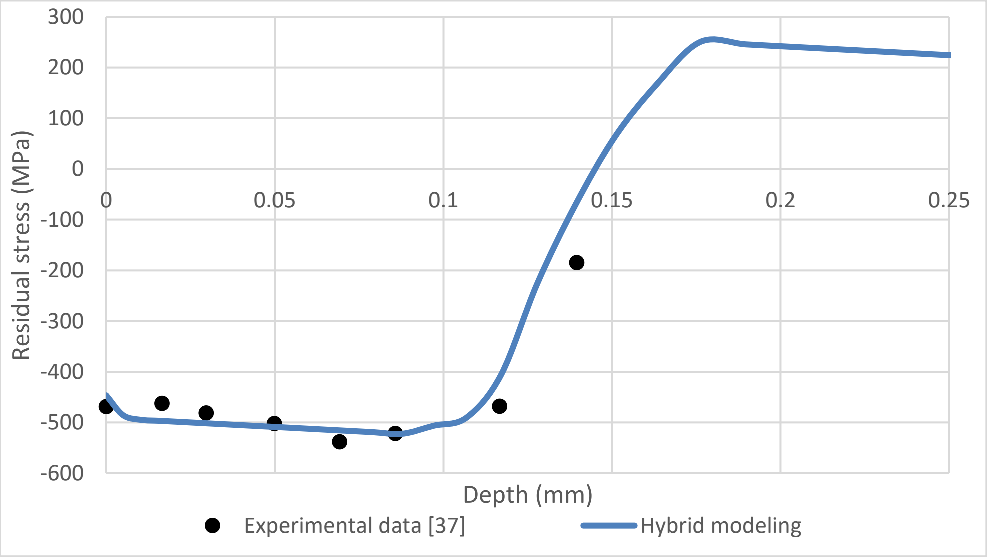

Figure 6.11 Results of residual stress distribution due to shot peening of SAE1070 spring steel and comparison with the experimental data [64]

Figure 6.12 shows the residual stress distribution results of the proposed model in the case of the shot peening on the Al2024-T351 sheet, as well as the experimental measurement by Miao et al. [192]. The experimental data [192] was available in two conditions: one for partial coverage (87% coverage) and the other one after over peening, so both data points are plotted in Figure 6.12. One expects the residual stress of full coverage to be somewhere in between partial and over coverages. Similar to results for steel plate, results for aluminum sheet presented in Figure 6.12 confirm that the proposed method predicts the residual stresses closely as compared to the experimental measurements. It shows that in all four important parameters of residual stress at the surface, maximum compressive residual stress, depth of maximum compressive stress, and depth of the compressive residual stress, the proposed method is very close to the experimental data. A good estimation of the loading strains, using FEM, and considering the actual unloading curves are the main reasons for the close results of the proposed method.

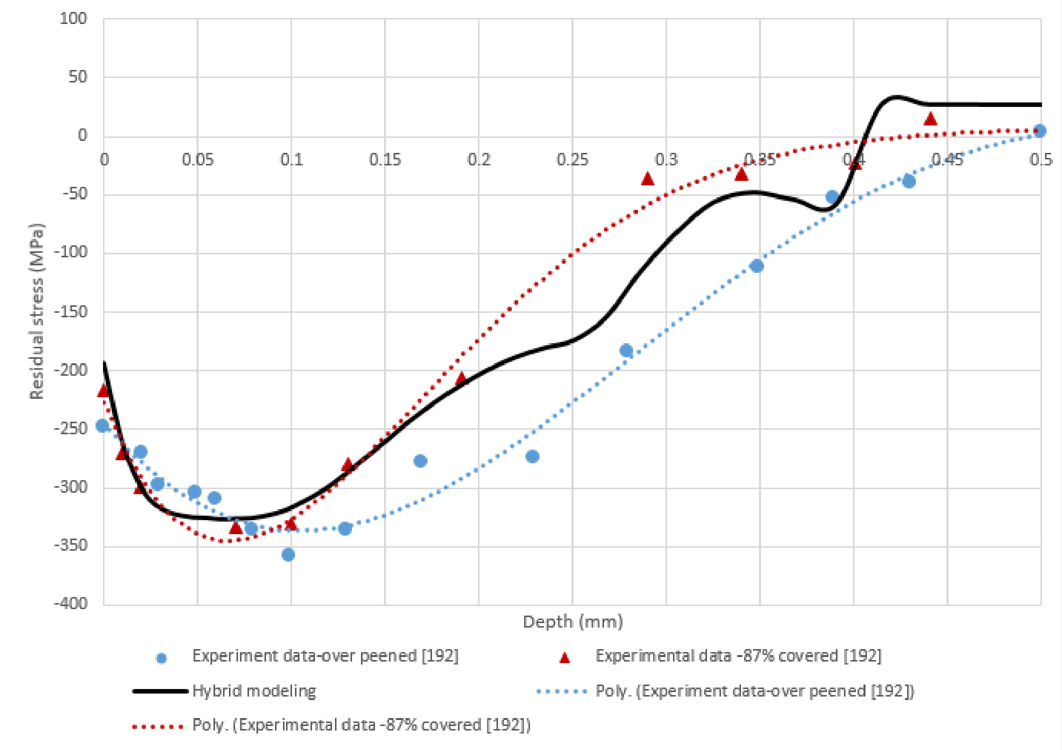

Figure 6.12 Results of residual stress distribution due to shot peening of Al2024-T351 sheet and comparison with the experimental data [192]

6.5 Discussion and sensitivity analysis

6.5.1 Peening on SAE 1070

To understand the role of different parameters on the residual stress profiles predicted by the hybrid method, the results of the sensitivity analysis of peening on SAE 1070 is discussed. First, sensitivity analysis has been done to better understand the significance of different parameters involved in the loading modeling using FEM. As discussed above, there are three main parameters of strain rate effect, friction, and actual strain hardening of a material that are involved in the FEM solution. In this section, one of these effects is ignored at a time, and the results of the loading plastic strains are obtained in each step. As depicted in

Figure 6.13, the results of this sensitivity analysis for the loading step of the shot peening shows the perfectly plastic behavior increases the maximum plastic strain as the material does not have any hardening resistance. Sensitivity analysis also shows that the friction only affects tens of micrometers from the surface, and shifts the distribution of equivalent plastic strains towards the surface. In this case, the maximum plastic strain in the loading step remains the same. Figure 6.13 also shows that removing the strain rate effect in FEM increases the maximum equivalent plastic strain as the material is getting stronger in higher strain rates.

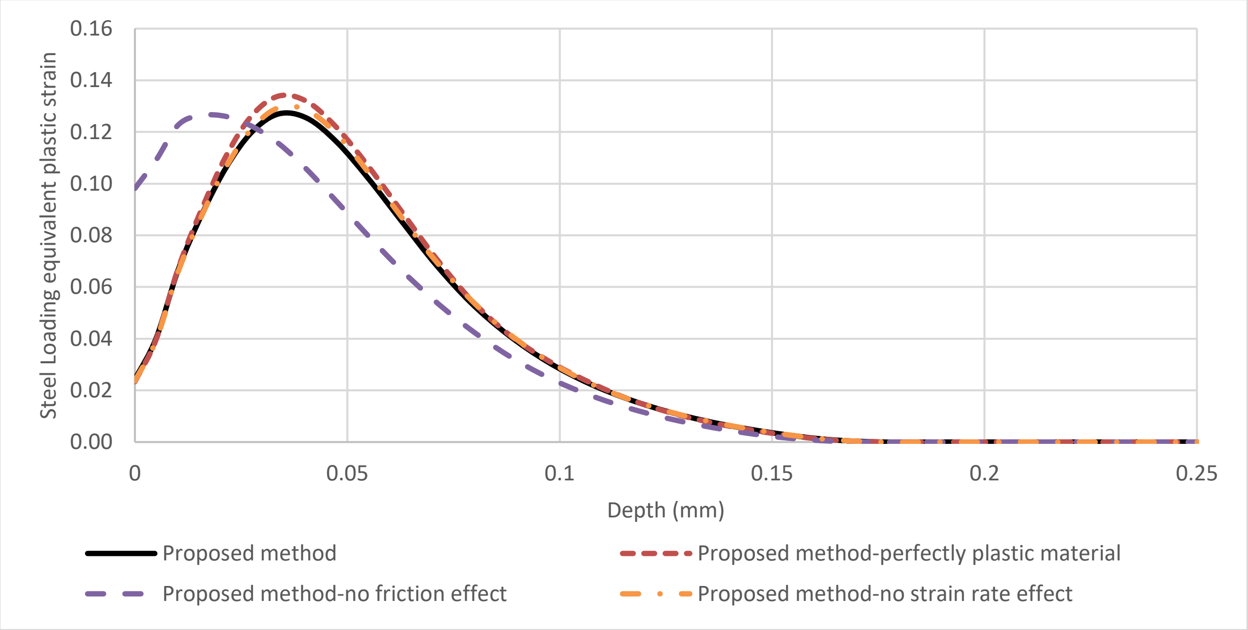

Figure 6.13 Equivalent plastic strain at the end of the loading step using FEM for SAE 1070 in different conditions of no hardening, no friction, and no strain rate

Second, sensitivity analysis is used to understand the significance of different parameters in the evaluation of the residual stress profile. Similar to the loading step, one of these parameters is ignored in each step, and its effect on the residual stress profile obtained by the hybrid method is discussed. Figure 6.14 shows that removing the strain rate effect changes the results only within the first 30 micrometers of SAE 1070 substrates. The strain rates of the surface elements are much higher than those of the underneath layers [198]. Thus, there is a small shift in the predicted residual stress distribution in the surface layer. The SAE 1070 is not significantly rate-sensitive, so the shift in the residual stress is small. The next analysis is to find the effect of friction between the shot and the substrate. In this case, as it is expected, the friction only affects the residual stress in the surface layer and similar to the effect of strain rate, it only changes within tens of few micrometers through the depth. The third parameter of the sensitivity analysis is the actual hardening of a material. Figure 6.14 shows the effect of considering the hardening of the material in the prediction of the residual stress profile. In this scenario, a shift in the residual stress prediction is obvious, and although the hardening of SEA 1070 is not significant ($\sigma_{ut} = 1.13\sigma_y$), it is well shown that hardening plays an important role in residual stress prediction. The above sensitivity analysis results confirm that strain rate and friction (in case of SAE 1070) slightly affect the surface residual stress evaluation, and the actual hardening affects the residual stress evaluation significantly.

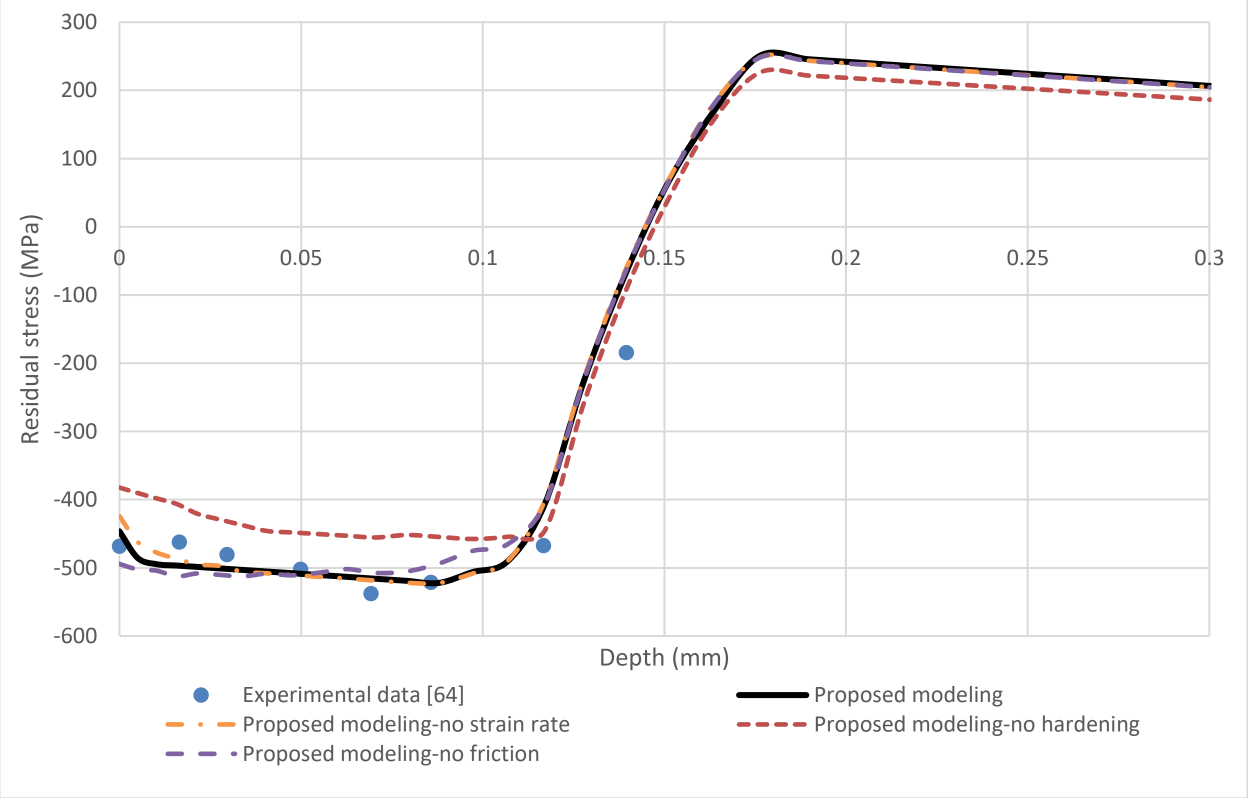

Figure 6.14 Results of residual stress distribution due to shot peening of SAE 1070 spring steel and comparison with the experimental data [64]**, and sensitivity analysis results of hybrid modeling of peening on SAE 1070**

6.5.2 Further discussion

These two examples, peening on SAE 1070 and AL2024-T351, have been selected based on the availability of experiments and process data. The reason the prediction of the proposed method when ignoring the hardening, friction, and strain rate in the sensitivity analysis shown in Figure 6.14 does not differ significantly from the experimental values, in SAE1070, is a result of the fact that the material behavior is close to the elastic-perfectly plastic condition at high strain values which makes the estimation of the equivalent plastic strain in the loading not affecting the estimation of the equivalent stress. Another condition that could create a significant difference in residual stress prediction is when the unloading behavior of a material is far different from the isotropic hardening behavior of SAE 1070. Thus, to determine how different the results of the residual stress distribution would be when the actual loading-unloading behavior of a material is involved, two peening examples are considered here. These two examples are meant to show the effects of actual hardening and actual unloading behavior of material. In all of the following examples, the peening process parameters are assumed to be the same as the peening condition of SAE 1070 example [64].

6.5.2.1 Material with a significant hardening

To better show the effect of material's loading behavior on the residual stress, a material with sigmoidal hardening is considered. This type of hardening behavior is typical in some HCP materials like wrought magnesium alloys [30], [36]. The peening parameters and the elastic behavior of these examples are assumed to be the same as the ones of peening on SAE 1070 [64]. Figure 6.15 shows the sigmoidal hardening and perfectly plastic behavior of the materials considered in this example.

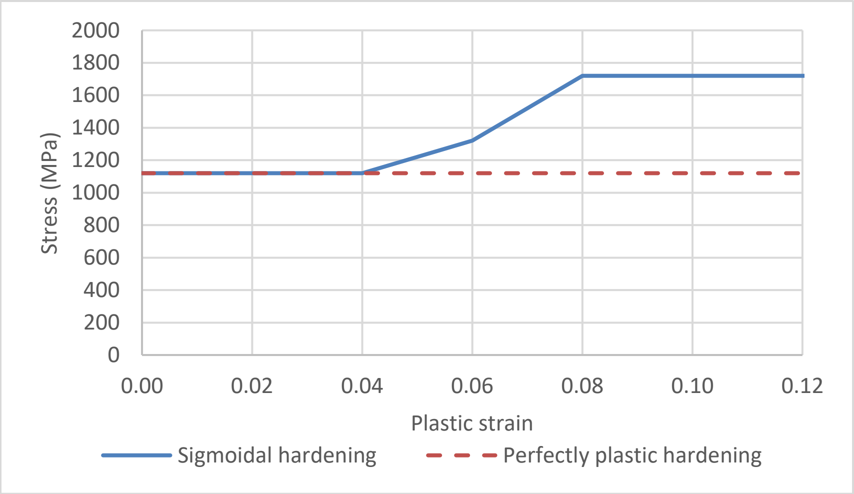

Figure 6.15 Hardening behavior of a material approximated by a few simple piecewise linear lines

Figure 6.16 shows that by considering the actual hardening of the material in this example, the maximum compressive residual stress is twice larger than the case of a perfectly plastic material.

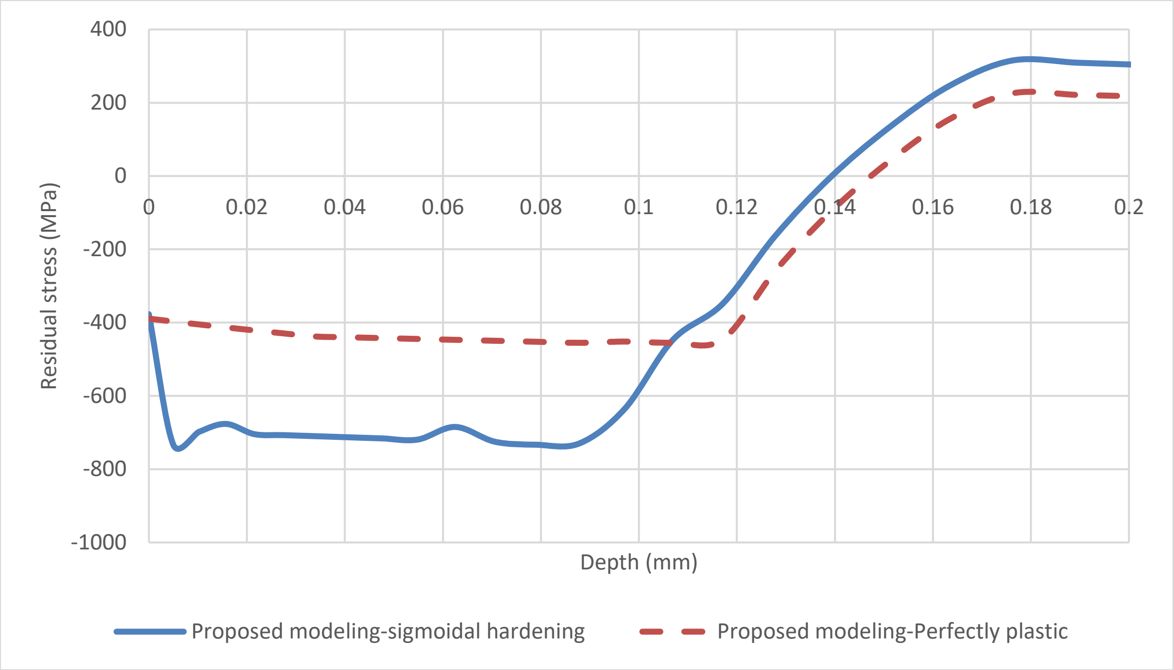

Figure 6.16 Residual stress distribution of peening on a non-hardening and hardening materials

6.5.2.2 Material with nonlinear kinematic-isotropic hardening

The significance of the actual unloading behavior on the residual stress distribution is discussed here. AISI M4333 has been selected as its unloading behavior is significantly different from isotropic hardening [199]. To show the effect of the actual unloading behavior, it is assumed that the material is elastic-perfectly plastic and strain rate insensitive. The yield stress is given as 1070 MPa. This material has a strong Bauschinger Effect which makes its elastic unloading happening at $1.3\sigma_{eq}^{ep}$, compared to $2\sigma_{eq}^{ep}$ in isotropic hardening case [199], [200]. The simplified loading and unloading behavior of AISI M4333 and the comparison of the unloading curve with an isotropic material is shown in Figure 6.17. The elastic behavior of AISI M4333 and the peening conditions are the same as the ones in SAE1070.

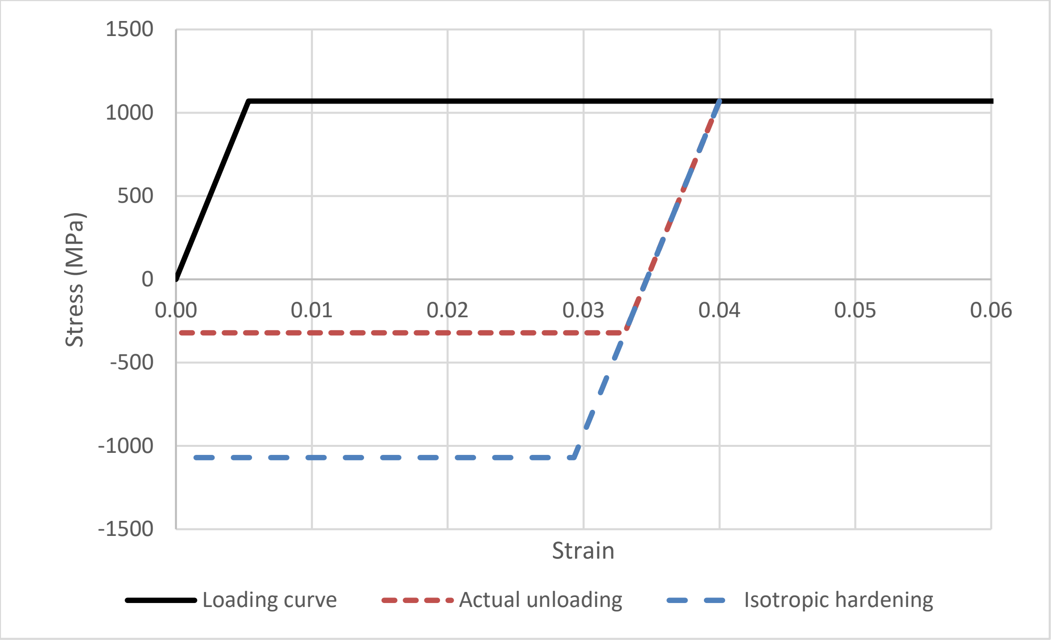

Figure 6.17 Simplified loading and unloading behavior of AISI M4333

Figure 6.18 clearly shows the significance of using the actual unloading behavior of a material in the calculation of residual stress profile. It shows that in case of AISI M4333, with significant Bauschinger Effect, the residual stress at the surface and the maximum compressive residual stress are around four times over predicted if Bauschinger Effect is not considered.

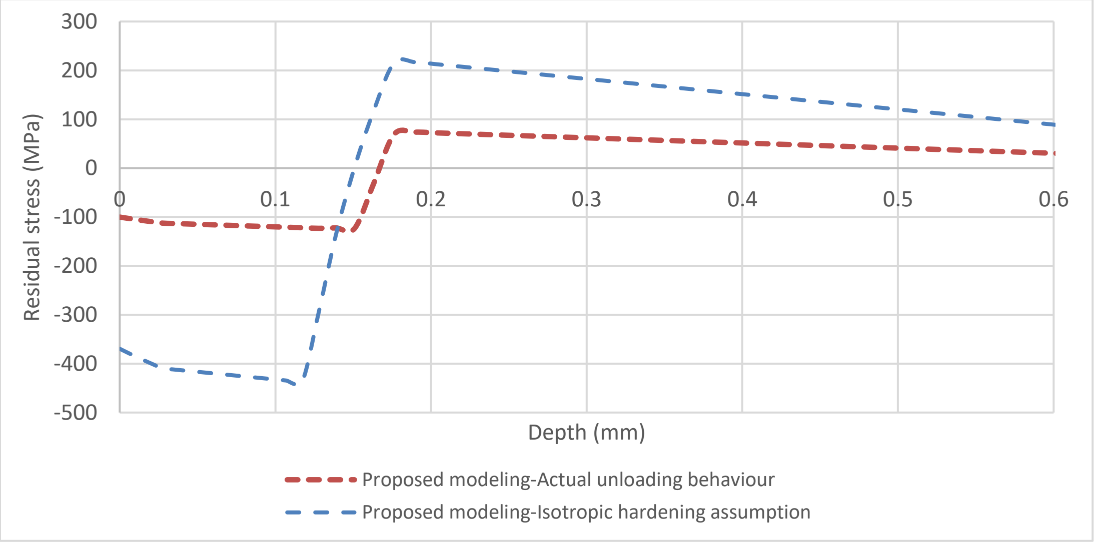

Figure 6.18 Residual stress distribution of peening on AISI M4333 with and without Bauschinger Effect

The above hypothetical examples clearly showed in case of peening on materials with the high strain hardening and complex unloading behavior, employing a method capable of capturing the actual material properties and process parameters is necessary for estimation of the residual stress distribution.

Conclusions

A hybrid FEM-analytical method was introduced which takes advantage of both numerical and analytical methods to provide a simple and accurate solution for modeling the residual stress distribution in the full coverage condition. This method models the loading step of shot peening by FEM and the unloading step analytically. The results of shot peening on steel and aluminum alloys confirmed that the prediction of residual stress using the hybrid method adheres well to the experimental measurements. The hybrid method not only predicted accurate results for steel and aluminum alloys, but also captured the actual loading-unloading behavior of a material. The model also makes the modeling of more complex material behavior possible. The major capabilities of the proposed model are in including: actual strain hardening behavior of material, strain rate effect, friction, and actual unloading behavior including Bauschinger Effect. Through different numerical examples presented in this study, the following conclusions regarding the impact of the above capabilities in the prediction of residual stress can be made:

1. Friction plays a small role in residual stress prediction. It mainly affects the value of residual stress at the surface.
2. Strain rate has been shown to affect the residual stress distribution in the vicinity of the surface layer.
3. The unloading behavior, and in particular Bauschinger Effect has a significant role in the magnitude and distribution of the residual stress.

Chapter 7

Modeling of residual stress distribution in shot peened magnesium alloys using the hybrid numerical-analytical method

Abstract

As Magnesium (Mg) is the lightest industrial metal, there is a significant interest in replacing vehicle components with Mg alloys. On the other hand, the low fatigue strength of these alloys has been an obstacle to use them in load-bearing components. Thus, the fatigue properties of Mg alloys should be improved. Shot peening is a cold-working process employed to improve the fatigue properties of materials. This process involves the impingement of small shots on a material's surface, inducing compressive residual stress, which is known to retard crack initiation and growth in load-bearing components. Modeling provides a low-cost estimation of residual stress distribution compared to experimental methods. This paper extends the application of an existing hybrid numerical-analytical model to use with an asymmetric and anisotropic material that also has complex unloading behavior, such as Mg alloys. First, the loading state of material under peening and the effects of the material's asymmetry and anisotropy are discussed, then the numerical modeling of the loading step is provided. Finally, the actual unloading curves of the material are used to estimate the residual stress profiles. The strain rate effect is also considered in the modeling. The results are matched with experimental measurements done by x-ray diffraction (XRD) and hole-drilling methods.

Keyword: ***Shot peening, Residual stress, Magnesium (Mg) alloy, Asymmetry, Anisotropy, Hybrid numerical-analytical methods***

Nomenclatures

A	Cross-section area of the target material	Subscripts		
D	Shot diameter		eq	Equivalent
E	Young’s modulus		s	Shot
h	Target thickness		t	Target
I	Moment of inertia of the target material		y	Yield
V	Shot velocity			
w	Target width	Superscripts		
ε	Strain		0	Initial
ν	Poisson’s ratio		e	Elastic solution
ρ	Density		ep	Elastic-plastic solution
σ	Stress		un	Unloading

7.1 Introduction

Steel and aluminum have been the dominant materials in vehicle manufacturing since the 1920s [1]. The material selected for a vehicle’s construction is a key factor in the vehicle’s overall weight, as it is directly linked to the vehicle’s fuel efficiency. Magnesium (Mg) was selected as an automotive-industry material in the early 20th century [9]. Since then, the drive to reduce fossil fuel consumption due to its environmental impacts has generated renewed interest in employing Mg and its alloys in vehicle manufacturing [9]. One of the qualifying metrics for structural application of Mg in transportation vehicles is its high durability.

Shot peening is a cold-working process primarily used to enhance the fatigue life of metallic components [161]. In this process, small spherical particles are propelled at the surface of a component, impacting it at a velocity of 30-100 m/s, and creating local plastic deformation. The induced plastic layer is approximately a few hundred micrometers in thickness, causing a compressive residual stress field to develop in the near-surface layer of the structural component [201]. The compressive stress induced by shot peening prevents crack formation and growth by negating the tensile loading contribution of the cyclic stress loading, which in turn results in increased fatigue life. Studies relevant to this paper are discussed in two sections: 1) studies on the effects of shot peening on Mg alloys, and 2) studies regarding the modeling of shot peening.

To date, the effects of shot peening on Mg alloys have only been studied experimentally. These studies were mostly concerned with determining the optimum shot peening conditions that will produce the maximum fatigue life. For this purpose, researchers have measured the residual stress and fatigue life of shot peened samples at different Almen intensities [202] and reported the optimum shot peening conditions. In most of these studies, glass shots are used for peening Mg alloys since steel shots deposit contamination on the surface of Mg alloys, consequently creating corrosion problems [164]. Two experimental techniques, hole drilling [92], [94] and XRD $\sin^2\psi$ [91], [93], [95], [97], [165], [166], have been used for measuring the residual stresses induced by the peening process. Table 7.1 summarizes various studies on the peening of magnesium alloys, including the materials, peening details, methods of residual stress measurement, and the maximum residual stresses induced during peening treatments. The experimental results show the maximum compressive residual stresses of between 20-120 MPa.

Table 7.1 Summary of the studies on the effect of shot peening on Mg alloys

Reference	Material	Shot material	Shot diameter (mm)	Almen intensity (mmN)	Method of stress measurement	Maximum compressive stress (MPa)
[88], 1999	AZ80	Glass, Steel, …	0.66	0.03-0.9	-	-
[89], 1999	AZ80	Glass, Steel	0.36 and 0.65	0.04-0.62	-	-
[90], 2003	wrought AZ80	Steel	0.36	0.18- 0.55	-	-
[91], 2005	wrought AZ80	Glass	0.3-0.4	0.04-0.4	XRD ($\sin^2\psi$)	80-110
[92], 2009	Cast Magnesium A8	Glass	0.245	0.127	Hole-drilling	100
[93], 2009	ZK60-T5	Glass	0.35	0.02-0.04	XRD ($\sin^2\psi$)	50-100
[94], 2010	wrought AZ80	Glass, B30, Ce-ZrO2	0.3-0.8	0.04-0.06	Hole-drilling	40-115
[95], 2011	Mg-10Gd-3Y alloys	Glass	0.35	0.05-0.6	XRD ($\sin^2\psi$)	83 to 95
[97], 2011	ZK60-T5, ZK60	Glass	0.35	0.1-0.4	XRD ($\sin^2\psi$)	20-120
[98], 2018	AZ31B	Ceramic	0.1–0.15	0.15	XRD ($\sin^2\psi$)	30

In modeling the process, loading and unloading terms are used frequently. The loading is the phase of shot impacting the substrate and penetrating through the material up to the point where its velocity decays to zero, and the unloading step starts when the shot media rebounds from the substrate's surface. There are three types of residual stress modeling: Analytical, FEM, and hybrid numerical-analytical modeling. The analytical modeling is the first priority due to its low estimation cost. The analytical estimation of residual stress has three sections: 1) obtaining the loading elastic solution, 2) converting the elastic to the elastic-plastic solution, and 3) evaluating unloading stresses.

Al-Hassani [63] introduced the first analytical modeling for elastic-perfectly plastic material, using a highly simplified method. One of the major analytical modeling studies was done by Li et al. [65]. They used the Hertz contact theory [66] to evaluate the loading stress components, assuming that the shot peening process is similar to a quasi-static process of pressing a spherical material into a semi-infinite plate. They also evaluated the loading strains by assuming that the ratio of the radius of plastic to elastic indentation is the same as the ratio of the plastic strain to elastic strain.

Li et al. [65] also assumed that the above-mentioned ratio is applicable in the unloading step. Shen [68] improved analytical modeling by removing the empirical relation and including the effect of shot velocity. Miao et al. [64] studied the influence of shot type, size, velocity, and peening angle on the Almen intensity. They also accurately estimated residual stress through the depth, induced by the shot peening of steel alloys.

The next modeling type is FEM modeling. Unlike the analytical method, all stress-strain related parameters can be evaluated by the FEM method. The numerical modeling of shot peening was started by 2D modeling of one or a limited number of shots propelled at the target surface [73], and continued by 3D modeling [74]–[76], [170]–[173]. The main purpose of these studies was to figure out the effect of different peening parameters on residual stress distribution. Two strategies were employed to model the residual stress after full coverage peening. First, symmetry cells were used to evaluate the residual stresses after limited shot impingement [80], [174]. Second, multiple random peening method was employed to model the complex nature of this process. In earlier studies, the required number of shots were assembled on top of a target surface, and impinged the plate consequently [177]–[179]. Later, combined DEM-FEM methods were introduced to model shot impingement from a nozzle and consider the shot-shot and shot-target interactions. The substrate's surface is monitored to reach full coverage [181]–[183]. The residual stress distribution is calculated by averaging the residual stress profiles through the depth of different points.

The last way to model the shot peening process is the hybrid numerical-analytical method introduced by the authors of this paper. This method uses the advantages of both numerical and analytical modeling and can capture the actual loading-unloading behavior of materials, plus the strain rate effect and friction. In the hybrid method, the loading step is modeled by FEM and the unloading step is modeled analytically. The main advantages of the hybrid method are that it removes the assumptions of analytical modeling, which are mostly in the loading step, and also enables the model to capture the actual unloading behavior of a material. As the loading behavior of Mg alloys differs greatly from that of elastic-perfectly plastic materials, modeling the whole process analytically is not accurate, and also as the hardening behavior is far different from isotropic or kinematic hardening, it is complex to model the actual behavior using FEM software in the unloading step.

A comprehensive review of the modeling of the shot peening process reveals that, to date, there has been no work reported on modeling the shot peening of Mg alloys. There are complexities in Mg alloys' behavior, including the asymmetry in tension and compression, anisotropy in different directions, complex unloading behavior, and complex strain rate effect on the stress-strain behavior in each direction. In this paper, the shot peening process is modeled to obtain the residual stress distribution through the depth for an asymmetric, anisotropic material with both complex hardening and strain-rate-sensitive behaviors.

7.2 Material and methods

7.2.1 Material

The material used in this study is AZ31B-H24 rolled sheets with thicknesses of 4 and 6.35 mm. Table 7.2 shows the chemical composition of this alloy [119]. The density and Young's modulus of elasticity are 1770 Kg/m3 and 45 GPa, respectively [120]. Figure 7.1 shows the texture of the 6.35 mm thick sheet, highlighting the strong basal texture in the normal direction (ND) of the sheet.

Table 7.2 Chemical composition of AZ31B rolled sheet [119]

Composition	Al	Zn	Mn	Mg
Weight %	2.73	0.915	0.375	Bal.

Modeling residual stress requires knowing the loading-unloading behavior of a material. As the material of interest in this paper is both asymmetric and anisotropic, the loading-unloading curves, the compression-tension (CT) and tension-compression (TC) curves in all three directions, might be needed for residual stress modeling. The authors of this study evaluated the CT and TC of the same material in different directions, concluding that the material could be assumed to be in-plane isotropic. Thus, the properties in the rolling direction (RD) are used for both the RD and transverse direction (TD), but the CT and TC properties in ND are different from those in the RD. As such, for the loading state of the peening, there could be four curves to consider, tension or compression in RD and or in ND. These four curves are shown in Figure 7.2, which clearly shows strong asymmetric behavior in tension and compression, and strong anisotropy between the material behavior in the RD and ND.

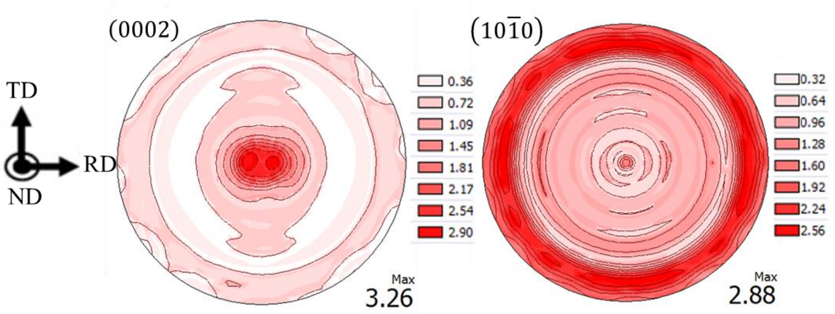

Figure 7.1 Texture of AZ31B-H24 rolled sheet with a thickness of 6.35 mm

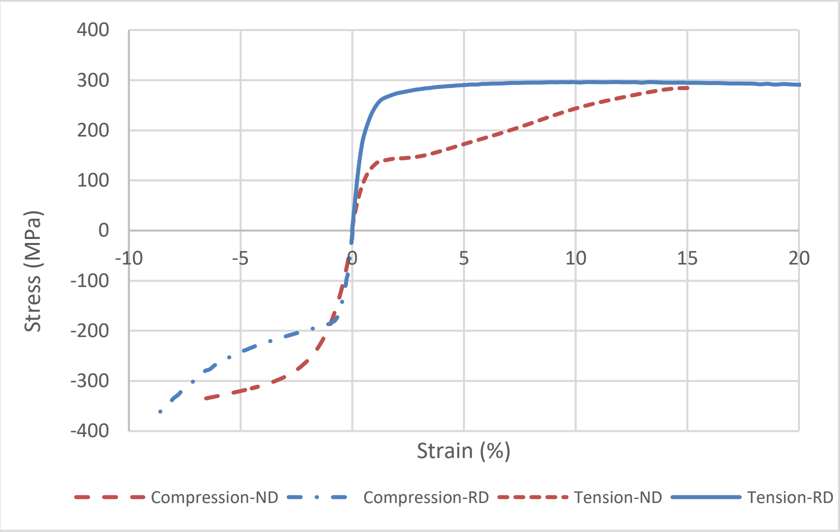

Figure 7.2 AZ31B tension and compression curves in RD and ND

7.2.2 Shot peening parameters

The shot peening process was done at Metal Improvement Co., in Brampton, Ontario, under Almen intensities of 0.05, 0.2 mmN using glass shots and under 0.4 mmN and using glass and steel shots. The diameters of the glass and steel shots were 350 and 280 micrometers, respectively. Samples of 35 x 35 x 4 mm sheets were shot peened from the working distance of 10 cm, in full coverage, and vertical peening.

7.2.3 Nano-indentation

Various values for the modulus of elasticity for glass shots have been reported in the literature [203] and [204]. A Nano-indentation test [205] was performed to measure the modulus of elasticity for the glass shots used in this study. The shots were put in a cylinder with a conic hole that was then filled with liquid glue. The shot size ranged from 270-360 μm. The samples were then finely polished with 6, 3, 1 and 0.1-μ diamond paste and an oil-based lubricant on imperial cloth. Finally, the samples were polished with 0.05 μ master prep colloidal silica on a black CHEM pad. Figure 7.3 shows the mounted samples and the surface of the polished sample. An in-situ Nano-indenter from Nanomechanics Inc. was used for this test. The level of indentation forces applied to the surface was below 1.3 μN. To verify the results, the Nano-indentation test was also carried out with typical steel shots with a known modulus of elasticity. The indentations and measurements were repeated 25 times for each material.

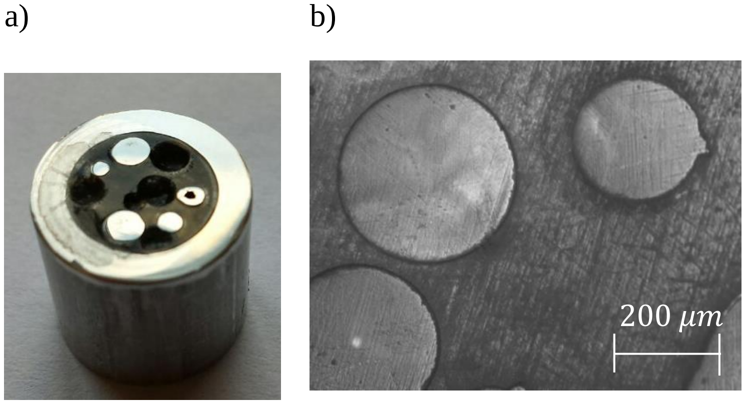

Figure 7.3 Measurement of glass shots modulus of elasticity: a) sample mount for Nano-indentation, b) Image of the polished surface

7.3 Modeling of residual stress induced by peening using the hybrid method

As discussed in Chapter 6, the authors have proposed a new hybrid numerical-analytical modeling of shot peening, which leverages the advantages of both analytical and FEM and removes the main disadvantages involved in the literature. The hybrid method models the loading step using FEM, enabling the model to capture the actual stress-strain behavior plus the effects of strain rate and friction. In the unloading step, an analytical approach is employed to evaluate the residual stresses by capturing the actual unloading behavior of materials.

7.3.1 Modeling the loading step

The hybrid method requires modeling of the loading phase of single-shot peening in two steps. First, the substrate is assumed to behave elastically, to obtain the elastic equivalent stresses of all elements at the center of the impact through the depth (Figure 7.4a). Second, the actual elastic-plastic behavior of the material is used in modeling the loading phase to evaluate the equivalent plastic strain and equivalent stress for each element (Figure 7.4b).

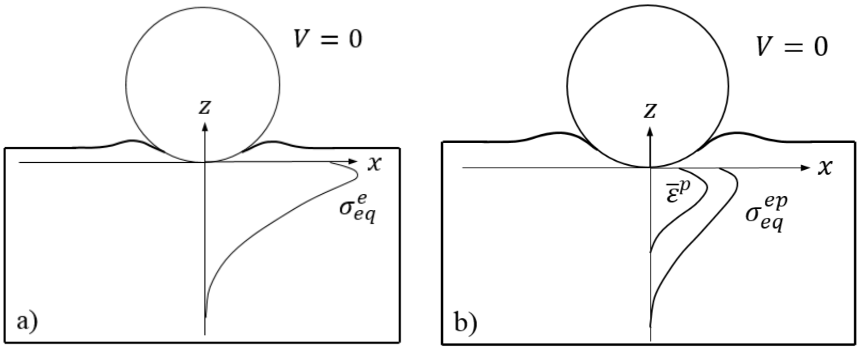

Figure 7.4 Schematic view of the impact zone and stresses and strains a) at the end of the loading step, showing elastic loading equivalent stress through the plate depth, assuming the elastic behavior for the substrate, b) at the end of the loading, showing equivalent stress and equivalent plastic strain distribution through the plate depth

Abaqus FEA software has been used to model the single shot peening process. Shots are assumed to have elastic behavior, and substrates are considered to have actual elastic-plastic behavior. The geometry and meshing of modeling the single shot peening are shown in Figure 7.5. The model uses eight-node linear brick elements with reduced integration (C3D8R) and the element size of 5 x 5 x 5 μm at the impact point. The sample width and height are greater than 5R, R being the radius of the shot. Mesh sensitivity analysis was performed to finalize the element size of the model. All degrees of freedom at the bottom face of the substrate were fixed, and symmetry conditions were applied at the xz and yz planes as depicted in Figure 7.5. The damping model proposed in [76] was used to damp unnecessary oscillations. The penalty contact algorithm was applied with the isotropic coulomb friction coefficient of 0.12. As the material shows asymmetric and anisotropic properties, first, the loading state in the peening process is discussed conceptually, then the predicted effects of these behaviors are confirmed using FEM software. To represent the effect of the material's asymmetric properties, the asymmetric material model (MAT 124) of LS-DYNA software has been employed in this study. The effect of the material's anisotropy has been modeled using the Hill's yield function [206] in Abaqus. The strain rate effects in the loading direction are estimated using experimental data on the effect of strain rate on the stress-strain behavior of AZ31B-H24 rolled sheet along compression tests in different directions [207]. Finally, for modeling the loading phase, the strain rate dependent plastic model of Abaqus is used, as it is able to capture the actual stress-strain curve at each strain rate value.

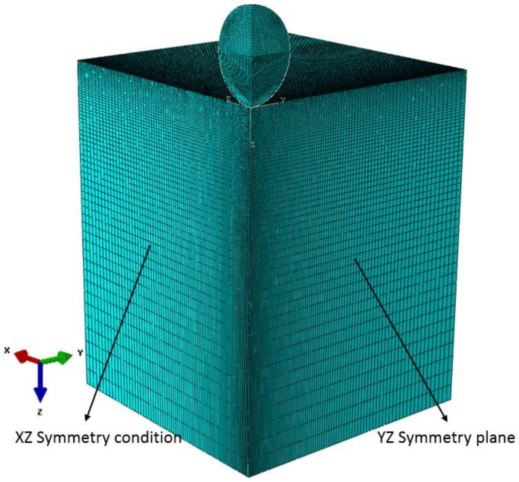

Figure 7.5 The geometry of the FEM model using Abaqus software

In the shot peening industry, the Almen intensity concept is used to show the amount of kinetic energy transferred to a material. Almen and Black [54] introduced this method to measure the value of shot peening intensity. In modeling, the velocity of shots should be evaluated first using the known Almen intensity and shot peening parameters. Miao et al. [64] proposed an accurate analytical approach to relate the Almen intensity to the velocity of shots. In the present study, the shot velocities were calculated based on their studies [64], using the average shot diameter. The shot peening parameters and shot properties are given in Table 7.3.

Table 7.3 Shot peening conditions and shot properties

Intensity (mmN)	Shot material	E_s (GPa)	ν_s	Density (Kg.m^{-3})	D (mm)	V (m/s)	Coverage
0.05	Glass shot	70.2	0.22	2500	0.350	8	Full coverage
0.2	Glass shot	70.2	0.22	2500	0.350	33	Full coverage
0.4	Glass shot	70.2	0.22	2500	0.350	94	Full coverage
0.4	Steel shot	210.0	0.30	7850	0.280	50	Full coverage

7.3.2 Modeling the unloading step

The unloading behavior of Mg alloys cannot be modeled by isotropic hardening nor by kinematic. It is even impossible to model the unloading curve by just considering the Bauschinger Effect. The reason for this difficulty is that not only do the yield stresses at unloading depend on the loading strains, but also the shape of the unloading curves differs. In this study, depending on the loading strain for each point through the depth, an unloading curve has been assigned to evaluate the residual stress for that point. The actual unloading curves are used to calculate the reverse yield stresses for each curve.

The unloading step of the residual stress prediction using the hybrid method employs a form of analytical modeling that is capable of capturing the actual unloading behavior of a material. Figure 7.6 demonstrates the schematic stress-strain curve of the substrate and the parameters involved in the modeling.

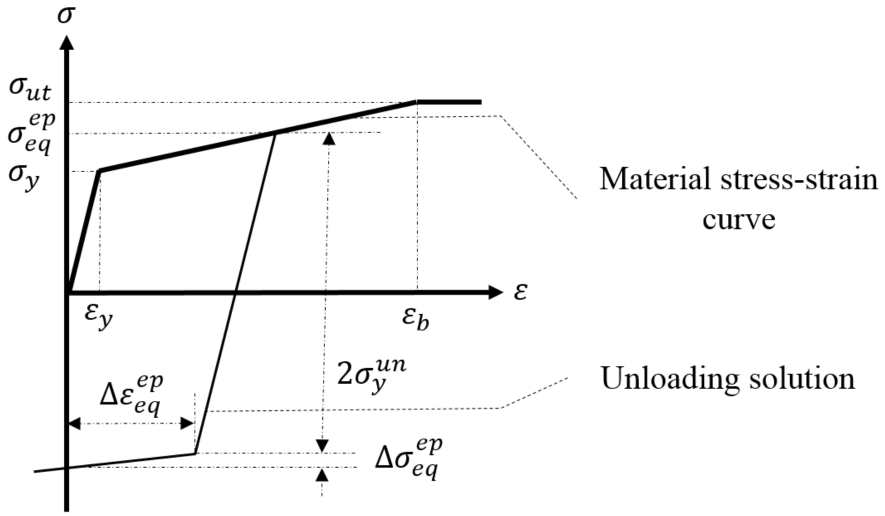

Figure 7.6 Schematic material stress-strain curve and proposed hybrid modeling parameters

As discussed in Chapter 6, equation 7.1 evaluates the induced residual stress components.

$$\begin{cases} \sigma_x^r = \sigma_y^r = \frac{1}{3}(\sigma_{eq}^{ep} - \sigma_{eq}^e) \\ \sigma_z^r = -2\sigma_x^r \end{cases} \qquad for \quad \sigma_t^y < \sigma_{eq}^e \le 2\sigma_y^{un} \tag{7.1}$$

Using the strain compatibility equations, it was shown that, in the cases when $\sigma_{eq}^e > 2\sigma_y^{un}$, the plastic strain is obtained by equation 7.2.

$$\Delta\varepsilon_{eq}^{ep} = \bar{\varepsilon}^p \tag{7.2}$$

Knowing the unloading behavior of a material and a strain value for each element at the end of the unloading step, an increase in the unloading stress ($\Delta\sigma_{eq}^{ep}$) can be calculated. Finally, if $\sigma_{eq}^e > 2\sigma_y^{un}$, the induced residual stress is estimated by equation 7.3.

$$\begin{cases} \sigma_x^r = \sigma_y^r = \frac{1}{3}(\sigma_{eq}^{ep} - 2\sigma_y^{un} - \Delta\sigma_{eq}^{ep}) \\ \sigma_z^r = -2\sigma_x^r \end{cases} \qquad for \quad \sigma_{eq}^e > 2\sigma_y^{un} \tag{7.3}$$

The next step in the hybrid method as in the analytical method is to extend the results of the induced residual stresses to the ones in the full coverage condition. To do so, the induced residual stresses after the full coverage peening can be calculated using equation 7.4.

$$\begin{cases} \sigma_x^{ind} = \sigma_y^{ind} = \frac{1 + \upsilon_t}{1 - \upsilon_t}\sigma_x^r \\ \sigma_z^{ind} = 0 \end{cases} \tag{7.4}$$

where ν_t is the target's (substrate's) Poisson's ratio. As the stress distribution is not self-equilibrated, a force and a bending moment will be released by removing a sample from the shot peening fixture. The force and the bending at the cross-section is obtained using equation 7.5,

$$\begin{cases} \int \sigma_x^{ind} w dz + F_x = 0 \\ \int \sigma_x^{ind} \left(\frac{h}{2} - z\right) w dz + M_y = 0 \end{cases} \tag{7.5}$$

where h and w are the height and width of the plate. Then the residual stress distribution can be evaluated using equation 7.6,

$$\sigma_x^{res} = \sigma_x^{ind} + \frac{F_x}{A} + \frac{M_y(\frac{h}{2} - z)}{I} \tag{7.6}$$

where A and I are the cross-section area and area moment of inertia of the target material, respectively.

7.4 Results

7.4.1 Evaluation of glass shots' Young modulus

Table 7.4 shows the results of the modulus of elasticity measurements using Nano-indentation for the steel and glass shots.

Table 7.4 Results of measurements of Young's modulus of elasticity by Nano-indentation

Material	Modulus of elasticity (GPa)	Standard deviation (GPa)
Steel shots	243.6	22.8
Glass shots	70.2	4.5

The results on steel shots indicate that this method can successfully be used to measure the modulus of elasticity of shots.

7.4.2 Results of the loading step

7.4.2.1 Effect of material asymmetry and anisotropy

In the hybrid method, the loading state of each point through the depth is assumed to be the same as the loading state at the point of impact through the depth. Thus, the loading state of the path from the impact point through the depth is of interest. The asymmetric properties of Mg alloys in tension and compression and anisotropic properties in RD and ND need to be addressed at this point. To show the dominancy of tension or compression curve in RD or ND, first the loading state of the elements in the path from the center of the impacts through the depth is considered here. Due to the loading and geometry conditions, the axisymmetric condition is applicable for this path. As the shot compresses the substrate in ND, we expect to get the strain field shown in equation 7.7, which is exactly the loading state in the monotonic compression of the material along ND. Thus, it is predicted that the loading-unloading state of the material in the peening process can be approximated by the compression-tension in ND of the sheet.

$$\varepsilon_z^p = -2\varepsilon_x^p = -2\varepsilon_y^p \tag{7.7}$$

To confirm the results, the asymmetric and anisotropic material properties are modeled in LS-Dyna and Abaqus, respectively. To account for the asymmetry, an available asymmetric material model (MAT_124) of LS-DYNA is employed to determine if one of the compression or tension curves is dominant. In the first attempt, both the tension and compression curves in ND were given to the software. In the next steps, just the tension and compression curves were used. In this part of the modeling, it is assumed that the material has isotopic hardening properties. Figure 7.7 shows the results of the loading plastic strain and equivalent stresses using tension-compression curves or just tension, or just compression. Figure 7.7 demonstrates the residual stresses after single shot peening assuming isotropic hardening. The figure shows that the results for the asymmetric material are the same as the ones when considering a symmetric material with the compression curve as a material behavior.

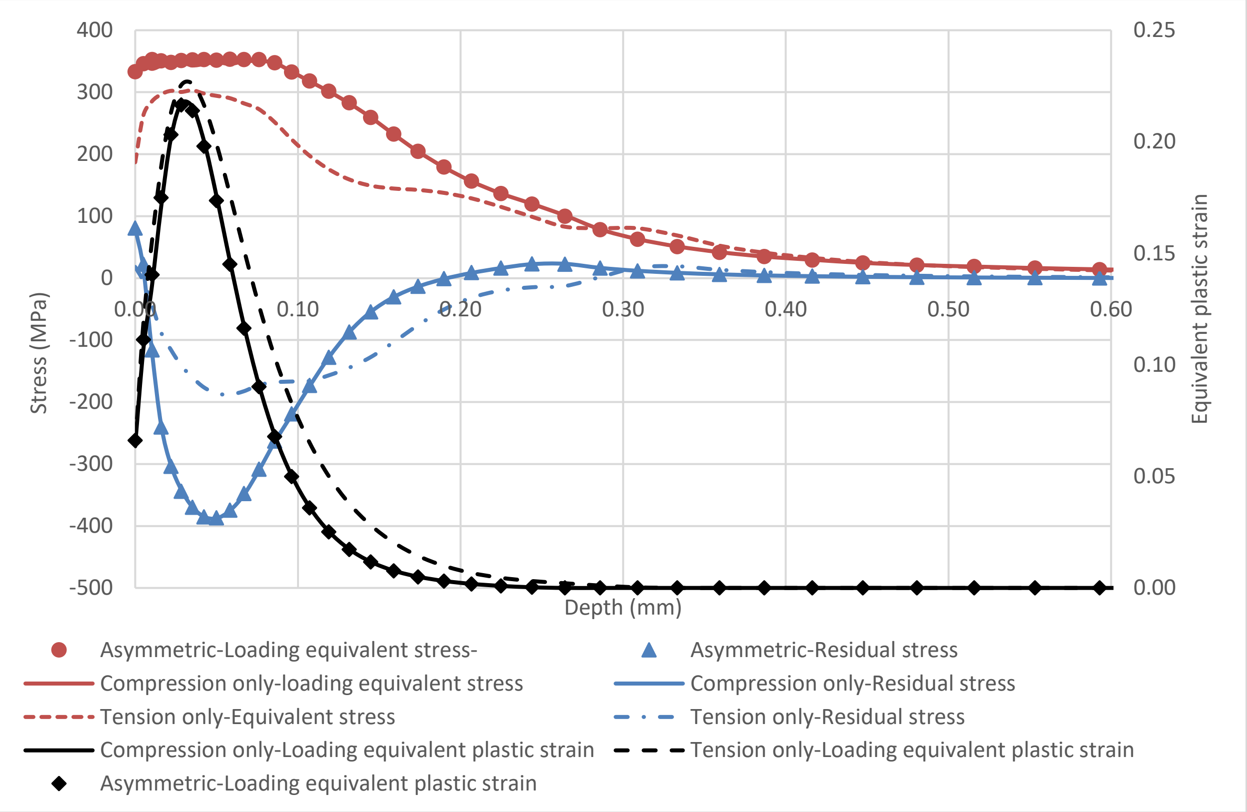

Figure 7.7 Distributions of equivalent plastic strain, equivalent stress and residual stress through the depth, considering asymmetric properties or just tension or just compression behavior

It is concluded that the compression stress-strain curve dictated the stresses in modeling the shot peening process.

To consider the effect of anisotropy in modeling the shot peening process, the POTENTIAL option has been used, which uses Hill’s yield function [206] to capture the anisotropy of the material. As this material model scales only the properties of the material in one direction to the other ones, using coefficients of $R_{11} = R_{22} = 1.32$, $R_{33} = 1$, $R_{12} = R_{13} = R_{23} = 1$ produced the scaled curves of compression along ND to be assumed for the in-plane material properties. These coefficients have been evaluated to capture the maximum difference between the compressive behavior of the material along RD and ND. Figure 7.8 shows the hypothetic stress-strain curve of the material in RD and TD, and the actual properties along ND.

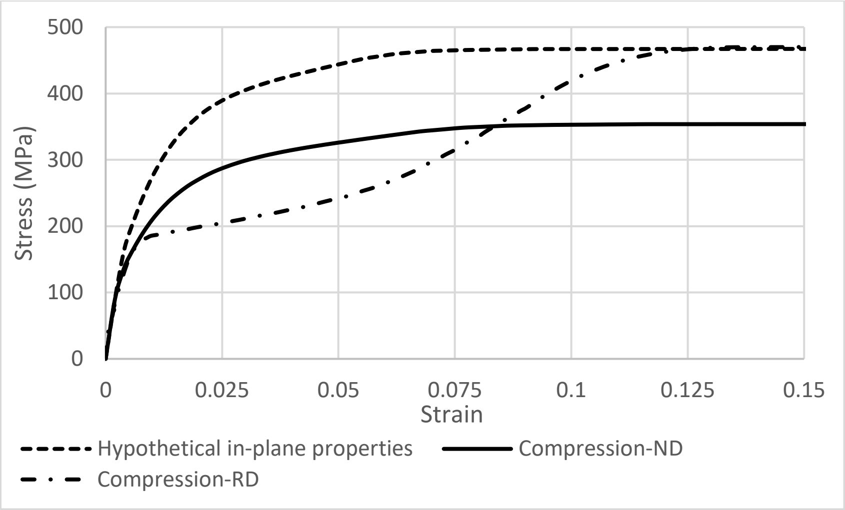

Figure 7.8 Material in-plane and along ND for determining the effects of anisotropy

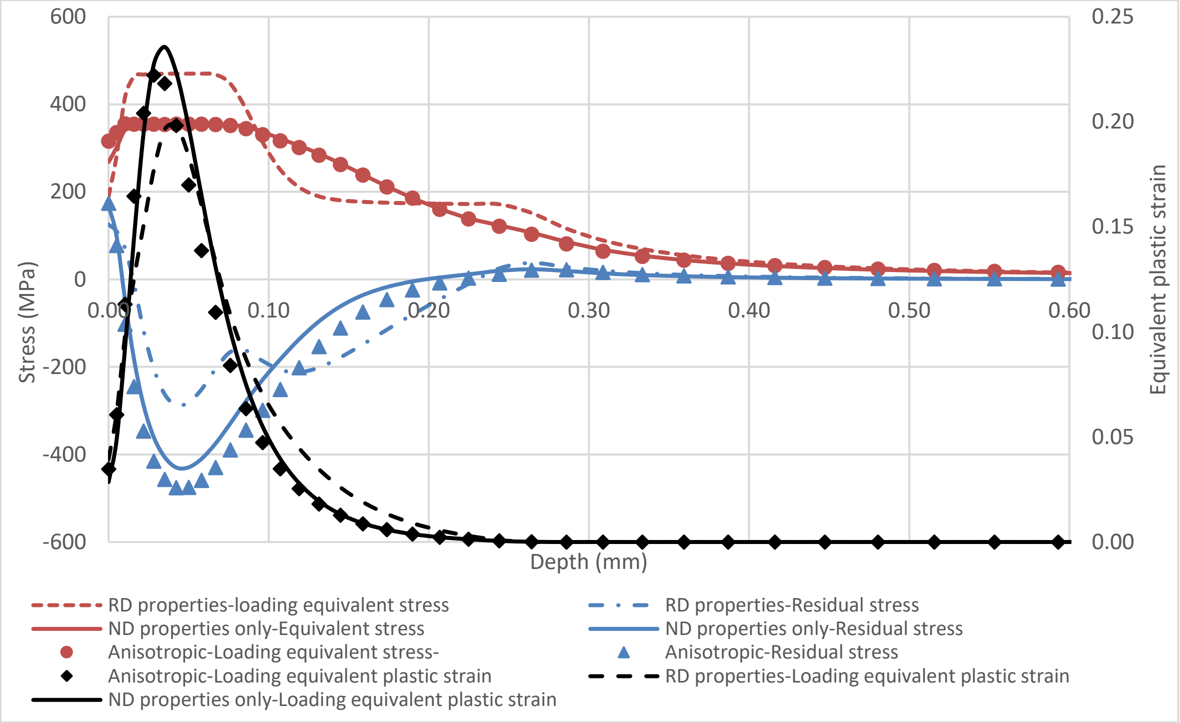

Figure 7.9 Distributions of equivalent plastic strain, equivalent stress and residual stress through the depth, considering anisotropic properties or just compression in RD or just compression in ND

7.4.2.2 Considering the strain rate effect

Zhao et al. [207] did experiments to obtains the flow curves of AZ31B-H24 at different strain rates in compression along ND of the sheet (Figure 7.10). Looking into the effect of strain rate on the compression behavior of the material in ND, it is found that the strain rate does not change the yield stress, but as the plastic strain is increased, the strain rate hardens the material more. The same pattern in the effects of strain rate on the compression behavior of AZ31B-O along ND has been proposed by [208]. The authors of the present study are proposing equation 7.8, fitted to the experimental data as shown in Figure 7.10.

$$\sigma_{C-ND} = a_0 + \left(a_1 + \exp\left(a_2 \ln\left(\dot{\varepsilon}_p\right)\right) \exp\left(a_3 + a_4 \bar{\varepsilon}_p\right)\left(\bar{\varepsilon}_p{}^{n}\right) + a_5 \exp\left(a_6 \ln\left(\dot{\varepsilon}_p\right)\right) \qquad (7.8)$$

where $\bar{\varepsilon}_p$ and $\dot{\varepsilon}_p$ are the effective plastic strain, and the rate of effective plastic strain, respectively. The coefficients are provided in Table 7.5.

Table 7.5 Values of coefficients used in equation 7.8

Coefficients	Value
a_0	-641.4
a_1	17.214
a_2	0.2479
a_3	3.577
a_4	-1.515
a_5	753.3
a_6	-0.001206
n	0.35

The quasi-static behavior of the material used in [207] is very close to the compression curve of the material used in this study. However, to obtain the strain rate effect on the compression behavior of AZ31B-H24, used in this study, it is assumed that the ratio of the stress value at a high strain rate to the stress at the quasi-static condition at each plastic strain is the same for both materials. Thus, equation 7.9 is used to generate the material behavior of AZ31B-H24 at high strain rates.

$$\sigma_{C-ND}^{AZ31B-H24}\left(\bar{\varepsilon}_p, \dot{\varepsilon}_p\right) = \frac{\sigma_{C-ND}\left(\bar{\varepsilon}_p, \dot{\varepsilon}_p\right)}{\sigma_{C-ND}\left(\bar{\varepsilon}_p, \dot{\varepsilon}_p = 0.001\ 1/s\right)} \sigma_{C-ND}^{AZ31B-H24}\left(\bar{\varepsilon}_p, \dot{\varepsilon}_p = 0.001\ 1/s\right) \qquad (7.9)$$

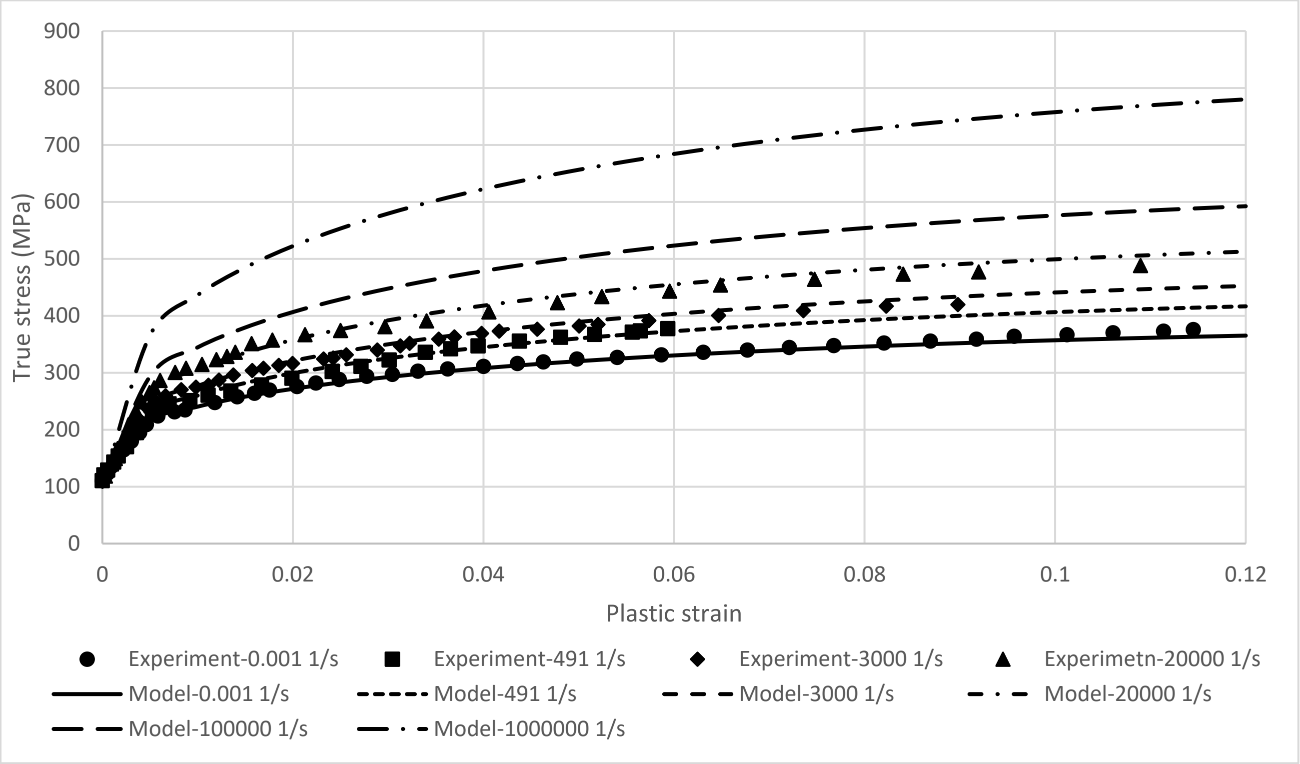

Figure 7.10 Strain rate effect on the compression of AZ31B-H24 along ND obtained experimentally [207] **and fitted model using equation 7.8**

7.4.2.3 Modeling the loading phase in peening the Mg alloy

Based on the results of the effect of material asymmetry and anisotropy, the properties of compression along the ND are considered for the loading phase simulation. The required parameters for predicting the residual stress distribution using the hybrid method are the equivalent plastic strain ($\bar{\varepsilon}^p$), equivalent elasto-plastic stresses σ_{eq}^{ep}, and equivalent stress in elastic modeling σ_{eq}^{e}. Figure 7.11 presents the FEM results of one-shot impingement on the AZ31B-H24 using a steel shot, showing the parameters of ($\bar{\varepsilon}^p, \sigma_{eq}^{ep}, \sigma_{eq}^{e}$) needed for estimating the residual stress distribution.

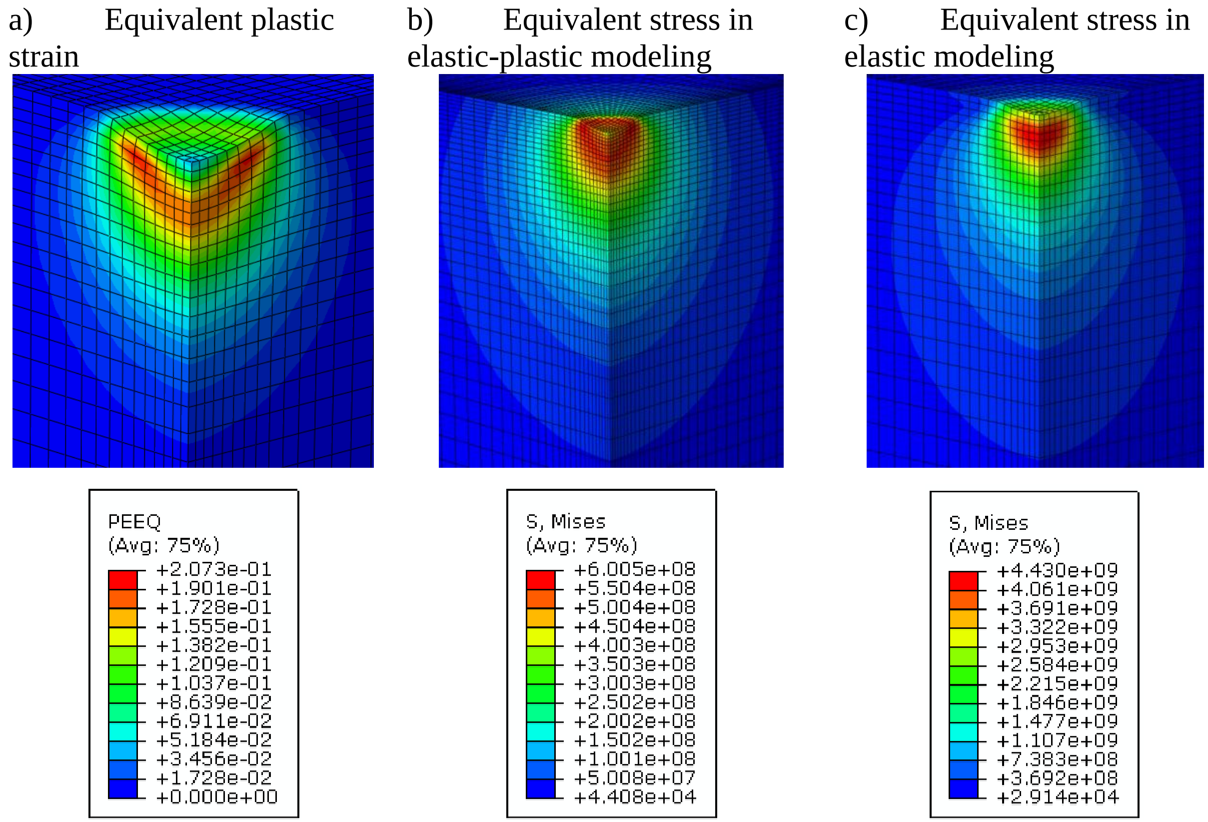
a) Equivalent plastic strain

b) Equivalent stress in elastic-plastic modeling

c) Equivalent stress in elastic modeling

Figure 7.11 FEM results of single-shot impingement on AZ31B using steel shots at the end of loading; a) Equivalent plastic strain, b) Equivalent stress (in Pa) in elastic-plastic modeling, c) Equivalent stress (in Pa) in elastic modeling

Figure 7.12, Figure 7.13, and Figure 7.14 show the results of the required parameters: loading equivalent plastic strain, equivalent stress, and equivalent elastic stress from the loading phase of the hybrid method, respectively. These parameters are then employed to calculate the residual stress distributions in the shot peening of AZ31B-H24 under different conditions. Figure 7.12 shows that increasing the peening intensity increases the maximum plastic strain and its associated depth in the loading phase of the modeling. In addition, the depth of the plastically deformed layer has a direct relation with the peening intensity. However, the peening intensity slightly affects the plastic strain at the surface of the substrate. In the case of peening under 0.4 mmN using glass and steel shots, both peening conditions have similar distributions; however, due to the differences in shot's properties, diameters, and velocities, these two curves are not well fitted.

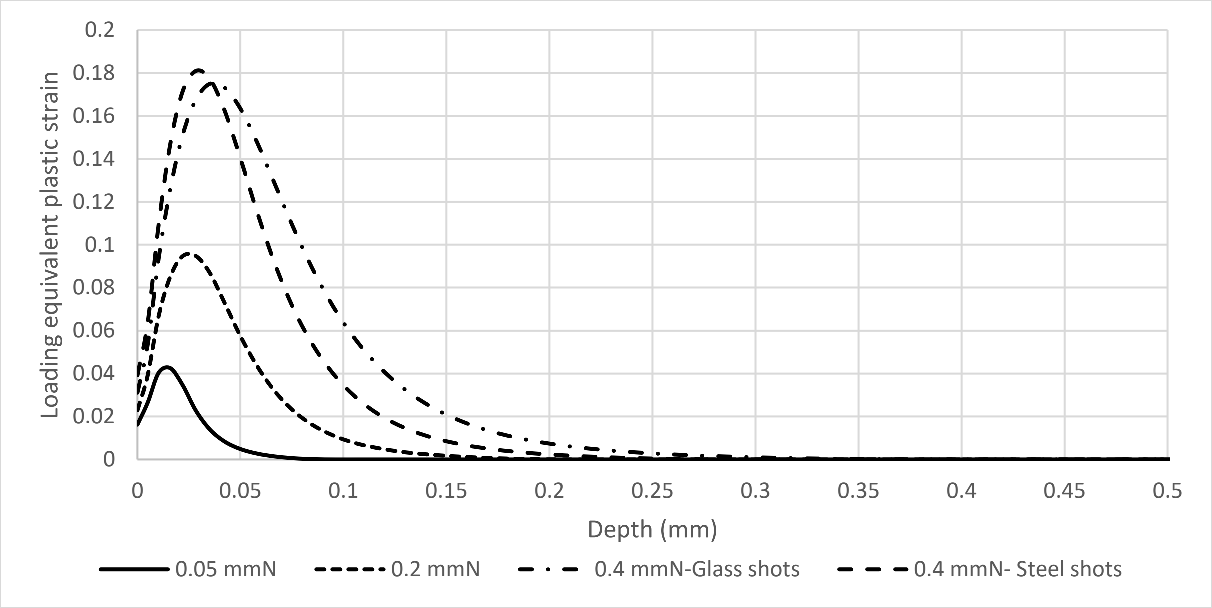

Figure 7.12 Distribution of the equivalent plastic strain through the depth at the end of the loading step in modeling peening under different peening conditions

Figure 7.13, showing the distribution of equivalent stress in elastic-plastic simulation through the depth, follows the patterns described in Figure 7.12. Increasing the intensity leads to get a higher maximum equivalent stress and deeper deformed layer. In the case of peening under 0.4 mmN and according to the shot velocities and diameters, the strain rates when peening with glass shots are a bit higher than the ones when peening with steel shots. Thus, although the maximum plastic strain in peening by steel shots is higher, the maximum equivalent stress in peening by glass beads is a bit higher than when the peening involves steel shots. The same trend for increasing the peening intensity is also visible in Figure 7.14, where the equivalent elastic stresses show higher values when peening happens at higher intensities.

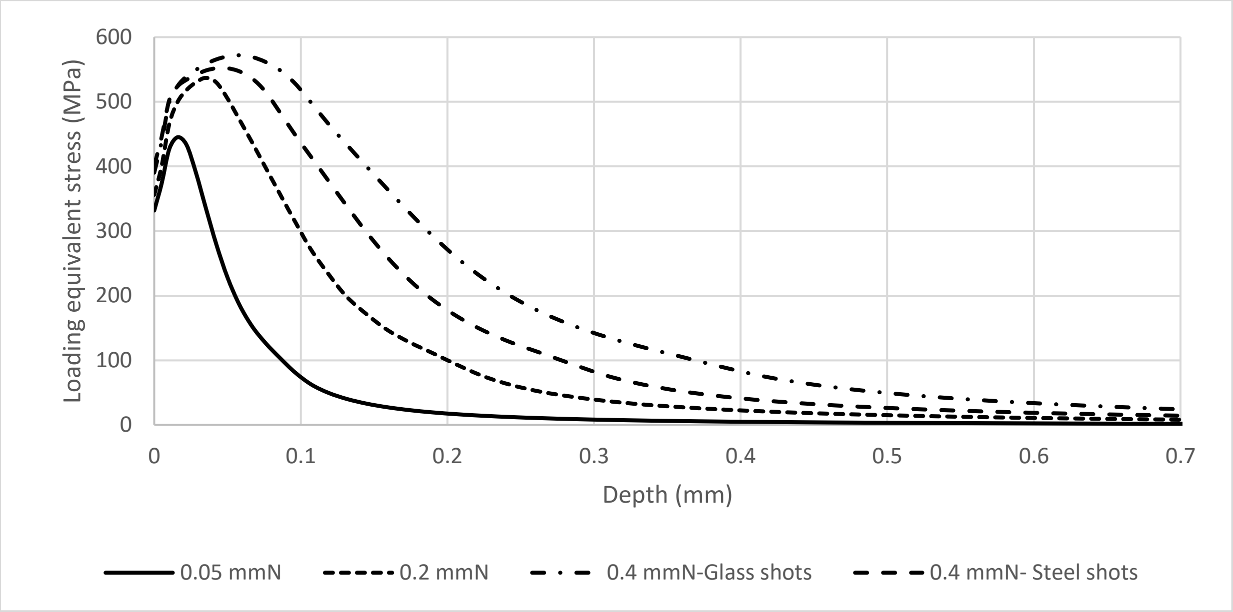

Figure 7.13 Distribution of the equivalent stress through the depth at the end of the loading step in modeling peening under different peening conditions

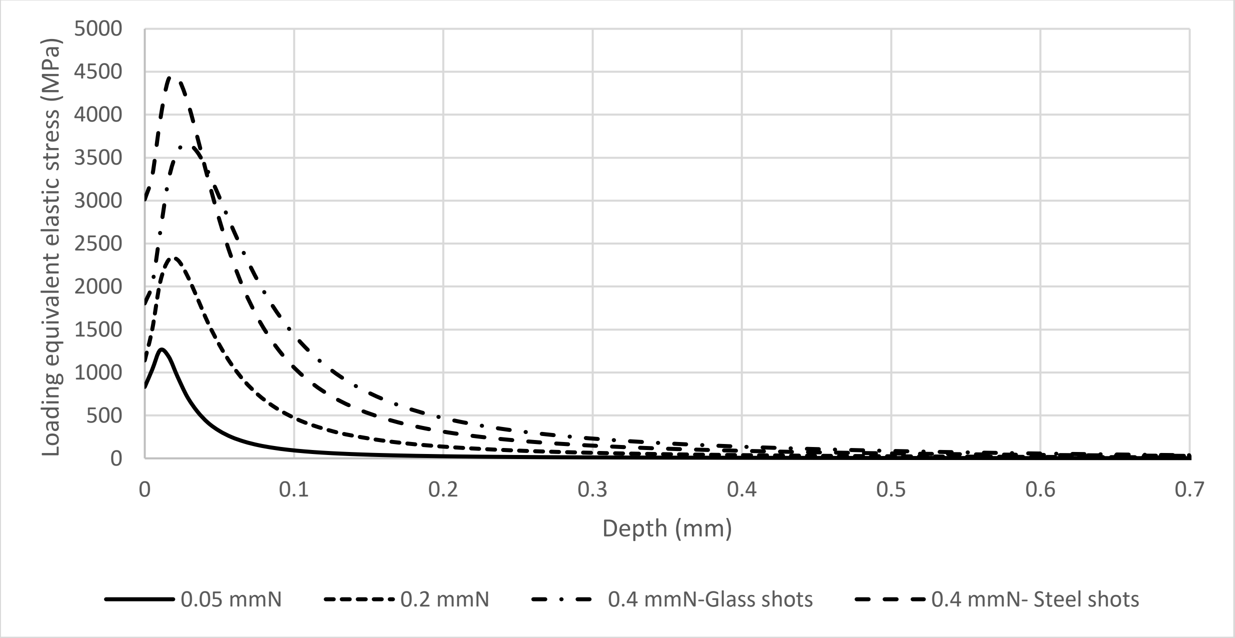

Figure 7.14 Distribution of the equivalent elastic stress through the depth at the end of the loading step in modeling peening under different peening conditions, assuming elastic behavior for the substrate

7.4.2.4 Modeling the residual stress distribution in peening the Mg alloy

Figure 7.15 shows the experimental compressive loading and tensile unloading curves along the ND of the material that are used in modeling the residual stress prediction of peening on rolled sheets. Each element through the depth follows one of these curves, depending on the equivalent plastic strain evaluated in the loading step.

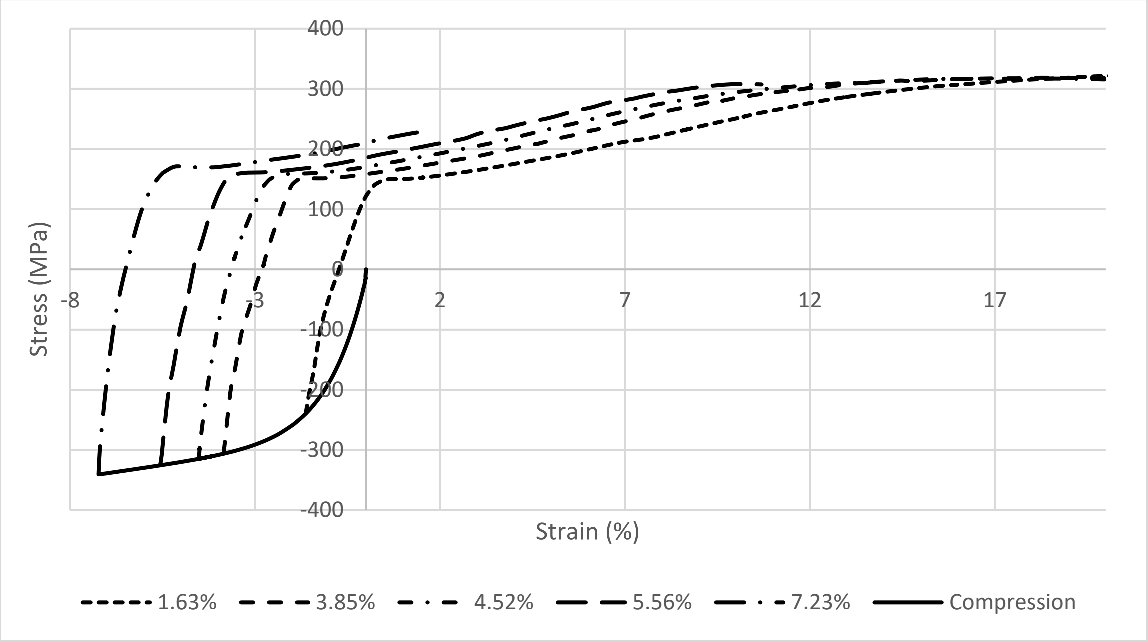

Figure 7.15 The compressive loading and tensile unloading at different strain values along ND

The residual stress profiles through the depth are evaluated analytically by using the results of the loading step obtained numerically for the four peening conditions mentioned in Table 7.3. The experimental hole drilling results have been evaluated for all four peening conditions. Due to a limitation of the hole drilling method, the first experimental data is obtained at 25 micrometers below the depth. Residual stresses have been also measured using the XRD method when the samples are peened at 0.4 mmN using glass and steel shots. Figure 7.16 to Figure 7.19 show the results of residual stress distributions through the depth of the samples peened under the various conditions. Figure 7.16 provides the modeling and experimental data for the peening under 0.05 mmN. The modeling predicts the maximum compressive residual stress to be at the surface (-52 MPa). Due to the low intensity of the peening, modeling predicts a small depth with the compressive residual stress (~100 μm). According to the small compressive residual stress and its shallow depth, the tensile residual stresses are predicted to be less than 3 MPa. In this figure and also under other peening conditions, due to the high rate-sensitivity of the material, and high gradient of stress and strain within a few hundreds of micrometers, and following a different procedure and an unloading path based on the results of the loading step for each element, the modeling data are noisy. Figure 7.16 shows that the modeling results are in good agreement with the experimental data.

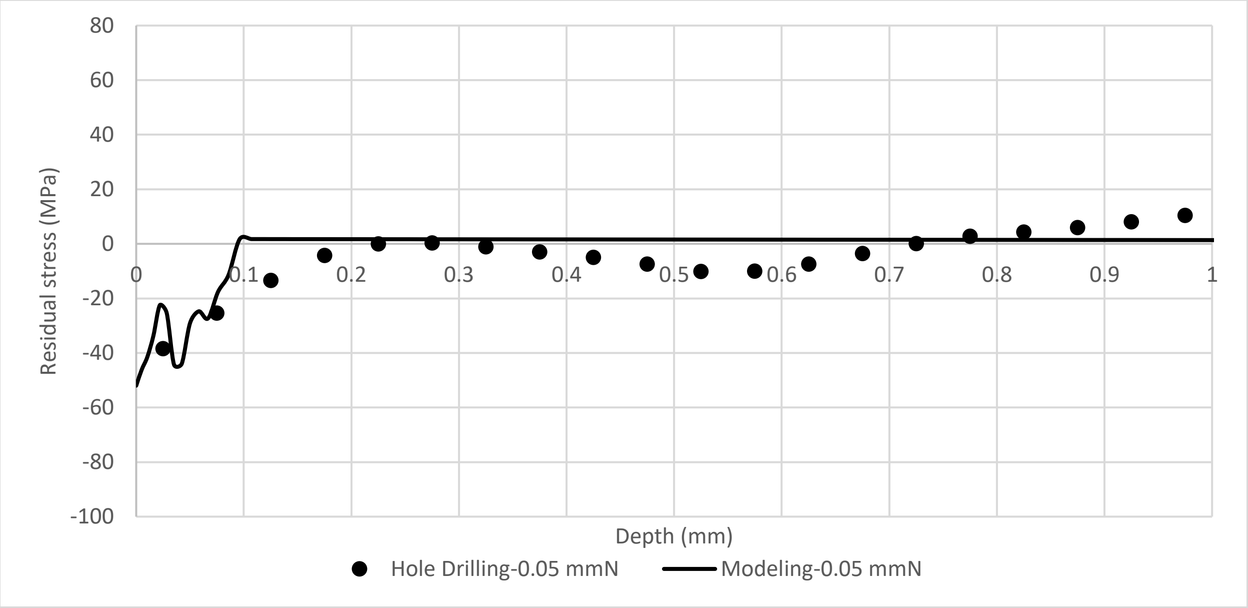

Figure 7.16 Residual stress profile through the depth due to shot peening at 0.05 mmN and comparison with the experimental results of hole drilling method

Figure 7.17 demonstrates the results of the hybrid method for the sample peened under the intensity of 0.2 mmN. It shows that, compared to the results of the residual stress profile of 0.05 mmN, the depth with the compressive residual stress is deeper (225 μm) and the depth of the maximum compressive residual stress shifts toward the underneath layer (100-150 μm) instead of occurring at the surface. In the case of peening at 0.2 and 0.4 mmN, a sudden change of the residual stress is visible within the first 50 μm, and modeling predicts the reason to be related to the high rate-sensitivity of the material and the existence of a high strain rate within this layer. In addition, modeling shows that as the material is significantly rate-sensitive, the friction coefficient plays an important role in the prediction of residual stress within the first 50 μm sub-surface. The difference between the modeling and experimental results in this thin layer may also contribute to the surface damage within this layer. As shown in Chapter 5, the surface is significantly damaged, and cracks start to initiate after the intensity of 0.075 mmN. Thus, the residual stresses start to disappear within this layer, while the modeling ignores the effects of surface topography and damage. Further discussion about the first 50 μm is provided in the discussion section. Figure 7.17 shows that the experimental results match well with the modeling ones after the first 50 μm, including in prediction of the maximum residual stress, its associated depth, and the depth of the compressive-induced residual stress.

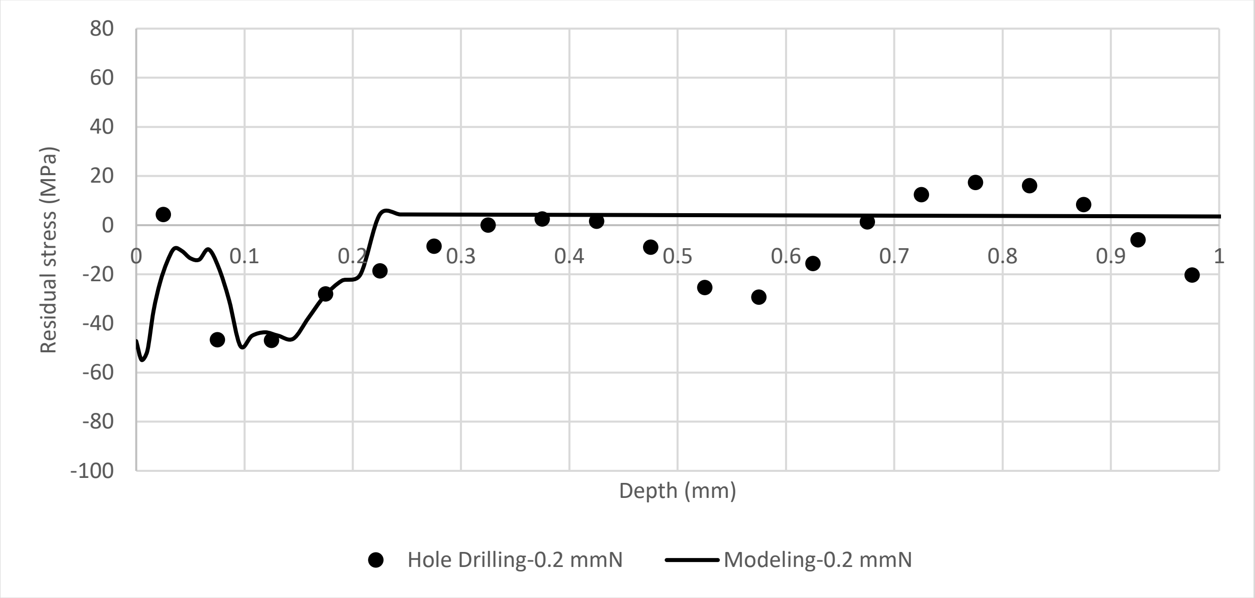

Figure 7.17 Residual stress profile through the depth due to shot peening at 0.2 mmN and comparison with the experimental results of hole drilling method

Figure 7.18 and Figure 7.19 show the residual stress distribution of the samples peened under 0.4 mmN, using glass and steel shots, respectively. In both cases, due to higher peening intensity, the depths of the plastically deformed layers and the depths with the compressive residual stresses are higher than when the sample was peened at 0.2 mmN. In addition, the maximum compressive residual stresses are higher than the ones at the lower intensities. In addition to the hole drilling results, the authors have evaluated the experimental results using the XRD method in these two cases. Similar to the peening under 0.2 mmN, the modeling results follow the experimentally measured residual stresses in all the important parameters, except those at the surface layer, whose possible reasons were discussed.

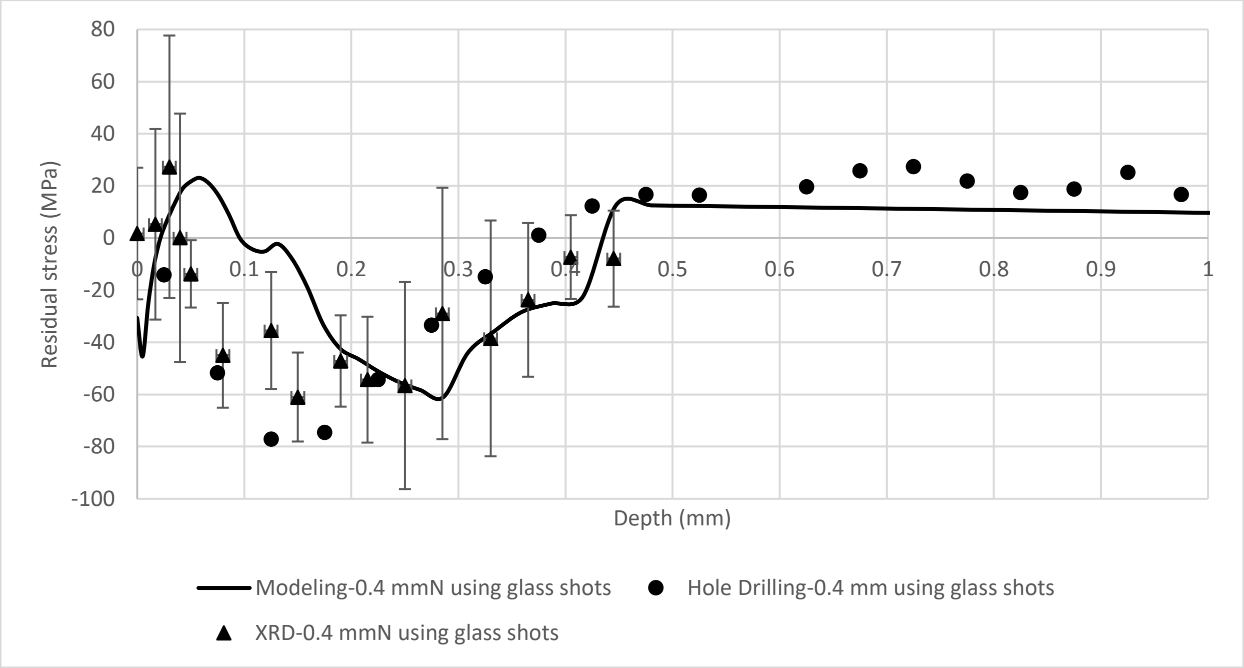

Figure 7.18 Residual stress profile through the depth due to shot peening at 0.4 mmN using glass shots and comparison with the experimental results of hole drilling method and XRD method

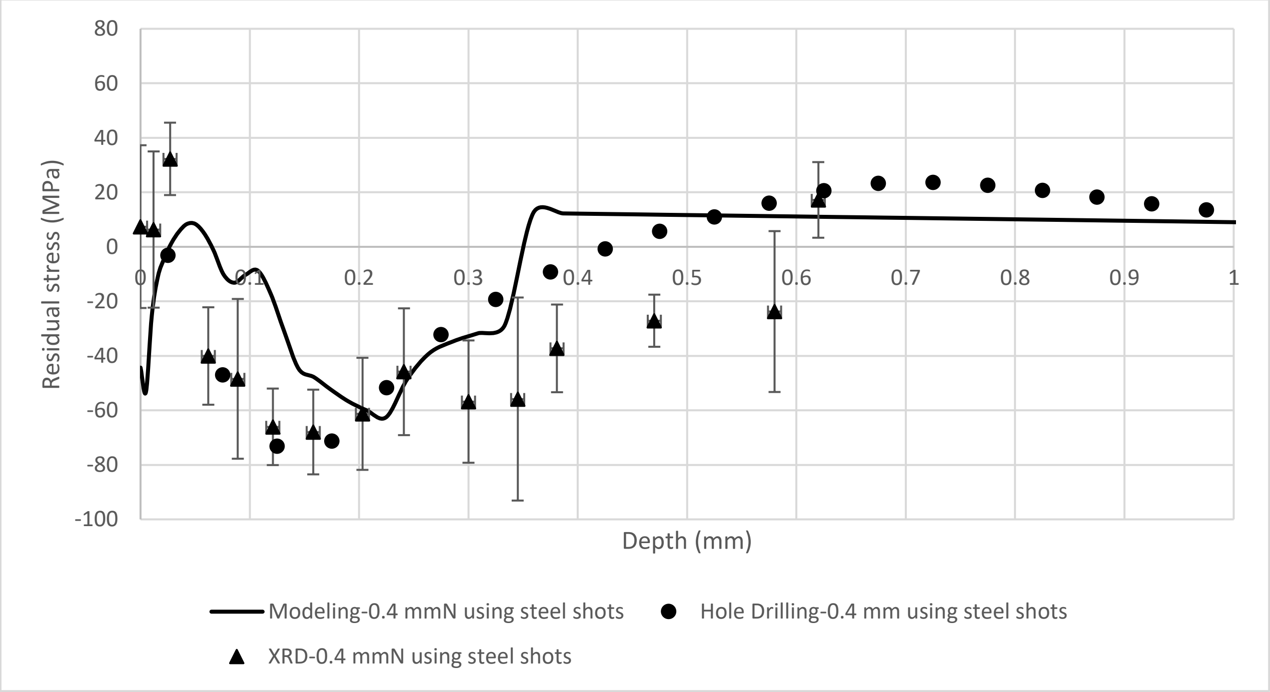

Figure 7.19 Residual stress profile through the depth due to shot peening at 0.4 mmN using steel shots and comparison with the experimental results of hole drilling method and XRD method

7.5 Discussion and sensitivity analysis

This section discusses the effects of different parameters on the residual stress evaluation due to the peening of AZ31B-H24. From the four peening examples, peening under 0.4 mmN using steel shots has been used for the sensitivity analysis, except during sensitivity analysis on the effect of friction coefficient, for which the example of peening under 0.05 mmN has been added.

7.5.1 The effect of material’s rate-sensitivity

In this section, the significance of considering the effects of strain rate on the stress-strain curve of the material is discussed. Figure 7.20 shows the experimental residual stresses and the modeling results with and without considering the strain rate effect. Due to the high rate-sensitivity of the material, the residual stress prediction when ignoring the rate effects is significantly different from the experimental results and from the modeling, when the rate effects are considered in the modeling. In the first 200 micrometers below the surface where the material is plastically deformed (Figure 7.12), the results of the modeling are different.

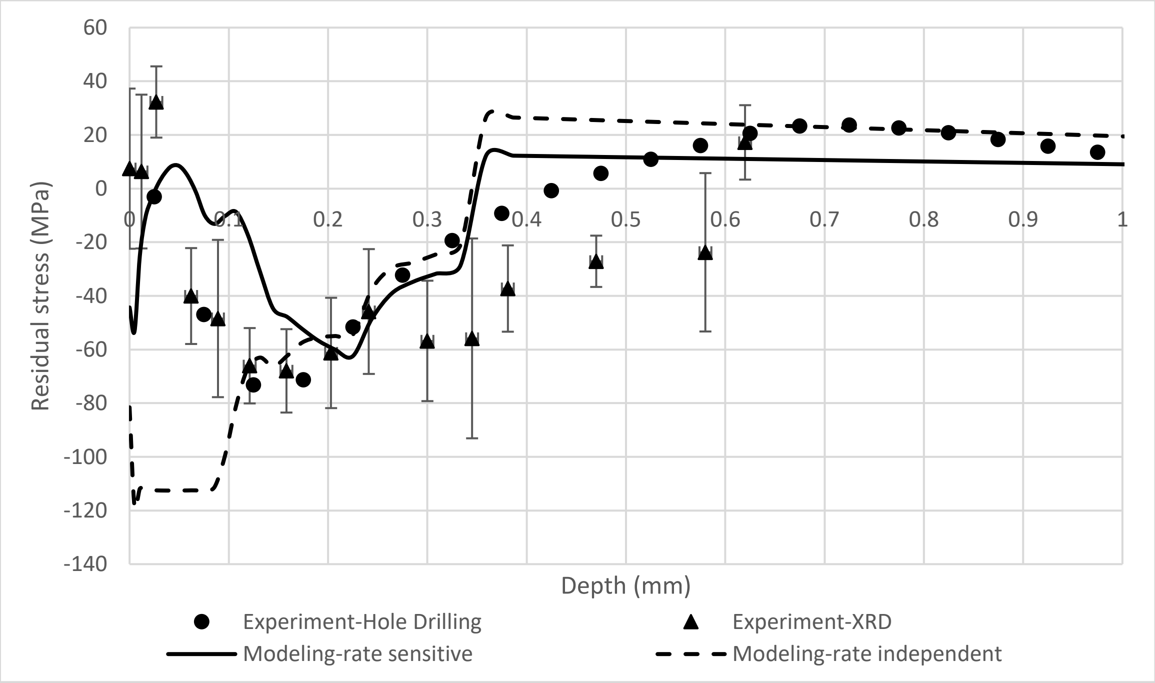

Figure 7.20 The effects of material’s rate sensitivity on the predicted residual stress profiles through the depth due to shot peening under 0.4 mmN, using steel shots and comparison with the experimental results of hole drilling method and XRD method

7.5.2 The effect of friction

To discuss the residual stress prediction's sensitivity to the friction coefficient, first, the residual stresses are evaluated using the friction coefficients of 0, 0.12, and 0.2 for two peening examples, peening under 0.05 mmN using glass shots and peening under 0.4 mmN using steel shots. These two examples have been selected as in one of them (peening at 0.05 mmN), the predicted residual stresses are in a good agreement with the experimental data within the first 50 micrometers below the surface, and in the other one (peening under 0.4 mmN), the predicted residual stresses and the experimental data differ within this layer. Figure 7.21 and Figure 7.22 show the results of residual stress distribution for the cases of peening under 0.05 mmN and 0.4 mmN, respectively. As shown in these figures, the friction coefficient significantly affects the residual stresses at the surface of the material.

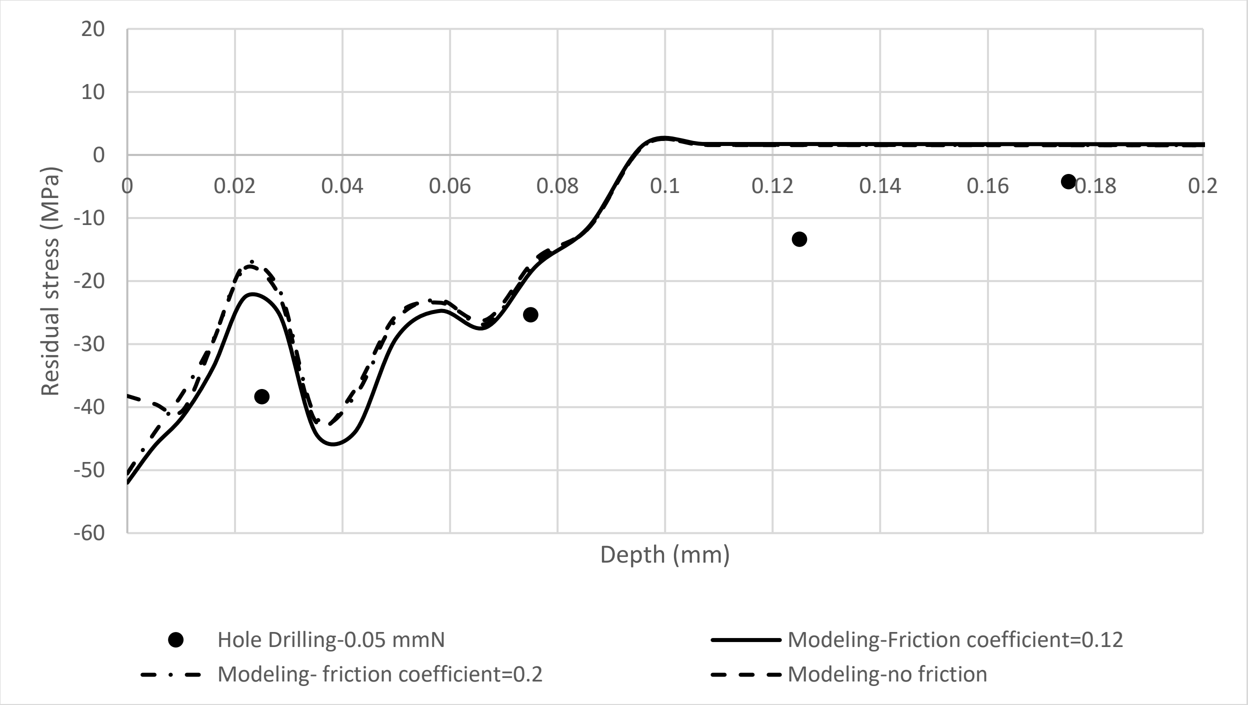

Figure 7.21 The effects of friction coefficient on the predicted residual stress profiles through the depth due to shot peening under 0.05 mmN, using glass shots and comparison with the experimental results of hole drilling method

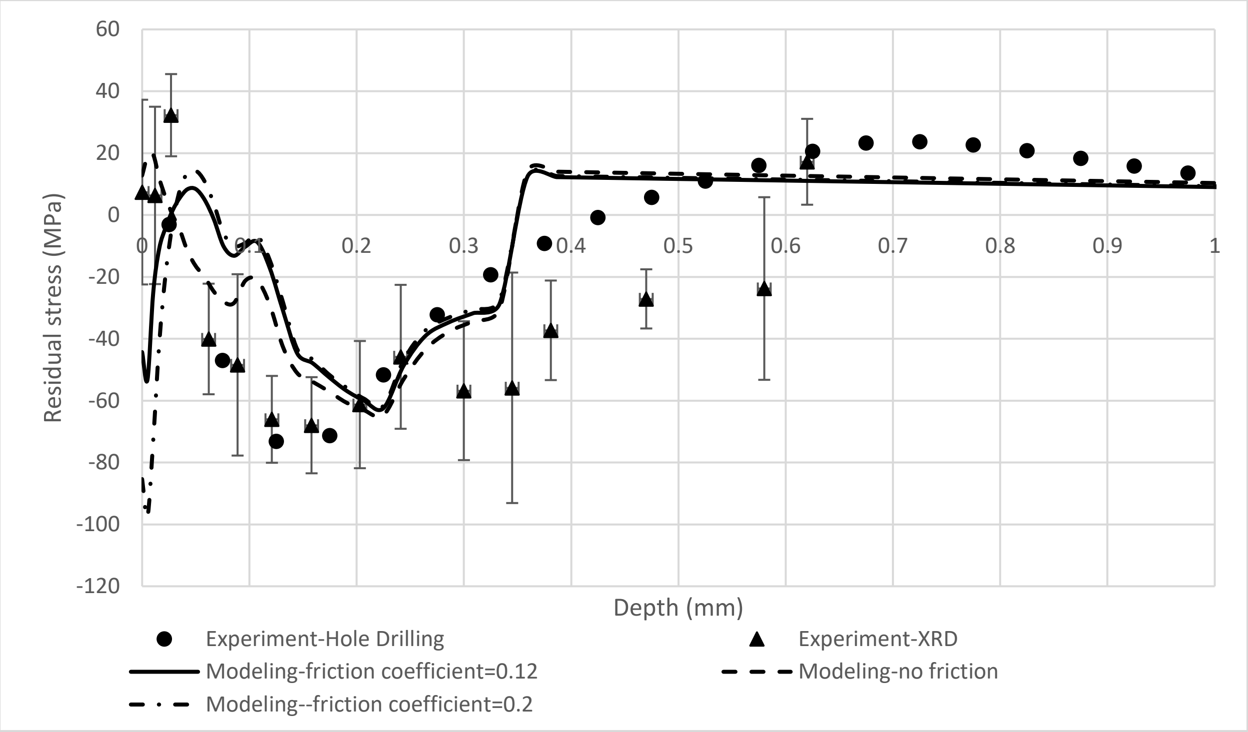

Figure 7.22 The effects of friction coefficient on the predicted residual stress profiles through the depth due to shot peening under 0.4 mmN, using steel shots and comparison with the experimental results of hole drilling method and XRD method

In the case of peening on AZ31B, as the material's sensitivity to strain rate is significant, and shows significant hardening after the initial yield, a change in the friction coefficient leads to a high difference in the estimation of equivalent stresses, which consequently changes the residual stresses.

7.5.3 The effect of material's unloading behavior

To determine the effect of employing the actual unloading curves of the material, the residual stress distributions modeled by assuming isotropic hardening and kinematic hardening have been obtained. Figure 7.23 confirms the significant contribution of considering the actual unloading behavior in modeling the residual stress distribution through the depth. Assuming isotropic or kinematic hardening for this material significantly changes the residual stress prediction, whereas considering the actual CT curves along ND as the material's loading-unloading behavior leads to results much closer to the experimental data.

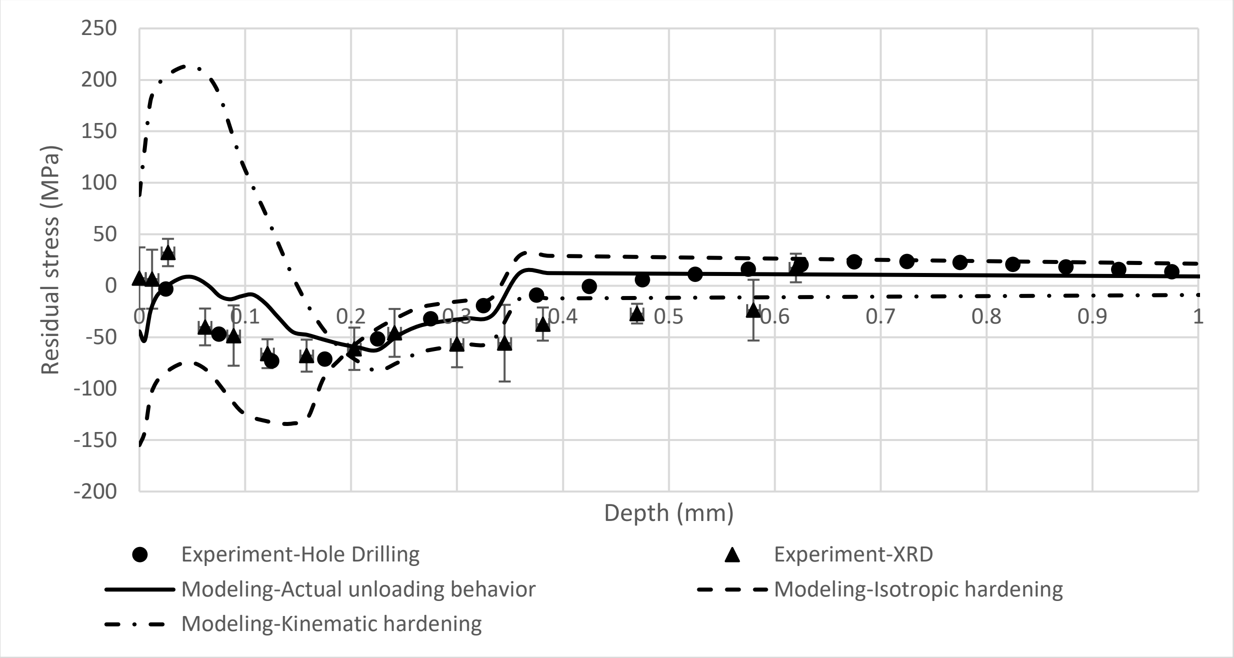

Figure 7.23 The effects of material's unloading behavior on the predicted residual stress profiles through the depth due to shot peening under 0.4 mmN, using steel shots and comparison with the experimental results of hole drilling method and XRD method

7.5.4 The effect of using the properties of the appropriate material's direction

It was shown that the loading-unloading behavior of the peening process can be assumed to be the CT along a direction in which the shots have impinged. In this section, the residual stresses are evaluated using the CT along RD. Figure 7.24 shows the CT curves of the material tested in RD.

Zhao et al. [207] also did experiments to obtain the flow curves of AZ31B-H24 at different strain rates in compression along RD of the sheet. In this present work, similar to the procedure in ND, the strain rate effect on the compression behavior of AZ31B-H24 along RD was obtained by assuming the same ratio of the stress value at a high strain rate to the stress at the quasi-static condition at each plastic strain. Thus, equation 7.10 is used to generate the material behavior of AZ31B-H24 at high strain rates along RD.

$$\sigma_{C-RD}^{AZ31B-H24}\left(\bar{\varepsilon}_p,\dot{\varepsilon}_p\right)=\frac{\sigma_{C-RD}(\bar{\varepsilon}_p,\dot{\varepsilon}_p)}{\sigma_{C-RD}(\bar{\varepsilon}_p,\dot{\varepsilon}_p=0.001\ 1/s)}\sigma_{C-RD}^{AZ31B-H24}\left(\bar{\varepsilon}_p,\dot{\varepsilon}_p=0.001\ 1/s\right) \qquad (7.10)$$

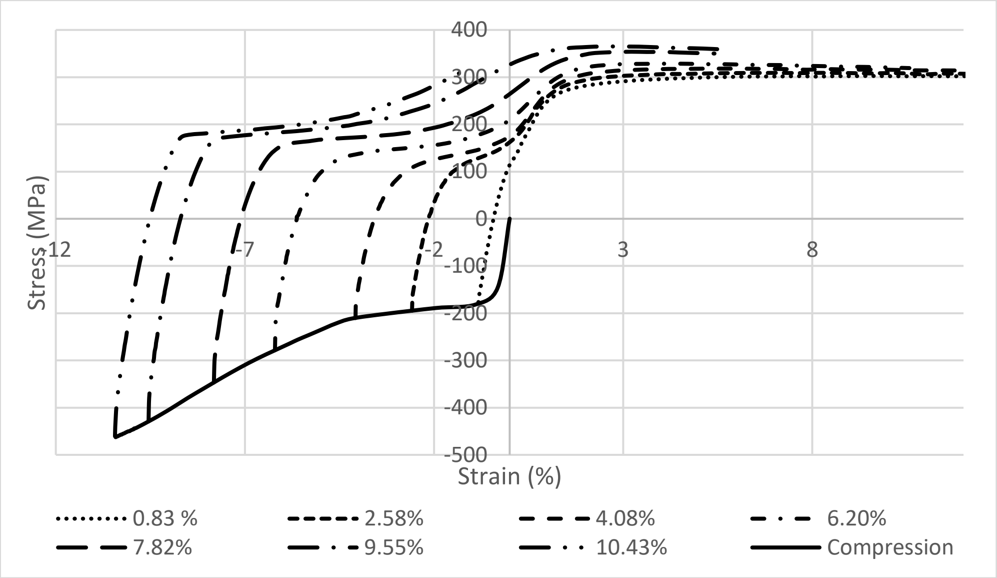

Figure 7.24 The compressive loading and tensile unloading at different strain values along RD

Figure 7.25 and Figure 7.26 show the residual stress profiles predicted by the hybrid method, when using the properties along RD, for the examples of peening under 0.05 and 0.4 mmN, respectively. These figures also provide the predicted residual stresses when the ND properties are used for the modeling, plus the experimental values as shown in Figure 7.16 and Figure 7.19 to help understanding the significance of using the appropriate material properties for modeling the peening process. The residual stresses when RD and ND properties are used differ significantly, as their compression behavior, rate-sensitivity and unloading behavior have numerous differences.

The figures show that in both cases, the compressive residual stresses at the surface layer and also the maximum compressive residual stresses are larger when the RD's properties are used. However, due to the higher yield stress in RD, the depth of the plastically deformed layer and consequently the depth with the compressive residual stress are shallower when the RD properties are used.

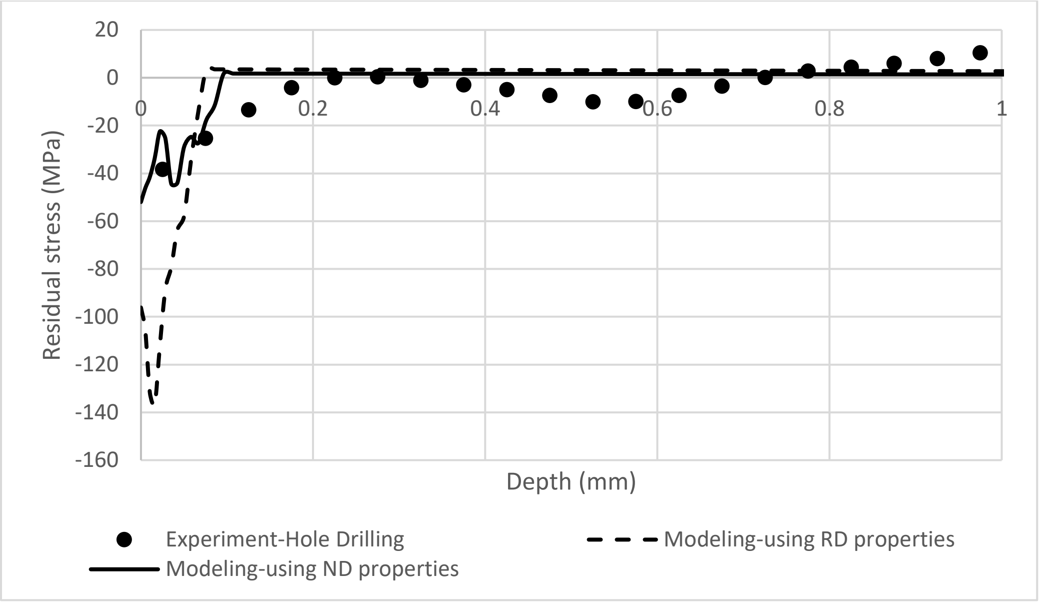

Figure 7.25 The predicted residual stress profiles through the depth due to shot peening under 0.05 mmN, using CT curves in RD and ND and comparison with the experimental results of hole drilling method

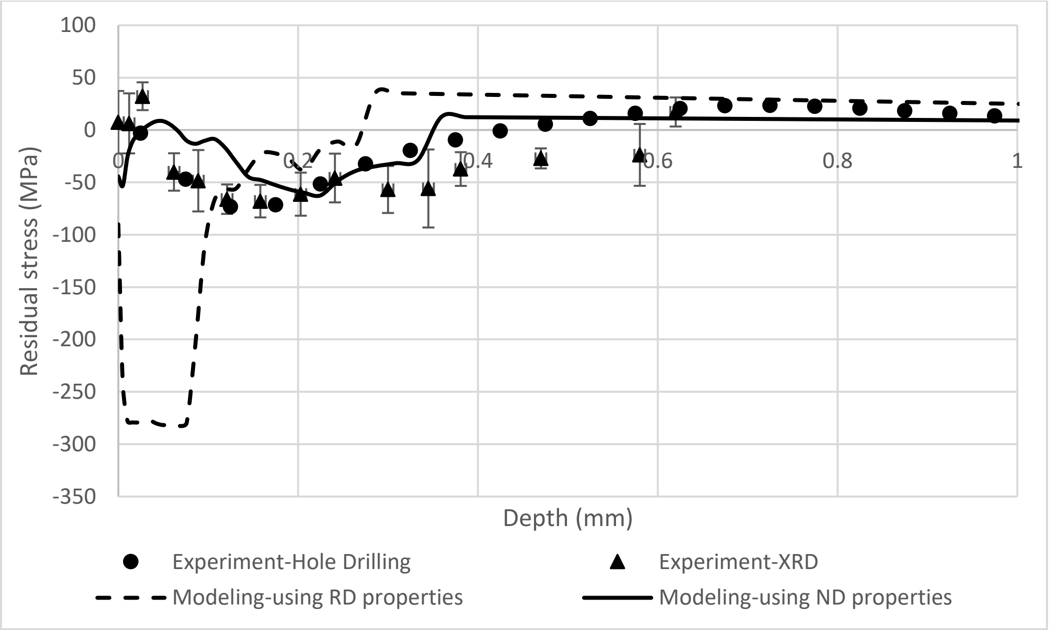

Figure 7.26 The predicted residual stress profiles through the depth due to shot peening under 0.4 mmN, using CT curves in RD and ND and comparison with the experimental results of hole drilling method and the XRD method

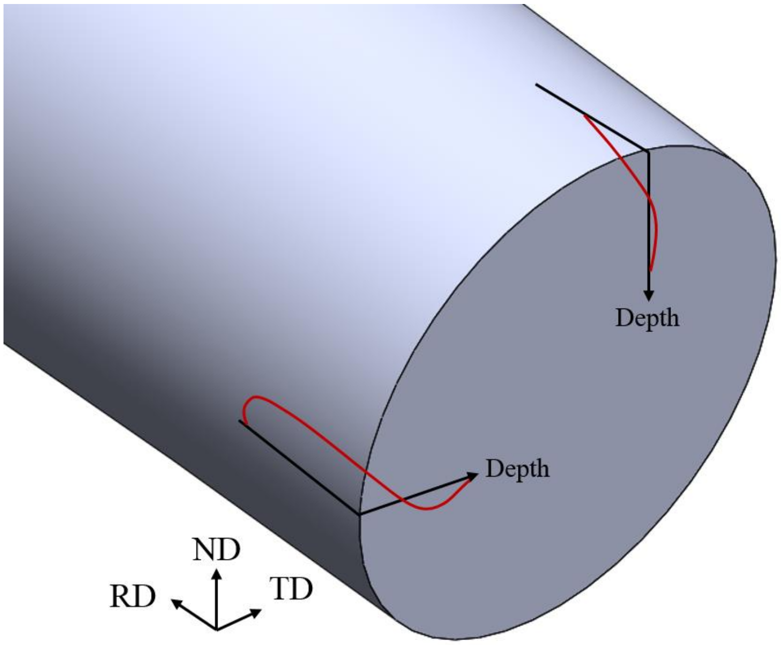

Figure 7.27 Schematic view of the predicted residual stresses in RD for the areas peened under 0.05 mmN along ND and TD

Figure 7.27 schematically shows the residual stresses induced in the RD for areas peened along the ND and TD. The hybrid method predicts that the residual distribution when TD properties are employed can be estimated as the induced residual profile when the sample is peened along TD (here, the TD properties are the same as RD ones). Thus, the predicted residual stress profile when using TD properties has assigned to the area peened along TD in Figure 7.27. Although a better approximation would be provided when a general solution for the anisotropy of the substrate in all directions is developed, as in the example of peening along TD, the in-plane properties (RD and ND) differs and the material is not in-plane isotropic. These findings can be verified experimentally. The first experimental verification is the residual stress measurements at the surface of the samples peened at different intensities along different directions, using XRD (Figure 7.28). This figure shows that the material has more compressive on-average residual stresses when the samples are peened along TD, which has the same properties as RD. The term on-average is used in this part because as mentioned in Chapter 3, respectively, 50% and 90% of the exposed x-rays are diffracted from the surface up to 36.2 μm and 126.8 μm through the depth.

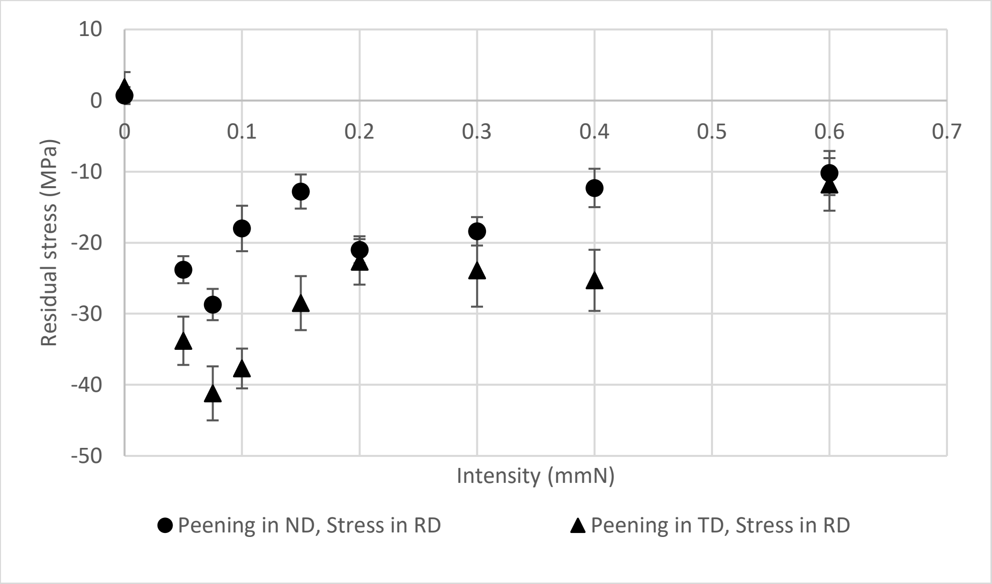

Figure 7.28 The on-average residual stresses measured at the surface of the peened samples along ND and TD

The second experimental verification for the higher compressive residual stress involves crack initiation areas in the rotating bending samples, in which some areas are peened along ND, and some areas are peened along TD. Fractography of the fracture surface revealed that more than 90% of the crack initiation zones are located close to the areas peened along ND. As these areas' compressive residual stresses are lower than the ones peened along TD, the cracks are initiated there.

7.5.5 The texture evolution and its prediction by the hybrid method

The hybrid method explained that the peening loading-unloading process can be modeled by the compression-tension of the sample in the peening direction. In addition, as mentioned in equation 7.2, when the material yields in the unloading phase, the final plastic strain of the unloading phase is equal to the plastic strain obtained in the loading step. The stress-strain behavior of the material required for modeling the residual stress distribution when peened along ND is shown in Figure 7.29. It shows the CT curves of the same material in ND in the negative strain values. The CT curves along ND predict the slip deformation in compression during the loading phase or penetration of a shot in the material, followed by the twinning during the unloading or rebounding of the shots from the surface. On the other hand, and as shown in Figure 7.12, higher peening intensity leads to higher plastic strain in the loading step of the peening, so the twinning in the unloading step would be greater, causing more grains to tilt from the ND toward the in-plane directions. Thus, the strongest basal texture along ND is expected in the as-received sample, and as the peening intensity increases, the texture randomizes more and the c-axis tilt more from the ND to the in-plane directions. Figure 7.30 shows the texture evolution of the as-received and peened samples under different intensities. The initial texture shows that the strong basal orientation is aligned in ND; however, the peening rotates the c-axis from ND and randomizes the texture. As the peening intensity increases, the maximum texture intensity decreases, meaning more and more grains have a basal texture perpendicular to the ND as the intensity increases. Thus, the experimental results are compatible with the prediction of the hybrid method regarding the loading-unloading state of the material.

To support the predictions of the hybrid method, the samples were also peened normal to the cross-section of the sheet, meaning the peening was done along TD. During the compression-tension of the material in TD, twinning happens both in compression, during the loading phase, and also in tensile unloading. Figure 7.31 shows the CT curves of the same material in RD. As the material is in-plane isotropic, the CT behavior in TD is assumed to be the same for the RD. This figure shows the twinning deformation during the compression and de-twinning during the following tension. Thus, predicting a trend for the texture evolution after the peening is difficult. Figure 7.32 shows the texture evolution during the peening in TD, demonstrating that no trend is predictable for the texture evolution after peening in this direction. Again, this finding is compatible with the texture evolution during compression-tension of the material in TD.

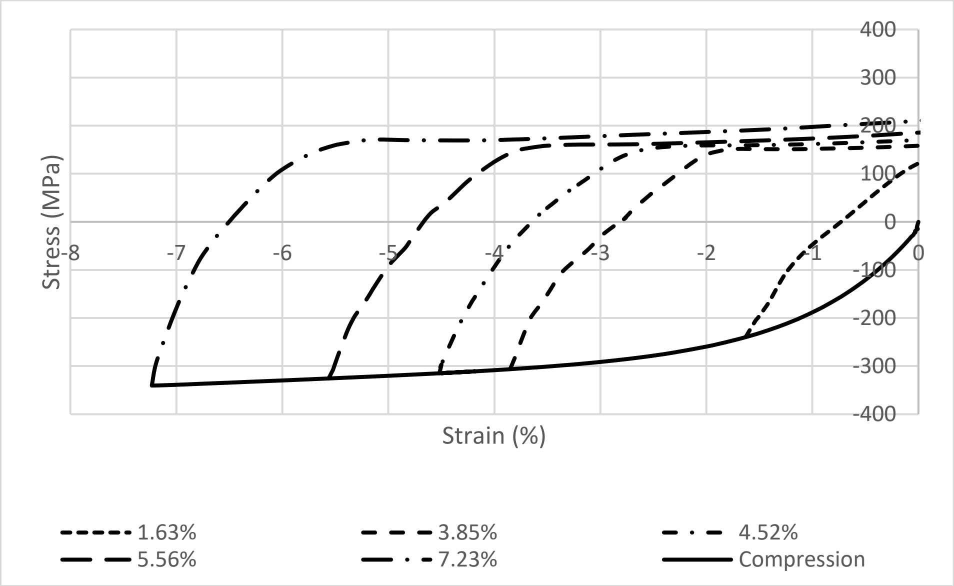

Figure 7.29 CT curves of AZ31B rolled sheet in ND

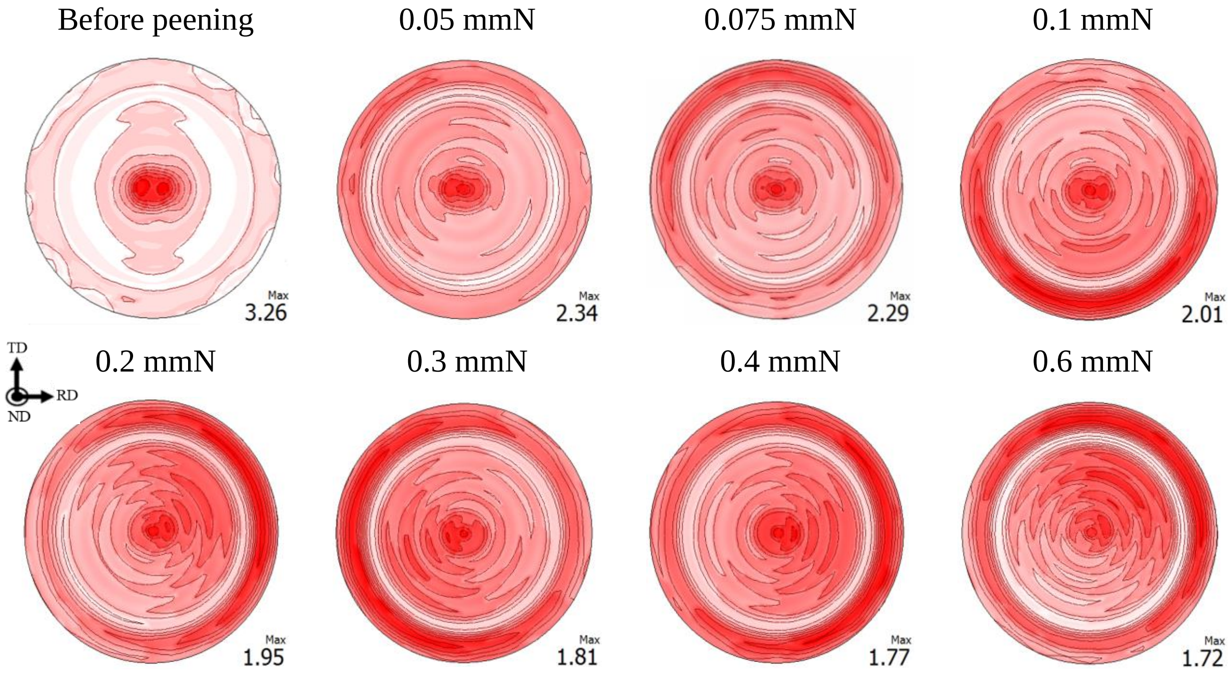

Figure 7.30 Texture evolution of the flat samples, peened in ND

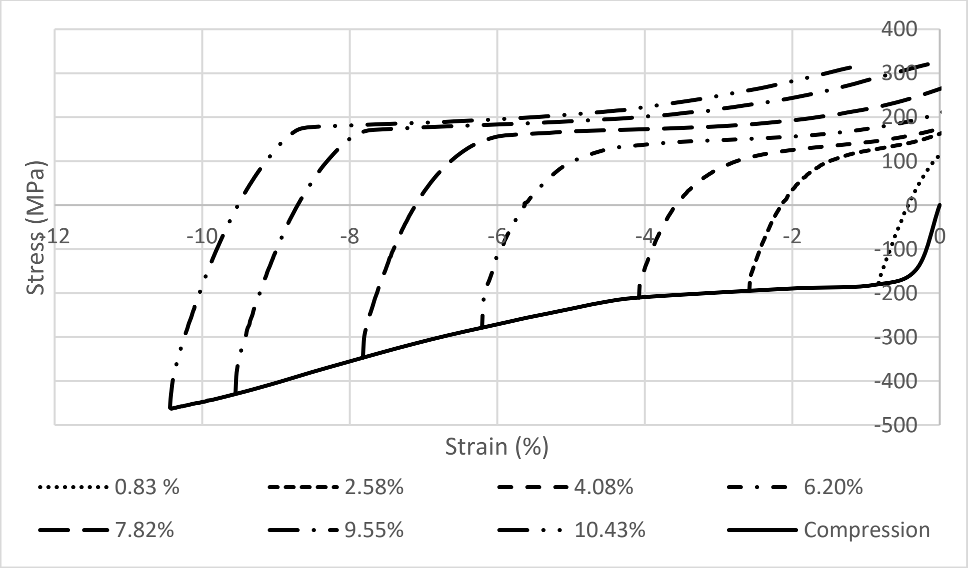

Figure 7.31 CT curves of AZ31B rolled sheet in RD

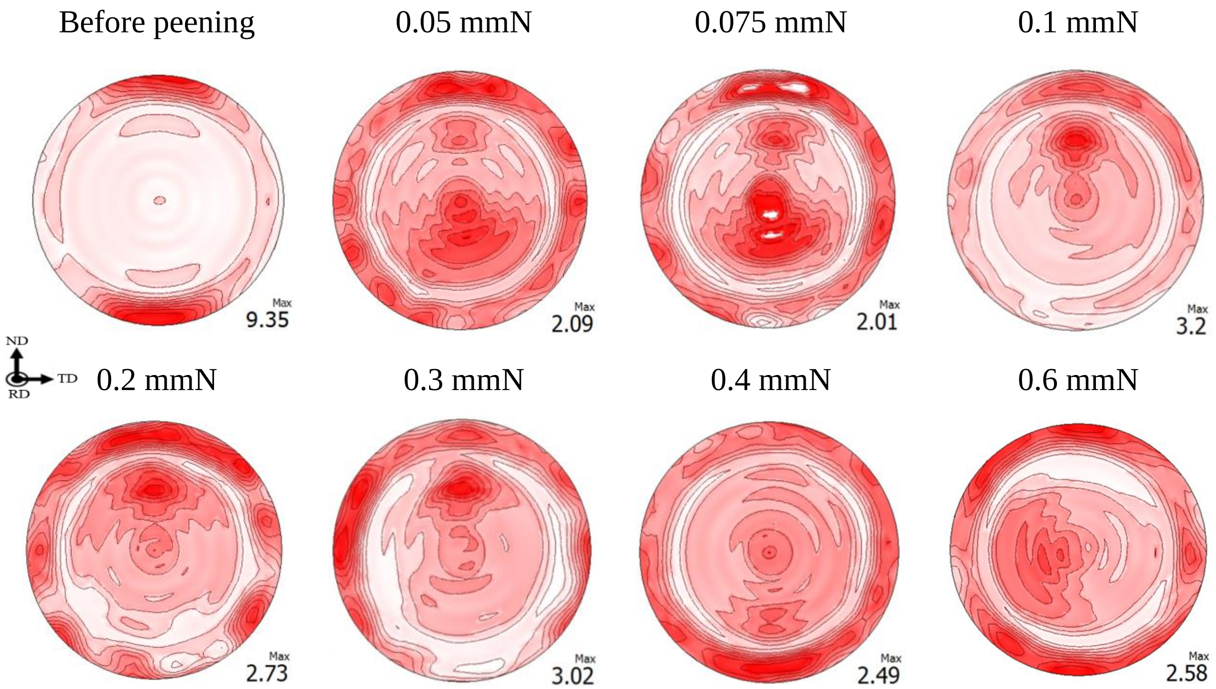

Figure 7.32 Texture evolution of the flat samples, peened in TD

Conclusion

The hybrid numerical-analytical modeling of the shot peening process was extended to model the residual stress distribution of Mg alloys, asymmetric and anisotropic materials, with significant rate-dependency and a complex unloading behavior. The results confirmed that the material's asymmetric and anisotropic behaviors do not play a role in modeling the shot peening process when the compression-tension behavior of the material along the peening direction is used for modeling. The residual stress results of the material peened under different intensities confirmed that the prediction of residual stress using the hybrid method adheres well to the experimental measurements. For the lowest intensity, 0.05mmN, the hybrid method follows the experimental data well. However, at higher intensities, the predicted residual stresses differ from the experimental values only at the first 50 μm from the surface, perhaps because the surface is damaged and the residual stresses have vanished. Through the different sensitivity analyses and experimental studies presented in this paper, the following conclusions can be made:

1- The actual unloading behavior has a significant role in the distribution of residual stress through the depth of the material.

2- Due to the high level of the material’s rate-dependency, incorporating the strain rate affects the residual stress distribution in the vicinity of the surface layer.

3- Friction plays a significant role in residual stress prediction at the surface layer of peened Mg alloys.

4- The results of using the properties along RD in the case of peening along ND prove that the predicted residual stresses differ significantly from the experimental values, confirming the accuracy of considering the compression-tension along the peening direction as a material behavior required for the modeling.

5- The texture evolution of the peened samples under different intensities and in different directions justifies the accuracy of the loading-unloading state used in the hybrid method.

Chapter 8

Conclusions and Future Works

8.1 Conclusions

The research supports the following conclusions:

1. As in contrast to steel and aluminum, Mg alloys have a low x-ray mass attenuation coefficient, x-rays penetrate Mg alloys deeply. In this case, applying the stress correction factors is critical, especially where there is a high stress gradient in the surface layer of the material.
2. Due to the low mass attenuation coefficient of Mg, the uncertainty of the corrected residual stress is high. This high uncertainty should always be considered when using x-ray diffraction (XRD) on materials with a low x-ray absorption coefficient, such as Mg alloys.
3. The differences between the observed (before correction) residual stresses and corrected ones were mainly within 40 micrometers of the surface, where the micro-cracks release the residual stresses, even though the observed measurements fail to confirm this fact. Grazing incidence x-ray diffraction (GIXD) method and surface topography did confirm that residual stresses vanish within the first 30-40 micrometers from the surface.
4. Results of the corrected residual stress measurements taken through the depth using 2D-XRD were in a good agreement with the results of the hole-drilling method.
5. Shot peening generates large plastic deformations on the substrate as the shots impact the material. Thus, obtaining the large-strain loading-unloading behavior of the material is necessary when modeling this process. During the compression tests in the rolling direction (RD), the negligible effect of using anti-buckling was confirmed by comparing the results with those from the compression of cubic samples.
6. A novel custom fixture and a specimen geometry were designed to obtain the compression-tension (CT) and tension-compression (TC) curves of a sample with a total length of 6.1 mm. The accuracy of the results obtained by the new method was confirmed by employing the new experimental set-up to evaluate the CT and TC behaviors in RD, for which the results of using an anti-buckling fixture were available for comparison. This fixture enables researchers to do cyclic testing in the normal direction (ND) of plates, having a small thickness.

7. The results of CT and TC in RD and ND reveal both the anisotropic and asymmetric behaviors of the AZ31B-H24 rolled sheet. Modeling the unloading behavior of the material requires using actual complex properties and so cannot be done using simplified isotropic or kinematic hardening.
8. Conducting the peening on AZ31B-H24 under different intensities reveals that small on-average comprehensive residual stresses (>-30 MPa) at the surface layer of up to around 130 μm are induced during peening under all intensities. Peening at 0.05 and 0.075 mmN intensities induces the maximum on-average compressive residual stress in the surface layer.
9. Residual stress distributions through the depth reveal the fact that as the peening intensity increases, the depth of the maximum compressive stress and the depth of the induced compressive residual stress layer increase, but the induced compressive residual stress at the surface is maximum at the 0.05 mmN.
10. It is found that the higher the intensity, the higher and deeper the hardness of the surface layer, also the higher R_a and R_z.
11. The peening randomizes the texture in the surface layer due to the twining.
12. Shot peening on AZ3B-H24 clearly shows an over-peening effect where the optimum intensity is 0.05 mmN. The deteriorated surfaces cancel out the beneficial effect of compressive residual stress, causing fatigue life to decrease at higher intensities. Peening at optimum intensity increases the endurance limit of the material by 15%. The fractography of the fracture surfaces reveals that cracks are initiated where the second phases are present in the surface layer of the material.
13. The fully analytical modeling of the peening process fails to consider the effects of the actual stress-strain behavior of a material, friction, and strain rate in the loading step of the shot peening process. On the other hand, FEM modeling of shot peening is computationally expensive, and it is complicated to model the actual unloading behavior of complex materials such as Mg alloys. In this thesis, a new hybrid analytical-numerical method is proposed that predicts the residual stress distribution more accurately and easily than earlier methods. This new method was shown to provide a general solution that accounts for the actual loading-unloading behavior of a material, plus the effects of the strain rate and friction. Before the hybrid method was applied in modeling the residual stress in Mg alloys, the method was verified by peening on steel and aluminum alloy examples. Comparing the results of the hybrid method with the available experimental measurements for these two alloys shows that this hybrid modeling provides more-accurate residual stress distribution prediction through the depth of the materials.
14. Using the FEM method showed that the loading state of the shot peening can be assumed to be the same as the loading state in the compression-tension of the material in the shot peening direction. Thus,

if shots hit the substrate vertically, the compression-tension in the normal direction of the plate would be the loading state. Thus, the residual stress distribution induced during the peening of the AZ31B-H24 rolled sheet was modeled using the hybrid model while considering the CT behavior of the material in ND. The texture evolution during the peening under different intensities supports the assumed loading state. In addition, The hybrid method predicts the higher residual stress at the surface layer when the sample is peened along RD or TD compared to the along the ND. The results of the fatigue tests, using rotating bending samples, reveal that in the majority of the samples, the cracks are initiated and grows along ND of the sheet.

15. Using the hybrid method confirmed that considering the strain rate, friction, and actual unloading behavior of the material significantly affects the residual stress prediction. It is also concluded that using the appropriate loading-unloading direction is anisotropic and asymmetric materials play an important role in residual stress modeling.
16. The predicted residual stress distributions through the depth of AZ31B under four different peening conditions follow the experimental results of the XRD and the hole drilling. The hybrid method fails to model the residual stresses at the first 50 μm from the surface at high intensities which could be attributed to the surface deterioration/cracking in those intensities, while in the lower one, 0.05 mmN, the predicted residual stress at the surface layer follows the experimental measurement.

8.2 Thesis Contributions

This research work has produced the following major contributions:

1- Methodology for Mg residual stress measurement using X-ray diffraction

2- Optimum peening of AZ31B sheet for maximum fatigue life, and characterization of different effects of peening on the material, including evaluation of residual stress, surface roughness, hardness, texture, and finally the fatigue life for samples peened under different intensities.

3- A Novel test methodology for obtaining the cyclic response of short samples with application for properties in the thickness directions of relatively thin sheets.

4- A novel computationally cost-effective and high-fidelity hybrid method for peening process modeling, incorporating strain rate, friction, and actual loading/unloading behaviors

5- Extension of the proposed hybrid method to model asymmetric and anisotropic materials that also have complex unloading behavior, such as the Mg alloys.

The novel findings of this research have been documented in the form of five journal papers either submitted or ready to be submitted to internationally renowned journals in the field of experimental mechanics and modeling and designs.

8.3 Future work

In continuation of the presented research, recommendations for future research directions are given next.

1. As shot peening modeling requires data on the high strain rate behavior of a material, experimental investigations are needed on the compression-tension behavior of materials at high strain rate, plus evaluation of the effect of loading strain rates on the unloading behavior of materials. Such characterization plays an important role in modeling the residual stress distribution through the depths of materials.

2. This study discussed the anisotropic properties of the rolled sheet between rolling direction and normal direction; however, the material was assumed to be isotropic between rolling and transverse directions. Conducting research to address the anisotropic behavior of a material in all directions would be valuable. Such a modeling method would act as a general method for modeling the residual stress in shot peened samples.

3. Predicting fatigue life and finding the optimum peening intensity have been valuable, as it reduced the cost of experimental research. It would also be useful to combine the modeling of the residual stress distribution, surface roughness, and hardness evaluation through the depth so as to obtain the fatigue life at each peening intensity. Incorporating fracture mechanics and considering the crack initiation criteria would help to find realistic results. After the model verification, optimization methods could help to find the optimum peening intensity that leads to the maximum fatigue life.

4. This thesis proposed a novel fixture for carrying out cyclic tests in the normal direction of thin plates. However, for sheets that are thinner than plates, it would be useful to design a fixture that can obtain the compression-tension behavior in the normal direction, independent of the sheet thickness (i.e., performing bi-axial TC in the RD and TD and measuring the in-plane or out-of-plane strains using DIC).

Bibliography

[1] W. Miller, L. Zhuang, J. Bottema, A. Wittebrood, P. De Smet, A. Haszler, and A. Vieregge, "Recent development in aluminium alloys for the automotive industry," *Mater. Sci. Eng. A*, vol. 280, no. 1, pp. 37–49, 2000, doi: 10.1016/S0921-5093(99)00653-X.

[2] M. K. Kulekci, "Magnesium and its alloys applications in automotive industry," *Int. J. Adv. Manuf. Technol.*, vol. 39, no. 9–10, pp. 851–865, 2008, doi: 10.1007/s00170-007-1279-2.

[3] J. Wang, X. Pang, and H. Jahed, "Surface protection of Mg alloys in automotive applications: A review," *AIMS Mater. Sci.*, vol. 6, no. 4, pp. 567–600, 2019, doi: 10.3934/matersci.2019.4.567.

[4] H. Friedrich and S. Schumann, "Research for a 'new age of magnesium' in the automotive industry," *J. Mater. Process. Technol.*, vol. 117, no. 3, pp. 276–281, 2001, doi: 10.1016/S0924-0136(01)00780-4.

[5] G. Cole, "Magnsium visoion 2020: A north american automotive strategic vision for magnesium," Southfield, MI, 2006.

[6] F. Petit-Renaud, "Optimization of the Shot Peening Parameters," *USF Impact Finish. USF vacu-Blast Int.*, pp. 119–129, 2002, doi: 65715DE27D1CC04DED164741A0C51433.

[7] D. Knight, *Oxford Dictionary of National Biography*. Oxford University Press, 2004.

[8] B. L. Mordike and T. Ebert, "Magnesium Properties - applications - potential," *Mater. Sci. Eng. A*, vol. 302, no. 1, pp. 37–45, 2001, doi: 10.1016/S0921-5093(00)01351-4.

[9] C. Blawert, N. Hort, and K. U. Kainer, "Automotive Applications of Magnesium and Its Alloys," *Magnesium*, vol. 57, no. 4, pp. 397–408, 2006, doi: 10.4028/www.scientific.net/MSF.419-422.67.

[10] M. Diab, X. Pang, and H. Jahed, "The effect of pure aluminum cold spray coating on corrosion and corrosion fatigue of magnesium (3% Al-1% Zn) extrusion," *Surf. Coatings Technol.*, vol. 309, pp. 423–435, 2017, doi: 10.1016/j.surfcoat.2016.11.014.

[11] Y. Xue, X. Pang, B. Jiang, and H. Jahed, "Corrosion and corrosion fatigue performances of micro-arc oxidation coating on AZ31B cast magnesium alloy," *Mater. Corros.*, vol. 70, no. 2, pp. 268–280, 2019, doi: 10.1002/maco.201810293.

[12] S. K. Shaha, S. B. Dayani, Y. Xue, X. Pang, and H. Jahed, "Improving corrosion and corrosion-fatigue resistance of AZ31B cast Mg alloy using combined cold spray and top coatings," *Coatings*, vol. 8, no. 12, 2018, doi: 10.3390/COATINGS8120443.

[13] Y. Xue, "Influence of Micro-arc Oxidation Coatings on Corrosion Performances of AZ80 cast alloy," *Int. J. Electrochem. Sci.*, vol. 13, pp. 7265–7281, 2018, doi: 10.20964/2018.08.38.

[14] M. Avedesian and H. Baker, *ASM Specialty Handbook: Magnesium and Magnesium Alloys,. 1999: Asm International.* ASM International, 1999.

[15] J. Casey and H. Jahedmotlagh, "The strength-differential effect in plasticity," *Int. J. Solids Struct.*, vol. 20, no. 4, pp. 377–393, 1984, doi: 10.1016/0020-7683(84)90047-7.

[16] R. Honeycombe, *The Plastic Deformation of Metals*. New York: St. Martin's Press, 1975.

[17] D. Stouffer and L. Dame, *Inelastic Deformation of Metals: Models, Mechanical Properties, and Metallurgy*. John Wiley & Sons, 1996.

[18] Z. Guo, *The Deformation and Processing of Structural Materials*. Woodhead Pub Limited, 2005.

[19] A. Staroselsky and L. Anand, “A constitutive model for hcp materials deforming by slip and twinning: Application to magnesium alloy AZ31B,” *Int. J. Plast.*, vol. 19, no. 10, pp. 1843–1864, 2003, doi: 10.1016/S0749-6419(03)00039-1.

[20] J. Albinmousa, H. Jahed, and S. Lambert, “Cyclic axial and cyclic torsional behaviour of extruded AZ31B magnesium alloy,” *Int. J. Fatigue*, vol. 33, no. 11, pp. 1403–1416, 2011, doi: 10.1016/j.ijfatigue.2011.04.012.

[21] J. Al Bin Mousa, “Multiaxial Fatigue Characterization and Modeling of AZ31B Magnesium Extrusion.” UWSpace, 2012.

[22] S. B. Behravesh, H. Jahed, and S. Lambert, “Fatigue characterization and modeling of AZ31B magnesium alloy spot-welds,” *Int. J. Fatigue*, vol. 64, pp. 1–13, 2014, doi: 10.1016/j.ijfatigue.2014.01.026.

[23] E. Kalatehmollaei, H. Mahmoudi-Asl, and H. Jahed, “An asymmetric elastic-plastic analysis of the load-controlled rotating bending test and its application in the fatigue life estimation of wrought magnesium AZ31B,” *Int. J. Fatigue*, vol. 64, pp. 33–41, 2014, doi: 10.1016/j.ijfatigue.2014.02.012.

[24] S. B. Behravesh, H. Jahed, S. B. Lambert, and M. Chengji, “Constitutive Modeling for Cyclic Behavior of AZ31B Magnesium Alloy and its Application,” *Adv. Mater. Res.*, vol. 891–892, pp. 809–814, 2014, doi: 10.4028/www.scientific.net/AMR.891-892.809.

[25] J. Albinmousa and H. Jahed, “Multiaxial effects on LCF behaviour and fatigue failure of AZ31B magnesium extrusion,” *Int. J. Fatigue*, vol. 67, pp. 103–116, 2014, doi: 10.1016/j.ijfatigue.2014.01.025.

[26] A. Gryguc, H. Jahed, B. Williams, and J. McKinley, “MagForge – Mechanical Behaviour of Forged AZ31B Extruded Magnesium in Monotonic Compression,” *Mater. Sci. Forum*, vol. 828–829, pp. 291–297, 2015, doi: 10.4028/www.scientific.net/MSF.828-829.291.

[27] A. Gryguc, S. K. Shaha, H. Jahed, M. Wells, B. Williams, and J. McKinley, “Tensile and fatigue behaviour of as-forged AZ31B extrusion,” *Frat. ed Integrita Strutt.*, vol. 10, no. 38, pp. 251–258, 2016, doi: 10.3221/IGF-ESIS.38.34.

[28] B. Marzbanrad, E. Toyserkani, and H. Jahed, “Cyclic hysteresis of AZ31B extrusion under load-control tests using embedded sensor technology,” *Fatigue Fract. Eng. Mater. Struct.*, vol. 40, no. 2, pp. 221–232, 2017, doi: 10.1111/ffe.12488.

[29] M. Sun, S. B. Behravesh, L. Wu, Y. Zhou, and H. Jahed, “Fatigue behaviour of dissimilar Al 5052 and Mg AZ31 resistance spot welds with Sn-coated steel interlayer,” *Fatigue Fract. Eng. Mater. Struct.*, vol. 40, no. 7, pp. 1048–1058, 2017, doi: 10.1111/ffe.12563.

[30] D. Toscano, S. K. Shaha, B. Behravesh, H. Jahed, and B. Williams, “Effect of forging on the low cycle fatigue behavior of cast AZ31B alloy,” *Mater. Sci. Eng. A*, vol. 706, no. May, pp. 342–356, 2017, doi: 10.1016/j.msea.2017.08.086.

[31] S. B. Dayani, S. K. Shaha, R. Ghelichi, J. F. Wang, and H. Jahed, “The impact of AA7075 cold spray coating on the fatigue life of AZ31B cast alloy,” *Surf. Coatings Technol.*, vol. 337, no. December 2017, pp. 150–158, 2018, doi: 10.1016/j.surfcoat.2018.01.008.

[32] D. Toscano, S. K. Shaha, B. Behravesh, H. Jahed, and B. Williams, “Multiaxial Cyclic Response of Low Temperature Closed-Die Forged AZ31B Mg Alloy,” *Miner. Met. Mater. Ser.*, pp. 289–296, 2019, doi: 10.1007/978-3-030-05789-3_43.

[33] L. F. V. Qian, A. A. Roostaei, U. Dighrasker, G. Glinka, and H. Jahed, “Notch plasticity and fatigue modelling of AZ31B-H24 magnesium alloy sheet,” *SAE Tech. Pap.*, vol. 2019-April, no. April, pp. 1–11, 2019, doi: 10.4271/2019-01-0530.

[34] Y. Ling, A. A. Roostaei, G. Glinka, and H. Jahed, “Fatigue of ZEK100-F magnesium alloy: Characterisation and modelling,” *Int. J. Fatigue*, vol. 125, no. March, pp. 179–186, 2019, doi: 10.1016/j.ijfatigue.2019.04.001.

[35] A. Gryguc, S. K. Shaha, S. B. Behravesh, H. Jahed, M. Wells, and B. Williams, “Compression Behaviour of Semi-closed Die Forged AZ80 Extrusion,” in *Characterization of Minerals, Metals, and Materials 2017*, 2017, pp. 361–369.

[36] A. Gryguc, S. K. Shaha, S. B. Behravesh, H. Jahed, M. Wells, B. Williams, and X. Su, “Monotonic and cyclic behaviour of cast and cast-forged AZ80 Mg,” *Int. J. Fatigue*, vol. 104, pp. 136–149, 2017, doi: 10.1016/j.ijfatigue.2017.06.038.

[37] A. Gryguc, S. B. Behravesh, S. K. Shaha, H. Jahed, M. Wells, B. Williams, and X. Su, “Low-cycle fatigue characterization and texture induced ratcheting behaviour of forged AZ80 Mg alloys,” *Int. J. Fatigue*, vol. 116, no. June, pp. 429–438, 2018, doi: 10.1016/j.ijfatigue.2018.06.028.

[38] P. Prakash, A. Hadadzadeh, S. K. Shaha, M. A. Whitney, M. A. Wells, H. Jahed, and B. W. Williams, “Microstructure and Texture Evolution During Hot Compression of Cast and Extruded AZ80 Magnesium Alloy,” in *Magnesium Technology 2019*, 2019, pp. 89–94.

[39] A. Gryguć, S. B. Behravesh, S. K. Shaha, H. Jahed, M. Wells, B. Williams, and X. Su, “Multiaxial cyclic behaviour of extruded and forged AZ80 Mg alloy,” *Int. J. Fatigue*, vol. 127, no. December 2018, pp. 324–337, 2019, doi: 10.1016/j.ijfatigue.2019.06.015.

[40] S. M. H. Karparvarfard, S. K. Shaha, S. B. Behravesh, H. Jahed, and B. W. Williams, “Fatigue characteristics and modeling of cast and cast-forged ZK60 magnesium alloy,” *Int. J. Fatigue*, vol. 118, no. November 2017, pp. 282–297, 2019, doi: 10.1016/j.ijfatigue.2018.03.019.

[41] A. H. Pahlevanpour, S. M. H. Karparvarfard, S. K. Shaha, S. B. Behravesh, S. Adibnazari, and H. Jahed, “Anisotropy in the quasi-static and cyclic behavior of ZK60 extrusion: Characterization and fatigue modeling,” *Mater. Des.*, vol. 160, pp. 936–948, 2018, doi: 10.1016/j.matdes.2018.10.026.

[42] M. Noban, H. Jahed, E. Ibrahim, and A. Ince, “Load path sensitivity and fatigue life estimation of 30CrNiMo8HH,” *Int. J. Fatigue*, vol. 37, pp. 123–133, 2012, doi: 10.1016/j.ijfatigue.2011.10.009.

[43] S. M. H. Karparvarfard, S. B. Behravesh, and S. Kumar, “On the phase angle role in the shear response of ZK60 Mg alloys under multiaxial fatigue,” vol. 08005, pp. 1–9, 2019.

[44] K. Kainer, *Magnesium Alloys and Technologies*. Wiley-VCH., 2003.

[45] T. S. Shih, W. S. Liu, and Y. J. Chen, “Fatigue of as-extruded AZ61A magnesium alloy,” *Mater. Sci. Eng. A*, vol. 325, no. 1–2, pp. 152–162, 2002, doi: 10.1016/S0921-5093(01)01411-3.

[46] Z. Zhihao, M. Yi, C. Jianzhong, “Effect of Mn on microstructures and mechanical properties of Al-Mg-Si-Cu-Cr-V alloy,” *China Foundry*, no. November, pp. 349–355, 2012.

[47] A. Hadadzadeh, S. K. Shaha, M. A. Wells, H. Jahed, and B. W. Williams, “Microstructure and Texture Evolution During Hot Deformation of Cast-Homogenized ZK60 Magnesium Alloy,” in *Magnesium Technology 2017*, 2017, pp. 513–519.

[48] A. Hadadzadeh, M. A. Wells, S. K. Shaha, H. Jahed, and B. W. Williams, “Role of compression direction on recrystallization behavior and texture evolution during hot deformation of extruded

ZK60 magnesium alloy," *J. Alloys Compd.*, vol. 702, pp. 274–289, 2017, doi: 10.1016/j.jallcom.2017.01.236.

[49] S. M. H. Karparvarfard, S. K. Shaha, A. Hadadzadeh, S. B. Behravesh, H. Jahed, M. A. Wells, and B. Williams, "Characterization of Semi-Closed Die-Forged ZK60 Mg Alloy Extrusion," in *Magnesium Technology 2017*, 2017, pp. 329–334.

[50] S. M. H. Karparvarfard, S. K. Shaha, S. B. Behravesh, H. Jahed, and B. W. Williams, "Microstructure, texture and mechanical behavior characterization of hot forged cast ZK60 magnesium alloy," *J. Mater. Sci. Technol.*, vol. 33, no. 9, pp. 907–918, 2017, doi: 10.1016/j.jmst.2017.04.004.

[51] A. H. Pahlevanpour, S. B. Behravesh, S. Adibnazari, and H. Jahed, "Characterization of anisotropic behaviour of ZK60 extrusion under stress-control condition and notes on fatigue modeling," *Int. J. Fatigue*, vol. 127, no. May, pp. 101–109, 2019, doi: 10.1016/j.ijfatigue.2019.05.030.

[52] H. Jahed and R. Ghelichi, "Residual Stresses and Fatigue Life Enhancement of Cold Spray," in *Modern Cold Spray: Materials, Process, and Applications*, J. Villafuerte, Ed. Cham: Springer International Publishing, 2015, pp. 225–252.

[53] S. Kyriacou, "Shot-peening mechanics, A theoretical study," in *6 th international conference on shot peening*, 1996, pp. 505–516.

[54] J. Almen and P. Black, *Residual stresses and fatigue in metals*. New york: McGrow Hill, 1963.

[55] B. Bhuvaraghan, S. M. Srinivasan, and B. Maffeo, "Numerical simulation of Almen strip response due to random impacts with strain-rate effects," *Int. J. Mech. Sci.*, vol. 53, no. 6, pp. 417–424, 2011, doi: 10.1016/j.ijmecsci.2011.03.004.

[56] J. L. Davis, "Analytical Modeling and Applications of Residual Stresses Induced by Shot Peening," University of Washington, 2012.

[57] H. Y. Miao, S. Larose, C. Perron, and M. Levesque, "On the potential applications of a 3D random finite element model for the simulation of shot peening," *Adv. Eng. Softw.*, vol. 40, no. 10, pp. 1023–1038, 2009, doi: DOI 10.1016/j.advengsoft.2009.03.013.

[58] "Excellence & Innovation in every design," *Patel furnace & forging PVT. LTD*, 2008. [Online]. Available: www.pshotblast.com.

[59] B. He, *Two-Dimensional X-Ray Diffraction*, 2nd ed. John Wiley & Sons, 2018.

[60] W. P. Evans, "Residual Stress Measurement by X-Ray Diffraction," *Soc. Automot. Eng. SAE HS784*, pp. 74–79, 2003.

[61] O. Takakuwa and H. Soyama, "Optimizing the Conditions for Residual Stress Measurement Using a Two-Dimensional XRD Method with Specimen Oscillation," *Adv. Mater. Phys. Chem.*, vol. 03, no. 01, pp. 8–18, 2013, doi: 10.4236/ampc.2013.31A002.

[62] J. F. Flavenot and A. Nikulari, "La mesure des contraintes residuelles, methode de la eche, methode de la source de contraintes," *Les memories, Tech. due*, 1977.

[63] S. Al-Hassani, "Mechanical aspects of residual stress development in shot peening," in *1st International Conference on Shot Peening*, 1981, pp. 583–602.

[64] H. Y. Miao, S. Larose, C. Perron, and M. Levesque, "An analytical approach to relate shot peening

parameters to Almen intensity," *Surf. Coatings Technol.*, vol. 205, no. 7, pp. 2055–2066, 2010, doi: 10.1016/j.surfcoat.2010.08.105.

[65] J. K. Li, Y. Mei, W. Duo, and W. Renzhi, "Mechanical approach to the residual stress field induced by shot peening," *Mater. Sci. Eng.*, vol. 147, pp. 167–173, 1991.

[66] K. Johnson, *Contact mechanics*. Cambridge University Press, 1985.

[67] A. Iliushin, *Plasticity*. National Press of Technical and Theoretical Literature, 1948.

[68] S. Shen and S. N. Atluri, "An analytical model for shot-peening induced residual stresses," *Comput. Mater. Contin.*, vol. 4, no. 2, pp. 75–85, 2006, doi: 10.3970/cmc.2006.004.075.

[69] S. Al-Hassani, "An engineering approach to shot peening mechanics," in *ICSP-2*, 1984.

[70] A. S. Franchim, V. S. de Campos, D. N. Travessa, and C. de M. Neto, "Analytical modelling for residual stresses produced by shot peening," *Mater. Des.*, vol. 30, no. 5, pp. 1556–1560, 2009, doi: 10.1016/j.matdes.2008.07.040.

[71] K. Sherafatnia, G. H. Farrahi, A. H. Mahmoudi, and A. Ghasemi, "Experimental measurement and analytical determination of shot peening residual stresses considering friction and real unloading behavior," *Mater. Sci. Eng. A*, vol. 657, pp. 309–321, 2016, doi: 10.1016/j.msea.2016.01.070.

[72] K. Sherafatnia, G. Hossein, and A. Hossein, "International Journal of Mechanical Sciences Effect of initial surface treatment on shot peening residual stress field : Analytical approach with experimental verification," *Int. J. Mech. Sci.*, vol. 137, no. February, pp. 171–181, 2018, doi: 10.1016/j.ijmecsci.2018.01.022.

[73] K. Mori, K. Osakada, and N. Matsuoka, "Finite element analysis of peening process with plasticity deforming shot," *J. Mater. Process. Technol.*, vol. 45, no. 1–4, pp. 607–612, 1994, doi: 10.1016/0924-0136(94)90406-5.

[74] S. A. Meguid, G. Shagal, and J. C. Stranart, "Finite element modelling of shot-peening residual stresses," *J. Mater. Process. Technol.*, vol. 92–93, pp. 401–404, 1999, doi: 10.1016/S0924-0136(99)00153-3.

[75] S. A. Meguid, G. Shagal, J. C. Stranart, and J. Daly, "Three-dimensional dynamic finite element analysis of shot-peening induced residual stresses," *Finite Elem. Anal. Des.*, vol. 31, no. 3, pp. 179–191, 1999, doi: 10.1016/S0168-874x(98)00057-2.

[76] S. A. Meguid, G. Shagal, and J. C. Stranart, "3D FE analysis of peening of strain-rate sensitive materials using multiple impingement model," *Int. J. Impact Eng.*, vol. 27, no. 2, pp. 119–134, 2002, doi: 10.1016/S0734-743X(01)00043-4.

[77] M. Guagliano, "Relating Almen intensity to residual stresses induced by shot peening: A numerical approach," *J. Mater. Process. Technol.*, vol. 110, no. 3, pp. 277–286, 2001, doi: 10.1016/S0924-0136(00)00893-1.

[78] G. H. Majzoobi, R. Azizi, and A. Alavi Nia, "A three-dimensional simulation of shot peening process using multiple shot impacts," *J. Mater. Process. Technol.*, vol. 164–165, pp. 1226–1234, 2005, doi: 10.1016/j.jmatprotec.2005.02.139.

[79] S. A. Meguid, G. Shagal, and J. C. Stranart, "Development and Validation of Novel FE Models for 3D Analysis of Peening of Strain-Rate Sensitive Materials," *J. Eng. Mater. Technol.*, vol. 129, no. 2, p. 271, 2007, doi: 10.1115/1.2712469.

[80] T. Kim, J. H. Lee, H. Lee, and S. kyun Cheong, "An area-average approach to peening residual stress under multi-impacts using a three-dimensional symmetry-cell finite element model with plastic shots," *Mater. Des.*, vol. 31, no. 1, pp. 50–59, 2010, doi: 10.1016/j.matdes.2009.07.032.

[81] R. F. Kubler, S. Berveiller, D. Bouscaud, R. Guiheux, E. Patoor, and Q. Puydt, "Ac ce pt us cr ip t," *J. Mater. Process. Tech.*, 2019, doi: 10.1016/j.jmatprotec.2019.02.031.

[82] M. Avrami, "Kinetics of Phase Change. I General Theory," *J. Chem. Phys.*, vol. 7, no. 11, 1939, doi: 10.1063/1.1750380.

[83] S. M. H. Gangaraj, M. Guagliano, and G. H. Farrahi, "An approach to relate shot peening finite element simulation to the actual coverage," *Surf. Coatings Technol.*, vol. 243, pp. 39–45, 2014, doi: 10.1016/j.surfcoat.2012.03.057.

[84] S. Bagherifard, R. Ghelichi, and M. Guagliano, "A numerical model of severe shot peening (SSP) to predict the generation of a nanostructured surface layer of material," *Surf. Coatings Technol.*, vol. 204, no. 24, pp. 4081–4090, 2010, doi: 10.1016/j.surfcoat.2010.05.035.

[85] J. Xiang, S. Pang, L. Xie, G. Cheng, R. Liang, F. Gao, and L. Bai, "A numerically low-cost and high-accuracy periodic FE modeling of shot-peened 34CrNiMo6 and experimental validation," *Int. J. Adv. Manuf. Technol.*, vol. 97, pp. 1673–1685, 2018.

[86] A. Gariépy, S. Larose, C. Perron, and M. Lévesque, "International Journal of Solids and Structures Shot peening and peen forming finite element modelling – Towards a quantitative method," vol. 48, pp. 2859–2877, 2011, doi: 10.1016/j.ijsolstr.2011.06.003.

[87] G. Shayegan, H. Mahmoudi, R. Ghelichi, J. Villafuerte, J. Wang, M. Guagliano, and H. Jahed, "Residual stress induced by cold spray coating of magnesium AZ31B extrusion," *Mater. Des.*, vol. 60, pp. 72–84, 2014, doi: 10.1016/j.matdes.2014.03.054.

[88] T. Dorrl, M. H, P. Beckmerhagen, A. Kiefer, and I. El, "Influence of Shot Peening on Fatigue Performance of High-Strength Aluminum- and Magnesium Alloys," in *ICSP-7*, 1999.

[89] L. Wagner, "Mechanical surface treatments on titanium, aluminum and magnesium alloys," *Mater. Sci. Eng. A*, vol. 263, no. 2, pp. 210–216, 1999, doi: http://dx.doi.org/10.1016/S0921-5093(98)01168-X.

[90] J. Wendt, A. Ketzmer, and L. Wagner, "Effect of Test Temperature on Fatigue of Shot Peened Magnesium Alloys," in *Shot Peening*, Wiley-VCH Verlag GmbH & Co. KGaA, Weinheim, FRG, 2003.

[91] P. Zhang and J. Lindemann, "Influence of shot peening on high cycle fatigue properties of the high-strength wrought magnesium alloy AZ80," *Scr. Mater.*, vol. 52, no. 6, pp. 485–490, 2005, doi: 10.1016/j.scriptamat.2004.11.003.

[92] N. Barry, S. V. Hainsworth, and M. E. Fitzpatrick, "Effect of shot peening on the fatigue behaviour of cast magnesium A8," *Mater. Sci. Eng. A*, vol. 507, no. 1–2, pp. 50–57, 2009, doi: 10.1016/j.msea.2008.11.044.

[93] W. Liu, J. Dong, P. Zhang, C. Zhai, and W. Ding, "Effect of Shot Peening on Surface Characteristics and Fatigue Properties of T5-Treated ZK60 Alloy," *Mater. Trans.*, vol. 50, no. 4, pp. 791–798, 2009, doi: 10.2320/matertrans.MRA2008415.

[94] P. Zhang, J. Lindemann, and C. Leyens, "Influence of shot peening on notched fatigue strength of the high-strength wrought magnesium alloy AZ80," *J. Alloys Compd.*, vol. 497, no. 1–2, pp. 380–

385, May 2010, doi: 10.1016/j.jallcom.2010.03.079.

[95] W. C. Liu, J. Dong, P. Zhang, A. M. Korsunsky, X. Song, and W. J. Ding, "Improvement of fatigue properties by shot peening for Mg-10Gd-3Y alloys under different conditions," *Mater. Sci. Eng. A*, vol. 528, no. 18, pp. 5935–5944, 2011, doi: 10.1016/j.msea.2011.04.004.

[96] J. Dong, W. Liu, W. Ding, and J. Zou, "Surface Characteristics and High Cycle Fatigue Performance of Shot Peened Magnesium Alloy ZK60," *J. Metall.*, vol. 2011, pp. 1–9, 2011, doi: 10.1155/2011/682191.

[97] W. C. Liu, J. Dong, X. W. Zheng, P. Zhang, and W. J. Ding, "Influence of shot peening on notched fatigue properties of magnesium alloy ZK60," *Mater. Sci. Technol.*, vol. 27, no. 1, pp. 201–207, 2011, doi: 10.1179/174328409X418973.

[98] S. Bagherifard, D. J. Hickey, S. Fintová, F. Pastorek, I. Fernandez-Pariente, M. Bandini, T. J. Webster, and M. Guagliano, "Effects of nanofeatures induced by severe shot peening (SSP) on mechanical, corrosion and cytocompatibility properties of magnesium alloy AZ31," *Acta Biomater.*, vol. 66, pp. 93–108, 2018, doi: https://doi.org/10.1016/j.actbio.2017.11.032.

[99] M. Marciszko *et al.*, "Application of multireflection grazing incidence method for stress measurements in polished Al-Mg alloy and CrN coating," *Appl. Surf. Sci.*, vol. 266, pp. 256–267, 2013, doi: 10.1016/j.apsusc.2012.12.005.

[100] W. Zinn and B. Scholtes, "Mechanical surface treatments of lightweight materials—Effects on fatigue strength and near-surface microstructures," *J. Mater. Eng. Perform.*, vol. 8, no. 2, pp. 145–151, 1999, doi: 10.1361/105994999770346972.

[101] L. Commin, M. Dumont, J. E. Masse, and L. Barrallier, "Friction stir welding of AZ31 magnesium alloy rolled sheets: Influence of processing parameters," *Acta Mater.*, vol. 57, no. 2, pp. 326–334, 2009, doi: 10.1016/j.actamat.2008.09.011.

[102] F. Khodabakhshi, B. Marzbanrad, L. H. Shah, H. Jahed, and A. P. Gerlich, "Friction-stir processing of a cold sprayed AA7075 coating layer on the AZ31B substrate: Structural homogeneity, microstructures and hardness," *Surf. Coatings Technol.*, vol. 331, no. April, pp. 116–128, 2017, doi: 10.1016/j.surfcoat.2017.10.060.

[103] F. Khodabakhshi, B. Marzbanrad, A. Yazdanmehr, H. Jahed, and A. P. Gerlich, "Tailoring the residual stress during two-step cold gas spraying and friction-stir surface integration of titanium coating," *Surf. Coatings Technol.*, vol. 380, no. May, p. 125008, 2019, doi: 10.1016/j.surfcoat.2019.125008.

[104] S. Ishihara, S. Taneguchi, H. Shibata, T. Goshima, and A. Saiki, "Anisotropy of the fatigue behavior of extruded and rolled magnesium alloys," *Int. J. Fatigue*, vol. 50, pp. 94–100, 2013, doi: 10.1016/j.ijfatigue.2012.02.011.

[105] T. Nitschke-Pagel and K. Dilger, "Residual Stress Condition of Tubular Laser Welds of an AZ31 Magnesium Alloy," *Mater. Res. Proc.*, vol. 2, pp. 277–282, 2016, doi: dx.doi.org/10.21741/9781945291173-47.

[106] Z. Zeng, X. Li, Y. Miao, G. Wu, and Z. Zhao, "Numerical and experiment analysis of residual stress on magnesium alloy and steel butt joint by hybrid laser-TIG welding," *Comput. Mater. Sci.*, vol. 50, no. 5, pp. 1763–1769, 2011, doi: 10.1016/j.commatsci.2011.01.011.

[107] R. S. Coelho, A. Kostka, H. Pinto, S. Riekehr, M. Koçak, and A. R. Pyzalla, "Microstructure and mechanical properties of magnesium alloy AZ31B laser beam welds," *Mater. Sci. Eng. A*, vol.

485, no. 1–2, pp. 20–30, 2008, doi: 10.1016/j.msea.2007.07.073.

[108] A. Kouadri and L. Barrallier, “Study of mechanical properties of AZ91 magnesium alloy welded by laser process taking into account the anisotropy microhardness and residual stresses by X-ray diffraction,” *Metall. Mater. Trans. A*, vol. 42, no. 7, pp. 1815–1826, 2011, doi: 10.1007/s11661-010-0568-9.

[109] J. C. Outeiro, A. C. Batista, and M. J. Marques, “Residual Stresses Induced by Dry and Cryogenic Cooling during Machining of AZ31B Magnesium Alloy,” *Adv. Mater. Res.*, vol. 996, pp. 658–663, 2014, doi: 10.4028/www.scientific.net/AMR.996.658.

[110] Z. Pu, J. C. Outeiro, A. C. Batista, O. W. Dillon, D. A. Puleo, and I. S. Jawahir, “Enhanced surface integrity of AZ31B Mg alloy by cryogenic machining towards improved functional performance of machined components,” *Int. J. Mach. Tools Manuf.*, vol. 56, pp. 17–27, 2012, doi: 10.1016/j.ijmachtools.2011.12.006.

[111] S. Faghih, S. K. Shaha, S. B. Behravesh, and H. Jahed, “Split sleeve cold expansion of AZ31B sheet: Microstructure, texture and residual stress,” *Mater. Des.*, vol. 186, p. 108213, 2020, doi: 10.1016/j.matdes.2019.108213.

[112] S. Faghih, S. K. Shaha, S. B. Behravesh, and H. Jahed, “Effect of Split Sleeve Cold Expansion on the Residual Stress, Texture and Fatigue Life of Rolled AZ31B Magnesium Alloy,” in *Magnesium Technology 2019*, 2019, pp. 353–358.

[113] T. Hosaka, S. Yoshihara, I. Amanina, and B. J. Macdonald, “Influence of Grain Refinement and Residual Stress on Corrosion Behavior of AZ31 Magnesium Alloy Processed by ECAP in RPMI-1640 Medium,” *Procedia Eng.*, vol. 184, pp. 432–441, 2017, doi: 10.1016/j.proeng.2017.04.114.

[114] B. Marzbanrad, H. Jahed, and E. Toyserkani, “On the evolution of substrate’s residual stress during cold spray process: A parametric study,” *Mater. Des.*, vol. 138, pp. 90–102, 2018, doi: 10.1016/j.matdes.2017.10.062.

[115] F. Khodabakhshi, B. Marzbanrad, L. H. Shah, H. Jahed, and A. P. Gerlich, “Surface Modification of a Cold Gas Dynamic Spray-Deposited Titanium Coating on Aluminum Alloy by using Friction-Stir Processing,” *J. Therm. Spray Technol.*, vol. 28, no. 6, pp. 1185–1198, 2019, doi: 10.1007/s11666-019-00902-z.

[116] R. Ghelichi, M. Guagliano, H. Jahed, and J. Villafuerte, “A Method for Residual Stress Estimation of AZ31 under Cold Spray Coating,” in *International Conference on thermal Spray*, 2011, pp. 1–6.

[117] S. K. Shaha, B. Marzbanrad, and H. Jahed, “Influence of Cold Spray on the Microstructure and Residual Stress of Resistance Spot Welded Steel-Mg,” in *TMS 2018 147th Annual Meeting & Exhibition Supplemental Proceedings*, 2018, pp. 635–644.

[118] Y. Zhang, J. You, J. Lu, C. Cui, Y. Jiang, and X. Ren, “Effects of laser shock processing on stress corrosion cracking susceptibility of AZ31B magnesium alloy,” *Surf. Coatings Technol.*, vol. 204, no. 24, pp. 3947–3953, 2010, doi: 10.1016/j.surfcoat.2010.03.015.

[119] S. B. Behravesh, L. Liu, H. Jahed, S. Lambert, G. Glinka, and N. Zhou, “Effect of nugget size on tensile and fatigue strength of spot welded AZ31 magnesium alloy,” *SAE Tech. Pap.*, 2010, doi: 10.4271/2010-01-0411.

[120] S. B. Behravesh, “Fatigue Characterization and Cyclic Plasticity Modeling of Magnesium Spot-Welds,” University of Waterloo, 2013.

[121] D. Toscano, S. K. Shaha, B. Behravesh, H. Jahed, and B. Williams, "Effect of Forging on Microstructure , Texture , and Uniaxial Properties of Cast AZ31B Alloy," *J. Mater. Eng. Perform.*, vol. 26, no. 7, pp. 3090–3103, 2017, doi: 10.1007/s11665-017-2743-2.

[122] Y. M. Mos, A. C. Vermeulen, C. J. N. Buisman, and J. Weijma, "X-Ray Diffraction of Iron Containing Samples: The Importance of a Suitable Configuration," *Geomicrobiol. J.*, vol. 35, no. 6, pp. 511–517, 2018, doi: 10.1080/01490451.2017.1401183.

[123] A. A. Bunaciu, E. gabriela Udriştioiu, and H. Y. Aboul-Enein, "X-Ray Diffraction: Instrumentation and Applications," *Crit. Rev. Anal. Chem.*, vol. 45, no. 4, pp. 289–299, 2015, doi: 10.1080/10408347.2014.949616.

[124] R. Sharma, D. P. Bisen, U. Shukla, and B. G. Sharma, "X-ray diffraction: a powerful method of characterizing nanomaterials," *Recent Res. Sci. Technol.*, vol. 4, no. 8, pp. 77–79, 2012.

[125] P. Prevey, "X-Ray Diffraction Residual Stress Techniques," in *Metals Handbook*, 10th ed., American Society for Metals, 1986, pp. 380–392.

[126] "Standard Guide for Electrolytic Polishing of Metallographic Specimens, E1558-09," *ASTM Int.*, vol. 09, pp. 1–13, 2014, doi: 10.1520/E1558-09.2.

[127] J. H. Hubbell and S. M. Seltzer, "Tables of X-Ray Mass Attenuation Coefficients and Mass Energy-Absorption Coefficients (version 1.4)," *Natl. Inst. Stand. Technol. Gaithersburg, MD.*, 2004.

[128] C. L. Azanza Ricardo, M. D'Incau, and P. Scardi, "Revision and extension of the standard laboratory technique for X-ray diffraction measurement of residual stress gradients," *J. Appl. Crystallogr.*, vol. 40, no. 4, pp. 675–683, 2007, doi: 10.1107/S0021889807022935.

[129] P. J. Withers, M. Preuss, P. Webster, D. Hughes, and A. M. Korsunsky, "Residual strain measurement by synchrotron diffraction," in *Materials Science Forum*, 2002, pp. 1–12.

[130] B. He, "Measurement of Residual Stresses in Thin Films by Two-Dimensional XRD," *Mater. Sci. Forum*, vol. 524–525, pp. 613–618, 2006, doi: 10.4028/www.scientific.net/MSF.524-525.613.

[131] B. Kania, P. Indyka, L. Tarkowski, and E. Beltowska-Lehman, "X-ray diffraction grazing-incidence methods applied for gradient-free residual stress profile measurements in electrodeposited Ni coatings," *J. Appl. Crystallogr.*, vol. 48, no. 1, pp. 71–78, 2015, doi: 10.1107/S1600576714025722.

[132] M. Marciszko, A. Baczmański, C. Braham, M. Wróbel, S. Wroński, and G. Cios, "Stress measurements by multi-reflection grazing-incidence X-ray diffraction method (MGIXD) using different radiation wavelengths and different incident angles," *Acta Mater.*, vol. 123, pp. 157–166, 2017, doi: 10.1016/j.actamat.2016.10.029.

[133] A. Baczmanski, C. Braham, W. Seiler, and N. Shiraki, "Multi-reflection method and grazing incidence geometry used for stress measurement by X-ray diffraction," *Surf. Coatings Technol.*, vol. 182, no. 1, pp. 43–54, 2004, doi: 10.1016/j.surfcoat.2003.07.005.

[134] G. S. Schajer, "Measurement of Non-Uniform Residual Stresses Using the Hole-Drilling Method. Part II—Practical Application of the Integral Method," *J. Eng. Mater. Technol.*, vol. 110, no. 4, pp. 344–349, Oct. 1988, doi: 10.1115/1.3226060.

[135] ASTM Standard E9-09, "Standard Test Methods of Compression Testing of Metallic Materials at Room Temperature," *Annu. B. ASTM Stand.*, vol. 3.01, no. 1, pp. 92–100, 2012, doi:

10.1520/E0009-09.2.

[136] W. Muhammad, M. Mohammadi, J. Kang, R. K. Mishra, and K. Inal, “An elasto-plastic constitutive model for evolving asymmetric/anisotropic hardening behavior of AZ31B and ZEK100 magnesium alloy sheets considering monotonic and reverse loading paths,” Int. J. Plast., vol. 70, pp. 30–59, 2015, doi: 10.1016/j.ijplas.2015.03.004.

[137] D. Ghaffari Tari, M. J. Worswick, U. Ali, and M. A. Gharghouri, “Mechanical response of AZ31B magnesium alloy: Experimental characterization and material modeling considering proportional loading at room temperature,” Int. J. Plast., vol. 55, pp. 247–267, 2014, doi: 10.1016/j.ijplas.2013.10.006.

[138] C. S. Aitchison and L. B. Tuckejuian, “The ‘Pack’ method for compressive tests of thin specimens of materials used in thin-wall structues,” 1939.

[139] F. Yoshida, T. Uemori, and K. Fujiwara, “Elastic – plastic behavior of steel sheets under in-plane cyclic tension – compression at large strain,” *Int. J. Plast.*, vol. 18, pp. 633–659, 2002.

[140] C. S. Aitchison, “Extension of Pack Method for Compressive Tests,” *Natl. Advis. Comm. Aeronaut.*, no. 789, 1940.

[141] J. A. Miller, “A fixture for compressive tests of thin sheet metal between lubricated steel guides,” *Natl. Advis. Comm. Aeronaut.*, no. 1022, 1946.

[142] J. N. Kotanchik, W. Woods, and R. A. Weinberger, “Investigation of methods of supporting singlethickness specimens in a fixture for determination of compressive stress–strain curves,” *Natl. Advis. Comm. Aeronaut.*, no. L5E15, 1945.

[143] H. LaTour and D. S. Wolford, “Single-strip compression test for sheet materials,” in *ASTM*, 1945, pp. 671– 688.

[144] R. L. Templin, “Discussion of single-strip compression test for sheet materials,” in *ASTM*, 1945, pp. 690– 693.

[145] P. E. Sandorff and R. K. Dillon, “Compressive stress–strain properties of some aircraft materials,” in *ASTM*, 1946, pp. 1039–1052.

[146] T. Kuwabara, Y. Morita, Y. Miyashita, and S. Takahashi, “Elastic–plastic behavior of sheet metal subjected to in-plane reverse loading. Proceedings of the Fifth International Symposium on Plasticity and Its Curren,” in *Fifth International Symposium on Plasticity and Its Curren*, 1995, pp. 841–844.

[147] J. Cao, W. Lee, H. S. Cheng, M. Seniw, H. P. Wang, and K. Chung, “Experimental and numerical investigation of combined isotropic-kinematic hardening behavior of sheet metals,” *Int. J. Plast.*, vol. 25, no. 5, pp. 942–972, 2009, doi: 10.1016/j.ijplas.2008.04.007.

[148] L. Dietrich, G. Socha, and Z. L. Kowalewski, “Anti-buckling fixture for large deformation tension-compression cyclic loading of thin metal sheets,” *An Int. J. Exp. Mech.*, vol. 50, no. 2, pp. 174–183, 2014, doi: 10.1111/str.12078.

[149] Z. L. Kowalewski, L. Dietrich, and G. Socha, “Experimental investigation of thin metal sheets under tension-compression cyclic loading 1 Introduction 2 Experimental details,” *8th Australas. Congr. Appl. Mech. ACAM 8*, no. November, 2014.

[150] T. Libura, Z. L. Kowalewski, L. Dietrich, and G. Socha, “Anti-buckling System for Flat Specimens Investigations under Cyclic Tension-compression,” *Mater. Today Proc.*, vol. 3, no. 4,

pp. 1045–1050, 2016, doi: 10.1016/j.matpr.2016.03.045.

[151] T. Kuwabara, Y. Kumano, J. Ziegelheim, and I. Kurosaki, “Tension-compression asymmetry of phosphor bronze for electronic parts and its effect on bending behavior,” Int. J. Plast., vol. 25, no. 9, pp. 1759–1776, 2009, doi: 10.1016/j.ijplas.2009.01.004.

[152] R. K. Boger, R. H. Wagoner, F. Barlat, M. G. Lee, and K. Chung, “Continuous, large strain, tension/compression testing of sheet material,” *Int. J. Plast.*, vol. 21, no. 12, pp. 2319–2343, 2005, doi: 10.1016/j.ijplas.2004.12.002.

[153] M. Omar, T. Kuwabara, and D. Steglich, “Material modeling of AZ31 Mg sheet considering variation of r -values and asymmetry of the yield locus,” *Mater. Sci. Eng. A*, vol. 549, pp. 82–92, 2012.

[154] M. G. Lee, J. H. Kim, D. Kim, O. S. Seo, N. T. Nguyen, and H. Y. Kim, “Anisotropic Hardening of Sheet Metals at Elevated Temperature: Tension-Compressions Test Development and Validation,” *Exp. Mech.*, vol. 53, no. 6, pp. 1039–1055, 2013, doi: 10.1007/s11340-012-9694-1.

[155] S. H. Park, S. G. Hong, W. Bang, and C. S. Lee, “Effect of anisotropy on the low-cycle fatigue behavior of rolled AZ31 magnesium alloy,” *Mater. Sci. Eng. A*, vol. 527, no. 3, pp. 417–423, 2010, doi: 10.1016/j.msea.2009.08.044.

[156] L. Wu, “Mechanical Behavior and the Role of Deformation Twinning in Wrought Magnesium Alloys Investigated Using Neutron and Synchrotron X-ray Diffraction,” University of Tennessee, 2009.

[157] R. Procházka, J. Džugan, and M. Kövér, “Miniature specimen tensile testing of AZ31 alloy processed by ECAP,” *Arch. Mater. Sci. Eng.*, vol. 76, no. 2, pp. 134–139, 2015.

[158] J. Džugan, R. Procházka, and P. Konopík, “Micro-Tensile Test Technique Development and Application to Mechanical Property Determination,” in *Small Specimen Test Techniques: 6th Volume*, ASTM Inter., vol. 12, M. Sokolov, Ed. 2015, pp. 12–30.

[159] I. van Zyl, M. Moletsane, P. Krakhmalev, I. Yadroitsava, and I. Yadroitsev, “Validation of miniaturised tensile testing on DMLS Ti6Al4V (ELI) specimens,” *South African J. Ind. Eng.*, vol. 27, no. 3SpecialIssue, pp. 192–200, 2016, doi: 10.7166/27-3-1666.

[160] S. Faghih, S. B. Behravesh, and H. Jahed, “Incorporating asymmetric hardening behavior in modeling the cold expansion process of AZ31B sheet,” in *CSME*, 2018.

[161] G. A. Webster and A. N. Ezeilo, “Residual stress distributions and their influence on fatigue lifetimes,” *Int. J. Fatigue*, vol. 23, pp. 375–383, 2001.

[162] L. Trško, O. Bokůvka, F. Nový, and M. Guagliano, “Effect of severe shot peening on ultra-high-cycle fatigue of a low-alloy steel,” *Mater. Des.*, vol. 57, pp. 103–113, 2014, doi: 10.1016/j.matdes.2013.12.035.

[163] W.-C. Liu, J. Dong, P. Zhang, X.-W. Zheng, W.-J. Ding, D.-H. Li, and A. M. Korsunsky, “Smooth and notched fatigue performance of aging treated and shot peened ZK60 magnesium alloy,” *J. Mater. Res.*, vol. 25, no. 07, pp. 1375–1387, 2010, doi: 10.1557/JMR.2010.0173.

[164] C. Müller and R. Rodríguez, “Influence of Shot Peening on the Fatigue and Corrosion Behavior of the Die Cast Magnesium Alloy AZ91,” in *Shot Peening*, Wiley-VCH Verlag GmbH & Co, 2003.

[165] L. Dieng, D. Amine, Y. Falaise, and S. Chataigner, “Parametric study of the finite element modeling of shot peening on welded joints,” *JCSR*, vol. 130, pp. 234–247, 2017, doi:

10.1016/j.jcsr.2016.12.018.

[166] L. Tan, D. Zhang, C. Yao, D. Wu, and J. Zhang, “Evolution and empirical modeling of compressive residual stress profile after milling , polishing and shot peening for TC17 alloy,” vol. 26, pp. 155–165, 2017.

[167] “Standard Practice for Heat Treatment of Magnesium Alloys,” *ASTM Int.*, 2018, doi: 10.1520/B0661-12.2.

[168] Z. Yang, J. P. Li, J. X. Zhang, G. W. Lorimer, and J. Robson, “Review on Research and Development of Magnesium Alloys,” *Acta Metall. Sin. (English Lett.*, vol. 21, no. 5, pp. 313–328, Oct. 2008, doi: 10.1016/S1006-7191(08)60054-X.

[169] P. Fu, K. Zhan, and C. Jiang, “Micro-structure and surface layer properties of 18CrNiMo7-6 steel after multistep shot peening,” *Mater. Des.*, vol. 51, pp. 309–314, 2013, doi: 10.1016/j.matdes.2013.04.011.

[170] C. Drost gen and H. K. Schiffner, “Simulation of residual stresses by shot peening,” *Comput. Struct.*, vol. 72, no. 1–3, pp. 329–340, 1999.

[171] S. Al-Hassani, K. Kormi, K. Webb, and D. Webb, “Numerical simulation of multiple shot impacts,” in *7 th international conference on shot-peening*, 1999, pp. 217–227.

[172] J. Schwarzer, V. Schulze, and O. Vöhringer, “Evaluation of the Influence of Shot Peening Parameters on Residual Stress Profiles Using Finite Element Simulation,” *Mater. Sci. Forum*, vol. 426–432, pp. 3951–3956, 2003, doi: 10.4028/www.scientific.net/MSF.426-432.3951.

[173] T. Kim, H. Lee, H. C. Hyun, and S. Jung, “Effects of Rayleigh damping, friction and rate-dependency on 3D residual stress simulation of angled shot peening,” *Mater. Des.*, vol. 46, pp. 26–37, 2013, doi: 10.1016/j.matdes.2012.09.030.

[174] S. A. Meguid, G. Shagal, and J. C. Stranart, “Development and validation of novel FE models for 3D analysis of peening of strain-rate sensitive materials,” *J. Eng. Mater. Technol. Trans. ASME*, vol. 129, no. 2, pp. 271–283, 2007, doi: 10.1115/1.2712469.

[175] S. M. H. Gangaraj, M. Guagliano, and G. H. Farrahi, “An approach to relate shot peening finite element simulation to the actual coverage,” *Surf. Coatings Technol.*, vol. 243, pp. 39–45, 2014, doi: 10.1016/j.surfcoat.2012.03.057.

[176] T. Q. Pham, N. W. Khun, and D. L. Butler, “New approach to estimate coverage parameter in 3D FEM shot peening simulation,” *Surf. Eng.*, vol. 33, no. 9, pp. 687–695, 2017, doi: 10.1080/02670844.2016.1274536.

[177] S. Bagherifard, R. Ghelichi, and M. Guagliano, “Mesh sensitivity assessment of shot peening finite element simulation aimed at surface grain refinement,” *Surf. Coatings Technol.*, vol. 243, pp. 58–64, 2014, doi: 10.1016/j.surfcoat.2012.04.002.

[178] A. Gariépy, S. Larose, C. Perron, and M. Lévesque, “Erratum: Shot peening and peen forming finite element modelling - Towards a quantitative method,” *Int. J. Solids Struct.*, vol. 83, p. 183, 2016, doi: 10.1016/j.ijsolstr.2016.01.012.

[179] P. Sanjurjo, C. Rodríguez, I. Peñuelas, T. E. García, and F. J. Belzunce, “Influence of the target material constitutive model on the numerical simulation of a shot peening process,” *Surf. Coatings Technol.*, vol. 258, pp. 822–831, 2014, doi: 10.1016/j.surfcoat.2014.07.075.

[180] A. Ghasemi, S. M. Hassani-Gangaraj, A. H. Mahmoudi, G. H. Farrahi, and M. Guagliano, “Shot

peening coverage effect on residual stress profile by FE random impact analysis," *Surf. Eng.*, vol. 32, no. 11, pp. 861–870, 2016, doi: 10.1080/02670844.2016.1192336.

[181] K. Murugaratnam, S. Utili, and N. Petrinic, "A combined DEM-FEM numerical method for Shot Peening parameter optimisation," *Adv. Eng. Softw.*, vol. 79, pp. 13–26, 2015, doi: 10.1016/j.advengsoft.2014.09.001.

[182] F. Tu, D. Delbergue, H. Miao, T. Klotz, M. Brochu, P. Bocher, and M. Levesque, "A sequential DEM-FEM coupling method for shot peening simulation," *Surf. Coatings Technol.*, vol. 319, pp. 200–212, 2017, doi: 10.1016/j.surfcoat.2017.03.035.

[183] J. Zhang, S. Lu, T. Wu, Z. Zhou, and W. Zhang, "An evaluation on SP surface property by means of combined FEM-DEM shot dynamics simulation," *Adv. Eng. Softw.*, vol. 115, no. August 2017, pp. 283–296, 2018, doi: 10.1016/j.advengsoft.2017.10.001.

[184] H. Jahed, B. A. Moghadam, and M. Shambooli, "Re-Autofrettage," *J. Press. Vessel Technol.*, vol. 128, no. 2, p. 223, 2006, doi: 10.1115/1.2172619.

[185] H. Jahed and G. Ghanbari, "Actual Unloading Behavior and Its Significance on Residual Stress in Machined Autofrettaged Tubes," *J. Press. Vessel Technol.*, vol. 125, no. 3, pp. 321–325, 2003, doi: 10.1115/1.1593070.

[186] S. Faghih, H. Jahed, and S. B. Behravesh, "Variable Material Properties Approach: A Review on Twenty Years of Progress," *J. Press. Vessel Technol.*, vol. 140, no. 5, p. 050803, 2018, doi: 10.1115/1.4039068.

[187] W. Johnston, *Impact strength of materials*. Edward Arnold, 1972.

[188] K. Johnston, *Contact mechanics*. Cambridge University Press, 1985.

[189] M. Jebahi, A. Gakwaya, J. Levesque, O. Mechri, and K. Ba, "Robust methodology to simulate real shot peening process using discrete-continuum coupling method," *Int. J. Mech. Sci.*, vol. 107, pp. 21–33, 2016, doi: 10.1016/j.ijmecsci.2016.01.005.

[190] J. Davis and M. Ramulu, "A semi-analytical model of time dependent plastic strains induced during shot peening," *Int. J. Appl. Mech.*, vol. 5, no. 3, 2013, doi: 10.1142/S1758825113500270.

[191] W. Cao, R. Fathallah, and L. Castex, "Correlation of Almen arc height with residual stresses in shot peening process," *Mater. Sci. Technol.*, vol. 11, no. 9, pp. 967–973, 1995.

[192] H. Y. Miao, D. Demers, S. Larose, C. Perron, and M. Levesque, "Experimental study of shot peening and stress peen forming," *J. Mater. Process. Technol.*, vol. 210, no. 15, pp. 2089–2102, 2010, doi: 10.1016/j.jmatprotec.2010.07.016.

[193] G. Johnson and W. Cook, "A Constitutive Model and Data for Metals Subjected to Large Strains, High Strain Rates, and High Temperatures," in *Proceedings 7th International Symposium on Ballistics*, 1983, pp. 541–547.

[194] B. Bhuvaraghan, S. M. Srinivasan, B. Maffeo, and O. Prakash, "Analytical solution for single and multiple impacts with strain-rate effects for shot peening," *C. - Comput. Model. Eng. Sci.*, vol. 57, no. 2, pp. 137–158, 2010, doi: 10.3970/cmes.2010.057.137.

[195] T. Özel and Y. Karpat, "Identification of constitutive material model parameters for high-strain rate metal cutting conditions using evolutionary computational algorithms," *Mater. Manuf. Process.*, vol. 22, no. 5, pp. 659–667, 2007, doi: 10.1080/10426910701323631.

[196] J. D. Seidt, “Plastic Deformation and Ductile Fracture of 2024-T351 Aluminum under Various Loading Conditions,” The Ohio State University, 2010.

[197] Y. Bao and R. Treitler, “Ductile crack formation on notched Al2024-T351 bars under compression-tension loading,” *Mater. Sci. Eng. A*, vol. 384, no. 1–2, pp. 385–394, 2004, doi: 10.1016/j.msea.2004.06.056.

[198] A. Yazdanmehr and H. Jahed, “Effect of loading strain rates on unloading behavior of shot peened materials,” in *The Canadian Society for Mechanical Engineering International Congress 2018*, 2018.

[199] A. Stacey, G. A. Webster, R. L. Campoux, J. H. Underwood, and J. A. Kapp, “Determination of Residual Stress Distributions in Autofrettaged Tubing\rStress Intensity Factors Caused by Residual Stress Fields in Autofrettaged Tubing,” *Int. J. Press. Ves. Piping, 31, 1988, 205-220*, vol. STP 1004, pp. 37–53, 1988.

[200] H. Jahed and R. N. Dubey, “An Axisymmetric Method of Elastic-Plastic Analysis Capable of Predicting Residual Stress Field,” *J. Press. Vessel Technol.*, vol. 119, no. 3, p. 264, 1997, doi: 10.1115/1.2842303.

[201] M. A. S. Torres and H. J. C. Voorwald, “An evaluation of shot peening, residual stress and stress relaxation on the fatigue life of AISI 4340 steel,” *Int. J. Fatigue*, vol. 24, pp. 877–886, 2002, doi: 10.1016/S0142-1123(01)00205-5.

[202] J. Almen, “Shot blasting test,” US2350440A, 1944.

[203] X. F. Sheng, Q. X. Xia, X. Q. Cheng, and L. S. Lin, “Residual stress field induced by shot peening based on random-shots for 7075 aluminum alloy,” *Trans. Nonferrous Met. Soc. China (English Ed.*, vol. 22, pp. 261–267, 2012, doi: 10.1016/S1003-6326(12)61717-8.

[204] J. Lee and A. F. Yee, “Fracture behavior of glass bead filled epoxies: Cleaning process of glass beads,” *J. Appl. Polym. Sci.*, vol. 79, no. 8, pp. 1371–1383, 2001, doi: 10.1002/1097-4628(20010222)79:8<1371::AID-APP40>3.0.CO;2-O.

[205] D. J. Shuman, A. L. M. Costa, and M. S. Andrade, “Calculating the elastic modulus from nanoindentation and microindentation reload curves,” *Mater. Charact.*, vol. 58, no. 4, pp. 380–389, 2007, doi: 10.1016/j.matchar.2006.06.005.

[206] R. Hill, “A theory of the yielding and plastic flow of anisotropic metals,” *Proc. R. Soc. London.*, vol. 193, no. 1033, pp. 281–297, 1948, doi: 10.1098/rspa.1948.0045.

[207] M. Zhao, V. Kannan, and K. T. Ramesh, “The dynamic plasticity and dynamic failure of a magnesium alloy under multiaxial loading,” *Acta Mater.*, vol. 154, p. 124−136, 2018, doi: 10.1016/j.actamat.2018.05.012.

[208] S. Kurukuri, M. J. Worswick, D. G. Tari, R. K. Mishra, and J. T. Carter, “Rate sensitivity and tension – compression asymmetry in AZ31B magnesium alloy sheet,” *Phil. Trans. R. Soc. A*, vol. 372, pp. 1–16, 2014.